

Shape Fabric Development
During
Progressive Deformation

Dissertation zur Erlangung des Grades

"Doktor der Naturwissenschaft"

am Fachbereich Geowissenschaften
der Johannes Gutenberg-Universität in Mainz

Sandra Caroline Piazolo,
geboren am 26.05.1971
in Ulm

Mainz, November 2000

Erklärung

Ich versichere hiermit, die vorliegende Arbeit selbständig und nur unter Verwendung der angegebenen Quellen und Hilfsmittel verfaßt zu haben.

All views and results presented in this thesis are those of the author, Sandra Piazzolo, unless stated otherwise

Mainz, Dezember 2000

Jahr der Prüfung: 2001

Acknowledgments

Although a PhD thesis is officially the work of one person, it is based on the sum of discussions, exchanges of ideas and experiences collected during the course of a thesis. Without the stimulating environment provided in Mainz, Melbourne and at international meetings, this thesis would not have been possible.

Special thanks to my supervisor for the initiation of this study and continuous support and interest, while leaving enough space to develop my own ideas and focus of the study. Many thanks to the assistant of the Tectonophysics group, who took intense interest in my study and who was always available for discussions, thorough and constructive reviews of chapters and papers to be submitted. I wish to thank my PhD peers of the geoscience department in Mainz. Special thanks to my office mate for hours of discussions, honest evaluation of ideas, friendship and fun. Many thanks to the “Kaffeerunde”. Further I would like to thank the various secretaries of the department for organizing things and doing all the necessary paper work.

Many thanks to the computer specialist at Monash University, who patiently endured my frequent questions and requests concerning Elle. Special thanks to the Elle group and the members of the Earth Science Department at Monash University for a warm welcome and support. Thanks to my St.Kilda flatmates without their friendship my stays in Melbourne would not have been as enjoyable as they were.

I would like to give special thanks to my flatmate in Mainz, who provided for me a true home in Mainz.

Very last, but very importantly, I would like to express many thanks to my parents and to my brothers, who always supported me in whatever I decided to do and who patiently bear a daughter or sister who is always on the move.

A big, big THANK YOU to all of you.

This work financially supported by the German Research Foundation (GRK 392/1) and the German Academic Exchange Program (DAAD).

**To
my parents**

*... every structure in a rock is significant, none is unimportant,
even if, at first sight it may seem irrelevant.*

E. Cloos, 1946

... unter solchen Fragen haben wir vor der Kapelle eine Bank erreicht ...
Verschiebung an glatten und hölzernen Flächen - unwillkürlich fühlen und imitieren wir sie mit den Fingern beider Hände. Und dann dehnen wir die leichten Spielzeuge ins Erdweite und Riesenhafte und belasten sie mit dem ganzen Gewicht der Felsen und der Kiesmassen, der Berge und Städte, der Wälder und der bunten Geflechte menschlicher Wege und Wohnungen. Und lassen sie aufs neue sinken und steigen, vernehmen das klirrende Bersten der steinernden Blöcke, den Knall aufreißender Spalten und das Rollen und Ächtzen gleitender und doch unter der Last von Gebirgen allzu rauher, reibender Verschiebung. Und spüren vielleicht die Hitze der an körnigen Fugen gebremsten Verrückung, vernehmen den Ätzgeruch von Gasen der Tiefe, die aus der frisch aufgeplatzten Spalte hervorbrechen und den chemischen Dampf der unterirdisch kreisenden Wasser. Und vielleicht schenkt uns ein günstiges Geschick, daß der Boden wirklich ein wenig zittert und wir also erfahren, die alte große Bewegung sei noch heute im Gange, millimeterhaft und im Abstand von Jahrzehnten. Aber was bedeutet dies, geschöpft aus dem
Zeitmeer der Erdgeschichte?

... Laßt sehen: Könnte man nicht Spuren der Bewegung selber finden? Den Pickel zur Hand! Ein Stück Fläche wird freigelegt, gewischt, gewaschen. Lampe und Lupe her: Ja, da sind die feinen geraden Linien, die beinahe mikroskopisch zarten Geleise, auf denen ein Gebirge zu Tal fuhr. Steil laufen sie über die Fläche bergab und verzeichnen die Bewegung wie einen Handschrift der Erde.

Rheingrabenverwerfung-Lorettoberg, Gespräch mit der Erde, H. Cloos, 1947

And I think to myself, what a wonderful world ...

L. Armstrong

Summary

The research project presented in this thesis focusses on shape fabric development during progressive deformation by means of field observations, numerical simulations and analogue modelling. Aim of the work was to gain a better understanding of how shape fabrics evolve and on this basis assess the use of shape fabrics in structural geology. In order to interpret the shape fabric of a rock both kinematically and dynamically, it is vital to know how the shape fabric form and evolve throughout deformation and time, what processes are involved and which factors influence the shape fabric development in a rock.

The development of shape fabrics observed in natural examples is described and discussed in Chapter 2. Samples used were collected from well-exposed discrete low to medium grade shear zones in the Cap de Creus area, NE Spain. This study shows that shape fabrics can only to a limited extent be used as direct indicators for strain magnitude. The proposed reason for this is that the intensity of a shape fabric is significantly influenced by the initial fabric of a rock i.e the grain size ratio between initial and recrystallized grains and the mode at which dynamic recrystallization modifies the shape fabric during progressive deformation. Due to the significant effect of other factors than strain magnitude on the development and strength of a shape fabric, a study looking at possible strain magnitude and movement direction should preferably involve the study of several rock types.

In Chapter 3 numerical simulations are used to develop an understanding of the findings given in Chapter 2. In simulations the fabric development of a monomineralic microstructure deformed in a simple shear at low to medium grade conditions is modelled. The developed numerical model simulates dynamic recrystallization involving viscous deformation, lattice rotation, subgrain formation, rotational recrystallization, recrystallization by nucleation of new grain and recovery. Simulations show that the ratio between the initial and recrystallized grain size, recrystallization rates and values for grain boundary mobility significantly and systematically influence the shape fabric of a deforming rock. In coarse grained microstructures which have a high ratio of initial and recrystallized grain size, strong shape fabrics are most likely to develop. In the course of this part of the study methods were developed to characterize a microstructure more accurately and/or quantitatively and some microstructures indicative for a certain set of parameters and dominance of mechanisms are delineated. In addition, it is shown that with the numerical modelling environment Elle it is possible to simulate the effects of a complex system of concurrent and interacting microstructural processes on a microstructure.

In Chapter 4 the use of polymers and related materials as rock analogues is discussed. It is shown that measurement of just viscosity is not sufficient to completely describe the mechanical behaviour of a material. Detailed rheological measurements are needed to assess the suitability of a material as a rock analogue.

A newly developed and built deformation apparatus (transpression/transension (TT) apparatus) is described in Chapter 5. With this apparatus it is possible to model homogeneous deformation in general flow regimes, in which all combinations of simple shear parallel to the xy-plane and pure shear parallel to x-, y- and z-axis can be realised. Possible materials which can be deformed in this apparatus include the materials investigated in Chapter 4.

The subject of Chapter 6 is the development of the shape preferred orientation of populations of rigid objects dispersed in different matrix materials. Experiments with different types of plane strain monoclinic flow are performed with the developed TT apparatus. Results show that for rigid object populations with high aspect ratios the intensity of the shape preferred orientation is positively related to an increase in pure shear component of the applied deformation. In a matrix material with non-Newtonian, power-law flow behaviour the intensity of the shape preferred orientation is higher than in a Newtonian viscous material. Significant strain partitioning is observed in both matrix materials; it is most profound in the power law matrix materials.

Analogue experiments modelling the shape development of isolated viscous inclusions embedded in a viscous matrix deformed in a circular high strain simple shear zone are described and discussed in Chapter 7. For experiments a modified viscometer was developed. This chapter sheds light on the limitations and possibilities of the use the three dimensional shape of isolated, deformable objects for strain analyses in terms of strain magnitude and type of flow. Different viscosity contrasts between matrix and inclusion result in characteristic types of shape development. Permanently stretching ellipsoids which become more and more elongated during progressive deformation can be used for strain analyses if the viscosity ratio is known. Pulsating ellipsoids which change their shape periodically from a sphere to an ellipsoid during progressive deformation cannot be used for strain analyses.

In Chapter 8 general conclusions are drawn. These are based on the findings of preceding chapters and evaluate the use of shape fabrics for strain analysis and other geological problems. Additionally, suggestions for further research are made.

Zusammenfassung

In der vorliegenden Arbeit wird die Entwicklung von Formregelungs-Gefügen während der fortschreitenden Verformung untersucht. Ziel ist es, ein besseres Verständnis für die Gefügeentwicklung zu erarbeiten und basierend auf diesem Verständnis, neue Methoden zur Charakterisierung und zur Interpretation von beobachteten Gefügen zu entwickeln. Um ein Formregelungs-Gefüge im Bezug auf die Dynamik und Kinematik eines Gesteins interpretieren zu können, ist es notwendig die Entstehung und Entwicklung eines solchen Gefüges während der Verformung zu verstehen. Wichtig ist es, die Mechanismen, Parameter und Faktoren zu kennen, die die Entwicklung eines Formregelungs-Gefüges maßgeblich beeinflussen.

Im zweiten Kapitel dieser Arbeit wird die Entwicklung von Formregelungs-Gefügen in Gesteinsproben untersucht. Die Proben stammen von diskreten, nieder- bis mittelgradigen Scherzonen der Cap de Creus Halbinsel, Spanien. Detaillierte Untersuchungen zeigen, daß der Grad der Formeinregelung nicht zwingend mit dem Ausmaß der Verformung gleichzusetzen ist. Wichtige beeinflussende Faktoren sind, neben der Rotation von rigiden Objekten, das Korngrößenverhältnis der ursprünglichen Korngröße und der Korngröße der rekristallisierten Körner und die Art und Weise wie dynamische Rekristallisation das Gefüge während der Verformung modifiziert. Da diese Faktoren in unterschiedlichen Lithologien das Gefüge unterschiedlich beeinflussen, ist es ratsam, die Gefügeentwicklung in verschiedenen Lithologien zu untersuchen, um sich ein gutes Bild über den tatsächlichen Grad und der Art der Verformung schaffen zu können.

Im dritten Kapitel werden mit Hilfe eines entwickelten numerischen Modellierungsprogramms die Ergebnisse aus den Untersuchungen an natürlichen Proben untermauert und Interpretationen weiterentwickelt. In den Simulationen wird die Gefügeentwicklung eines monomineralischen Gesteins modelliert, welches bis zu einem Verformungsausmaß von 2 geschert wird. Das Model simuliert viskose Verformung, Rotation von kristallographischen Achsen, Entwicklung von Subkörnern, Rotationsrekristallisation, Rekristallisation durch Neuwachstum, Korngrenzenwanderung und Verheilung von Defekten im Kristallgitter. Simulationen zeigen, daß das Verhältnis von ursprünglicher zu rekristallisierter Korngröße, die Rekristallisationsrate und die Mobilität der Korngrenzen maßgeblich und systematisch das Gefüge eines Gesteins beeinflussen. In grobkörnigen Gefügen, welche ein hohes Verhältnis von ursprünglicher zu rekristallisierter Korngröße aufweisen, entwickelt sich in der Regel ein starkes Formregelungs-Gefüge. Im Zuge dieser Untersuchungen wurden Methoden entwickelt, um die Charakteristika eines Gefüges genau darstellen und quantifizieren zu können. Außerdem wurden festgestellt, daß bestimmte Charakteristika eines Gefüges auf eine bestimmte Kombination von Parameterwerten und dominanten Mechanismen hinweisen. Simulationen veranschaulichen, daß es mit der numerischen Modellierungsumgebung Elle möglich ist den komplexen Einfluß von mehreren, zeitgleich aktiven Prozessen auf die Gefügeentwicklung eines Gesteins zu modellieren.

In Kapitel 4 wird auf den Nutzen von Polymeren und verwandten Materialien als Analogmaterialien für deformierte Gesteine eingegangen. Es zeigt sich, daß Polymere ein kompliziertes Fließverhalten haben. Reine Viskositätsmessungen sind unzureichend, um ein solches Material rheologisch zu charakterisieren.

Ein neu entwickeltes Verformungsgerät wird in Kapitel 5 vorgestellt. Mit diesem Apparat ist es möglich, eine große Anzahl von verschiedenen monoklinen Beanspruchungsplänen kontrolliert zu modellieren. Materialien, die in diesem Gerät verformt werden können, sind zum Beispiel die in Kapitel 4 beschriebenen Polymere und verwandten Materialien.

Das Thema von Kapitel 6 ist die Entwicklung von Formregelungs-Gefügen von Populationen von rigiden Objekten, die in verschiedenen Matrixmaterialien verteilt sind. Experimente in verschiedenen Typen von monoklinem Fließen werden mit dem in Kapitel 5 beschriebenen Verformungsgerät durchgeführt. Ergebnisse zeigen, daß der Grad der Einregelung einer Population von rigiden Objekten mit hohen Längen- zu Breitenverhältnis positiv mit der Zunahme der Komponente der Reinen Scherung korreliert ist. In einem Matrixmaterial, welches ein nicht-Newtonianisches, nicht-lineares Fließverhalten aufweist, ist der Grad der Einregelung höher als in einen Newtonianischen Material. Lokalisation von Verformung ist in beiden Materialien zu sehen. In der nicht-Newtonianische, nicht-linearen Matrix ist diese Lokalisation stark ausgeprägt.

In Kapitel 7 wird mit Hilfe von Analogexperimenten die dreidimensionale Formentwicklung von viskosen Objekten untersucht, die in einer viskosen Matrix eingebettet sind. Eine kreisförmige einfache Scherzone, in der ein Material bis zu sehr hohen Verformungsgraden deformiert werden kann, wird mit einem modifizierten Viskosimeter modelliert. Dieses Kapitel gibt Aufschluß über die Grenzen und Möglichkeiten der Nutzung der Formentwicklung eines viskosen Objektes zur Erfassung des Grades und dem Typ der Verformung des umgebenden Materials. Verschiedene Viskositätskontraste zwischen Matrix und Objekt resultieren in verschiedenen Typen der Formentwicklung. Wird ein Objekt kontinuierlich zu einem mehr und mehr länglichen Objekt verformt, so kann dieses für die Analyse der Verformung zur Hilfe genommen werden. Voraussetzung ist es jedoch, den Viskositätskontrast zwischen Matrix und Objekt zu kennen. Verhält sich das Objekt wie ein pulsierendes Ellipsoid, das heißt dessen Form ändert sich periodisch von einer Kugel zu einem Ellipsoid und wieder zu einer Kugel, so kann es nicht für die Verformungsanalyse benutzt werden.

In dem abschließenden Kapitel 8 werden Schlußfolgerung gezogen, die sich aus den Einzelergebnissen der Kapitel dieser Arbeit folgen. Diese Schlußfolgerung beziehen sich vorallem auf den Nutzen von Formregelungs-Gefügen zur Charakterisierung der Verformung eines Gesteins. Zusätzlich werden einige Möglichkeiten für weitere Untersuchungen geben.

Contents

Acknowledgements

Summary

Zusammenfassung

Chapter 1

Introduction: Background, problems and aims	13
1.1 Background and previous work	13
1.2 The use of shape fabrics in structural geology - Problems and associated questions	19
1.3 Methods of investigation	21
1.4 Setup of thesis	22
1.5 Published parts	23

Chapter 2

Lineation developmetn in low to medium grade shear zones: A study from the Cap de Creus peninsula, NE Spain.	25
2.1 Introduction	25
2.2 Terminology of lineations	26
2.3 Geology of the Cap de Creus Peninsula, Spain	27
2.4 Development of volume lineations in low to medium grade shear zones at Cap de Creus	30
2.5 Mechanisms of volume lineation development	38
2.6 Conclusions - Predictions for volume lineation development	42

Chapter 3

Numerical modelling of dynamic recrystallization using Elle: Description of the model, new techniques of microstructural analysis and first results of simulations	49
3.1 Introduction	50
3.2 Numerical model Elle	52
3.3 Analytical methods	73
3.4 Simulations	78
3.5 Discussion of numerical model and analytical techniques	120
3.6 Conclusions	123

Chapter 4

Are polymers suitable rock-analogs?	127
4.1 Introduction	127
4.2 Structure and deformation of polymeric liquids	128
4.3 Rheological measurements	135
4.4 Implications for the use of polymers and related materials as rock analogs	142
4.5 Conclusions	142

Chapter 5

A new apparatus for controlled general flow modeling of analog materials	145
5.1 Introduction	145
5.2 Description of the apparatus	147
5.3 Experimental materials	150
5.4 Types of flow modeled by new apparatus	151
5.5 Flow tests and boundary conditions	153
5.6 Pilot experiments: Rotation of mica-fish in plane strain	156
5.7 Conclusions	158

Chapter 6	
Influence of rheology and vorticity on fabric development of populations of rigid objects during progressive plane strain deformation	159
6.1 Introduction	159
6.2 Experimental setup	160
6.3 Analytical methods	162
6.4 Experimental results	163
6.5 Discussion	168
6.6 Conclusions	169
Chapter 7	
A new apparatus for controlled general flow modeling of analog materials	171
7.1 Introduction	171
7.2 Experimental method	173
7.3 Experimental results	180
7.4 Validity of experimental results for natural examples	188
7.5 Application of experimental results on the interpretation of the shape and orientation of inclusions observed in rocks	190
7.6 Conclusions	194
Chapter 8	
Conclusions and suggestions for further work	197
8.1 General remarks	197
8.2 Shape fabric development during progressive deformation	198
8.3 Possibilities and limitations of the use of shape fabric in structural analyses	200
8.4 Microstructural features associated with shape fabric: their possible use for kinematic analyses and new tools for their description and analysis	202
8.5 Remaining problems and suggestions for future research	202
Appendix A	
Detailed description of samples of investigated shear zones	205
Appendix B	
The von Mises Distribution	207
Appendix C	
Additional information on Elle and test experiments	211
Appendix D	
Rheology of a mixture of 60wt% Plastilina/ 40wt% Rhodorsil Gomme	221
Appendix E	
Description and use of programs controlling the new deformation apparatus	223
Appendix F	
CD-Rom: Calculations and Movies	231
References	233
Zusammenfassung für Laien	249
Curriculum vitae	251

Chapter 1

Introduction: Background, problems and aims

1.1 Background and previous work

1.1.1 General introduction

Macroscopic and microscopic structural features which are present in deformed rocks are a source of information which can be used by geologists to derive conditions during which the rock was formed, deformed and/or metamorphosed. Additionally, processes responsible for the formation of these structures may be derived (Vernon, 1976; Hobbs et al., 1976; Ramsay and Huber, 1983; Twiss and Moores, 1992; Hamner and Passchier, 1991; Passchier and Trouw, 1996). One of these features is the shape fabric that is commonly used for strain analyses in terms of strain magnitude and the type of flow.

The shape fabric of a rock has two aspects. These are (a) the mean values of the three dimensional, non-equidimensional shape and (b) the shape preferred orientation of a population of objects (Fig. 1.1). Objects can be rigid or deformable. Examples for a shape fabric with deformable objects are populations of individual grains and/or aggregates of a specific mineral species, such as strongly elongated quartz or feldspar grains (e.g. Olding, 1984), aggregates of biotite and feldspar, reduction spots in a shale, elongated pebbles in a conglomerate (Lisle et al. 1983; Lisle, 1985; Freeman, 1987; Freeman and Lisle, 1987), or ellipsoidal mafic inclusion in an igneous rocks (e.g. Tobisch and Williams, 1998). Examples for a shape fabric with rigid objects are populations of elongate mm-scale to cm-scale mica, kyanite and sillimanite grains in metamorphic rocks and feldspar laths in granitoids (e.g. Ildefonse et al., 1990 and references therein; Bouchéz, 1997 and references therein).

The shape of an individual, deformable object and the mean shape of a population of object show two main features. These are the aspect ratios of its axes in two and three dimensions and the absolute values of the length of the axes. Flinn (1978) suggested to use a specific graph to quantify and graphically illustrate the three dimensional shape characteristics. In this graph two defined axial ratios are plotted against each other. In such a plot three different types of tectonites are distinguished according to the three dimensional shape fabric characteristics. These are LS-, L- and S-tectonite (Fig. 1.2); whereby L-tectonites show a strongly elongate shape fabric, a S-tectonite a planar, oblate shape fabric and LS-tectonite a combination of the latter two shape fabrics.

Populations of elongate and rigid or deformable objects may show a shape preferred orientation (SPO), which describes the preferred orientation of the long axes of a population of non-equidimensional objects. These populations of objects are either dispersed in a matrix material or encompass most of the rock. The development of the SPO of a population of rigid objects has been investigated experimentally (e.g. Fernandez, 1987; Ildefonse, 1992a, 1992b; Ildefonse and Mancktelow, 1993; Arbaret et al., 1997; Fernandez and Fernandez-Catuxo, 1997) and analytically (e.g. Jezek et al., 1994, 1996; Masuda et al., 1995b).

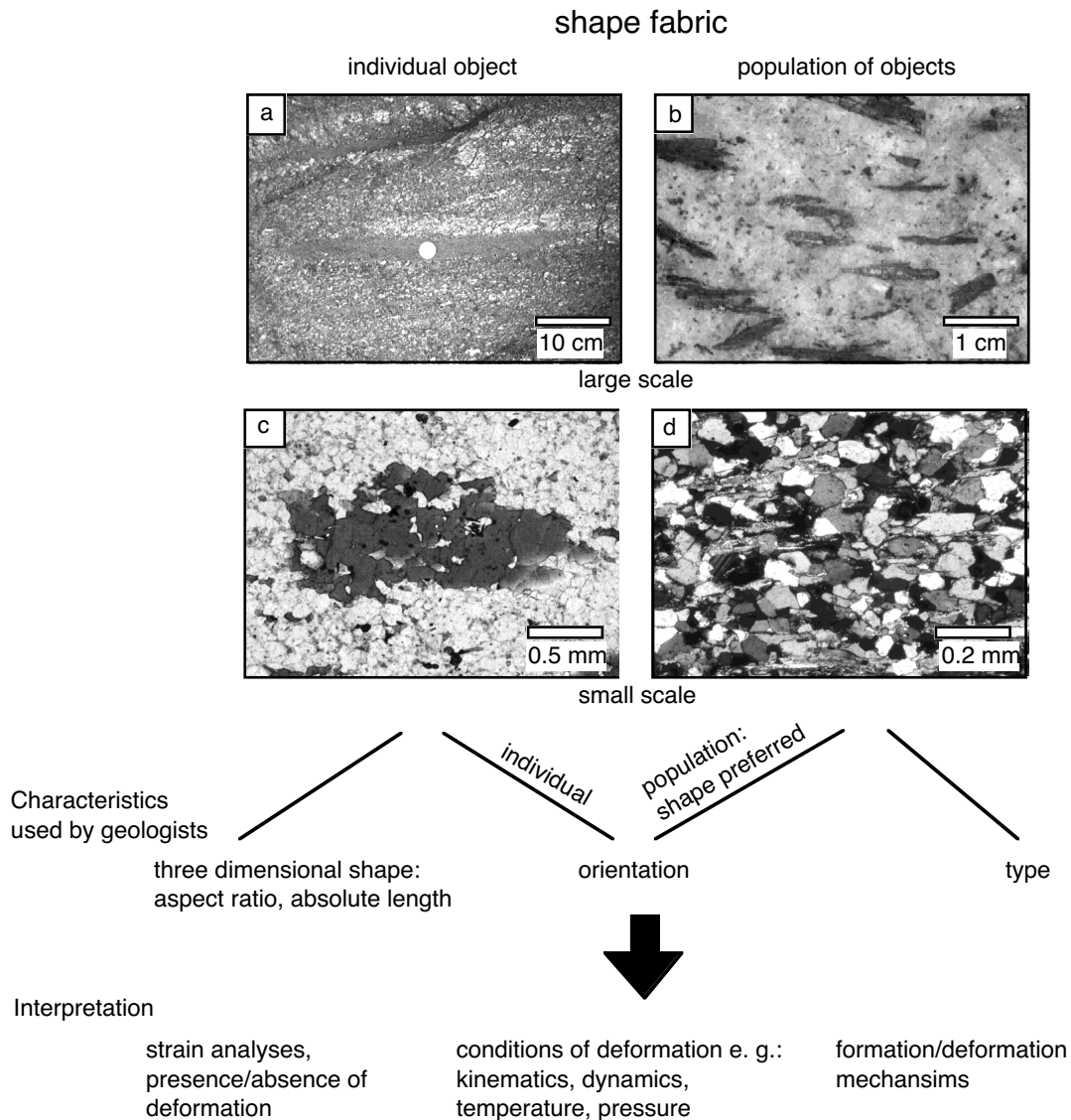


Figure 1.1 Schematic diagram of the use of shape fabrics in structural geology. (a) Photograph depicting an elongate mafic enclave which forms an element of a shape fabric - stretching lineation developed in a granitoid, Rosas granitoid, NE Spain. (b) Photograph of a shape fabric formed by alignment of actinolite grains in marble; scale bar = 1 cm. Sample is from the Wywyanna Formation, Lower Adelaidean, NW from Arkaroola Village, Northern Flinders Ranges, South Australia (courtesy of P. D. Bons, University of Mainz, Germany). (c) Photomicrograph of biotite grain which forms an element of a shape fabric - mineral lineation developed in fine grained metapsammite, Cap de Creus, Spain, crossed nicols. (d) Photomicrograph a shape fabric formed by the alignment of biotite and quartz grains in a metapsammite, Cap de Creus, Spain, crossed nicols.

Stretching and mineral lineations (Fig. 1.1a and Fig. 1.1b; e.g. Price and Cosgrove, 1990; Ghosh, 1993; Passchier and Trouw, 1996) are prolate shape fabrics and as such form subsets of all shape fabrics.

Methods to quantify the orientation and intensity of a shape fabric in two dimensions include the $R_f\text{-}\Phi$ method (Ramsay, 1967), the use of the density distribution function (Fernandez, 1978), the automatic analysis of Launeau et al. (1990), the PAROR and SURFOR methods (Panozzo, 1983, 1984), the autocorrelation function (Heilbronner, 1992) and the use of the von Mises distribution of directional data (Masuda et al., 1999).

In order to interpret the shape fabric of a rock both kinematically and dynamically, it is vital to know how the fabric elements form and evolve throughout deformation and time, what processes are involved and which factors influence the shape fabric development of a rock. The development of shape fabrics and with this the implications for the use of shape fabrics in structural geology, is the subject of this thesis. In the following sections, shape fabric forming processes are described, the use of shape fabrics in structural geology outlined, and the problems and related remaining question with respect to the limitations and possibilities of the use of shape fabric in structural analyses are discussed. This is followed by an outline of methods that can be used to study shape fabric development and investigations undertaken in this thesis.

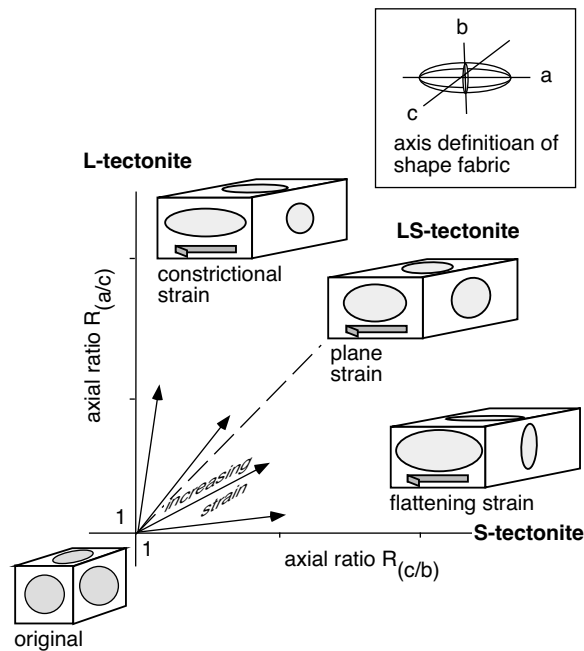


Figure 1.2 Flinn diagram depicting the different fields of deformation types and tectonites according to the shape fabric of a rock. $R_{(a/c)}$ and $R_{(c/b)}$ are the aspect ratios of the different axes of the three dimensional shape of a deformable object (for definition of axes see inset).

1.1.2 Shape fabric forming processes

1.1.2.1 Rotation and deformation

The shape and orientation of a rigid or viscous object can change during progressive deformation, whereby the volume of the object is assumed to remain constant. Rock deformation experiments (e.g. Means and Paterson, 1966; Etheridge, 1971) show that rotation which is frequently coupled with deformation is a process probably responsible for the development of shape fabrics. Such rotations and deformation are thought to occur in three different ways, each of which is described by a specific model (Fig. 1.3):

(a) Jeffery's model:

Jeffery (1922) described the motion (e.g. rotation rate) of a rigid elliptical object embedded in a Newtonian viscous matrix in two dimensional simple shear flow. Basing their work on the model of Jeffery (1922), Ghosh and Ramberg (1976) and Jezek et al. (1994, 1996) investigated the rotation of rigid elongate particles in homogeneous viscous Newtonian matrixes within different types of flow. Additionally, experiments with rigid inclusions in viscous matrixes have been performed (e.g. Bhattacharyya, 1966; Gay, 1966, 1968; Rees, 1968, 1979; Ferguson, 1979; Ildefonse et al., 1992a, 1992b). In simple shear an individual object rotates cyclically in a Newtonian viscous matrix. It may therefore undergo multiple revolutions during bulk straining. In two dimensional homogeneous flow, the rotation rate of a rigid elliptical object embed-

ded in a viscous Newtonian matrix material depends on the type of flow in terms of kinematic vorticity number of deformation (Means et al., 1980), slip on the object interface and the orientation and the axial ratio of the inclusion (Ghosh and Ramberg, 1976; Odonne, 1994; Pennacchioni, 2000). Investigations of Ferguson (1979), Bons et al. (1997) and Pennacchioni (2000) show that the power law exponent of a non-Newtonian matrix does not significantly influence the rotation rate of an individual rigid object embedded in such a matrix material.

(b) March model:

The rotation of a passive region in a homogeneous continuum is different from that of a rigid object in a viscous matrix. During simple shearing, for example, passive objects do not rotate continually but instead approach a limiting orientation parallel to the shear plane (March, 1932). They cannot rotate past the shear plane, and the rotation rate approaches zero as objects approach parallelism with the shear plane. This results in the concentration of passive objects subparallel to the shear plane; hence a shape preferred orientation is produced. This model is often used to explain the development of foliation planes in deformed rocks (Means, 1981 and references therein).

(c) Dislocation glide and the Taylor-Bishop-Hill model:

Flow by the conservative motion, or glide, of dislocations on internal crystallographic slip planes of a mineral grain result in deformation and rotation of a crystal. This model (Taylor, 1938; Bishop and Hill, 1951a, 1951b; Lister and Paterson, 1979) has been used to explain the development of crystallographic preferred orientations (e.g. Jessell and Lister 1990; Wenk et al. 1991; Takeshita et al., 1999).

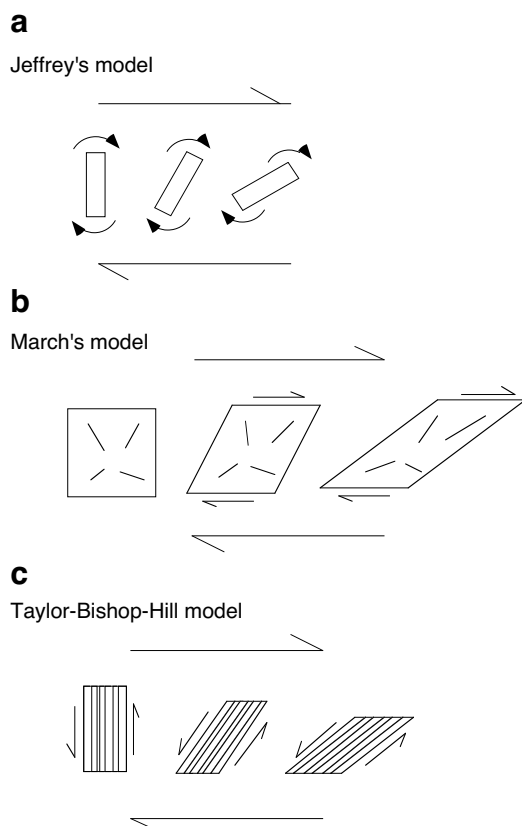


Figure 1.3 Illustration of the three models for mechanical rotation in shear rocks. (a) Jeffrey's model, (b) March's model and (c) Taylor-Bishop-Hill model. For further details see text.

1.1.2.2 Syntectonic growth, metamorphic reaction, dissolution/precipitation and recrystallization

Shape fabric forming processes during which the object does not retain its original volume and the geometry of its boundaries are syntectonic growth, metamorphic reaction, dissolution/precipitation and recrystallization.

Syntectonic growth of new mineral phases and metamorphic reactions change the mineral content of a rock and thereby determine what minerals are available to form a shape fabric (e.g. Etheridge, 1971; Vernon, 1987). Newly grown elongate objects will rotate (see above) or may grow in the shear direction during progressive deformation. In both cases, a strong shape fabric can develop. Redistribution of phases due to dissolution, diffusion, transport and redeposition of quartz, feldspar (e.g. O'Hara, 1990) and carbonates (Robin, 1979; Bell and Cuff, 1989; Dewers and Ortoleva, 1990; Azor et al., 1997) may destruct or cause the formation of a shape fabric.

Recrystallization leads to a rearrangement of grain boundaries, shape and structure; therefore, it can strongly influence the development of shape fabrics in rocks. It involves the establishment of arrays of grain boundaries in new material positions (Means, 1983) and the formation and/or migration of grain boundaries (Vernon, 1981). In many cases this leads to the development of new grains at the cost of old ones (Urai et al., 1986). In general, two main mechanisms of recrystallization are cited: rotational recrystallization and grain boundary migration recrystallization (e.g. Poirier and Nicolas, 1975; Guillopé and Poirier, 1979; Fitz Gerald et al., 1983; Means, 1983; Olsen and Kohlstedt, 1985; Poirier, 1985; Urai et al., 1986; Lloyd et al., 1992; Takeshita et al., 1999; Shigematsu, 1999; Heidelbach et al., 2000). In addition, Drury (1984), Drury et al. (1985) and Drury and Urai (1990) distinguish between subgrain formation, rotational recrystallization, recrystallization by nucleation and grain boundary migration (Fig. 1.4); each of these mechanisms results in characteristic microstructures and modification or development of a shape fabric. For example, in a monomineralic rock composed of large equidimensional grains, recrystallization synchronous with deformation i.e. dynamic recrystallization may result in the development of a microstructure characterized by elongate, large relict grains surrounded by small equidimensional grain (Fig. 1.5). In hand specimen such elongate grains are recognized as a shape fabric.

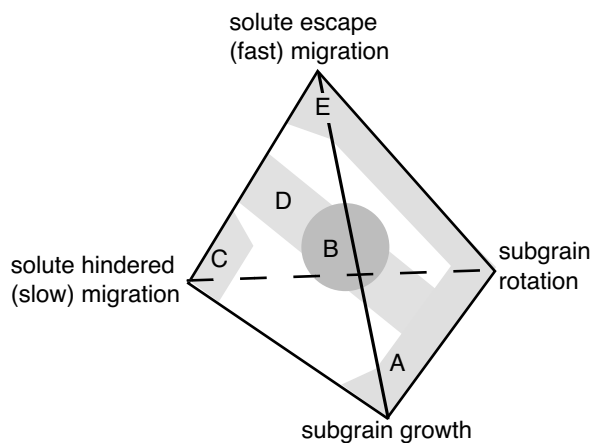


Figure 1.4 Recrystallization mechanism diagram (modified after Drury and Urai, 1990). Grey field show different recrystallization regimes that are characterized by the dominance of specific mechanisms or combinations of mechanisms: regime A: continual rotational recrystallization; B: continual rotation and migration with discontinual migration; regime C: continual migration recrystallization; regime D: rotation recrystallization with discontinual stage of new grain development; regime E: continual rotation and discontinual migration.

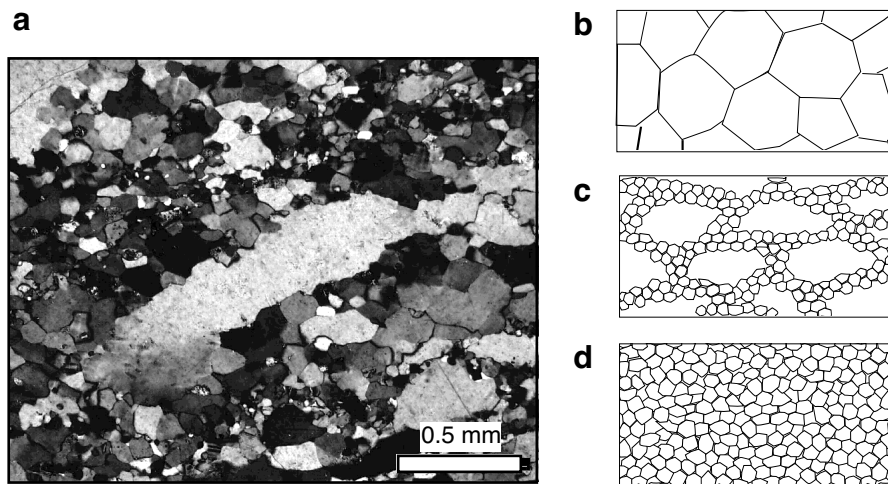


Figure 1.5 (a) Photomicrograph of an elongate quartz grain which forms an element of a shape fabric developed in a partially recrystallized quartz-feldspar mylonite, Schirmacher Oasis, Antarctica; crossed nicols. (b) - (d) Schematic diagram showing the effect of recrystallization on the development of a shape fabric in a monomineralic rock. (b) Initially coarse grained textures, no shape fabric, (c) moderate degree of dynamic recrystallization at rims of large, coarse grained crystals, well developed shape fabric, (d) high degree of dynamic recrystallization, grains are fine in size and the grain size distribution is unimodal, no shape fabric.

1.1.3 Use of shape fabrics in geology

1.1.3.1 Strain analysis – analysis of strain magnitude

The intensity of a shape fabric in terms of shape preferred orientation of a population of objects is commonly thought to be directly related to the magnitude of deformation i.e. finite strain. Qualitatively, absence and presence of a shape preferred orientation is often interpreted to point to the absence or presence of deformation (e.g. Sutton and Watson 1955, Ramsay 1958, Ellis and Watkinson 1987, Shackleton 1993, Peterson and Robinson 1993). Investigations concerning the development of the shape preferred orientation of a population of rigid objects dispersed in a viscous matrix lead Fernandez (1987) and Ildefonse et al. (1992a) to propose that the angle β between the mean orientation of the long axis of objects and the shear zone boundary corresponds to the orientation angle α of the maximum finite stretching axis with the shear zone boundary. This relationship is in accordance with the March's model and therefore the mean orientation of long axes of a population of rigid objects could be used to quantitatively derive finite strain. Another approach is taken in the analytical investigation of the development of the shape preferred orientation of a population of rigid objects dispersed in a deforming matrix (e.g. Jezek et al. 1994, 1996; Masuda et al. 1995b). These models are based on the equations provided by Jeffery (1922) and conclude that the relationship between angle α and angle β cannot directly be used for strain analysis.

The three dimensional shape of a viscous inclusion embedded in a viscous matrix is commonly thought to be directly related to finite strain (e.g. Flinn, 1978, Lisle et al., 1983). Eshelby (1957) provided a general mathematical description of flow of a viscous matrix around a viscous object. Lisle et al. (1983), Lisle (1985), Freeman (1985, 1987), Freeman and

Lisle (1987) and Weijermars (1993, 1997) analytically extended the equations provided by Eshelby (1957) and applied the solutions to geological problems to quantify deformation. Additionally, experimental work has been performed investigating the deformation of deformable objects (Gay, 1968a, 1968b, 1976; Ghosh and Sengupta, 1973; Bilby et al., 1975, 1976; Gay and Fripp, 1975; Paterson, 1983 and references therein; Rallison, 1984; Bentley and Leal, 1986; Passchier and Sokoutis, 1993; Treagus et al., 1996; Treagus and Lan, 2000).

1.1.3.2 Strain analysis – analysis of type of flow and movement direction

It is common practice to use the orientation of the long axis of a shape fabric to infer the orientation of movement in non-coaxial flow, whereby the principal direction of extension of the strain ellipsoid is thought to be parallel to the principle directions of the longest axis of the shape fabric (Price and Cosgrove, 1990; Twiss and Moores, 1992; Ghosh, 1993; Passchier and Trouw, 1996).

The change in the three dimensional shape of a viscous inclusion embedded in a viscous matrix is thought to be related not only to strain magnitude but also to the type of deformation in terms of constrictional, plane or flattening strain. (Fig. 1.2; Flinn, 1978; Lisle et al., 1983; Rallison, 1984; Freeman, 1985, 1987; Bentley and Leal, 1986; Freeman and Lisle, 1987; Weijermars, 1993, 1997)

Combining the characteristics of an observed shape fabric and other fabric elements i.e. geometric components that make up a rock (Sander, 1948, 1950) can help to derive the local structural history of an area, both in terms of kinematics and dynamics. For example, shape preferred orientation and the dimensional shape of a shape fabric, and its geometric relationship to the orientation of foliation can be used to interpret the structural history of a rock in terms of the type of deformation i.e. different types of transpression and transtension (e.g. Tikoff and Green, 1997; Fossen and Tikoff, 1998; Tikoff and Fossen, 1999).

1.2 The use of shape fabrics in structural geology - Problems and associated questions

1.2.1 Strain analysis — analysis of strain magnitude

The qualitative evaluation of the intensity of shape fabric as an indicator for the magnitude of strain may only be valid in some cases. For example, different rock types that experienced the same amount of finite strain within one shear zone may show different shape fabric intensities and some high-strain mylonites, especially mylonitized marbles and fine-grained schists often completely lack shape fabrics. Is there a direct relation between the intensity of a shape fabric and strain magnitude? If not, what factors influence the development of shape fabrics, their presence or absence and their intensity?

Dynamic recrystallization may play an important role in the intensity of a shape fabric as it significantly modifies the microstructure of a rock. How do parameters such as rate of recrystallization, grain size of recrystallized grains and grain boundary mobility influence the intensity of a shape fabric during progressive deformation?

The use of the intensity of shape preferred orientation of rigid objects dispersed in a viscous matrix to derive strain magnitude is problematic as analyses are based on endmember models i.e. the March's model (Fernandez, 1987; Ildefonse et al., 1992a) or the Jeffery's model (e.g. Jezek et al. 1994, 1996; Masuda et al. 1995b). The rotation rate of rigid objects depends on the orientation of the long axis of the object, slip at the object-matrix interface, matrix material and the axial ratio (R_{ob}) of the inclusion (Ghosh and Ramberg, 1976; Ferguson, 1979;

Odonne, 1994; ten Brink, 1996; Bons et al., 1997; Pennacchioni 2000). Additionally, the rotation rate of individual objects within a population of objects is significantly affected by object interactions and flow perturbations in the matrix (Ildefonse et al., 1992b; Ildefonse and Mancktelow, 1993). What then is the effect of the aspect ratio and the rheology i.e. non-Newtonian, power law flow of the matrix material on the intensity of the shape preferred orientation a population of rigid objects? How does the intensity evolve during progressive deformation?

The use of the absolute values of the axial ratios of deformable objects for strain analyses has already been shown to be difficult if the viscosity of the object and the matrix material differ from each other (Lisle et al., 1983; Rallison, 1984; Freeman, 1985, 1987; Bentley and Leal, 1986; Freeman and Lisle, 1987; Weijermars, 1993, 1997). What is the influence of specific viscosity ratios between matrix and object? What are the possibilities and limitations of this kind of strain analysis?

1.2.2 Strain analysis — analysis of type of flow and movement direction

The problem of the effect of the viscosity ratio between matrix and deformable objects on the three dimensional shape development of an object (see above) also affects the use of such objects for determination of the type of deformation in terms of constrictional, plane and flattening strain and transpression/transension. How reliable is the use of the three dimensional shape of deformable objects in terms of type of deformation?

Analytical work of Ghosh and Ramberg (1976) has shown that in two dimensional homogeneous flow the rate of rotation of a rigid elliptical object in a Newtonian viscous fluid varies in a systematic manner depending on the kinematic vorticity number of deformation W_n (Means et al., 1980). Is therefore the intensity of a shape preferred orientation of elongate objects a function of W_n ? If so, is it possible to use the shape fabric characteristics of a population of elongate objects to determine the W_n ?

1.2.3 Additional possibilities of the use of shape fabrics

Besides the use of shape fabric in analyses of strain magnitude and type of deformation, additional information may be derived from characteristics of a shape fabric. For example, the influence of viscosity contrast on the three dimensional shape of a deformable object, could possibly be used to gain insight in the viscosity or rheology of the involved materials. In which way could such rheology estimates be performed?

The rotation rate of rigid objects of a population of object is to some extent a function of the rheology of the matrix material (e.g. Ildefonse et al., 1992b; Ildefonse and Mancktelow, 1993). Is it therefore possible to use the characteristics of the shape fabric to determine to some extent the rheology of the matrix material?

The intensity of a shape fabric is defined by the spatial distribution and orientation of the grain boundaries (Panozzo, 1983, 1984). Trimby et al. (1998) suggested that specific grain boundary are characteristic for the dominance of processes such as rotational recrystallization, recovery or grain boundary migration. Could such characteristics of the shape fabric be used to delineate active mechanisms and values of parameters such as grain boundary mobility and rate of recrystallization?

1.3 Methods of investigation

In order to use shape fabrics for structural analyses, it is necessary to understand how shape fabrics develop during progressive deformation. Unfortunately, direct observation of progressive deformation of rocks in nature or in experiments is precluded as the described macro- and microstructures develop over long time scales and at high pressure and temperature conditions. Accordingly, indirect methods to address the questions given above are needed. Several different methods are available:

- (1) observations in nature in "ideal" areas, where a progression in strain is observed and therefore the evolution of a microstructure can be studied by studying selected samples.
- (2) analogue modelling with which it is possible to directly observe fabric development during progressive deformation,
- (3) numerical modelling of progressive deformation coupled with analytical considerations.
- (4) rock deformation experiments at elevated temperatures, pressures and deformation rates.

Each of these approaches has its strengths and limitations.

Detailed field work and analyses of rock samples can yield information about the microstructural development during deformation, but the history of the rock, related boundary conditions and material properties during deformation are generally not exactly known. Additionally, natural histories are often multiphase and complex. Therefore, it is often not possible to quantify the effect of specific parameters and active mechanisms on the microstructural development of a rock.

In contrast to field studies, in analogue modelling material properties, boundary conditions and conditions of deformation are known. See-through analogue experiments are an especially useful tool for structural geologists because in these experiments the development of the structures and fabrics can be observed throughout the experiment. (e.g. Means, 1983; Jessell, 1986; Herwegh and Handy, 1988; Means, 1989; Bons and Urai, 1994; Bons and Jessell, 1999). Boundary conditions are chosen to meet two prerequisites; it must be possible to apply the chosen boundary conditions in a technical sense and boundary conditions must be reasonably similar to those expected in nature. This results in experimental setups that approximate nature but are always limited due to technical considerations. Analogue materials do not normally deform due to same mechanism as applicable to rocks, and specific rheological characteristics may not correspond to those of rocks.

In numerical modelling boundary conditions are completely known, but limited in their variability just as in analogue modelling. The user defines which mechanisms and processes take place during deformation, in which way a mechanism effects a microstructure and defines the values of parameters such as grain boundary mobility. Although this allows a detailed analysis of the effect of the chosen mechanisms and parameters, it also restricts the analyses to those chosen mechanisms, parameters and effects. Results are strongly dependent on the initial input in terms of algorithms and values. It must be known how specific mechanisms affect the microstructure physically and numerically before these mechanisms can be modelled. The more complex the numerical model the harder it is to test the validity of the model for natural deformation. Additionally, the complexity of numerical models and their resolution is limited.

Rock deformation experiments can yield important information about the fabric development under certain conditions. This method played a significant role in the development of piezometry, hence the interpretation of fabrics in terms of dynamics (i.e. stress magnitude) (e.g. Twiss, 1977; Christie et al., 1980; Kronenberg and Tullis, 1984). Nevertheless, the use of rock experiments is limited due to a) the lack of direct microstructural observations during experiments, because samples are deformed in opaque pressure vessels and therefore observations are restricted to the beginning and end state, (e.g. Tullis and Yund, 1985, 1989; Gleason and Tullis, 1993; Hirth and Tullis, 1992) and b) results need to extrapolate results from experimental conditions to natural conditions (e.g. Twiss, 1977; Brace and Kohlstedt, 1980; Wenk et al., 1987).

In this study (a) observation in nature, (b) numerical modelling and (c) analogue modelling were undertaken in order to combine the strength of each one of the methods and in this way establish an improvement in our understanding of shape fabric development during progressive deformation.

1.4 Setup of the thesis

This study investigates the use of shape fabrics for structural analyses. Tools to derive and describe kinematics, active mechanisms and parameter from shape fabrics and associated fabric elements are developed based on the understanding of how fabrics evolve during progressive deformation and which parameters influence the development of shape fabrics.

In Chapter 2 the development of shape fabrics was studied in detail. Field work was performed in the Cap de Creus area, NE Spain. Samples were taken from different localities of well-exposed discrete low to medium grade shear zones. Microstructural analyses show that shape fabrics can only to a limited extent be used as indicators for strain magnitude and rocks were significantly recrystallized during progressive deformation.

In Chapter 3 a better understanding of the findings of Chapter 2 is developed. A numerical model for dynamic recrystallization is described and used to model fabric development of a monomineralic microstructure deformed in simple shear. As a side effect, methods are developed to characterize a microstructure more accurately and/or quantitatively. The model is part of the numerical modelling environment Elle (Jessell et al., 2001). With Elle it is possible to simulate a variety of concurrent microstructural processes which are active at the grain scale during continuous deformation. The existing code had to be modified significantly to be able to simulate dynamic recrystallization. In collaboration with Mark Jessell and Lynn Evans (both Monash University, Melbourne, Australia) the structure of Elle was extended, 5 new routines which each model one specific process, a statistics routine and routine to check the mesh for topological problems were written in C and C++. For these new routines a large number of new functions were added to the code.

In Chapter 4 and Chapter 5 studies dealing exclusively with rheological and technical considerations regarding analogue modelling are undertaken. In Chapter 4 the use of polymers and related materials as rock analogues is discussed. In Chapter 5 a newly developed and built deformation apparatus (transpression/transension (TT) apparatus) is described with which it is possible to model a large number of different shear zone types. Both Chapter 4 and Chapter 5 resulted from close collaboration with Saskia ten Grotenhuis.

In Chapter 6 the developed TTG apparatus is used to model the development of the shape preferred orientation of populations of rigid objects during progressive deformation. Objects with different aspect ratios are dispersed in two rheologically different matrix materials and deformed in different types of plane strain monoclinic flow.

In Chapter 7 a detailed account on analogue experiments of isolated viscous inclusions embedded in a viscous matrix is given. Experiments are performed with an newly developed apparatus (modified viscometer) in which a circular high strain simple shear zone can be modelled. In this chapter light is shed on the limitations and possibilities of the use of shape fabrics for strain analyses.

General conclusions and suggestions for further research is provided in Chapter 8.

In appendices additional information and data is given. These are: a detailed description of samples used in Chapter 2 (Appendix A), an explanation of the statistical method used in Chapter 2 and Chapter 6 and a chart to qualitatively determine the intensity of a shape fabric from handspecimen or thin section (Appendix B), test experiments and some additional computational information of the numerical model Elle described and used in Chapter 3 (Appendix C), results from rheological measurements of a polymeric mixture not provided in any chapter of this thesis (Appendix D), an explanation of and user manual for the computer programs which regulate the deformation of the apparatus described in Chapter 5 and used in Chapter 6 (Appendix E). A CD-Rom (Appendix F) contains an Excell sheet to derive the concentration parameter κ of a von Misses distribution from a set of directional data, the used version of the simulation program Elle and some representative movies of numerical experiments (Chapter 3) and analogue experiments (Chapters 6, Chapter 7).

1.5 Published parts

Parts of the presented work are in press or have been submitted for publication:

Chapter 2 has been submitted to the Journal of Structural Geology in July 2000 ("The development of different types of lineations in low to medium grade shear zones: A study from the Cap de Creus peninsula, NE Spain"). Coauthor is C. W. Passchier.

Chapter 4 is largely identical to a manuscript submitted to Journal of Geophysical Research in June 2000 ("Are polymers really suitable for geologically relevant analogue modelling?"). Coauthors are S. M. ten Grotenhuis, T. Pakula, C. W. Passchier and P. D. Bons.

Chapter 5 is largely identical to a paper in press in the Geological Society of America Bulletin, Special Volume 193, ("A new apparatus for controlled general flow modelling of analogue material", in H. A. Koyi, N. S. Mancktelow, eds. Society of the American Geological Memoir, 193). Coauthors are S. M. ten Grotenhuis and C. W. Passchier.

Chapter 7 has been submitted to Journal of Geophysical Research in September 2000 ("Experimental modeling of viscous inclusions in a circular high strain shear rig: Implications for the interpretation of shape fabrics and deformed enclaves"). Coauthor is C. W. Passchier.

Additionally, results of this thesis were presented at a number of international conferences (presenter is written in italics):

- S. Piazzolo* and C. W. Passchier (2000) The development of stretching lineations in monoclinic shear zones: Results from analogue modelling, Geological Society of London, Abstracts 127; oral presentation: Rheological properties of polymers used in analogue modelling and Significance of rheology for fabric development.
- S. Piazzolo* and C. W. Passchier (2000) The formation of lineations in mylonites, 17th Swiss Tectonics Studies Group Meeting Program and Abstract Volume, 73; oral presentation
- S. Piazzolo*, P. D. Bons, M. W. Jessell, L. Evans, C. W. Passchier, T. D. Barr (1999) Development of stretching lineations: a view from dynamic recrystallization using the numerical model ELLE, Göttinger Arbeiten zur Geologie und Paläontologie, Sonderband 4, 152-153; poster presentation.
- S. Piazzolo* and C. W. Passchier (1999) How to make stretching lineations - a recipe, Journal of Conference Abstracts 4, 828; oral presentation.
- S. Piazzolo* and C. W. Passchier (1999) Experimental modelling of stretching lineations within simple shear zones, Geological Society of Australia Abstracts Series 53, 198; poster presentation.
- P. D. Bons*, *S. Piazzolo*, L. Evans, M. W. Jessell, T. Barr, K. Stüwe, C. W. Passchier (2000) Modelling coupling of processes and microstructure with ELLE, Geological Society of London, Abstracts 126; oral presentation.

Additionally, results will be presented:

- S. Piazzolo*, M. W. Jessell, P. D. Bons, L. Evans, C. W. Passchier (2000) Telltale Microstructural Features as Indicators for Rates of Recrystallization and Grain Boundary Mobility During Deformation: Insights From Numerical Modeling, AGU Fall Meeting; oral presentation.

The published/submitted chapters have been modified to fit the layout of this thesis. The setup of the thesis as Chapters written as scientific papers inevitably results in a certain degree of repetition.

Chapter 2

Lineation development in low to medium grade shear zones A study from the Cap de Creus peninsula, NE Spain

Abstract

Lineations are commonly used to determine the direction of tectonic transport in rocks and the strength of such lineations is often taken as an indicator of strain intensity. However, field observations in discrete greenschist to lower amphibolite facies shear zones of the easternmost Variscan Pyrenees show that strain is only one of several factors that determine the strength and type of a lineation. Different lithologies with different initial fabrics produce distinctly different types and strengths of lineations even if deformed to the same finite strain in the same shear zone. An initial fine grain size and a monomineralic composition of a parent rock type commonly hinder the development of lineations. In contrast, in coarse-grained polymineralic parent rocks usually good lineations develop. The initial fabric in a specific rock type determines how processes that are active during and after deformation affect the fabric, and consequently the development of lineations. The most important of these processes is dynamic recrystallization. The ratio initial/dynamically recrystallized grain size is crucial for development of lineations constituted of mineral aggregates. Metamorphic reaction, rigid body rotation and anisotropies within a lithology also play a role in the development of lineations. We propose a new terminology of lineations including the term volume-lineation to cover older generic terms.

2.1 Introduction

Since the middle of the 19th century, "stretching-" and "mineral-" lineations have been used to determine the tectonic transport direction of rock masses and to decipher the superposition of deformation events and metamorphic grade during deformation (e.g. Sutton and Watson, 1955; Ramsay, 1958; Ellis and Watkinson, 1987; Shackleton, 1993; Peterson and Robinson, 1993). Although the general validity of this approach has been questioned in some specific cases (e.g. Druguet et al., 1997; Tikoff and Greene, 1997; Fossen and Tikoff, 1998; Krabbendam and Dewey, 1998), lineations are generally regarded as reliable tools in deformed rocks. Nevertheless, there are some problems with lineations. For example, different rock types that experienced the same amount of finite strain within one shear zone may have different lineation "strength" and some high-strain mylonites, especially in marbles and fine-grained chlorite schist, completely lack linear fabrics. What factors, then, influence the development of lineations? Finite strain may play a major role, but other factors must be important as well. The understanding of such factors is essential for the correct interpretation of lineations. In this study, we systematically describe a variety of lineations that occur in discrete low- to medium

grade shear zones of the Cap de Creus peninsula, Spain, discuss the factors that can play a role in the development of these lineations and put forward a model for the development of different types of lineations emphasizing the significance of recrystallization besides rigid body rotation and metamorphic reaction.

2.2 Terminology of lineations

2.2.1 Commonly used terminology

In structural geology, the technical term lineation describes any linear feature which occurs penetratively in a rock. Traditionally, four main types of lineations are distinguished (e.g. Price and Cosgrove, 1990; Twiss and Moores, 1992; Ghosh, 1993; Passchier and Trouw, 1996). Crenulation-lineations are formed by hinge lines of microfolds and/or kinkbands in the foliation plane. Intersection-lineations are formed by two intersecting foliations one of which could be bedding. Stretching-lineations are defined either by (a) prolate aggregates of equidimensional or slightly elongate grains that can be distinguished from neighbouring fabric elements, or (b) prolate deformed single grains of minerals such as quartz, calcite or feldspar which normally have an equidimensional shape when undeformed (Passchier and Trouw, 1996). Deformed objects such as xenoliths in a granitoid or pebbles in a conglomerate may also form stretching-lineations on a larger scale if they are present throughout a volume of rock. Mineral-lineations are defined by the preferred orientation of single undeformed mineral grains with an elongate or platy habit. Examples are lineations of sillimanite, tourmaline or actinolite but also mica grains which share a common axis. In addition to these four commonly used types of lineations, extensional-lineation was defined as a lineation that formed due to extension, e.g. by opening small-scale fractures and filling these fractures with material (Mackinnon et al., 1997).

A major problem with the existing terminology is the ambiguity or generic association of terms like "stretching", "mineral" and "extensional". For example, it is difficult to distinguish the second type of stretching-lineations from a mineral-lineation. The interpretative connotation of lineation names can be a problem in many cases. If a polycrystalline layer in a mylonite is dismembered by shear bands, the result may be a "stretching-lineation" at right angles to the orientation of the longest bulk finite strain axis; such a "stretching-" lineation is not due to stretching into an ellipsoidal shape. We therefore modified some of the definitions for lineation types in an attempt to avoid such ambiguities (Fig. 2.1).

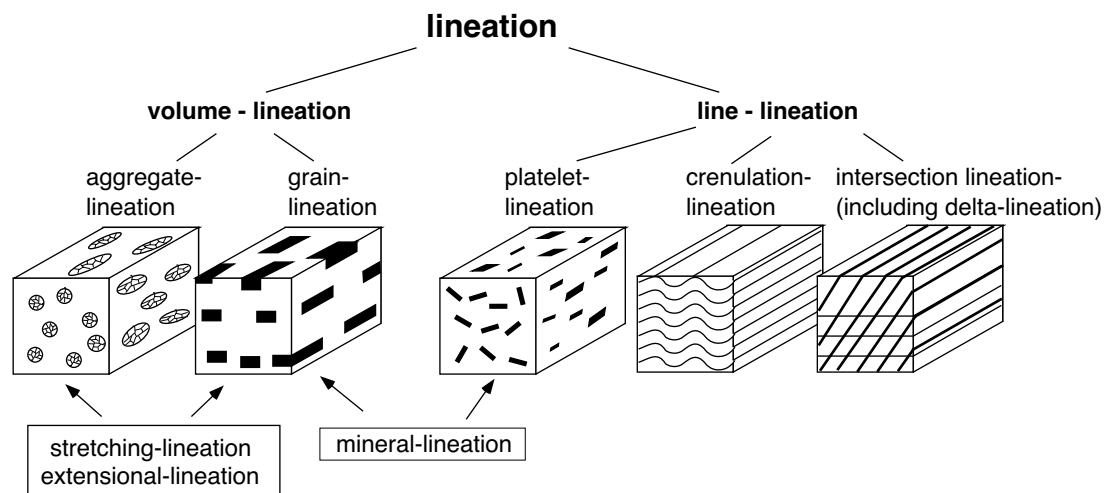


Figure 2.1 Diagram illustrating the terminology for lineations proposed; in *italic*: terms with interpretative connotation.

2.2.2 Definitions

We define the descriptive term volume-lineation as a lineation which is formed by a specific material body with a measurable volume in contrast to line-lineation which is formed by the intersection of surfaces (Fig. 2.1).

Volume-lineations are further divided into aggregate- and grain-lineations. We define a grain-lineation as a lineation that is formed by prolate individual single grains of a mineral species whereby the long axes of the minerals are similarly oriented. A grain-lineation has elements from both stretching- and mineral-lineations and the use of this term eliminates the ambiguity mentioned above. An aggregate-lineation is defined by prolate aggregates of grains of the same or several different mineral species in which individual grains have a smaller aspect ratio than the aggregate.

The terms grain-lineation and aggregate-lineation have the advantage that they are purely descriptive and non-generic in contrast to stretching- and extensional-lineation. However, the terms stretching-lineation and extensional-lineation can still be used if their orientation with respect to the finite strain axes and mode of development can be established. Both generic terms fit in the descriptive groups "grain-lineation" or "aggregate-lineation" (Fig. 2.1).

Line-lineations represent material lines of zero volume. Typical examples are intersection-lineations between foliation planes and crenulation-lineations but a platelet-lineation can also be defined as a line-lineation type consisting of disc-shaped, platy mineral grains or fractures, which share a common axis (Fig. 2.1).

The descriptive terms defined here are probably most useful in the field, where it is not always possible to decide on the mechanisms of lineation development. The conception of lineations in the field is strongly dependent on the scale of observation i.e. the width of "lineation stripes". Lineations that are larger than handspecimen or outcrop scale can only be recognized by larger scale observations such as regional mapping or aerial photographs.

In this study we illustrate problems in the interpretation of lineations using examples from the Cap de Creus area (Spain) where different types of mm to dm scale lineations occur within a small area .

2.3 Geology of the Cap de Creus Peninsula, Spain

2.3.1 General Outline

The Cap de Creus peninsula represents the easternmost outcrop of the Variscan axial zone of the Pyrenees in Spain containing rocks with a complex polytectonic and -metamorphic history (Carreras, 1975; Carreras et al., 1977; Carreras and Casas, 1987; Carreras and Druguet, 1994a, 1994b; Druguet et al., 1997; Druguet, 1997; Druguet and Hutton, 1998). During the Variscan orogeny an alternation of quartzitic, metapelitic and metapsammitic rocks and minor metacalcisilicate and amphibolite of poorly restricted age (Neoproterozoic to Ordovician) was metamorphosed at low pressure resulting in a steep metamorphic gradient from chlorite-muscovite shales in the south to sillimanite-potassium feldspar bearing schists and migmatites in the north. Two small Variscan granodioritic plutons (Roses and Rodes intrusions) in the south of the area intruded the rock pile. Numerous small volumes of quartz diorite, leucogranite and tonalite occur in the migmatitic zone. Druguet and Hutton (1998) have shown that these rock

types are penecontemporaneous with the Variscan peak metamorphism. Just south of the migmatitic area abundant muscovite-tourmaline pegmatitic bodies occur and these have been interpreted to be associated with peak metamorphism as well (Druguet 1997). Several generations of quartz veins are present in the metasediments.

Two Variscan deformation events, D1 and D2 (after Druguet et al., 1997; Druguet, 1997) effected pre-Variscan lithologies. According to Druguet et al. (1997) D1 produced an early foliation and boudinage of pre- or syn-D1 quartz veins. Both S1 and the vein-boudins are parallel to bedding except in rare D1-fold closures of bedding. Relicts of D1 aggregate-lineations are common in bedding and quartz veins.

The main phase of deformation (D2) developed during prograde metamorphism. The majority of pegmatitic bodies and at least one generation of quartz veins are syn-D2 and syn-peak metamorphism. Druguet et al. (1997) propose that D2 was a phase of highly vortical sinistral transpressional flow with a strong vertical extension component that produced a new foliation (S2) and subvertical lineations.

Lineations which developed during D1 and D2 exhibit varying lineation “strength” and are either constituted of single or aggregates of grains. Fine-grained metasediments tend to exhibit D2 lineations of higher “strength” than coarse-grained ones, some of which were obviously strongly deformed during D2, such as in D2 boudin structures. These structures are overprinted by predominantly E-W and NW-SE trending anastomosing D3-ductile shear zones of unknown age (Carreras et al., 1977; Druguet 1997) (Fig. 2.2).

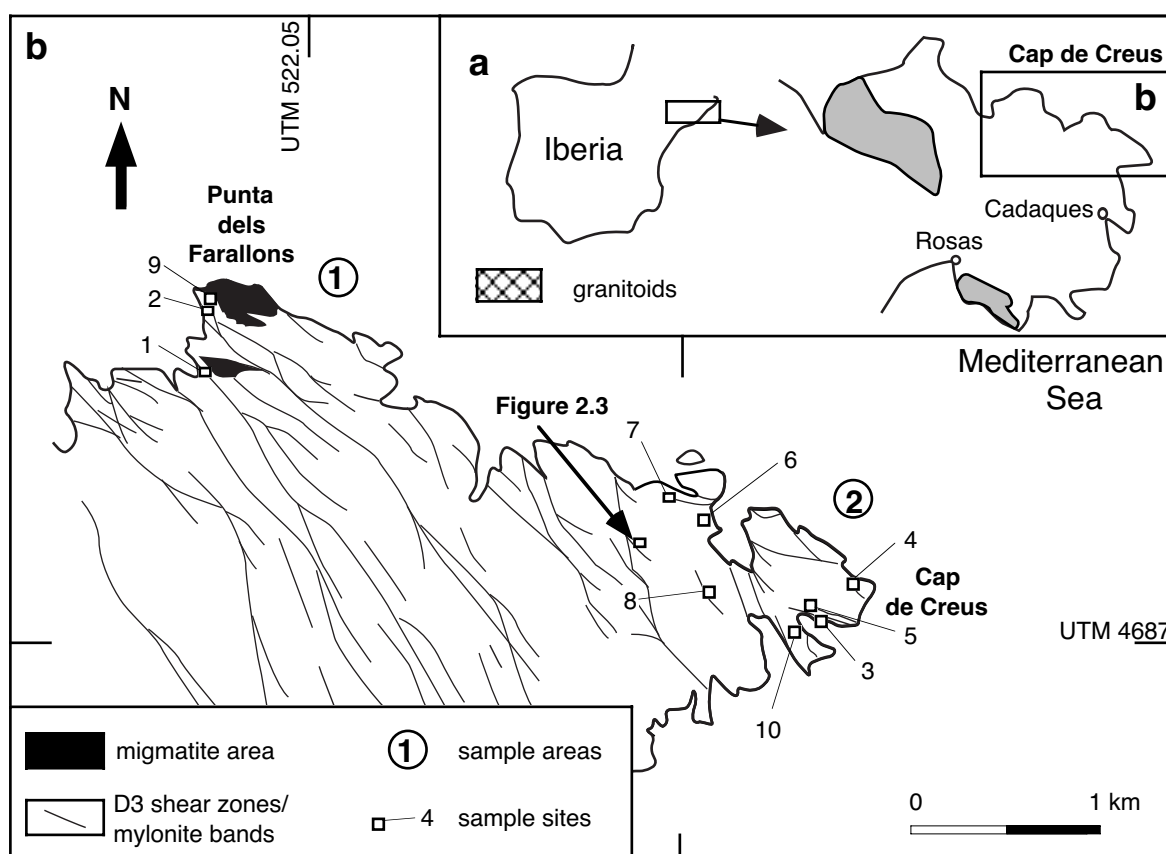


Figure 2.2 Overview map of the study area; (a) its locality within Iberia, (b) within Cap de Creus peninsula. Lines correspond schematically to isolated low grade shear zones (modified after Carreras and Casas, 1987). The two sample areas are near Cap de Creus (1) and Punta dels Farallons (2). Other numbers signify shear zone numbers and sample localities discussed in text.

These shear zones are oblique to layering and S2, developed under greenschist and lower amphibolite facies conditions and have been the focus of a large number of publications (e.g. Carreras, 1975; Carreras et al., 1977; Carreras and García, 1982; Carreras and Casas, 1987). Syntectonic fluid infiltration caused retrogression in the zones and this resulted in mineral assemblages with a high volume of H₂O-rich minerals such as chlorite and sericite, tourmaline and fibrolitic sillimanite and a "bleached" aspect of shear zone centres in the field. The presence of fibrolite is not in contradiction with the low grade nature of shear zone deformation. Kerrick (1987 and reference therein) has shown that fibrolite may form at temperatures significantly below the sillimanite stability field (450-560 °C) in the case of a boron-rich fluid infiltration during deformation. The presence of tourmaline and muscovite within the shear zones which bear fibrolite supports such a metasomatic fibrolite-tourmaline-muscovite association.

2.3.2 Characterization of deformation in D3 shear zones

The retrograde, greenschist- to lower amphibolite facies D3 shear zones of the Cap de Creus area offer a unique opportunity to document and analyse the development of volume-lineations in different lithologies deformed in a number of spatially defined and well exposed individual zones (cf. Fig. 2.6). The shear zones are characterized by a progressive and continuous rotation of S1 and S2 towards parallelism with the shear zone boundary. The angle between S1 or S2 and the shear zone boundary is 60 and 90 degrees and the shear zone width is up to 20 m (from first deflection of the regional foliation on the one side of the shear zone to first deflection on the other side). In the centre of the shear zones deformation was so intense that the foliation is parallel to the shear zone boundary.

D3 deformation is weak to absent outside the D3 shear zones. In the absence of volume change, strong localization of deformation as present in these shear zones is therefore most likely caused by simple shear flow (Weijermars, 1992). Carreras and Garcia (1982) investigated the character of one specific shear zone located in one of the sample areas and indeed concluded that the geometry of the shear zone closely corresponds to that expected for simple shear flow conditions. We compared field measurements with theoretical values for simple shear progressive deformation without volume change (Ramsay, 1980) to investigate if other D3 shear zones formed by simple shear progressive deformation as well. Measurements in the shear zones show a close fit to theoretical values for shear zones formed by progressive simple shear (Fig. 2.3). Strain partitioning seems to have played a minor role during shear zone formation as the orientation of volume-lineations in different rock types within the same shear zone are subparallel; if significant strain partitioning had taken place, lineations in different lithologies would be expected to vary significantly in orientation. Another argument for insignificant strain partitioning is that the orientation and position of the investigated shear zones is not lithologically controlled; therefore, the rock seems to have been rheologically homogeneous within the active shear zones.

In many shear zones finite shear strain could be determined by the displacement of marker layers (e.g. pegmatites, quartz veins) and shear zone width. Finite shear strain in the shear zones is in the order of 50 to 250 assuming simple shear deformation.

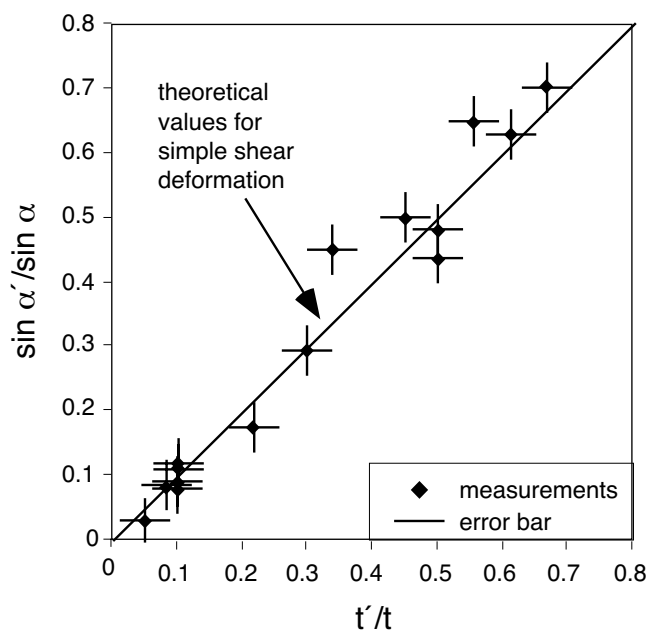


Figure 2.3 Graph illustrates the type of deformation in D3 shear zones. After Ramsay (1980) a simple shear shear zone is characterized by $t'/t = \sin \alpha' / \sin \alpha$, whereby t' is the thickness of a layer within the shear zone, t the original thickness, α' the angle between shear zone boundary and mylonitic foliation, α the original angle between foliation and shear zone boundary. If the shear zone is a simple shear shear zone values should lie on a line which has a slope of 1. Measurements within error closely correspond to theoretical values and therefore D3 shear zones deformed by simple shear deformation. Deviation from the model simple shear values are predominately to the left of the simple shear line which signify a non-rotational flattening component perpendicular to the band (for further details see Carreras and Celma, 1982).

2.4 Development of volume lineations in low to medium grade shear zones at Cap de Creus

2.4.1 Classification of volume-lineations

In the D3 shear zones of the Cap de Creus peninsula several types of volume lineations are present. In order to satisfactorily characterize these we needed to describe them accurately and to quantify their strength. Strength of a volume-lineation can be expressed by the degree of preferred dimensional orientation of the lineation as described by the statistical value κ of a von Mises distribution (Masuda et al., 1999). This value is based on the common orientation of the longest axis of individual grains (grain-lineation) or polycrystalline lenses (aggregate-lineation). In this study, κ was determined as described in Appendix B from observation on the foliation planes of hand-specimens, or in thin sections cut parallel to the foliation in the rock, in order to bring out the lineation geometry.

We used the following classification which is based on (a) the value represented either by the adjectives strong (κ -value ≥ 5), good ($2 \leq \kappa$ -value < 5) and poor (κ -value < 2) or by the exact κ -value; (b) the modal percentage of lineation-forming material compared to matrix represented by the letters s (small; $< 20\%$), i (intermediate; 20 - 45%), l (large; 45 - 97%) and m (monomineralic; 97 - 100%); (c) lineation material (one or several mineral species) written in mineral abbreviations proposed by Kretz (1983); (d) the terminology for volume lineations put forward above (see 2.1).

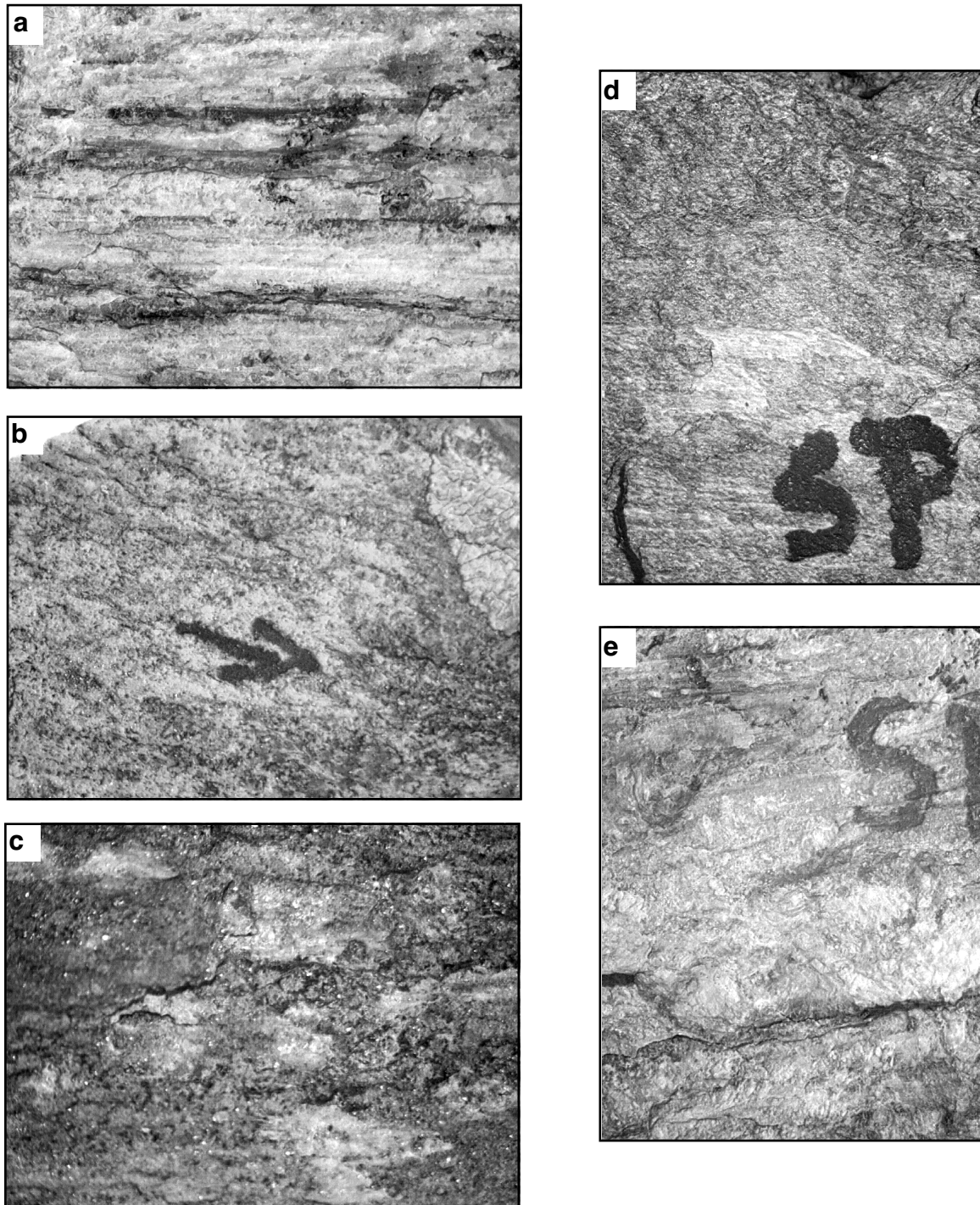


Figure 2.4 Photos of handspecimen; (a) strongly deformed pegmatite with a very good *i*-Qtz aggregate lineation; (b) good Bt grain-lineation in Bt-bearing quartzite (SP 358); (c) good Fibr. aggregate-lineation (SP 290); (d) in lower third: good Qtz aggregate lineation in quartz-rich part of metapsammite (SP 127), in upper two thirds: no lineation in fine-grained metapsammite (SP 126); (e) deformed granodiorite with good Fsp aggregate-lineation (SP 151B); for photos (a) - (e) field of view = 2 cm.

A high κ -value signifies a high degree of preferred dimensional orientation i.e. similar orientation of individual lineation elements (e.g. individual elongated grains or grain aggregates) and therefore a well developed, strong volume-lineation. An example of the proposed classification could for instance be "3.7 s-Sil grain-lineation" for a grain-lineation made of similarly oriented sillimanite grains, with a good degree of preferred orientation ($\kappa = 3.7$) and a small modal percentage of lineation material. Figure 2.4 shows some examples of different volume-lineations present in the study area. This classification may seem somewhat complicated, but was necessary for an accurate and quantitative comparison of volume-lineations in the Cap de Creus area. It could also be useful elsewhere when comparing volume-lineations from different areas and rock types. In the scheme proposed here, one can choose the degree of "complexity" in nomenclature that is needed for a specific problem i.e. either Sil grain-lineation or good Sil grain-lineation or 3.7 s-Sil grain-lineation.

2.4.2 Sample localities

Ten shear zones were investigated in detail in two sample areas which are situated in the north-eastern part of the Cap de Creus peninsula (Fig. 2.2). Shear zone 1, 2 and 9 lie in the northern area where pre-D3 migmatites occur (Punta dels Farallons; (1) in Fig. 2.2). The other samples are taken from the eastern part of the peninsula ((2) in Fig. 2.2). Details of the geometry of individual shear zones and volume-lineations investigated are given in Tab. 2.1.

2.4.3 Development of volume-lineations in low to medium grade shear zones

Aggregate-lineations are composed of elongate aggregates of specific minerals that develop from large equidimensional parent grains by a ductile shape-change and associated dynamic recrystallization. Freeman and Lisle (1987) have shown that the relationship between the shape of the finite strain ellipsoid and the shape of such aggregates is complex and dependent upon the rheology of each of the rock constituents. Nevertheless, it would be expected that the "strength" of aggregate lineations reflects the maximum finite strain ratio in some way. However, such a direct relationship does not exist in the Cadaques shear zones. The character of volume-lineations in traverses through each of the D3-shear zones investigated varies significantly between different lithologies, even where finite strain values in the different adjacent lithologies are similar (Fig. 2.5 and Tab. 2.1). Therefore, differences in the type of lineations in different lithologies and shear zones must at least partly originate from other parameters than bulk strain. To give the reader an idea of the textural development within different lithologies during progressive deformation Figures 2.6 - 2.8 illustrate different fabrics and corresponding volume-lineation strengths developed in three of the investigated shear zones (locations are given in Fig. 2.2).

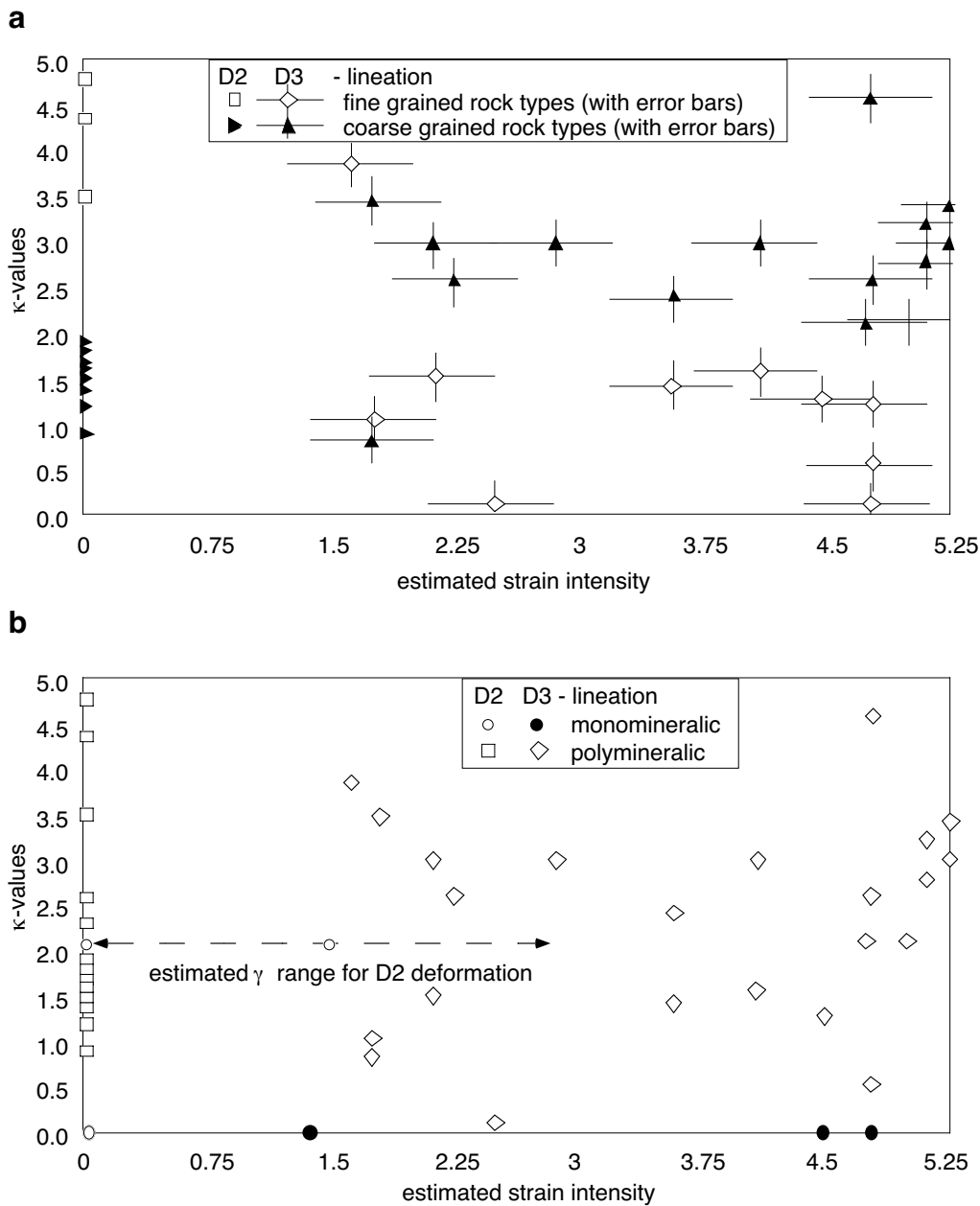


Figure 2.5 (a) Graph illustrating the change in κ -values (measure of the "strength" of a lination) with strain. The progressive rotation α' of a layer towards the mylonitic foliation provides a relative estimate of shear strain γ using the equation $\cot \alpha' = \cot \alpha + \gamma$ (e.g. Ramsay, 1980; Lloyd et al., 1992), where α is the original orientation of the layer. Two major rock groups are distinguished: initially coarse-grained lithologies (pegmatite, metapsammite, metapelite, granodiorite) and initially fine-grained lithologies (metapsammite, metapelite, quartzite). Note that in coarse-grained rocks κ -values increase with increasing strain, whereas in fine-grained rocks κ -values decrease; **(b)** graph illustrating the change in κ -values (measure of the "strength" of a lination) with strain of monomineralic rocks and polymineralic rocks. Note that polymineralic rocks tend to exhibit higher κ -values than monomineralic rocks.

Shear zone 6 is a typical D3 shear zone in the area. The wall rock consists of alternating beds of fine-grained metapsammite (fg-mps) and coarse-grained metapelite (cg-mpl), and a quartz vein (qtz-vein) parallel to bedding (Fig. 2.6). Orientation of these units is almost orthogonal to the D3 shear zone. In the wall rock a moderately to well developed D2 Bt grain-lineation exists in metapsammite and metapelite, which is orthogonal to the shear zone. Lineation strength in and around shear zone 6 was measured in three samples for each lithology after having established in the field that the change in nature of the lineations is gradual over the shear zone boundary (Fig. 2.6). In the coarse-grained metapelite (samples SP 272 to SP 270) κ -values increase from 1.68 to 2.8 from shear zone boundary to centre (Fig. 2.6). In the fine-grain rock, however, κ -values of the D2 Bt grain-lineation decrease from 4.8 to 1.27. In the quartz vein (qtz-vein) no volume-lineation is present either outside or inside the shear zone. Grain sizes are unimodal and do not vary significantly between the three samples in the quartz vein.

More details of the lineation development can be observed in shear zone 1 (Fig. 2.7). A coarse-grained pegmatite (quartz and feldspar grains up to 2 cm in diameter) and two different types of metapsammite are deformed in this shear zone. Outside the shear zone the pegmatite (peg) is parallel to bedding, coarse-grained (> 2 mm) and has quartz lenses in its centre. The pegmatite fabric is dominated by large feldspar and tourmaline, medium-grained quartz, and minor biotite and muscovite (sample SP 128A). In the centre of the shear zone the quartz-feldspar zones of the pegmatite exhibit a well defined aggregate lineation (SP 131) which is made up of strongly elongated domains of recrystallized quartz interbedded with fragments of brittly deformed feldspar and aggregates of fine recrystallized grains of feldspar.

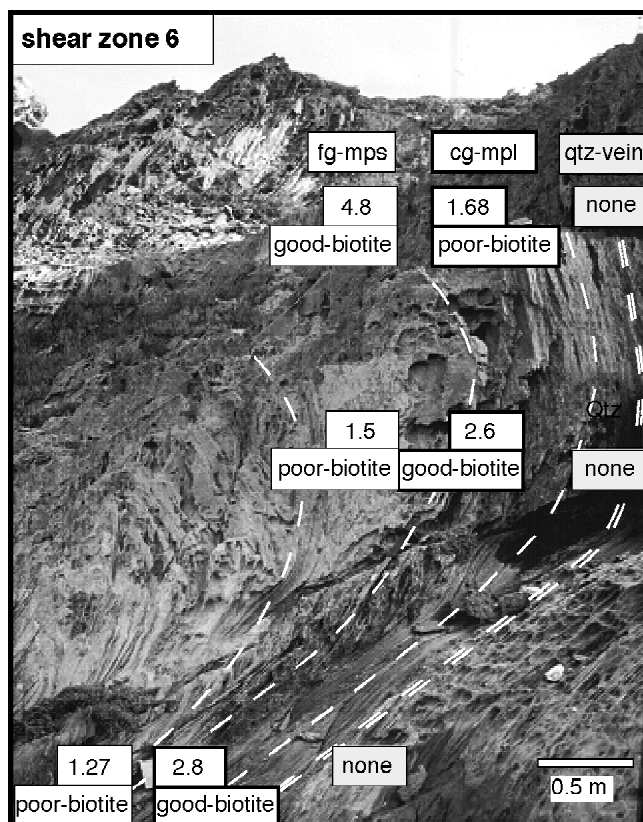


Figure 2.6 Field view of shear zone 6 depicting one side of the shear zone from outer part to centre. This shear zone exhibits the development of lineations in different rock types. Numbers represent κ -values, (measure for degree of dimensional preferred orientation; for further explanation see text and Appendix B) and successions of letters and numbers the lineation type using the proposed classification; cg-mpl = coarse-grained metapelite, fg-mps = fine-grained metapsammite, qtz-vein = quartz-rich part of pegmatite; boundaries of different lithologies are outlined by dashed white lines.

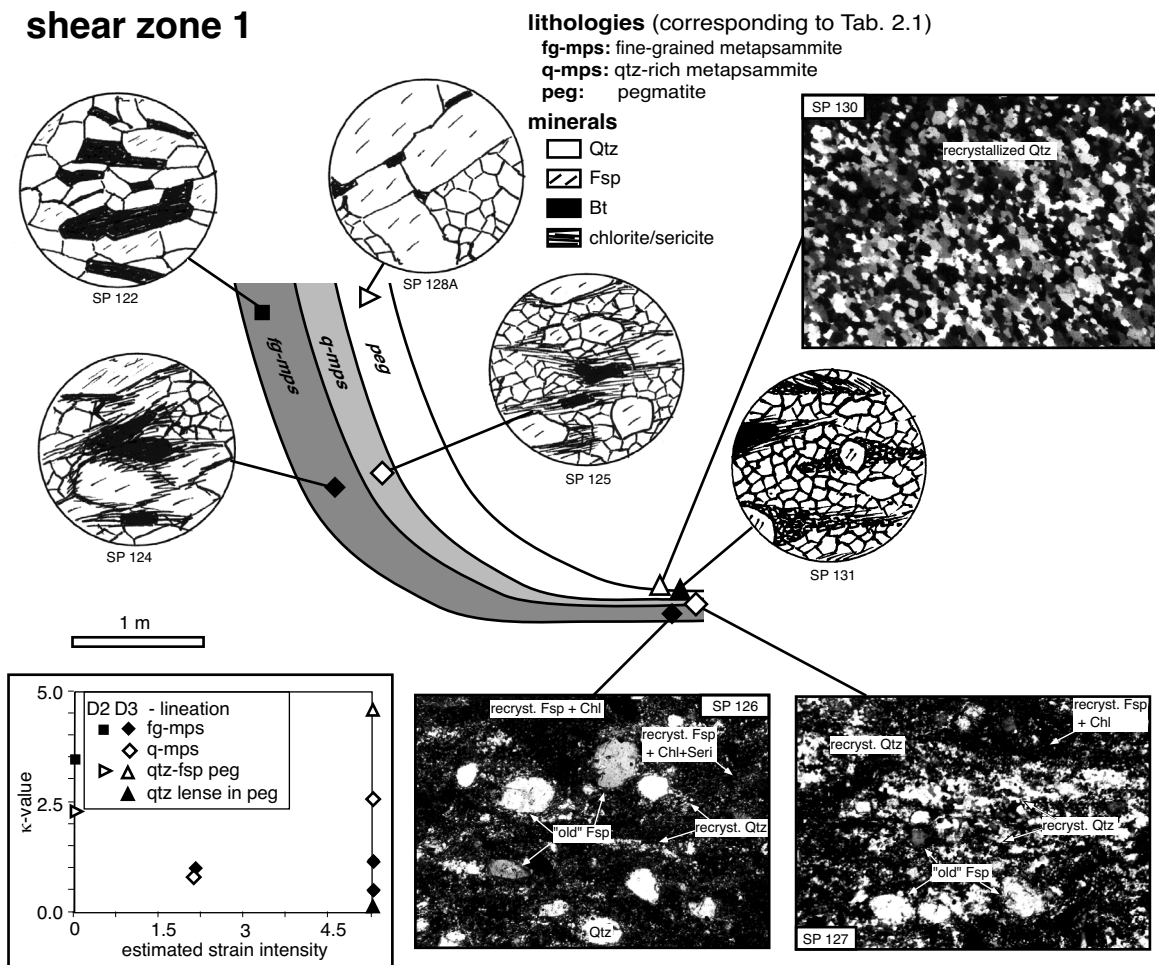


Figure 2.7 Schematic diagram of textures observed in different lithologies in shear zone 1. Diameter of circles (with textures) = 2 mm; inset shows a graph plotting κ -values against estimated strain; photomicrographs (width of view (horizontal) = 0.6 mm) depict selected samples, sections are cut parallel to foliation; SP 126 is a fine-grained metapsammite in the centre of shear zone 1 with no statistically significant lineation, crossed nicols; SP 127 is a fine-grained metapsammite in the centre of shear zone 1, the lineation is a 2.6 s-Qtz aggregate-lineation, crossed nicols; SP 130 is a quartz dominated part of a pegmatite, no lineation is present, crossed nicols; width of view for photomicrographs is 0.6 mm for all samples; fg-mps = fine-grained metapsammite, q-mps = quartz-rich metapsammite, peg = pegmatite.

No macroscopic volume-lineation forms in zones of fine-grained (0.02 mm) recrystallized pure quartz in the pegmatite (q-peg; SP 130; Fig. 2.7) although in thin section a crystallographic preferred orientation is present indicating ductile deformation of quartz. A lineation is only developed in those parts of the quartz domains in which a small amount of strongly recrystallized feldspar is present which form long stringers of recrystallized feldspar grains and thereby a good aggregate-lineation. Outside the shear zone, a fine- to medium-grained metapsammite (fg-mps) has a D2 lineation (3.5 s-Bt grain-lineation; SP 122). At the bend (SP 124) and centre (SP 126) of the shear zone the same lithology exhibits a poor Bt grain-lineation, whereby the κ -value decreases towards the centre of the shear zone. Quartz and biotite form aggregates of small grains, feldspar appears as small to medium-grained rounded clasts or as fine-grained constituents of the matrix and aggregates of small sericite and chlorite grains are present. A fine-grained, quartz rich metapsammite (q-mps) exhibits a higher modal percentage

of quartz than fg-mps (22% in SP 127 against 8% in SP 126). Outside the shear zone q-mps shows a poor D2 Bt grain-lineation, less developed than in fg-mps. The contrast between elongate quartz aggregates and chlorite-sericite domains makes up the volume-lineation in both lithologies. SP 127 shows a well developed lineation (2.6 i-Qtz aggregate lineation; Fig. 2.7) while in SP 126 a lineation is only weakly developed (0.5 i-Qtz aggregate lineation; Fig. 2.7); apparently, the modal percentage of quartz pre-determines the lineation strength in these rocks.

Shear zone 4 in which coarse-grained (cg-mps) and fine-grained metapsammite (fg-mps) and a coarse-grained pegmatite (cg-peg) are deformed, shows a development similar to zones 1 and 6 (Fig. 2.8). Outside the shear zone in the fine-grained metapsammite, a 4.4 i-Bt grain-lineation of D2-age is present (SP 195). At the bend of the shear zone the strength of the lineation decreases (κ -value = 3.9; SP 194) and in the centre of the shear zone the lineation is poorly developed (1.6 i-Bt grain-lineation; SP 193). In the undeformed pegmatite (SP 198) feldspar and tourmaline are very coarse-grained (up to 10 mm) and quartz is medium-grained (0.5 mm). Where pegmatite was sampled in the shear zone centre (SP 197), both quartz and feldspar exhibit a strong grain size reduction, and some quartz grains are elongate with strong undulatory extinction. Domains of very fine-grained feldspar and fine-grained quartz in contrast to larger elongate crystals form a 3.0 i-(Qtz-feldspar) aggregate lineation.

shear zone 4

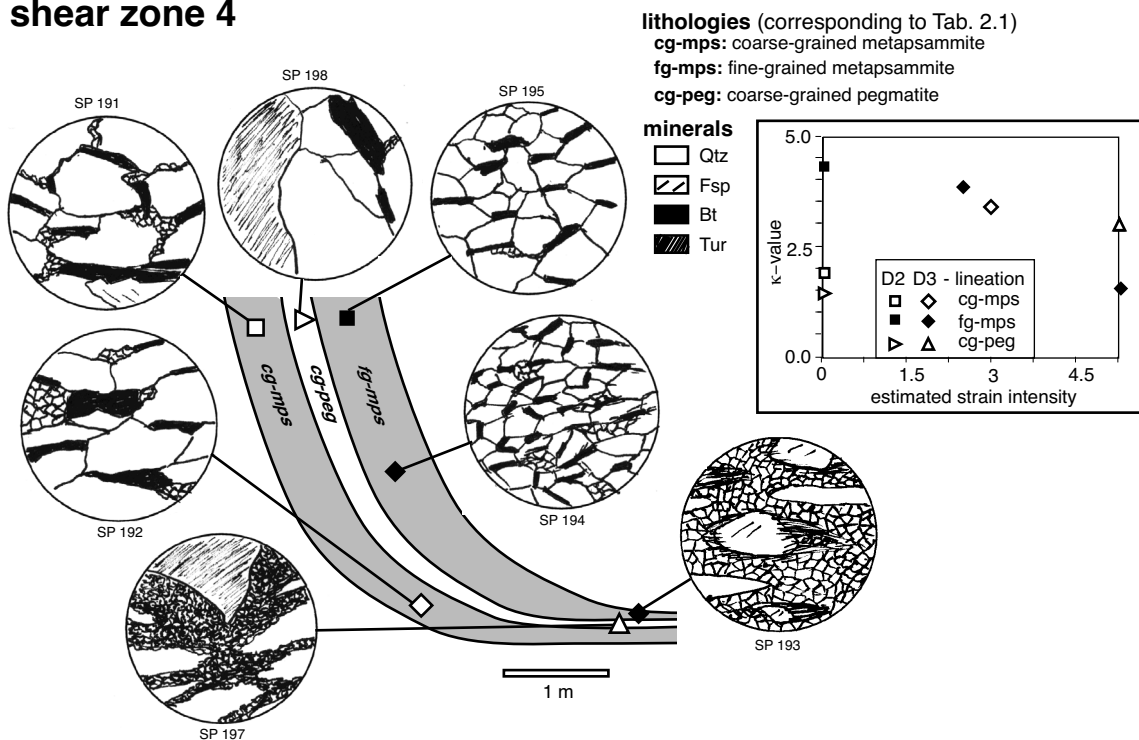


Figure 2.8 Schematic diagram of textures observed in different lithologies in shear zone 4. Diameter of circles (with textures) = 2 mm; small grains = small grained Qtz; in SP 197 quartz and feldspar; fg-mps = fine-grained metapsammite, cg-mps = coarse-grained metapsammite, cg-peg = coarse-grained pegmatite; inset shows a graph plotting k-values against estimated strain for sample of shear zone 4.

A characteristic feature of deformed pegmatite sample SP 197 is that the highest percentage of small quartz and very small feldspar grains is seen close to the brittily deforming tourmaline crystals. The coarse-grained metapsammite exhibits outside the shear zone a 1.7 s-Bt grain-lination of D2-age (SP 191) which develops into a 3.5 s-Bt aggregate-lination (SP 192) close to the centre of the zone.

Similar changes in the nature of volume-linations described for these three shear zones have been observed in all ten zones that were subject to quantitative investigation (Tab. 2.1, Appendix A), and were confirmed in all visited shear zones in the Cap de Creus area. Summarising the observations, one can say that although the lination “strength” is generally related to finite strain, the gradient of the “strength” (κ -value) of volume-linations from shear zone boundary to centre is strikingly different in coarse and fine-grained rocks (Fig. 2.5a). Initially, coarse-grained but isotropic rocks, which lack a D1 or D2 fabric (pegmatite, granodiorite, some metapelite and -psammite) with an initial grain size of 2 mm or more exhibit a progressive increase in volume-lination “strength” with strain intensity. On the contrary, initially fine-grained rocks (metapelite and -psammite, quartzites or quartz veins) with a grain size below 2 mm do not develop a volume-lination at all. Some initially fine-grained metapelites and -psammites which have a D1 or D2 volume lination preserved, show a decrease in the strength of this lination with increasing D3 strain.

Another factor that plays a role in volume-lination development is the monomineralic or polymineralic nature of a rock and the grain-size distribution therein (Fig. 2.9). In mylonitised polymineralic rocks (quartzofeldspatic pegmatite, metapsammite and -pelite) good volume-linations are common. In mylonitised monomineralic rocks (some quartz-rich pegmatites and quartz veins) which develop or retain a unimodal grain-size distribution (Fig. 2.9), volume-linations are absent or weak (e.g. monomineralic, fine-grained quartz-dominated pegmatite; SP 130; Fig. 2.7). In monomineralic rocks that develop a bimodal distribution of grain-size (e.g. quartz veins such as SP 463; Fig. 2.9 and Fig. 2.10a), good to strong grain-linations develop. Grain size distribution therefore must play an important role in the type and strength of lineations even in monomineralic rocks.

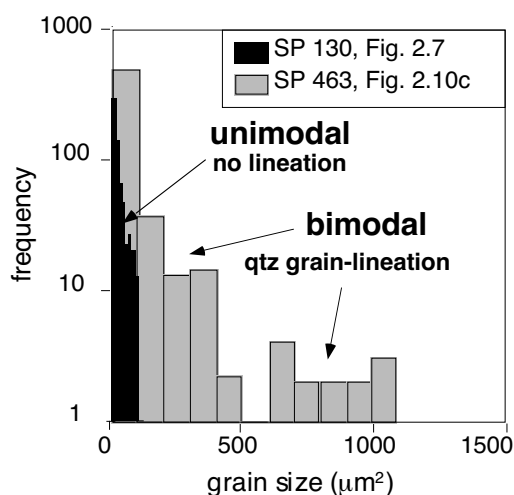


Figure 2.9 Figure depicting two different fabrics developed in mylonitised monomineralic (quartz) rocks illustrated in different distributions in a grain size distribution diagram; rock types are a quartz dominated part of a pegmatite (sample SP 130, cf. Fig 2.7 (photomicrograph)) and a quartz-vein deformed during D2 (sample SP 463, cf. Fig 2.10a (photomicrograph)).

2.5 Mechanisms of volume lineation development

Observations from Cap de Creus show, that elements of the initial fabric of the host rock such as initial grain size, mineral composition and grain size distribution "predetermine" to a large extent whether volume lineations will develop or not. Furthermore, specific mechanisms can be identified which determine how lineations develop during progressive deformation. The following mechanisms of volume-lineation development have been described as significant in the literature: (1) shape change by ductile deformation; (2) reorientation of rigid objects in a homogeneous matrix (e.g. Bhattacharyya, 1966; Gay, 1966; Rees, 1968; Ghosh and Ramberg, 1976; Ferguson, 1979; Rees, 1979; Ildefonse, 1992a, 1992b; Jezek et al., 1994, 1996) based on the work of Jeffrey (1922), Taylor (1923), March (1932) and Eshelby (1957); (3) growth of elongate minerals parallel to the direction of shear (Etheridge, 1971; Vernon, 1987) and (4) change in shape of a mineral due to dissolution, precipitation and diffusion (Bell and Cuff, 1989; Azor et al., 1997). We found that in the Cap de Creus area, three of these mechanisms seem to play a major role for the development of volume-lineations: shape change by ductile deformation assisted by dynamic recrystallization; growth of new mineral phases and rigid body rotation. The way in which these processes may generally affect the development of volume lineations is outlined below and supported by examples from the Cap de Creus area.

2.5.1 Recrystallization

Dynamic recrystallization influences significantly the formation of volume-lineations since dynamic recrystallization strongly affects fabric development during progressive deformation (e.g. White, 1977, 1979a; Guillopé and Poirier, 1979; Masuda and Fujimura, 1981; Tullis and Yund, 1985; Olsen and Kohlstedt, 1985; Wilson, 1986; Urai et. al, 1986; Dell'Angelo and Tullis, 1989; Fitz Gerald et al., 1993; Fliervoet et al., 1995; Drury and Urai, 1990). At low grade metamorphic conditions the dominant dynamic recrystallization mechanism is rotational recrystallization (Guillopé and Poirier, 1979); also known as *in situ* (Sellars, 1978); regime I (Hirth and Tullis, 1992) and regime-D recrystallization (Fig. 1.4; Drury and Urai, 1990). This kind of recrystallization influences grain size distribution in the rock (e.g. White, 1979a; Means, 1981; Tullis and Yund, 1985; Trimby et al., 1998) since recrystallized grains are commonly of smaller size than "parent" grains; because the recrystallized grain size is a function of mineral species and differential stress during the deformation (e.g. Twiss, 1977; Christie et al., 1980; Kronenberg and Tullis, 1984; Post et al., 1996). This means that old grains in a polymineralic rock with an original grain size significantly exceeding that of recrystallized grains can develop into aggregates of fine grains that will define an excellent stretching lineation; if the old grains are of approximately the same size as recrystallized grains; such aggregates cannot form, and no lineation develops, except if the small grains are already clustered into aggregates of one or several distinct mineral phases before deformation. In the latter case the effect is the same as for an initially coarse-grained rock, and good aggregate lineations may form.

The effect of dynamic recrystallization will be less important in monomineralic rocks; neither coarse nor fine-grained monomineralic rocks are likely to develop aggregate-lineations, since dynamically recrystallized aggregates derived from a single old grain cannot be distinguished from neighbouring ones. However, if only a small fraction of a second phase is present, a good aggregate lineation can develop even in "almost" monomineralic rocks. This is proba-

bly the reason why some quartzites develop aggregate lineations and others do not. Since dynamically recrystallized grain size depends on differential stress during deformation, strong aggregate lineations can be expected in rocks deformed at low metamorphic grade or high strain rate.

Besides grain size, the "degree" of recrystallization (defined as the relative modal amount of newly recrystallized grains to "old" relict grains) can be expected to influence the strength of volume-lineations. In many cases, a core-and-mantle structure (Passchier, 1982; Passchier and Simpson, 1986) will develop by partial recrystallization along boundaries of large old grains, and this produces weak lineations when the "relict", old grain relicts are equidimensional. However, if old grain cores are elongate and aligned, a grain-lineation component will be present. This element could be parallel to an aggregate lineation component in the case of polymineralic rocks, strengthening the lineation, or could be the only volume-lineation element, e.g. in originally coarse-grained monomineralic rocks. In the upper crust shear zones of low metamorphic grade are important routes for fluid channelling and circulation (e.g. Sinha et al., 1984; Kerrich, 1986; Hippert, 1998 and reference therein). Such fluid circulation enhances dislocation glide and climb resulting in an increased amount of dynamic recrystallization and crystal plasticity (Kronenberg and Tullis, 1984; Tullis and Yund, 1988, 1989; Hippert et al., 1998); hence it influences the "strength" and development of volume-lineations.

The considerations trends outlined above are to a large extent confirmed in our observations on lineation development in the Cap de Creus shear zones. In metapelitic, metapsammitic and metagranodioritic rocks of Cap de Creus (shear zones 1, 4, 5 and 6) quartz and feldspar are partly or even completely dynamically recrystallized. In polymineralic rocks feldspar and quartz recrystallize to aggregates with a mean size of 10 mm and 200 mm respectively. Where the initial grain size significantly exceeds this dynamically recrystallized grain size of quartz, feldspar (Fig. 2.10b) or biotite (Fig. 2.10c), deformation and recrystallization results in the development of recrystallized elongate aggregates, i.e. aggregate lineations. Usually, dynamic recrystallization starts at the boundaries of the original grains resulting in core-and-mantle structure. In some cases, relict old grains are equidimensional (SP 126; SP 226), e.g. round feldspar clasts in a fine-grained recrystallized matrix and no grain-lineation develops. If relicts of old grains are elongate, their preferred orientation defines a grain-lineation element (Fig. 2.10a, Fig. 2.10b). In monomineralic originally coarse-grained rocks, dynamic recrystallization only leads to a fabric with lineations if the a core-and mantle structure develops, and old grain relicts are elongate (Fig. 2.10a).

Theoretically, static recrystallization can result in destruction or weakening of a volume-lineation since the fabric is markedly changed during static recrystallization mainly by grain growth (e.g. Bons and Urai, 1992). In monomineralic rocks where a volume-lineation is defined by a bimodal grain-size distribution of elongate old grain relicts in a mass of fine recrystallized grains, static recrystallization will generally result in destruction of the lineation since grain growth destroys the bimodal grain size distribution.

In polymineralic rocks with aggregate lineations formed by alternating strips or prolate lenses of dynamically recrystallized grains of one mineral, static recrystallisation will not destroy the lineation, but will change its nature; alternating aggregates of different minerals are modified into elongate aggregates of few grains, or even single grains. The spatial distribution of different phases and the elongate shape will to a large extent be preserved. This implies a change from an aggregate- to a grain-lineation.

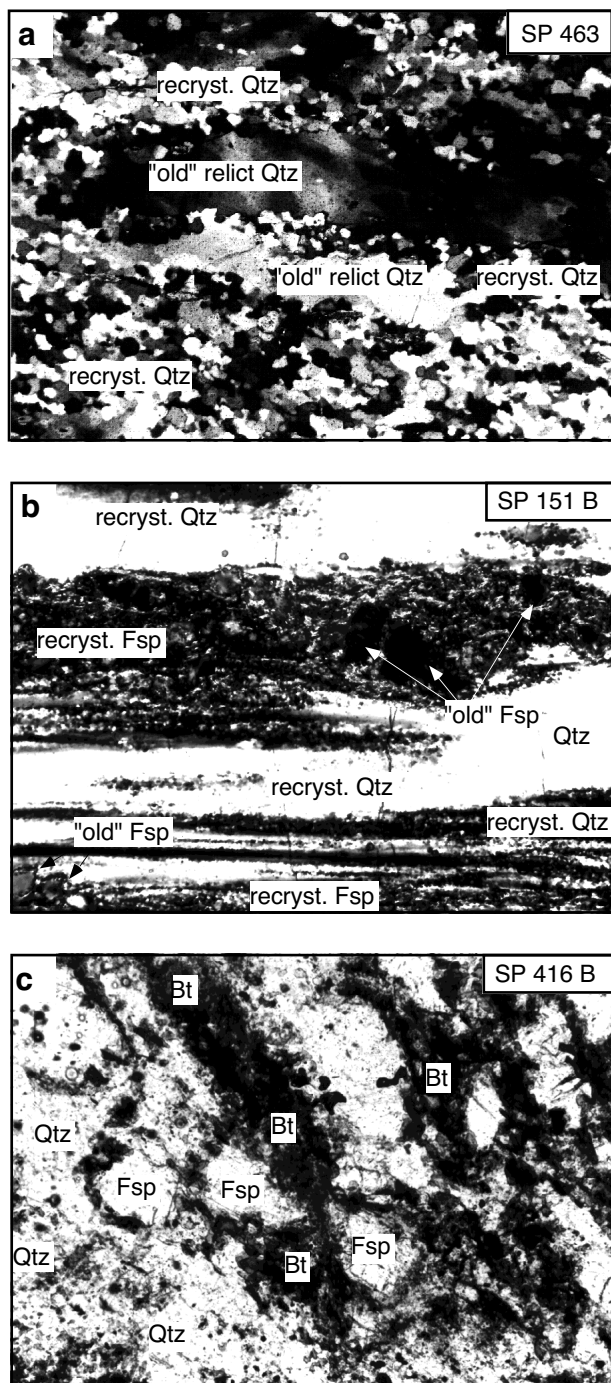


Figure 2.10 Photomicrographs depicting the variable effect of dynamic recrystallization on the fabric of selected samples, sections are cut parallel to foliation. (a) Quartz vein deformed during D2 (sample SP 463) exhibiting a bimodal grain size distribution (cf. Fig. 2.9) due to moderate degrees of dynamic recrystallization dominantly at the boundaries of large, elongate relict grains; these relict grains now form a good Qtz grain-lineation; (b) strongly deformed granodiorite (sample SP 151B) with elongate aggregates of recrystallized feldspar forming a 3.0 i -(Qtz/Fsp) aggregate-lineation. Relicts of brittly deformed feldspar and quartz ribbons are also seen. Sample is taken from central part of shear zone 2; crossed nicols; (c) strongly deformed granodiorite (sample SP 416A) with numerous small recrystallized Fsp grains and elongate aggregates of recrystallized Bt constituting a 2.1 i -Bt aggregate-lineation; crossed nicols; width of view is 0.6 mm for all samples.

The mobility of grain boundaries can be expected to have a strong influence on the extent to which static recrystallization affects the "strength" of a volume-lineation. Grain boundary mobility besides surface and internal, stored energy of grains controls the velocity at which a grain boundary will move. It is strongly influenced by impurities (e.g. Gottstein and Shvindlerman, 1999 and references therein), particle dispersion (e.g. Olgaard, 1986, 1988; Jessell, 1987) and the presence of fluid (e.g. Gottstein and Shvindlerman, 1999 and references therein; Tullis and Yund, 1985, 1988, 1989). Rocks that are dry and have grain boundaries with a high percentage of impurities and small dispersed particles will exhibit only minor effects of static recrystallization.

Static recrystallization may be responsible for the peculiar features of the D2-fabric in the Cap de Creus area as outlined under 2.4.3 and shown in Fig. 2.5. We attribute the difference in D2 volume-lineations 'strength' in fine-grained (high) and coarse-grained rocks (low) to the effect of static recrystallization. Strong static recrystallization acting on a deformed fine- to medium-grained rock exhibiting a volume-lineation will result in a coarse-grained rock type with poorly developed lineations, while the lineation is preserved where static recrystallization is hampered, e.g. because of pinning due to dispersion of other mineral phases. Static recrystallization probably occurred in the period between D2 and D3 since typical equilibrium textures (e.g. polygonal fabric with straight grain boundaries, 120° angles between quartz grains) are commonly seen in D2 fabrics unaffected by D3.

2.5.2 Growth of new phases

Metamorphic reactions change the mineral content of a rock and hence determine what minerals are available to form a volume-lineation. Lineation type and "strength" depends on the type of minerals growing during deformation, since the habit of these newly growing grains has a noticeable effect on the type and "strength" of developing volume-lineations (e.g. Etheridge, 1971; Vernon, 1987). If at least one of the new phases is characterized by an elongate habit, a grain-lineation can form due to either the oriented growth of the new mineral phase or its syntectonic rigid body rotation (Vernon, 1987). Also, if new phases have an equidimensional habit an aggregate-lineation can form under suitable circumstances e.g. deformation of clusters of newly grown equidimensional phases or dynamic recrystallization of a new parental grain.

In upper crust shear zones, the fluid which is necessary for most retrograde reactions is commonly provided by fluid circulation. The presence of such fluid also affects the rates of chemical and mechanical processes and therefore rates of metamorphic reactions (e.g. Beach, 1980; Dipple and Ferry, 1992), and consequently the development of volume-lineations.

In the Cap de Creus area, growth of new mineral phases is due to several reactions that took place during mylonitization such as: (a) plagioclase + K^+ + H_2O \rightarrow white mica + Na^+ + Ca^+ (e.g. shear zone 2 and 9); (b) potassium feldspar + andalusite/biotite + B-rich fluid \rightarrow fibrolite + muscovite + tourmaline (e.g. shear zone 5 and 7); (c) amphibole + feldspar \rightarrow epidote/zoisite (shear zone 3) and (d) sericitisation of feldspar during and after deformation (e.g. shear zone 1 and 6). Where these reactions led to growth of elongate minerals during deformation this strengthened or created volume-lineations. For example, syntectonic growth of fibrolite at the expense of andalusite results in good aggregate- and grain-lineations i.e. elongate bundles of fibrolite or grain-lineations i.e. isolated fibrolite needles in mylonitised, initially coarse-grained metapelites. In the metapsammitic samples of shear zone 1 the contrast between quartz aggregates and chlorite/sericite domains which formed during metamorphic

retrogression makes up an aggregate-lineation. The amount of metamorphic replacement of one mineral species by another plays a role in the "strength" of aggregate lineations. For example, the higher the amount of epidote/zoisite, which replaces amphibole (reaction c), the higher degree of preferred orientation. In SP 160 and SP 163 (shear zone 3) the amount of replacement of amphibole by a member of the zoisite group is 70% and 100%, respectively; corresponding κ -values are 3 and 3.4. Breakdown of minerals after deformation (reaction d) may weaken pre-existing volume-lineations. For instance, poor aggregate lineation are present in SP 126 and SP 267 due to retrogression of a large percentage of the rock to fine-grained assemblages involving chlorite, quartz and sericite (Tab. 2.1).

Redistribution of phases due to dissolution, diffusion, transport and re-deposition of quartz, feldspar (e.g. O'Hara, 1990) and carbonates (Robin, 1979; Bell and Cuff, 1989; Dewers and Ortoleva, 1990) can also have a significant effect on the fabric of a rock and therefore the development of volume-lineations. This effect will become more profound and noticeable at higher temperatures i.e. at amphibolite and granulite facies conditions. At high temperatures this could lead to "fuzzy" boundaries between aggregates in polymineralic, recrystallized rocks, producing weaker volume-lineations. In the investigated shear zones, though, no conclusive evidence, such as pressure shadows or bands of one mineral species, points to significant redistribution of material.

2.5.3 Rigid body rotation

Rigid body rotation of mineral grains in a rock can account for an increase in the "-strength" of a volume-lineation during progressive deformation since elongate mineral grains with high aspect ratios tend to rotate towards the extensional flow eigenvector. If rigid body rotation is one of the dominant process of volume-lineation development, the degree of dimensional preferred orientation depends on finite strain and on the modal amount of the lineation-forming material (e.g. Ildefonse, 1992a, 1992b). Rigid body rotation of elongate minerals such as sillimanite and biotite may also results in good to strong grain-lineations. Here again, grain size is important. If the matrix material enveloping the rigid mineral (e.g. biotite) is relatively fine-grained and deforms in a ductile manner, rigid body rotation can take place. Such an apparently viscous rheology is commonly achieved by dislocation climb, dynamic recrystallization and/or pressure solution.

In the Cap de Creus area, we may see this effect of rigid body rotation to some extent. The Sil-bearing volume-lineations may be at least partly formed by rigid body rotation (see 2.5.2). In samples SP 227 (shear zone 5) and SP 358 (shear zone 8) biotite grains exhibit a strong preferred orientation that defines a grain-lineation. This preferred orientation is probably due to rigid body rotation since biotite grains are not recrystallized while the quartz matrix is fine-grained (0.02 mm).

2.6 Conclusions - Predictions for volume lineation development

The presence and "strength" of a volume-lineation in a deformed rock is not only a function of bulk strain but is strongly influenced by other factors. The most important factors are (a) initial fabric and mineralogy and (b) the ratio of initial grain size to dynamically recrystallized grain size. These factors determine how processes active during and after deformation affect the development of volume-lineations. Most important among these processes are dynamic and static recrystallization, metamorphic reactions and rigid body rotation. Based on the observa-

tions in the Cap de Creus shear zones, we predict a number of trends in the development of volume-lineations. These trends are summarised in Figures 2.11 and 2.12 which can serve as guidelines to predict where good volume-lineations can be expected. Both diagrams show lineation development in a simplified way, but serve to illustrate main trends.

During deformation and dynamic recrystallization but without metamorphic reactions producing new phases (Fig. 2.11), good aggregate lineations form in originally coarse-grained polymineralic and in clustered polymineralic fine-grained rocks. In all other coarse- and fine-grained rocks, good aggregate-lineations cannot form. If a coarse-grained monomineralic rock is deformed to a moderate degree and a bimodal grain size distribution develops, good to strong grain-lineations result; otherwise no lineation will develop.

During deformation and dynamic recrystallization in the presence of metamorphic reactions, the result depends on the shape of the new mineral phases; syndeformational growth of elongate minerals causes good to strong grain- and aggregate-lineations to develop from coarse-grained rocks (Fig. 2.12) but if new grains are equidimensional in shape weak to good aggregate lineations form. In initially fine-grained, dispersed fabrics syntectonic growth of elongate grains results in the development of weak to good grain-lineations. If new grains are equidimensional, volume-lineations are absent. If the initial fabric is fine-grained but clustered (not shown on Fig. 2.12) the developing lineation is weak to good and of the aggregate type.

Static recrystallization subsequent to deformation generally causes monomineralic rocks to exhibit a significant decrease in volume-lineation “strength” and even to lose the lineation completely since grain size distribution will become more and more unimodal with the degree of static recrystallization (Fig. 2.11). In polymineralic rocks, the “strength” of a volume-lineation will also decrease but will still be present even after a high degree of static recrystallization, as the spatial distribution of mineral phases is not significantly affected (Fig. 2.11 and Fig. 2.12).

Breakdown of minerals after deformation may alter pre-existing lineations and can obscure them totally due to changes in the grain size distribution and overgrowth.

Besides these endogenous trends, mineral colour and weathering may play a role in the visibility of volume-lineations. For example, bimodal grain size distribution strongly enhances heterogeneous weathering and coatings in certain areas and frequently result in volume-lineations that are obvious in handspecimen. In “almost” monomineralic rocks with a uniform grain size distribution an aggregate-lineation may still be seen in handspecimen even if the colour of the second mineral species is similar to the rest of the rock (e.g. feldspar in quartzite) since weathering will affect the second mineral species differently.

Due to the significant effect of other factors than finite strain on the development and strength of a volume-lineation, a study looking at possible strain intensity, presence and orientation of tectonic transport should preferably involve the study of several rock types.

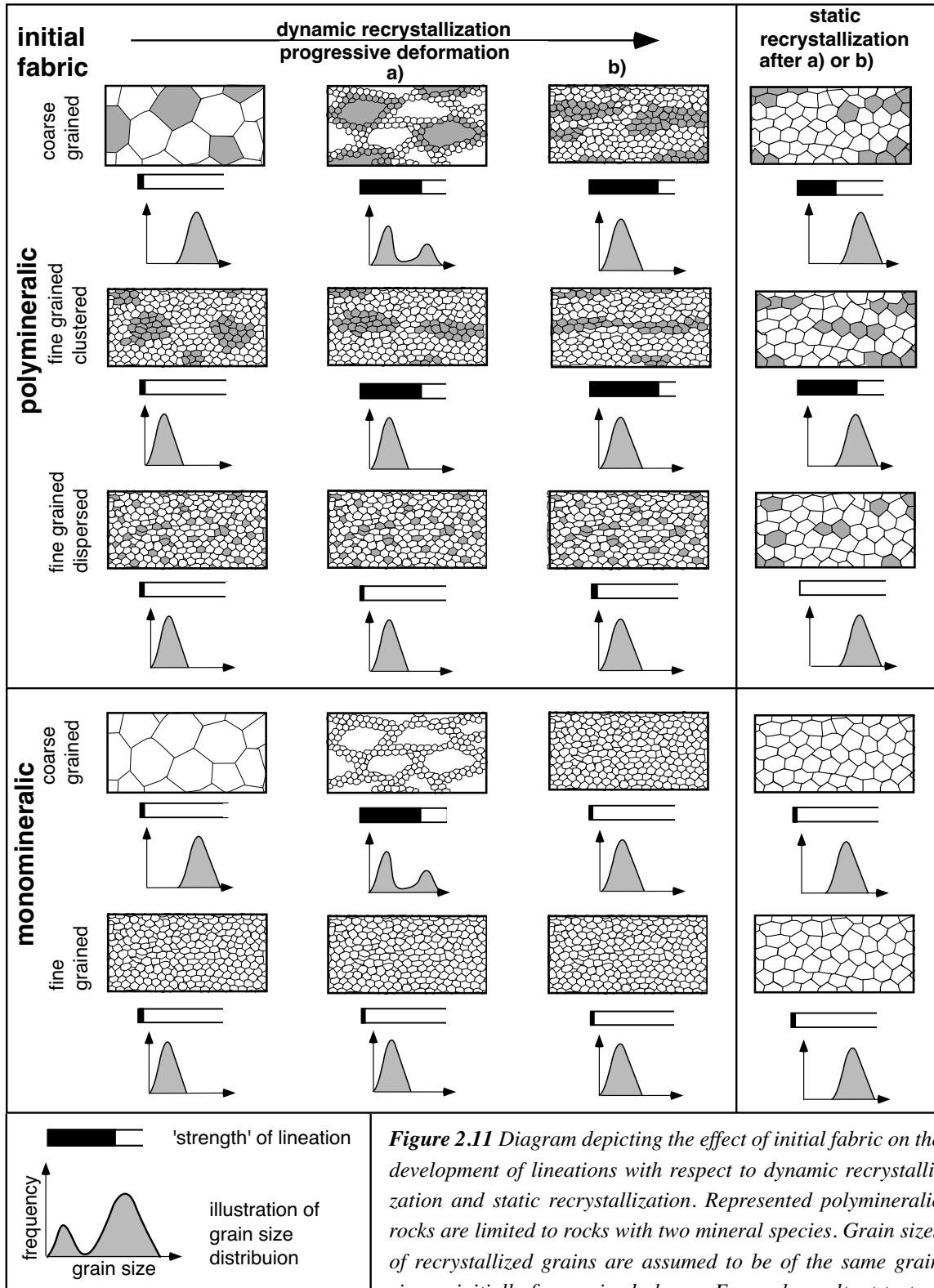


Figure 2.11 Diagram depicting the effect of initial fabric on the development of lineations with respect to dynamic recrystallization and static recrystallization. Represented polymineralic rocks are limited to rocks with two mineral species. Grain sizes of recrystallized grains are assumed to be of the same grain size as initially fine-grained phases. For each resultant texture a schematic grain size distribution diagram and a bar illustrating the “strength” of lineation is shown. The longer the black bar the “stronger” the lineation.

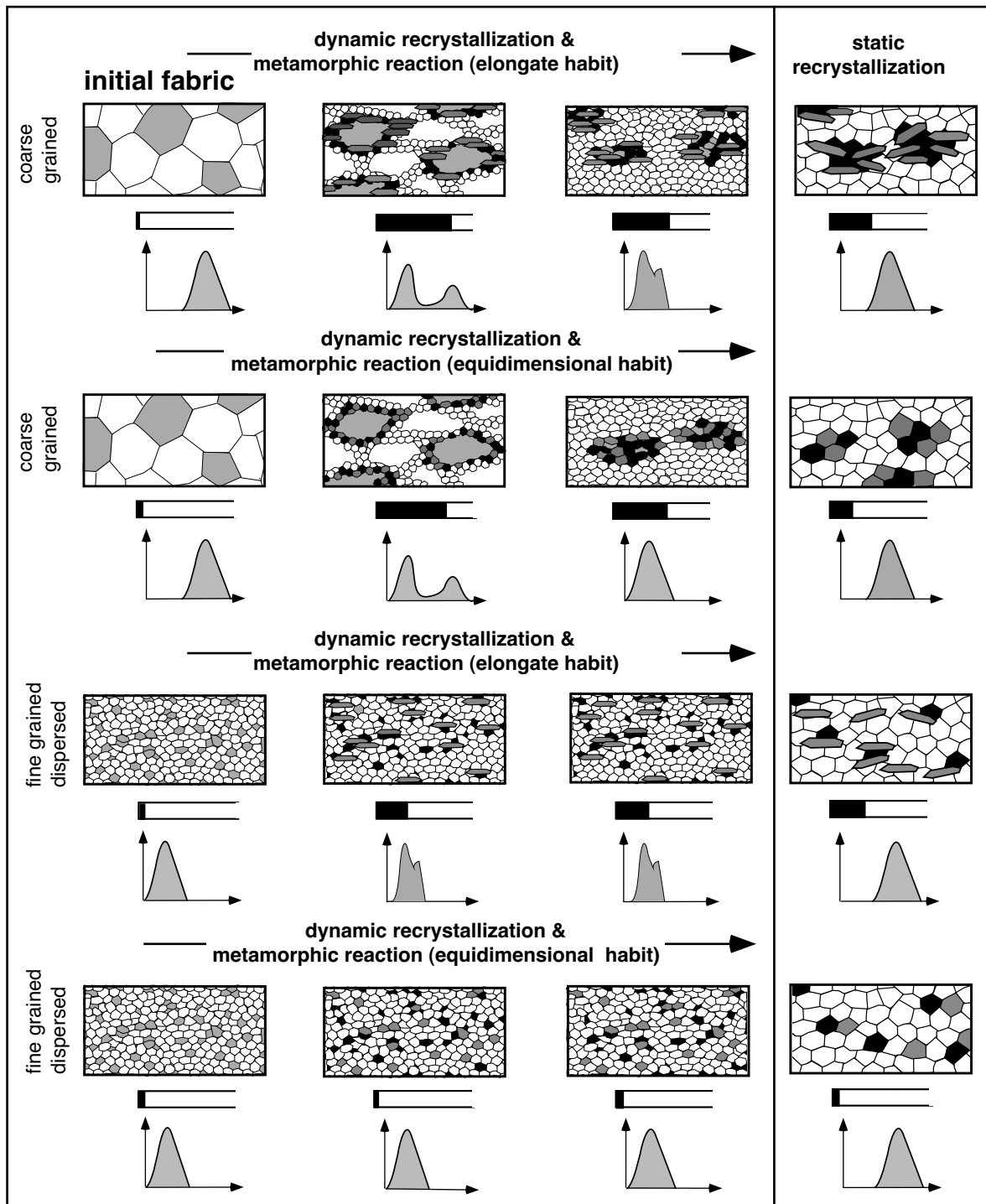


Figure 2.12 Diagram depicting the effect of initial fabric, dynamic- and static recrystallization and metamorphic reaction on the development of lineations during and after deformation. Two different types of metamorphic reactions are distinguished whereby (a) one new phase is elongate and (b) two new phases are equidimensional in shape. For each resultant texture a schematic grain size distribution diagram and a bar illustrating the “strength” of lineation is shown. The longer the black bar the “stronger” the lineation. See Fig. 2.11 for explanation of symbols.

No.	SZ No.	S2 orient	S _{myl}	γ	rock type	rock	D2	SZ bend	SZ centre	main mineralogy	κ	lineation type
122	1	290/25	65/60	0.0	metapsammite	a	x			Qtz, Fsp, Bt, Ms	3.5	3.5 s-Bt grain
124				1.8	metapsammite	a		x		Qtz, Fsp, Bt, Seri, Tur	1.0	1.0 i-Bt grain
125				1.8	metapsammite	b		x		Bt, Seri/Chl, Fsp, Qtz, Ms, Tur	0.8	0.8 i-Bt grain
126				4.8	metapsammite	a			x	Qtz, Seri/Chl, Fsp, Ms, Tur	0.5	0.5 s-Qtz aggregate
127				4.8	metapsammite	b			x	Fsp, Qtz, Chl/ Seri, Tur, Ms	2.6	2.6 i-Qtz aggregate
128 A				0.0	cg. pegmatite	c	x			Qtz, Fsp, Bt, Ms	2.3	2.3 l-Qtz grain
130				4.8	Qtz-rich peg.	c			x	Qtz	no	
131				4.8	cg. pegmatite	c			x	Qtz, Fsp, Ms	4.6	4.6 i-Qtz aggregate
151 A	2	270/40	82/30	0.0	granodiorite	a	x			Qtz, Fsp, Bt, Ms	1.4	1.4 i-(Qtz/Fsp) aggregate
151 B				2.9	granodiorite	a			x	Qtz, Fsp, Bt, Ms, Gr, Tur	3.0	3.0 i-(Qtz/Fsp) aggregate
160	3	260/40	20/76	5.3	Fsp-amphibole rock	a			x	Qtz, Ep, Fsp, amphibole, Ms	3.0	3.0 i-Ep grain
163				5.3	Fsp-amphibole rock	a			x	Qtz, Ep, Fsp, amph, Ms	3.4	3.4 i-Ep grain
191	4	140/75	40/80	0.0	cg. metapsammite	a	x			Qtz, Fsp, Bt, Ms, Tur	1.9	1.9 s-Bt grain
192				3.0	cg. metapsammite	a		x		Qtz, Fsp, Ms, Bt	3.5	3.5 s-Bt aggregate
193				4.1	fg. metapsammite	b			x	Qtz, Fsp, Bt, Ms, Tur	1.6	1.6 i-Bt grain
194				0.0	fg. metapsammite	b	x			Qtz, Fsp, Bt, Ms	4.4	4.4 i-Bt grain
195				1.6	fg. metapsammite	b		x		Qtz, Fsp, Ms, Bt	3.9	3.9 i-Bt grain
197				4.1	cg. pegmatite	c			x	Qtz, Fsp, Tur, Ms	3.0	3.0 i-(Qtz/Fsp) aggregate
198		164/8		0.0	cg. pegmatite	c	x			Qtz, Fsp, Ms, Tur	1.5	1.5 i-Qtz aggregate
223	5	120/8	30/85	0.0	fg. metapsammite	a	x			Fsp, Qtz, Bt	2.6	2.6 i-Bt grain
225				2.5	fg. metapsammite	a		x		Qtz, Fsp, Bt, Ms	no	
226				3.6	fg. metapsammite	a			x	Qtz, Fsp, Bt/Seri/ Chl, Tur	1.4	1.4 i-(Bt/Chl) aggregate
227				0.0	mg. metapelite	b	x			Qtz, Fsp, Bt, Fibr, Seri	6.0	6.0 s-Bt grain
228				3.6	cg. metapelite	c			x	Qtz, Fsp, Fibr, Bt, Ms, Tur	2.4	2.4 i-Fibr aggregate
229				0.0	cg. metapelite	c	x			Qtz, Fsp, Ms, Bt, Fibr, And	1.2	1.2 s-Fibr aggregate
264	6	22/65	40/5	0.0	Qtz vein	a	x			Qtz	No	
265				1.4	Qtz vein	a		x		Qtz	No	
266				4.5	Qtz vein	a			x	Qtz	No	
267				4.5	fg. metapelite	b			x	Qtz, Fsp, Bt, Ms, Tur	1.3	1.3 i-Bt grain
268				2.1	fg. metapelite	b		x		Qtz, Fsp, Tur, Bt, Ms, Chl	1.5	1.5 i-Bt grain
269				0.0	fg. metapelite	b	x			Qtz, Fsp, And, Ms, Fibr	4.8	4.8 i-Bt grain
270				5.1	cg. metapelite	c			x	Qtz, Fsp, Bt, Ms	2.8	2.8 i-Bt aggregate
271				2.3	cg. metapelite	c		x		Qtz, Fsp, Ms, Bt, Fibr	2.6	2.6 i-Bt grain
272				0.0	cg. metapelite	c	x			Qtz, Fibr, Fsp, Tur, Ms, Bt	1.7	1.7 i-Bt grain
289	7	240/85	21/43	5.1	metapelite	a			x	Qtz, Fsp, Fibr, Bt, Tur, Ms	3.2	3.2 s-Fibr aggregate
290				2.1	metapelite	a		x		Qtz, Fsp, Bt, Fibr, Ms, Tur	3.0	3.0 s-Fibr aggregate
291				0.0	metapelite	a	x			Qtz, Fsp, Bt, Ms, Fibr, And	1.8	1.8 s-Fibr grain
				0.0							0.9	0.9 s-And grain
358	8	-	-	2.3	quartzite	a	x			Qtz, Bt	2.1	2.1 s-Bt grain
416 A	9	270/45	62/50	4.8	granodiorite	a			x	Qtz, Fsp, Bt, Ms, Tur	2.1	2.1 i-Bt aggregate
416 B				0.0	granodiorite	a	x			Qtz, Fsp, Bt	1.6	1.6 s-Bt grain
463	10	-	-	2.3	small Qtz vein	a	x			Qtz	2.1	2.1 i-Qtz grain

Table 2.1 (opposite page) The table tabulates the characteristics of shear zones and samples investigated in this study. Shear zone (SZ) and sample numbers (No.) correspond to those referred to in the text and figures.; S2 orient.= azimuth/angle of dip of foliation outside shear zone; S_{myl} = azimuth/angle of dip of mylonitic foliation; γ = estimated strain magnitude assuming simple shear deformation; rock type = description of rock type; rock = index of specific lithology within specific shear zone. Crosses in the three columns D2, SZ bend and SZ centre signify where the sample was taken. The κ -value refers to the statistical parameter κ of a von Mises distribution and signifies the degree of preferred dimensional orientation (the higher κ , the higher the degree of preferred dimensional orientation; Appendix B). Lineation type corresponds to the proposed general classification. Seri = sericite, Am = amphibole, Fibr = fibrolite, cg. = coarse-grained, fg. = fine-grained.

Acknowledgments

S. P. thanks M. W. Jessell, G. Lister, P. Bons and other members of the Earth Science Department at Monash University, Australia for making facilities available. Thanks to Dr. M. Clark (Monash University, Australia) for introduction to the statistical methods and to E. Druguet (Universidad Autonoma, Barcelona) for introducing S. P. to the field area. Comments by E. Druguet, K. Gessner (University of Mainz) and P. Bons (University of Mainz) considerably improved an earlier version of this manuscript.

Chapter 3

Numerical modelling of dynamic recrystallization using Elle Description of the model, new techniques of microstructural analysis and first results of simulations

Preface

The numerical modelling system Elle (Jessell et al., 2001) was used to test the findings and interpretations of Chapter 2. In Chapter 2 it was argued that the characteristics and development of a shape fabric is strongly affected by the way in which dynamic recrystallization modifies the microstructure of a rock during progressive deformation. This effect seems to be related to the ratio of initial to recrystallized grain size.

To test this hypothesis it was necessary to further develop the numerical modelling system Elle so that the model could be used to simulate dynamic recrystallization. This chapter gives a detailed account of the numerical system Elle as it was used for the simulations. The chapter is not written in short paper format because in such a format too much information and details would have had to be left out. Furthermore, a detailed description seems to be appropriate since this is the first published account on most of the currently available processes within the numerical modelling system Elle.

Abstract

To investigate the influence of the mode of dynamic recrystallization on the development of a fabric during progressive deformation a two dimensional numerical model that simulates dynamic recrystallization was developed. With this model it is possible to model plane strain deformation with different kinematic vorticity numbers. Additionally, crystallographic lattice rotation, formation of subgrains, recrystallization by nucleation, rotational recrystallization, grain boundary migration and recovery are simulated during progressive deformation.

New methods to describe a microstructure quantitatively and to delineate active processes were developed in the course of this study. These are the ratio of low to high angle boundary lengths, plots of the grain boundary distance distribution measured in two perpendicular directions and analysis of the grain size distribution in plots of ranked grain size against rank number.

A set of 12 simulations with varying parameters were performed to investigate the effect of the initial microstructure, grain boundary mobility and nucleation threshold which is related to recrystallization rate on the microstructural development of a rock. Initially coarse grained fabrics i.e. fabric with high ratio of initial grain size to recrystallized grain size did not develop a unimodal grain size distribution. A strong shape fabric is seen as large elongate grains remain in a matrix of small recrystallized grains.

Abstract (continued)

Initially fine grained fabrics i.e. fabric with low ratio of initial grain size to recrystallized grain size retain in most cases their unimodal grain size distribution throughout progressive deformation and a weak shape fabric is developed. High ratios of low/high angle boundaries lengths are characteristic for low nucleation thresholds in initially coarse grained fabrics. Large grain sizes with a slightly bimodal grain size distribution and low grain aspect ratios indicate a high grain boundary mobility. Strain softening is observed in all experiments. It is most profound at low nucleation thresholds and high grain boundary mobilities. The grain size distribution seen in initially coarse grained fabrics follows a power law function in a certain range of grain sizes. The slope of the function, i.e. the fractal dimension seem to be characteristic for the value of the recrystallization rate.

This new numerical model opens up a new field in microstructural investigations. With this model it is now possible to test and modify existing theory and systematically investigate the effect of different parameters on the microstructural development of a rock. Simulations which model the evolution of a rock at changing strain rates, temperatures and pressures can be performed and analysed. Comparison of simulations and natural samples are likely to yield new information about the evolution of studied samples.

3.1 Introduction

Dynamic recrystallization is an important process during deformation of many rock forming minerals and occurs under a wide range of metamorphic conditions (Urai et al., 1986; Drury and Urai, 1990). It is one of the processes that enables a crystalline aggregate to lower its free energy during deformation. Dynamic recrystallization involves the establishment of an array of grain boundaries in new material positions (Means, 1983) and the formation and/or migration of grain boundaries (Vernon, 1981) during deformation. In general, it leads to the formation of new grains at the expense of old ones. Therefore, dynamic recrystallization significantly influences the microstructure as well as the mechanical properties of a rock. Resultant microstructures are used to derive processes active during deformation (e.g. Guillopé and Poirier, 1979; Urai et al., 1986; Knipe, 1989; Drury and Urai, 1990; Hirth and Tullis, 1992; Takeshita et al., 1999; Shigematsu, 1999; Heidelbach et al., 2000) and delineate the conditions during which the rock was formed and/or deformed (e.g. Vernon, 1976; Hobbs et al. 1976; Hirth and Tullis, 1992; Twiss and Moores, 1992; Passchier and Trouw, 1996 and references therein). The dynamically maintained grain size is often related to the steady state flow stress (e.g. Twiss, 1977; Kohlstedt and Weathers, 1980; Christie et al., 1980; Kronenberg and Tullis, 1984).

Several papers have been published (Drury et al., 1985; Gottstein and Mecking, 1985; Urai et al., 1986; Drury and Urai, 1990) that aimed to summarize observations of different microstructures thought to have developed due to dynamic recrystallization such as core-and-mantle structures (Passchier, 1982; Passchier and Simpson, 1986).

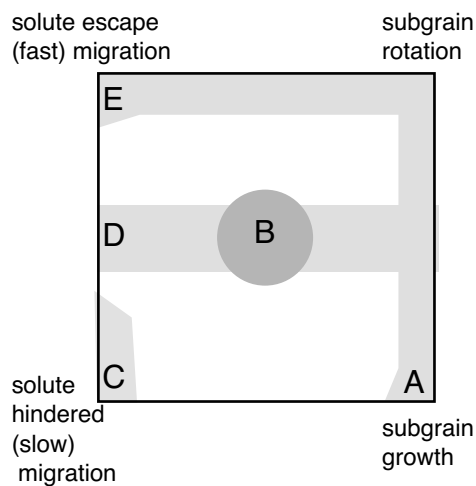


Figure 3.1 Recrystallization mechanism diagram (modified after Drury and Urai, 1990). The following regimes are shown in grey boxes (in **bold**: term used in this chapter, otherwise: term given by Drury and Urai (1990)): regime A: continual rotational recrystallization - **rotation recrystallization**; B: continual rotation and migration with discontinual migration; regime C: continual migration recrystallization - **grain boundary migration**; regime D: rotation recrystallization with discontinual stage of new grain development - **rotational recrystallization and recrystallization by nucleation**; regime E: continual rotation and discontinual migration.

Two main mechanisms active during dynamic recrystallization are rotational recrystallization and grain boundary migration recrystallization (e.g. Poirier and Nicolas, 1975; Guillopé and Poirier, 1979; Fitz Gerald et al., 1983; Urai et al. 1986 and references therein). Drury (1984) and Drury and Urai (1990) suggest a further subdivision of mechanism in subgrain formation, rotational recrystallization, recrystallization by nucleation and grain boundary migration. The recrystallization mechanism diagram (Fig. 3.1) illustrates that the dominance of one mechanism over other mechanisms result in different dynamic recrystallization types. Hirth and Tullis (1992) experimentally determined three different dislocation creep regimes in quartz aggregates according to strain rates, dominance of processes and temperatures. Each of these regimes shows characteristic microstructural features (for further details see section 3.4.4.1).

To be able to interpret microstructures that developed due to dynamic recrystallization, it is vital to know how they form. Questions to be answered involve the way and extent at which specific processes, combination of processes and value of parameters such as grain boundary mobility affect the microstructure and the rheology of a rock during progressive deformation. Are there characteristic microstructures indicative for a specific range of parameters and combinations of mechanisms? Additionally, we still have insufficient knowledge of the way and to what extent the initial fabric of a rock influences the microstructural development and flow properties of a rock during subsequent deformation.

Knowledge of microstructural development during progressive deformation in terms of dynamic recrystallization is still largely qualitative and empirical. For instance, determination of the dominant processes that operated is largely based on the experience and intuition of the observer since no quantitative tools in this respect have been developed so far. One of the main problems is that geological microstructures develop over long time scales and at high pressure and temperature conditions. This precludes direct observation in nature. Nevertheless, our understanding of microstructures has been considerably improved due to microstructural studies in naturally (e.g. Masuda and Fujimura, 1981; Olsen and Kohlstedt, 1985; Urai et al., 1986; Knipe and Law, 1987; Lloyd et al., 1992; Drury and Urai, 1990; Fitz Gerald et al., 1993; Trimby et al., 1998) and experimentally deformed rocks (e.g. Guillopé and Poirier, 1979; Tullis and Yund, 1985, 1989; Ion et al., 1982; Kronenberg and Tullis, 1984; Karato and Masuda, 1989; Dell'Angelo and Tullis, 1992; Hirth and Tullis, 1992). In-situ experiments with analogue materials in which samples can be observed under a microscope throughout an experiment have provided invaluable insight in microstructural development (e.g. Means, 1983; Jessell, 1986; Means and Ree, 1988; Bons and Jessell, 1996; Herwegh and Handy, 1998). However, it

is difficult to "translate" the observations of deforming organic crystalline compounds to rock forming minerals. Analytical and numerical investigations of the full microstructural development during deformation has so far been hampered by the complexity of simultaneously operating processes. The fundamentals of many operating processes are well known; e.g. dislocation creep (e.g. Frost and Ashby, 1983 and references therein; Kocks et al., 1975; Hirth and Tullis, 1992), grain boundary migration (Cobbold, 1983; Anderson et al., 1984; Grest et al., 1985; Randle et al., 1986; Jessell, 1987; Means and Ree, 1988; Gottstein and Shvindlermann, 1999) and lattice rotation (Taylor, 1938; Bishop and Hill, 1951a, 1951b; Lister and Paterson, 1979; Lister et al., 1978; Lister and Williams, 1979; Lister and Hobbs, 1980; Wenk et al., 1987). Published single-process numerical models include codes to model viscous or viscoplastic deformation (e.g. Board, 1989; Masuda and Mizuno, 1996; Barr and Houseman, 1996, 1999), lattice rotation (e.g. Lister et al., 1978; Wenk et al. 1991; Castelnau et al., 1996; Zhang and Wilson, 1997; Wenk and Tomé, 1999) and node network codes to model grain boundary migration and grain growth (Soares et al., 1985; Bons and Urai, 1992; Bons, 1993; Pan et al., 1997; Jessell et al. 2001; Bons et al., in press). However, these models usually neglect the influence of additional concurrent or interacting processes although such interactions may have a profound effect on the microstructural development of a rock (Jessell and Lister, 1990).

In this study, a numerical model for dynamic recrystallization is presented using the numerical modelling system Elle (Jessell et al., 2001). With Elle, it is possible to simulate a variety of concurrent microstructural processes that are active at grain scale during progressive deformation. A set of simulations modelling dynamic recrystallization of a monomineralic quartzite deformed under greenschist to amphibolite facies conditions and simple shear were performed. The focus of the latter part of the study lies in the understanding and quantification of the effects of different recrystallization rates which correspond to the energy thresholds for recrystallization by nucleation, grain boundary mobilities and different ratios of initial and recrystallized grain size on the development of a microstructure during progressive deformation. In addition to the explanation of the model, new microstructural criteria which aim to quantitatively describe and characterize a microstructure, to delineate active and/or dominant processes and to quantify intrinsic and extrinsic parameters are proposed.

3.2 Numerical model Elle

3.2.1 General approach

The modelling system Elle is designed to model the two-dimensional evolution of a microstructure that is a result of several concurrent micro-processes. Numerical modelling of several concurrent processes results in a nonlinear problem. Complex algorithms and differential equations would have to be employed if the different equations which each describe the microstructural change according to one individual process should be solved simultaneously. So far, such algorithms are largely lacking.

Another approach is taken with Elle. It is assumed that a fabric is a result of microstructural changes due to process a, b, c, ..., n, and that the fabric development can be simulated by the sum of the microstructural changes of each of the individual processes according to the general relationship

$$\delta f(a, b, \dots, c) = \delta f(a) + \delta f(b) + \dots + \delta f(c) \quad (\text{Eq. 3.1})$$

Equation 3.1 is only given if each process can be discretized in space and time. In Elle Eq. 3.1 is valid as processes operate at a very small scale and only for a small time increment.

This approach which describes the nonlinearity of the problem by discretization of the problem into distinct, linear and small segments in space, time and process, may lead to some inaccuracy of results. Nevertheless, right now, there is no other numerical model available that simulates the different simultaneously active processes needed for simulations of dynamic recrystallization.

3.2.2 General description of modelling environment used

The modelling system Elle (Evans et al., 2000; Jessell et al., 2001) is based on a data structure that describes a polycrystalline material using a two-dimensional network of nodes and connecting boundaries at the grain scale (Fig. 3.2). The network of nodes and boundaries forms a square unit cell with periodic boundaries. Individual nodes possess attributes of position and topology and may have additional attributes such as chemistry and stress state. The polygonal domains defined by these nodes and their connecting boundaries may possess attributes such as mineralogy, viscosity, strain, stress, dislocation density, age and lattice orientation. Each polygon has an attribute which specifies if the polygon is a true grain or if it is part of a larger grain; hence a subgrain. The specific distinction between grain and subgrain will be described in detail in section 3.2.3.5. Data on the geometry of the structure and values of nodes and polygons are stored in an Elle data file. To simulate the progress of a process, distinct process algorithms can interact with this data structure (a) by using it to determine the local values of driving forces, (b) by repositioning, creation and removal of nodes, (c) by reconnecting boundary segments, and (d) by altering attributes. A central shell program controls the evolution of extrinsic variables, such as temperature, and determines which micro-processes will be involved by controlling the order and rate of execution of individual process algorithms (Fig. 3.3a).

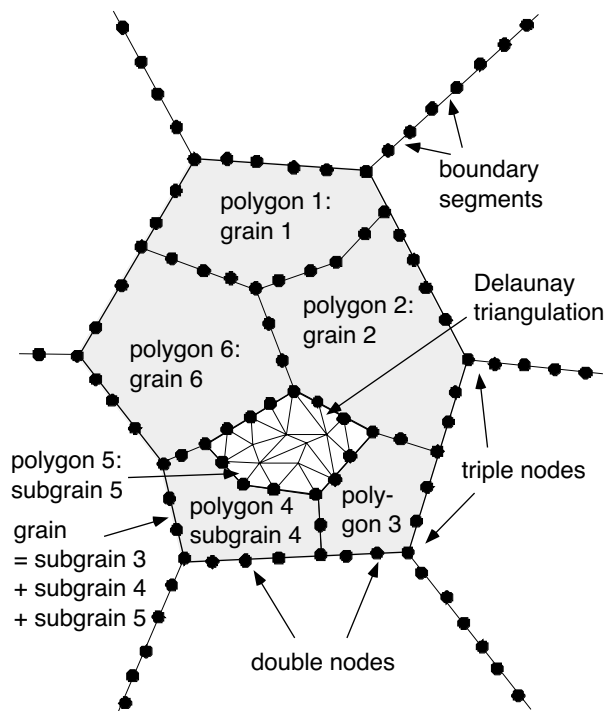


Figure 3.2 Representation of the 2-dimensional finite element map of a grain aggregate. Each polygon domain (grain; polygon 1, 2, 6, 7) can be subdivided into a number of polygonal sub-domains (subgrains; polygon 3, 4, 5), each of which in turn has a number of properties assigned to them, such as crystal lattice orientation. All polygons can be if desired triangulated to smaller elements using a Delaunay triangulation routine. This triangulation is, in contrast to the polygons, nodes and boundary segments, not permanent and can be used temporarily e.g. for the subgrain formation routine (ELLE_SPLIT; see text). Triangulation elements may also have individual properties, including the stress and strain state during deformation, and/or trace element concentration..

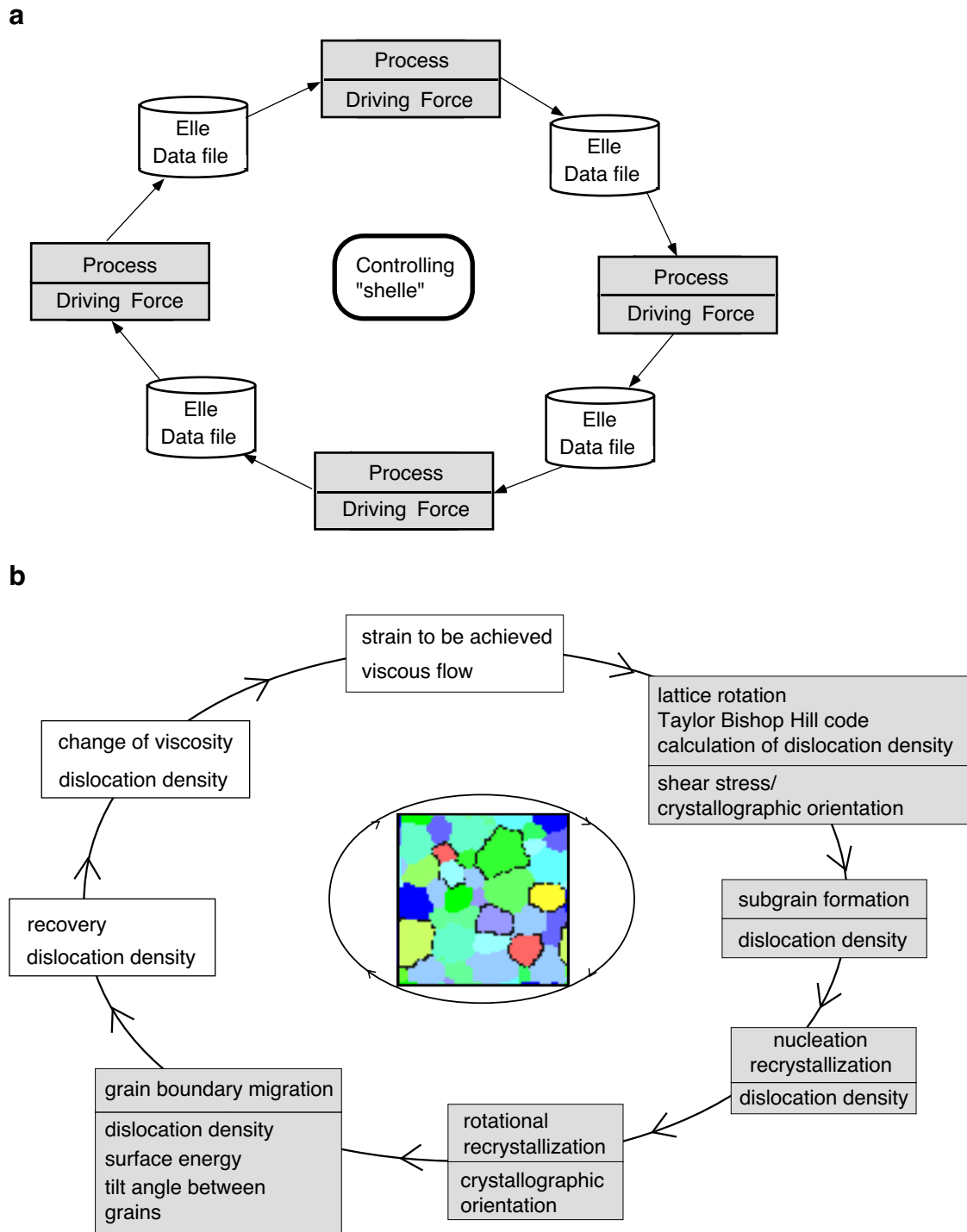


Figure 3.3 (a) General schematic flow diagram of the Elle modelling system. (b) Flow diagram of the dynamic recrystallization model. Processes given in the white boxes are those which have no true driving force (e.g. calculation of viscosity), while processes (top of boxes) and driving forces (bottom of boxes) are depicted in grey boxes.

In the model plane strain deformation of a viscous material, crystallographic rotation, formation of subgrains, recrystallization by nucleation, rotational recrystallization, grain boundary migration and recovery is simulated (Fig. 3.3b).

To implement real world values in the model and to translate the calculated numerical values to real world values several scaling factors are needed. Scaling factors which need to be specified are the time (t_{scale}), length (l_{scale}), dislocation density (ρ'_{scale}) and the stress (τ_{scale}). To specify the spatial resolution of the node-boundary mesh a minimum and maximum node separation and a so called *SwitchDistance* has to be chosen which control the computational minimum and maximum separation of nodes and minimum distance for adjacent triple nodes, respectively (Fig. 3.4).

Routines that simulate individual processes are described below. In these routine descriptions there is first a section on the general background of the microstructural process and a second section on how the routine works in the Elle. Routine names are written in CAPITAL LETTERS, functions in **bold** and variables specific to the Elle model in *italics*. Appendix C gives some additional information about additional routines which deal with computational problems, validity considerations and on test experiments that were performed to test the validity of assumptions made and the influence of variations in parameters. In Tab. 3.1 used symbols are listed and Tab. 3.2 lists the abbreviations used for routines and short description of routines. (fold out page at the end of this Chapter; pg. 125).

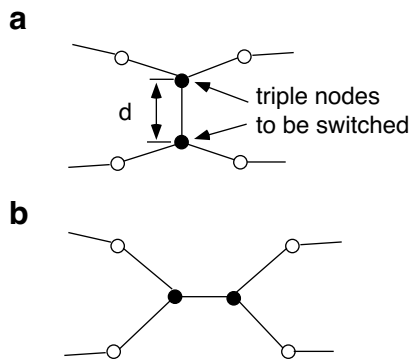


Figure 3.4 Schematic illustration of a *NeighbourSwitch*; here a so-called *T1-event* (Weaire & Rivier, 1984). If a node is a triple junction and if any of the neighbours within the minimum distance d (*SwitchDistance*) are triples, the node will triple-switch with its closest triple neighbour.

3.2.3 Description of individual processes

3.2.3.1 Viscous deformation (BASIL)

Viscous deformation is modelled by the program BASIL (Barr and Houseman, 1992; Barr and Houseman, 1996), which uses a finite element method to calculate stress and strain in linear and non-linear incompressible viscous, non-elastic materials, up to strains of the order of 100%. The calculations describe viscous Earth materials that undergo irreversible large-strain deformation under the influence of body forces and surface tractions. The program permits a spatially variable Newtonian or non-Newtonian viscosity in a 2-D geometry with traction and/or velocity boundary conditions. The 2-D deformation field represents either plane strain deformation, or it permits a specified distribution of normal stress in the third direction. In Elle plane stress calculations are used, which result in a special case of a thin viscous sheet formulation. The observation surface corresponds to the xy -plane of a sheared rock (Fig. 3.5). The type of plane strain deformation of the unit cell in terms of the kinematic vorticity number W_n (Means et al., 1980) and boundary conditions are defined by the user. The program can either simulate the movement of two pistons at top and bottom of the model or movement according to a set of velocity vectors at all points of the cell boundaries. To model deformation with pistons, the displacement of the 4 corners of the cell per time step are defined by the user. Otherwise the minimum and maximum values of the finite element node velocity components are

defined. The Elle microstructure will be distorted into a parallelogram during deformation. The square unit cell can be regained by repositioning nodes that are outside the unit cell. To be able to do this two prerequisites have to be met: (a) the mesh of nodes and node-to-node-boundaries must be a unit cell structure with periodic boundaries (i.e. it wraps around in the x- and y-direction) and (b) the simulated deformation must have been simple shear. To visualize and to check if the values calculated by BASIL are reasonable a display program (SYBIL) is provided (Barr and Houseman, 1996). SYBIL reads the solution files, and enables the user to plot selected quantities in the form of contour plots of strain, stress or displacement quantities, arrow plots of vectors of principal stresses, mesh plots or other derived quantities.

This deformation routine has been shown to be valid for modelling viscous deformation of linear and non-linear viscous materials (Barr and Housemann, 1992; Barr and Housemann, 1996; Bons et al., 1997)

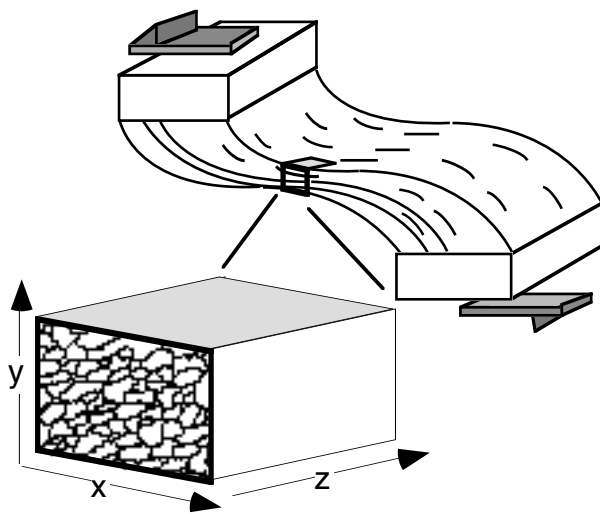


Figure 3.5 Schematic diagram of sheared rock, orientation of x, y, z axis and observation surface (xy-plane) in numerical simulations.

3.2.3.2 Lattice rotation and accumulation of dislocations (ELLE_TBH)

One of the basic deformation mechanisms in most crystals is crystallographic slip, which involves the movement of dislocations in certain planes and directions in each crystal which gives rise to the rotation of the crystal during deformation (e.g. Weiss and Wenk, 1985 and references therein; Law 1990). For a given crystal structure there are well-defined combinations of planes and directions in which slip occurs. For example, in the case of quartz, slip can occur on the $\{001\}$ plane (i.e. the basal plane) and in the $\langle 100 \rangle$ directions (i.e. parallel to the a-axes). (e.g. Hobbs, 1985 and references therein), but also in several other direction on different planes.

The occurrence of crystallographic slip during plastic deformation gives rise to two phenomena. One phenomenon that occurs is the rotation of the crystal lattice during deformation (Taylor, 1938; Bishop and Hill, 1951a, 1951b; Lister and Paterson, 1979). The crystal rotation is required for accommodating an arbitrary deformation because deformation by slip is possible only along a small number of slip systems. The other phenomenon is the increase in dislocation density during deformation due to the built up of tangles (locks) within the crystal. These tangles arrest further movement of dislocations. Because the resistance to dislocation movement increases in the presence of the locks, the crystal requires additional stress in the slip system to move further dislocations, and the crystal is said to "work-harden" (Kocks et al.,

1975; Kocks, 1976; Mecking and Kocks, 1981; Barber, 1985). Entanglement of dislocations is one of the mechanisms by which the deformation energy is stored within the crystal. The microstructure of the work-hardened material consists of a large number of cells, or subgrains, whose boundaries are essentially composed of a dense wall of dislocations (see section 3.2.3.3).

ELLE_TBH consists of two parts. The first part is the calculation of the crystal lattice rotation and the associated work (Taylor Bishop Hill calculations; Taylor, 1938; Bishop and Hill, 1951a, 1951b; Lister and Paterson, 1979) and the second part the calculation of the accumulation of dislocations. For the Taylor Bishop Hill calculations several assumptions are made. (a) Dislocation glide is the only deformation mechanism and each grain (smallest order polygons) deforms homogeneously to same strain. This is an approximation to nature where crystals deform heterogeneously (e.g. mica deform by sliding on its basal planes). (b) Each grain has at least 5 independent slip systems (known as the von Mises criterion (von Mises, 1928)). (c) The activity on any one slip system results in a small increment of simple shear parallel to the slip plane in the direction of the slip vector. Until the entire strain increment can be achieved for a grain, no deformation takes place at all, so the stress gradually increases until the critical resolved shear stress (CRSS) threshold is surpassed on just enough slip systems to allow the specific strain to take place (Lister et al., 1978; Jessell and Lister, 1990). Once this state is achieved, the work term can be calculated as the products of the small strains achieved by each slip system and the imposed stress. (d) No lattice reorientation due to rigid body rotation is taken into account and strain is assumed to be plane strain.

The Taylor Bishop Hill routine was developed by Lister et al. (1978), further developed by Jessell and Lister (1990), and later modified to match the needs of the Elle project by Mark Jessell. Inputs for this process are crystal symmetry and slip system definition with CRSS values for a given mineral species. According to the CRSS values and the stress tensors provided by BASIL, the new crystal orientation and the work necessary to achieve this crystallographic lattice rotation are calculated.

For the second part of ELLE_TBH the following considerations have to be taken into account. A general positive correlation of dislocation density and differential stress is predicted from theory (Kohlstedt and Weathers, 1980) and observed in experiments (e.g. Durham et al., 1977; Beermann and Kohlstedt, 1988; De Bresser, 1996). At steady state the relationship between dislocation density and stress is given by

$$\rho = K(\sigma/|b|)^2 \quad (\text{Eq. 3.2})$$

(Argon, 1970), where ρ is the density of mobile dislocations, K a constant, σ stress and $|b|$ the magnitude of the Burgers vector of the dislocation.

In ELLE_TBH, the change in dislocation density is assumed to be linearly proportional to the amount of work per unit area.

The new dislocation density (ρ'_{new}) of a polygon undergoing work is calculated according to the following equation

$$\rho'(new) = a \cdot \rho'(initial) + b \cdot ework \quad (\text{Eq. 3.3})$$

where a and b are constants. Additionally, $a+b=1.1$ to ensure an increase of dislocations with progressive deformation (Fig. 3.6). $\rho'(initial)$ corresponds to the "initial" dislocation density of a polygon given in the Elle data file before the onset of ELLE_TBH and $ework$ the calculated work for deformation of the grain according to the Taylor Bishop Hill code (for more details see Lister et al., 1978; Jessell and Lister, 1990). The calculated $\rho'(new)$ of the relevant polygon is written to the new Elle data file. If one simply uses a direct function of the $ework$ without any reference the previous dislocation density, a strong oscillation of dislocation density occurs. Grains with high dislocation density (i.e. high viscosity; section 3.2.3.7) in one time step will do little work and hence will have low dislocations densities (i.e. viscosities) in the next time step.

The part of the routine that is used to calculate the crystallographic rotation and work term have been shown to be relevant to rock deformation by Lister et al. (1978) and Jessell and Lister (1990).

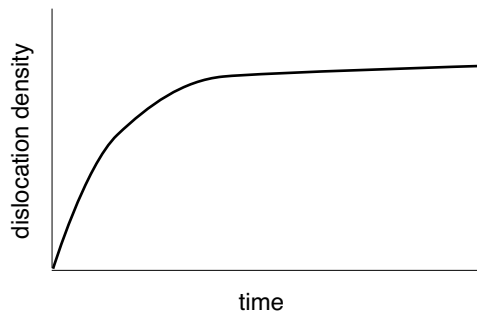


Figure 3.6 Graph of the increase of dislocation density with time assuming a time-independent value for the work necessary to deform a grain.

3.2.3.3 Formation of subgrains (ELLE_SPLIT)

During deformation dislocations are generated and stored in a crystal. Dislocations do not occur in thermodynamic equilibrium and tend to move to lower the energy of the system (Barber, 1985 and references therein; Gottstein and Svindlerman, 1999 and references therein). One way to minimize the free energy of dislocations is the rearrangement of dislocations in low energy dislocation structures such as planar dislocation arrays (tilt walls, cell walls, subgrain walls) (e.g. Gottstein and Mecking, 1985; Kocks, 1985). Such arrays show dislocations of one sign at one side of a wall and of the other sign at the other side (Gottstein and Mecking, 1985 and references therein). First, the cell walls sharpen, until they become subgrain boundaries, then the substructure coarsens (Sandström, 1977; Gottstein and Mecking, 1985; Kocks, 1985; Gottstein and Svindermann, 1999, and references therein). An increase in the number of dislocations results in an increase in internal stresses. These stresses inside the developing cells provide the local driving force for rearrangement of dislocations in tilt walls (Kocks, 1985). Therefore, it is assumed that the higher the dislocation density the higher the possibility that dislocations arrange themselves in such tilt walls (Barber, 1985; Kocks, 1985). At the first for-

mation of subgrain boundaries the new subgrains have a similar dislocation density because the original grain as the dislocations are only rearranged but not annealed (e.g. Kocks, 1976). The size of the new subgrains size is characteristic for a mineral species (e.g. Twiss, 1977; Kohlstedt and Weathers, 1980; Christie et al., 1980; Kronenberg and Tullis, 1984).

The subgrain formation routine ELLE_SPLIT performs "splitting" i.e. subdivision of a polygon into several new polygons. Accordingly, it models the discontinuous development of subgrain boundaries. Although such a model is a simplification of the mechanism of subgrain boundary formation in nature, cell walls evolve to coarse subgrain walls that can be recognized macroscopically only as subgrain but not cell walls. The driving force $F(\rho)$ for subgrain formation is the total strain energy per unit area in the used two dimensional model. In the used node network this is the energy per node. $F(\rho)$ is calculated according to

$$F(\rho) = \rho' \cdot \rho_{energy} \cdot \rho'_{scale} \quad (\text{Eq. 3.4})$$

where ρ' is the dislocation density, ρ_{energy} the energy of dislocations and ρ'_{scale} the dislocation density scaling factor. If $F(\rho) > Th_{split}$ (threshold value for splitting of a polygon), the grain has a probability to "split" into subgrains. The probability for "splitting" increases with increasing $F(\rho)$ and is determined according to the probability function \mathbf{P}_{action} .

```
test_threshold=action_threshold/ F(\rho);
/* for high values of F(\rho) the test_threshold is small and vice versa */
test=drand48();
/* randomly picked number between 0 and 1 */
if (test>test_threshold) CallForAction
```

(Eq. 3.5)

where $action_threshold$ (e.g. Th_{split}) is the energy threshold value for a certain action (e.g. splitting) defined by the user. The function `drand48()` belongs to a family of functions that generate pseudorandom numbers using the linear congruential algorithm and 48-bit integer arithmetic. The `drand48()` function returns a random non-negative, double-precision, floating-point value between 0 and 1.0. **CallForAction** is a function that calls a certain action such as the splitting of a polygon. This probability function is also used for the probability for recrystallization by nucleation (section 3.2.3.4).

The division of a "parent" polygon into several smaller polygons (i.e. subgrains) is done by successive splitting of one "parent" polygon into two smaller "daughter" polygons. The boundary between the new "daughter" polygons is found in the following way. First, the "parent" polygon is triangulated according to the Delaunay triangulation routine (Shewchuk, 1996). A direction vector of a preferred direction of splitting O is specified either according to a certain probability to be in a specified orientation relative to the crystallographic axes of the "parent" polygon or by a random number generator. The direction of the different triangulation legs joined to the starting node at the "parent" boundary is compared with the given direction vector. The triangulation leg that has the smallest angle with O and forms an angle above 45 degrees with the "parent" polygon boundary is chosen for the first part of the splitting-walk (Fig. 3.7). The next triangulation leg used for the splitting-walk (new subgrain boundary) is again chosen according to its angle with the direction vector. Once the splitting-walk arrives at the boundary of the "parent" polygon the size of the resultant two "daughters" is calculated. If one of the resultant polygons is smaller than the given minimum area ($MinArea$) the walk is

rejected and a new splitting-walk is attempted starting from another boundary node. If the area of a "daughter" polygons is above the maximum polygon area ($MaxArea$) it is split again into another set of "granddaughter" polygons. The range of subgrain size ($MinArea < \text{subgrain size} < MaxArea$) is defined by the user and is assumed to be characteristic for a mineral species. Most of the attributes of the "parent" (e.g. mineral species, dislocation density) are passed on to the "daughters". Additionally, the two daughters are marked as subgrains (split attribute = 1) and are given the same grain number attribute which specifies them as subgrains of a larger grain (see section 3.2.2 and Fig. 3.2).

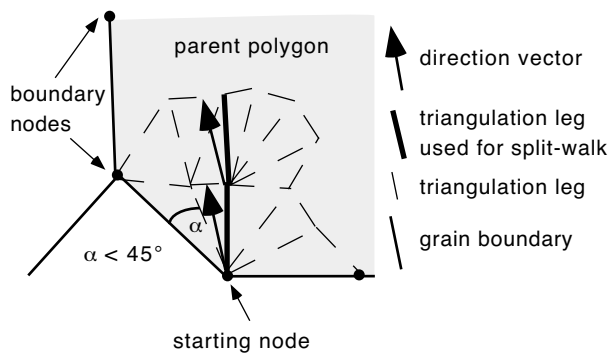


Figure 3.7 Schematic diagram of the determination of the "splitting-walk" along triangulation legs.

3.2.3.4 Recrystallization by nucleation (ELLE_NUCLXX)

In many natural examples e.g. albite, magnesium, quartz (Knipe and White, 1979; Ion et al., 1982; Fitz Gerald et al., 1983; Tullis and Yund, 1985, Urai et al. 1986; Drury and Urai, 1990) subgrains show distinct discontinuous stages where the dislocation structure in a subgrain is cleared out producing relatively strain- and dislocation-free grains (regime D in Fig. 3.1). In contrast to geology, in metallurgy this process is commonly referred to as dynamic recrystallization (Hardwick et al., 1961; Stüwe, 1965; Nicholis and McCormick, 1970; Gottstein and Mecking, 1985). A subgrain that has a high dislocation density is characterized by a high number of even smaller subgrains (cells) to very small scales (μm) which themselves have low internal dislocation density values (Kocks, 1985). One of these minute cells can act as a new nucleus, that will grow rapidly at the cost of its neighbouring cells (Fig. 3.8a; Gottstein and Mecking, 1985; Gottstein and Svindlerman, 1999, and references therein). Three prerequisites have to be fulfilled to allow such a nucleation: (1) the total free energy must decrease during expansion of the nucleus and for this a critical nucleus size r_c has to be exceeded, (2) there must be an instability of the microstructure i.e. differences in dislocation density, and (3) at least at one side of the nucleus the boundary must be a mobile grain boundary i.e. a high angle boundary (for more details see section 3.2.3.5) (Gottstein and Mecking, 1985). The possibility that a strain free nucleus satisfies the prerequisites as stated above increases with increasing dislocation density (Kocks, 1985). The new grain exhibits a low dislocation density because during nucleation and growth of the nucleus dislocations are swept into the moving tilt wall.

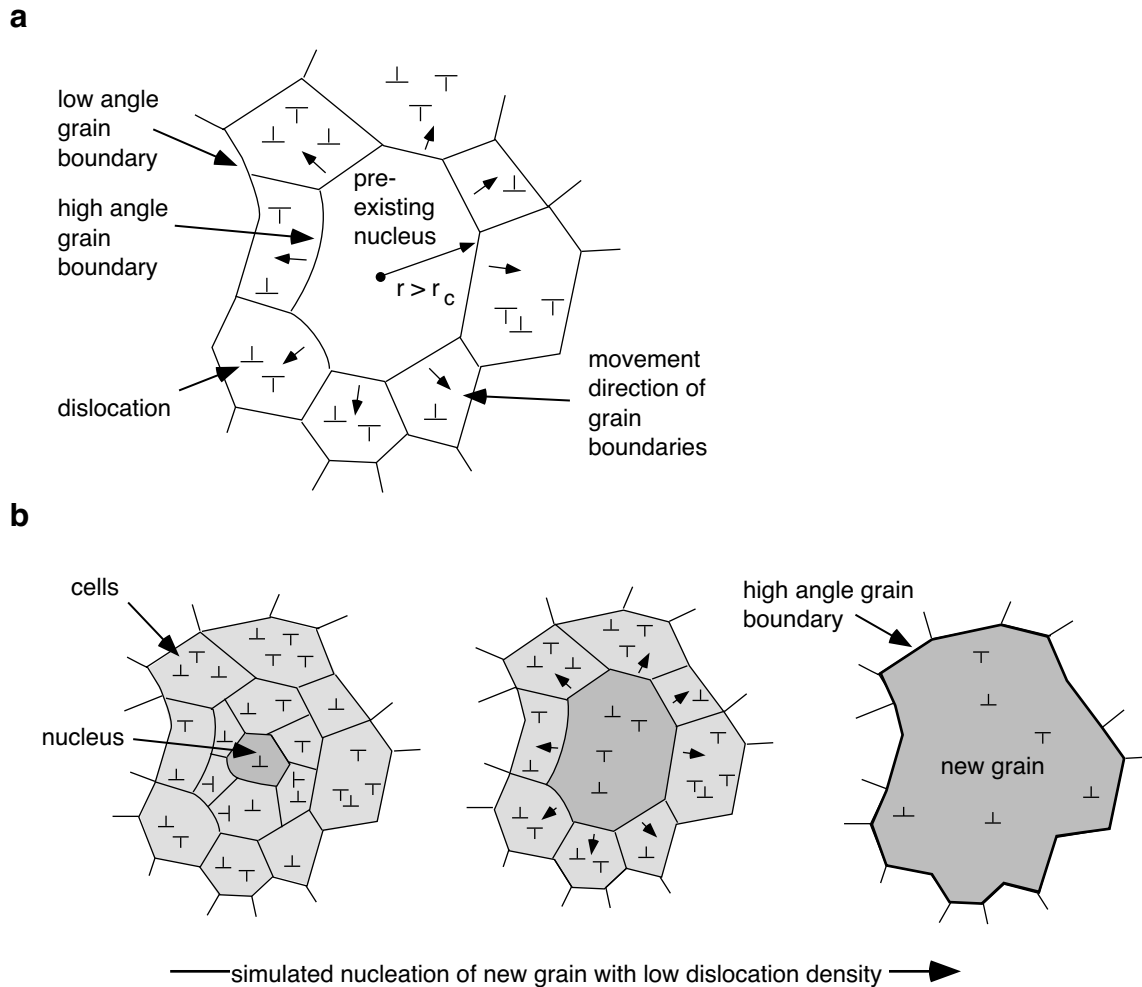


Figure 3.8 Schematic illustration of the mechanism of recrystallization by nucleation. (a) recrystallization nucleus with growth potential in a deformed structure (modified after Gottstein and Svindlermann, 1999). A nucleus can only grow if the total free energy decreases during expansion of the nucleus. For this a critical nucleus size r_c has to be exceeded (Gottstein and Svindlermann, 1999). (b) Schematic illustration of recrystallization by nucleation as simulated in the Elle model.

The mobility of dislocations, which is directly related to the growth rate of a nucleus is temperature dependent according to the general form

$$v_m = \beta |b| \kappa \exp \frac{\Delta G}{kT} \quad (\text{Eq. 3.6})$$

where v_m is the mean velocity of a dislocation segment, ΔG the Gibbs free energy of activation for the cutting or by-passing of an obstacle, β is a dimensionless, material dependent constant, $|b|$ the magnitude of the Burgers vector and κ the frequency of obstacle jumps (Frost & Ashby, 1983). According to Eq. 3.6 the boundaries of a new nucleus will sweep over its neighbouring grains at higher speed at higher temperature than at low temperature.

In ELLE_NUCLXX, the critical threshold value RX for the necessary energy at which a grain can nucleate is material and temperature dependent. According to Eq. 3.6 the possibility of a nucleus to successfully nucleate within a time step is higher at higher temperatures. In accordance with this relationship, the RX at a specific temperature is related to RX_{nucl} . RX_{nucl} is the base nucleation threshold value specific to a mineral species. RX is calculated in the following way:

$$RX = (RX_{nucl}) \cdot c/(T+c) \quad (\text{Eq. 3.7})$$

where c is a constant and T the temperature. This formula ensures the general trend of decreasing RX with increasing T . If $F(\rho)$ (Eq. 3.4) $> RX$ there is a certain probability (calculated according to \mathbf{P}_{action} (Eq. 3.5)) that a nucleus which fulfils the three requirements for recrystallization by nucleation is present in a polygon (see above). The dislocation density of a newly nucleated grain is set to a specified low dislocation density value (ρ'_{nucl}) and a new randomly picked crystallographic orientation. The randomly picked orientation must satisfy the condition that the boundaries at all sides of the grain of the recrystallized grains are mobile, high angle boundaries. A new nucleus will only be able to grow if at least some of its boundaries are high angle boundaries (Fig. 3.8b). The position of subgrain boundaries does not change in this routine due to computational limitations. Therefore, all subgrain boundaries must be high angle boundaries to allow the "successful" nucleation of a grain.

3.2.3.5 Rotational recrystallization (ELLE_ROTXX)

Low angle boundaries, which are defined by a tilt wall, develop into high angle boundaries by progressive misorientation of stationary subgrain boundaries. Such high angle boundaries have a different structure than tilt walls. They are characterized by the independence of its structure from domains on either side of it and overlapping dislocation cores (Gottstein and Shvindlerman, 1999, and references therein). In geology, this process of progressive misorientation is referred to as rotational recrystallization (Guillopé and Poirier, 1979; Poirier, 1985). The transition from a low to a high angle grain boundary structure is thought to occur at a critical angle of misorientation δ that is specific to a mineral phase (Fig. 3.9; e.g. Gottstein and Mecking, 1985; Drury and Urai 1990).

ELLE_ROTXX distinguishes between subgrains and grains. If all sides of a polygon are classified as high angle boundaries, the polygon is recognized as a grain and not as a subgrain. The value of the critical angle between a high and low angle boundary (*MisorientAngle*) is specific to the mineral phase. Only the grain/subgrain attribute is changed (cf. section 3.2.2). No physical properties of the polygon are affected by this routine. The calculation of the misorientation is performed according to the procedure described by Randle (1995) and Lloyd (1992) as this procedure is commonly used in grain boundary studies (e.g. Trimby et al., 1998; Fliervoet and White, 1995; Fliervoet et al., 1999).

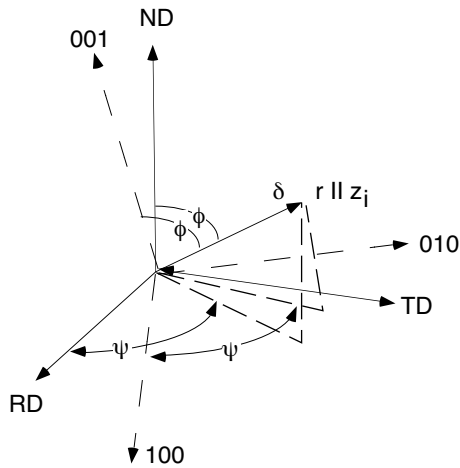


Figure 3.9 Definition of the MisorientAngle δ between to crystals A $\{RD, TD, ND\}$ and B $\{(100), (010), (001)\}$ (modified after Gottstein & Svindlermann 1999).

3.2.3.6. Grain boundary migration (ELLE_GBM)

A positive driving force for grain boundary migration occurs if a grain boundary displacement results in a decrease of the total free energy of the system. The driving force is a combination of two separate forces. These are (a) the force resulting from the difference in stored, internal energy i.e. strain energy and (b) the difference in chemical potential between adjacent grains.

A deformed grain stores a certain amount of energy by the build-up of dislocations (e.g. Frost and Ashby, 1983 and references therein; Kocks, 1985; Barber, 1985). The higher the dislocation density the higher the stored energy according to

$$E_{\text{stored}} = \rho_{\text{energy}} \cdot A \cdot \rho \quad (\text{Eq. 3.8})$$

where ρ_{energy} is the energy of dislocations, ρ dislocation density and A the area.

The difference of dislocation density between two adjacent grains is a driving force for grain boundary migration. The grain boundary migrates towards the grain with the highest dislocation density to reduce the total local energy state of the system (Fig. 3.10). The area swept is devoid of dislocations as dislocations move into the moving grain boundary (Barber, 1985; Kocks, 1985).

The difference in chemical potential between grains occurs as a function of the surface free energy. The difference in grain boundary curvature between grains of different sizes results in a chemical potential gradient across the interface grain boundary according to the Gibbs-Thompson equation (e.g. Lewis and Randall, 1961):

$$\mu_i - \mu_i^0 = \frac{2\varepsilon V}{r} \times \zeta \quad (\text{Eq. 3.9})$$

where ε is the surface energy of the phase. The equation relates the chemical potential of component i at the surface of a spherical phase, radius r and molar volume V to that of a planar surface at the distance r from the centre of the crystal. A geometric factor ζ is applied to account in differences in grain shape.

Additionally, the surface energy has been shown to be anisotropic. Surface energy anisotropies are a function of the (a) the relative crystallographic orientation of the boundary i.e. tilt angle between two neighbouring grains (anisotropy A_{XX}) and (b) crystallographic orientation of the boundary (anisotropy A_{α}) (e.g. Urai et al. 1986; Grest et al., 1985; Gottstein and Shvindlerman, 1999).

In ELLE_GBM the simulation of grain boundary migration is performed by successive movement of each individual node present in the node network. The movement of an individual node consists of two components: (a) the node movement routine and (b) the calculation of the change in energy due to the movement of a node.

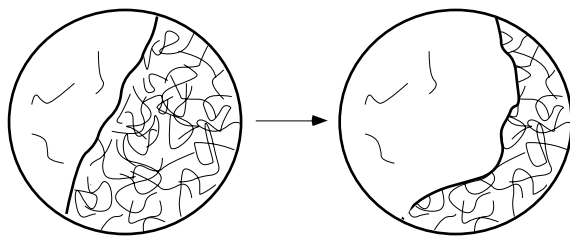


Figure 3.10 Schematic diagram illustrating grain boundary migration due to energy differences derived from the energy of dislocations. The grain with low dislocation density migrates in the grain with high dislocation density to lower the total free energy of the system (modified after Passchier and Trouw, Fig. 3.17a).

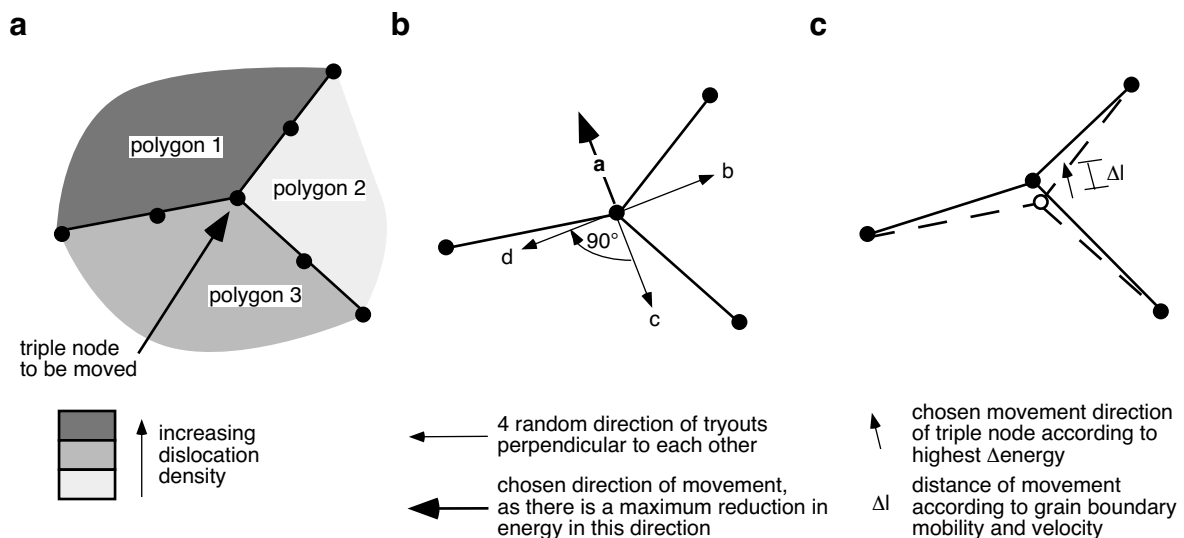


Figure 3.11 Schematic diagram which illustrates the numerical procedure performed to achieve movement of one node according to the maximum reduction of energy. (a) Initial node-boundary-polygon configuration with different dislocation densities in different polygons. (b) Illustration of the randomly chosen four tryout directions; (c) resultant movement.

In ELLE_GBM a small displacement of a node changes the total energy state by ΔE_{trial} . A small displacement vector p_{trial} of length D_{trial} , in a random direction is chosen and ΔE_{trial} is calculated. The length D_{trial} is calculated according to a defined fraction d (usually 0.01) of the *SwitchDistance* between two nodes

$$D_{trial} = SwitchDistance \cdot d \quad (\text{Eq. 3.10})$$

The calculation of ΔE_{trial} is repeated for another three displacements, each time rotating the trial displacement vector p_{trial} by 90 degrees. The displacement vector p_{trial} along which a node displacement results in the largest reduction of the local energy state is taken as the movement vector for the actual migration of the node concerned (Fig. 3.11). Once this movement vector p has been chosen the amount of true displacement D of the node is calculated and the node moved by this displacement along p .

To choose the relevant p_{trial} the change in energy due to the displacement D_{trial} in the p_{trial} direction must be calculated. In ELLE_GBM the calculation of the change in energy is divided in two main components. These are the change strain energy stored in adjacent polygons (ΔE_{ρ}) and the change in surface energy (ΔE_{ϕ}). These values are calculated according to the displacement of the node by D_{trial} .

To calculate the trial change in energy due to dislocation density ($\Delta E_{\rho-trial}$) first the "real world" area (*initialArea*) for each polygon adjacent to a double or triple node under consideration is calculated according to

$$initialArea = Elle_area \cdot l_{scale}^2 \quad (\text{Eq. 3.11})$$

where *Elle_area* is the area stored in the Elle file. The dislocation density $\rho'(initial)$ stored in the Elle file of each polygon is retrieved. It is assumed that the dislocation density within one polygon is homogeneous, therefore the initial energy due to dislocations $E_{\rho}(initial)$ of each polygon can be calculated according to

$$E_{\rho}(initial) = \rho_{energy} \cdot initialArea \cdot \rho'(initial) \cdot \rho_{scale} \quad (\text{Eq. 3.12})$$

where ρ_{energy} is the energy of dislocations, $\rho'(initial)$ the dislocation density stored in the Elle data file and ρ_{scale} the dislocation density scaling factor. Then the node position is changed according to D_{trial} and p_{trial} . This new node position results in a change in the areas of the polygons concerned. If the new area (*newArea*) of the polygon is smaller than the *initialArea* no change in dislocation density and therefore no energy difference will be present. If $newArea > initialArea$ the dislocation density of the polygon is assumed to change according to the following equation.

$$\rho'(new) = (initialArea/newArea) \cdot \rho'(initial) \quad (\text{Eq. 3.13})$$

This change in dislocation density with increasing area, results in an decrease of the dislocation density of a "growing" grain. This calculation is valid under the assumption that the swept area is dislocation free. This is reasonable, because dislocations that were present in the swept area before movement of the node accumulate in the grain boundary (Kocks, 1985). For a "growing" polygon where $newArea > initialArea$ the new energy $E_{\rho}(new)$ is calculated according to

$$E_{\rho}(new) = \rho_{energy} \cdot newArea \cdot \rho' \cdot \rho_{scale} \quad (\text{Eq. 3.14})$$

The difference in stored energy $\Delta E_{\rho}(polygon)$ of a "growing" polygon is calculated by

$$\Delta E_{\rho}(polygon) = E_{\rho}(initial) - E_{\rho}(new) \quad (\text{Eq. 3.15})$$

The total change in $\Delta E_{\rho-trial}$ is the sum of the $\Delta E_{\rho}(polygon)$ of the polygons involved (Note: for a polygon where $newArea < initialArea$ $\Delta E_{\rho}(polygon) = 0$).

$$\Delta E_{\rho} = \sum E_{\rho}(polygon) \quad (\text{Eq. 3.16})$$

In ELLE_GBM the second driving force considered is the change in surface energy due to the movement of a node. The calculation of the surface energy change (ΔE_{ϕ}) has 3 components. These are (a) surface energy due to length of the boundary segments involved E_{length} , (b) anisotropy A_{XX} of this surface energy due to relative crystallographic orientation of two adjacent grains and (c) anisotropy A_{α} of the surface energy due to orientation of the boundary with respect to its crystallographic orientation (Bons et al., in press). In two dimensions E_{length} is at a minimum if boundaries are straight and intersections angle are 120° . In E_{length} calculations, the initial and end length of the boundary segments that change their length due to the movement of a node is calculated. Assuming an isotropic surface energy, the energy state is the length of the segments multiplied by the surface energy.

For the example, of a double-node in Fig. 3.12 with bounding two segments of lengths l_1 and l_2 , the energy E_{length} is generally given by

$$E_{length} = \Gamma \cdot (l_1 + l_2) \quad (\text{Eq. 3.17})$$

where Γ is the surface energy and l_1, l_2 the lengths of the two segments next to the node. The movement over vector D_{trial} results in a change in segment lengths l_1 and l_2 to new lengths (l'_1, l'_2).

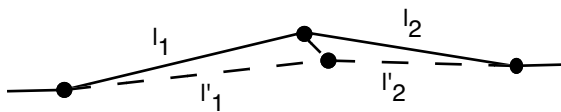


Figure 3.12 Schematic diagram illustrating the parameters used for the calculation of surface energy.

In ELLE_GBM the initial and new segment lengths E_{length} for the boundaries concerned is calculated. The change in energy (ΔE_{length}) is the difference between the two. This part of the routine is based on the model of P. D. Bons (1993) and Jessell et al. (2001). And it has been shown to be a valid for grain boundary energy driven grain boundary migration (Bons, 1993; Jessell et al., 2001; Bons et al., in press). In Appendix C3 a detailed account on the validity of this energy calculation in relation to the curvature calculation (Eq. 3.9) is given. The anisotropy of surface energy of a grain boundary is low if the angle of crystallographic orientation between two adjacent grains is low and high at high angles (Fig. 3.13). Read and Shockley (1950) showed that for a symmetrical tilt boundary with tilt angle φ , the surface energy σ_b per unit area is in a general form

$$\sigma_b = \varphi (K \cdot \ln \varphi) \quad (\text{Eq. 3.18})$$

where K is a material constant. In ELLE_GBM, the relationship between the isotropic surface energy (Γ_i) and anisotropic surface energy (Γ_a) due to the angular relationship the crystallographic misorientation of the c-axis between two adjacent crystals A and B (tilt angle Π) on either side of the grain boundary is assumed to follow the general form

$$\Gamma_a = \Gamma_i \cdot xx_factor(\Pi) \quad (\text{Eq. 3.19})$$

where xx_factor ranges between 0 and 1 and is a function of tilt angle Π . The values of xx_factor are derived from a file. In this file the xx_factor values for specific tilt angle Π ranges are listed. This part of ELLE_GBM is an implementation of an existing code written by P. D. Bons and M. W. Jessell.

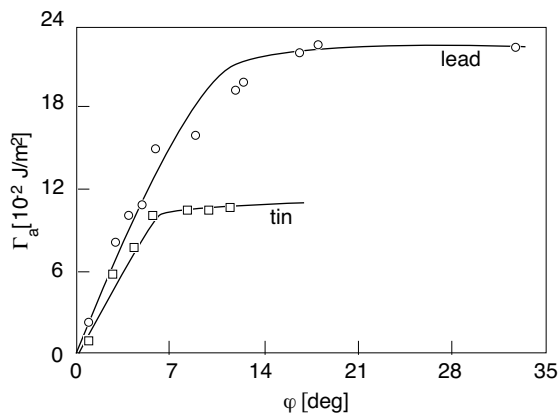


Figure 3.13 Surface energy Γ_a of grain boundaries with a specific tilt angle between two adjacent grains (φ). Open dots and squares signify measurements of specimen of lead and tin respectively (modified after Gottstein and Svindlerman, 1999).

In ELLE_GBM the anisotropy of the surface energy A_α relates the angular relationship between the orientation of the grain boundary and crystal lattices. A_α is a function of the five angles $\alpha_1, \alpha_2, \alpha_3, \alpha_4, \alpha_5$ which define the orientation of a boundary and the lattices of the adjacent crystals on either side of the boundary:

$$A_\alpha = F(\alpha_1, \alpha_2, \alpha_3, \alpha_4, \alpha_5) \quad (\text{Eq. 3.20})$$

Different functions which describe A_α can be chosen depending on the character of anisotropy to be modelled. Details of the assumption for different surface energy anisotropies and possible functions to be chosen from are described in detail in Bons et al. (in press). Again, this part of ELLE_GBM was written by P. D. Bons and its applicability to the microstructural development of metals and crystalline analogue materials has been shown in Bons et al. (in press).

The following equation is used to draw together the effect of the three components E_{length} , A_{XX} and A_α that influence the surface energy of a boundary segment,

$$E_\phi = l \cdot xx_factor \cdot \Gamma \cdot A_{XX} \cdot l_{scale} \quad (\text{Eq. 3.21})$$

where l is the length of boundary and Γ a predefined surface energy. The change in energy ($\Delta E_{\phi-trial}$) is the difference between the energies E_ϕ calculated for the initial node position and its position after D_{trial} along vector p_{trial} .

In ELLE_GBM the total energy change ΔE_{trial} which would arise from node movement with D_{trial} along p_{trial} is calculated according to

$$\Delta E_{trial} = \Delta E_{\phi-trial} + \Delta E_{\rho-trial} \quad (\text{Eq. 3.22})$$

where ΔE_ϕ is calculated according to Eq. 3.21 and ΔE_ρ according to Eq. 3.16.

ΔE_{trial} is calculated for each of the four trial node positions. Vector p for which ΔE_{trial} is the highest is taken as the valid vector for the true movement of the node. Once p is chosen the true displacement D in direction of the chosen direction vector p can be calculated according to

$$D = v_{node} \cdot t_{scale} \quad (\text{Eq. 3.23})$$

whereby v_{node} is the velocity of node movement and t_{scale} the time scaling factor. The rate at which grain boundary migration i.e. the velocity of the boundary movement occurs depends on the mobility of the boundary and the value of the driving force according to the general relationship

$$v \propto M \cdot F \quad (\text{Eq. 3.24})$$

(Frost and Ashby, 1983 and references therein) where v is the velocity, M the mobility and F the driving force for grain boundary migration.

In ELLE_GBM, this means

$$v_{node} = GBMob \cdot \Delta E \quad (\text{Eq. 3.25})$$

where ΔE is the calculated change in energy due to the D_{trial} along the chosen vector p and $GBMob$ the mobility. Once the $GBMob$ is known the velocity of the node v_{node} can be calculated.

To calculate the value of $GBMob$ the following considerations have to be taken into account. In general, the grain boundary mobility M is mainly function of temperature and material (Fig. 3.14; Frost and Ashby, 1983; Gottstein and Shvindlermann, 1999 and references therein). Additionally, the amount of impurities (Olgaard and Evans, 1986; Randle et al., 1986) are important for the effective grain boundary mobility. Assuming no impurities the relationship of M to temperature follows a general Arrhenius equation of the form

$$M = M_0 \cdot e^{(-H/(B \cdot T))} \quad (\text{Eq. 3.26})$$

(e.g. Frost and Ashby, 1983; Gottstein and Svindlerman, 1999, and references therein) where H is the activation energy, B is the Boltzmann constant, and M_0 a ‘base mobility’ specific to a material.

In ELLE_GBM, the grain boundary mobility is calculated according to

$$GBMob = GBMob_0 \cdot e^{(-Q_{GBM}/(B \cdot t))} \quad (\text{Eq. 3.27})$$

where $GBMob$ is the grain boundary mobility, Q_{GBM} is the activation energy, B is the boltzmann constant and $GBMob_0$ a “base mobility“ specific to a material. The direct relationship of grain boundary velocity, grain boundary mobility and driving force assumes no variations due to impurities and drag effects. Additionally, it is assumed that the intensive variables pressure, temperature and magnetic field show no gradients in the experiments. They can therefore be neglected.

Now, the new position of the node can be calculated using v (calculated by Eq. 3.25 and Eq. 3.27), D (calculated by Eq. 3.23) and the chosen vector p .

In ELLE_GBM a number of assumptions and approximations are made and therefore the relevance of such a calculation of the node movement had to be tested in several ways. The validity the general mode of determination of the relevant movement direction (trial vectors p_{trial} ; Fig. 3.11) is discussed in Appendix C3 and in Bons et al. (in press).

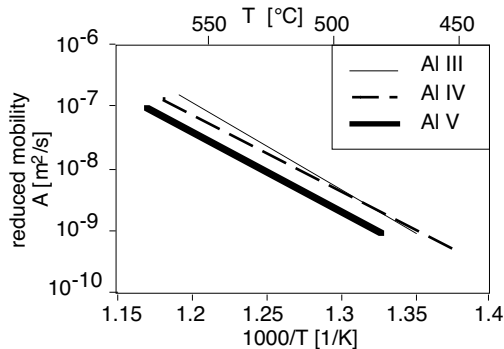


Figure 3.14 Dependence of the mobility on material and temperature. Depicted is the reduced mobility A for $40.5^\circ <111>$ tilt boundaries in differently pure Al: Al III, Al IV and Al V have an impurity content of 3.6 ppm, 4.9 ppm and 7.7 ppm, respectively (modified after Gottstein & Svindlermann 1999).

Several tests were performed simulating the microstructural evolution of a fabric due to grain boundary migration. ELLE_GBM was divided into two individual routines (ELLE_DISLOC, ELLE_SURF). In ELLE_DISLOC exclusively the change in stored energy due to dislocations is considered for the driving force calculation for grain boundary migration. In ELLE_SURF exclusively the change in surface energy due to the change in length (E_{length}) and the anisotropy A_{xx} of a grain boundary are considered. The change in microstructure of a combination of ELLE_DISLOC and ELLE_SURF show very similar results as simulations using ELLE_GBM which assumes $A_{\alpha} = 1$ (Appendix C3). In addition, results of several simulations with identical parameters and initial microstructure, shown that simulations are reproducible (Appendix C3).

3.2.3.6. Recovery (ELLE_RECOVERY)

Deformed crystals tend to remove lattice defects that are not in thermodynamic equilibrium in order to lower the energy of its system. In the metallurgical sense, recovery results in low energy dislocation structures by either dislocation annihilation or locally rearrangement in cell and subgrain walls. The amount of annihilation per unit area and time step depends on both material and temperature (Hu, 1963; Kocks et al. 1975; Kocks, 1985; Gottstein and Shvindlerman, 1999 and references therein). Recovery that results in the rearrangement of dislocations is simulated by the subgrain formation routine (ELLE_SPLIT; section 3.2.3.3).

ELLE_RECOVERY exclusively simulates recovery that describes the time- and temperature-dependent annihilation of non-geometrically necessary dislocations within a crystal. In the routine the dislocation density of each grain or subgrain is reduced per time step according to a recovery factor RF . First the temperature dependent RF is calculated according to:

$$RF = e \cdot RF_{base} + ((1-e) \cdot RF_{base} \cdot f/(T+f)) \quad (\text{Eq. 3.28})$$

where RF_{base} is the base recovery factor specific to a mineral species, e a constant between 0 and 1 and f a constant. This formula is arbitrary. We know, though, that the recovery rate is a function of the mineral species and some form of $1/T$, therefore we regard the formula above as a reasonable approximation of the process active in nature (Kocks, 1985). The new dislocation density is then calculated according to

$$\rho'(new) = \rho'(initial) \cdot RF \quad (\text{Eq. 3.29})$$

This type of equation ensures a progressive decrease in dislocation density provided no new dislocations are generated (Fig. 3.15).

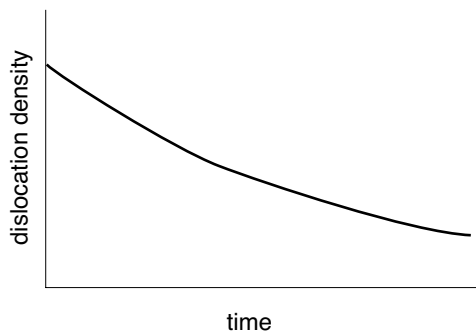


Figure 3.15 Schematic graph illustrating the decrease in dislocation density with time. It is assumed that the only active process that changes in dislocation density is recovery.

3.2.3.7 Calculation of viscosity (ELLE_VISCOSITY)

The rate at which crystals deform viscously depends on the applied stress and the viscosity of the grain.

$$\dot{\gamma} \propto \frac{\sigma}{\eta} \quad (\text{Eq. 3.30})$$

The viscosity of a grain is largely a function of the mineral species, dislocation density of the crystal, temperature and presence of a fluid phase. Fluid presence enhances dislocation glide and climb by hydraulic weakening (Kronenberg & Tullis 1984, Tullis & Yund 1988, 1989, Post et al., 1996).

Dislocations interact with each other, and since many dislocations must move distances which are large compared to their spacing to achieve macroscopic flow, dislocation interactions are of fundamental importance for plasticity and viscosity (e.g. Kocks 1976, 1985; Frost and Ashby, 1983 and references therein) (see also 3.2.3.2). The general relationship between strain rate and dislocation density assuming dislocation glide as the main deformation mechanism is given by the Orowan's equation

$$\dot{\gamma} = \rho |b| v \quad (\text{Eq. 3.31})$$

where $|b|$ is the magnitude of the Burgers' vector and v the average velocity determined almost entirely by the time to overcome obstacles. The velocity of dislocations in a polycrystal is frequently determined by the strength and density of the discrete obstacles it contains. If it is assumed that the activation energy required to overcome the obstacle is the rate limiting factor for the deformation of a material, which means that the obstacle is "strong", the strain rate is related to dislocation density and stress in the following manner.

$$\dot{\gamma} \propto \frac{\sigma}{\sqrt{\rho}} \quad (\text{Eq. 3.32})$$

(Frost and Ashby, 1983). Therefore, the viscosity is related to the dislocation density according to the general relationship

$$\eta \propto \sqrt{\rho} \quad (\text{Eq. 3.33})$$

This is in the accordance to the described "work-hardening" phenomenon (section 3.2.3.2; Kocks, 1976; Kocks et al. 1975). The term work hardening describes an increased resistance to dislocation movement with increasing dislocation density. Thus, a crystal requires additional stress to move further dislocations.

In ELLE_VISCOSITY (due to computational limitations) it is assumed that the material is viscous, rather than plastic. The following viscosity calculation was used

$$\eta = (\eta_{base} + Fluid_Factor \cdot \text{SQRT}(\rho')) \quad (\text{Eq. 3.34})$$

where η_{base} is the "base" viscosity specific to a mineral species. This equation ensures the dependence of viscosity (η_{base}), dislocation density and the degree of hydraulic weakening i.e. value of *Fluid_Factor* (Fig. 3.16).

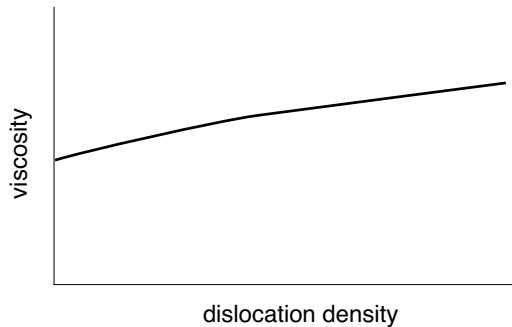


Figure 3.16 Schematic graph illustrating the general relationship between viscosity and dislocation density as assumed in Elle calculations. The fluid activity is assumed to be constant.

3.2.4 Data storage, display, statistics and clean-up of computationally problematic mesh geometries

3.2.4.1 Data storage

At each time step an Elle data file is automatically stored. The data file gives a full description of the geometry of the simulated microstructure. It also stores for each polygon the grain number it belongs to, its mineralogy, viscosity, dislocation density, crystallographic orientation (Euler angles), strain attributes, age, the number of recrystallization cycles it was involved in and if it is a subgrain or a not. Additionally, for each node the stress values are stored.

3.2.4.2 Display of Elle data (SHOWELLE)

With the display program SHOWELLE the data stored in the Elle data file, such as the position of nodes and connection boundaries, as well as polygon and the calculated boundary attribute "angle of misorientation (see below and section 3.2.3.5) can be visualized in colour or in grey scale. In section 3.4. (Simulations) this program is used to show the characteristics of simulated microstructures.

3.2.4.3 Statistics (ELLE_STATS)

A separate routine ELLE_STATS generates a statistics file to keep track of the microstructural evolution of a microstructure for each time step. It analyses the data given in the data file and writes results to a statistics file. The following data are stored: total number of polygons, polygon number, polygon area, polygon mineral attribute, age, cycle of recrystallization, total number of grains, grain number, grain area, length of grain boundaries according to different angle of misorientation categories, total grain boundary length. A grain is defined as the sum of polygons, which are adjacent to each other and exhibit no high angle boundaries between each other. The same procedure as used for the rotational recrystallization routine (section 3.2.3.5) was used to calculate the angle of misorientation. A grain shape analysis (Panozzo, 1983, 1984) is performed using the algorithm written by P. D. Bons (Bons, 1993). This method

(Panozzo, 1983, 1984) assumes that the average grain shape preferred orientation (SPO) can be described by an ellipse with an aspect ratio (R_a) and an orientation of the long axis of the ellipse (α) using the orientation of the grain boundaries. Only grain boundaries that did not touch the network boundaries were used for the calculation. Output of the analyses are the ratio of long to short shape axis of the average fitted ellipsoid, maximum angle of long shape axis, minimum angle of long shape axis and accuracy of shape related calculations.

3.2.4.4 Clean-up of computationally problematic mesh geometries (ELLE_CHECKANGLE)

ELLE_CHECKANGLE is a routine to "clean-up" topologically problematic mesh geometries. BASIL has problems triangulating regions with very sharp angles or very small areas which may develop. If either of these problems occurs, BASIL will usually run out of memory due to the creation of many unnecessary small triangles which are used in BASIL. Therefore, a routine was developed to get rid of these sharp angles and very small areas (Fig. 3.17). The threshold values at which this routine is applied are minimum angle *MinAngle* and the area of a triangle with sides of the length of the minimum node separation (*MinNodeSep*).

Such a routine is justified as in natural examples in which very sharp angles between grain boundaries are not observed and very small grains are rare. This is in accordance to thermodynamic instability of very small angles and very small grains according to Eq. 3.9. High curvature, hence high radii, result in high driving forces to move the boundary towards the centre of curvature.

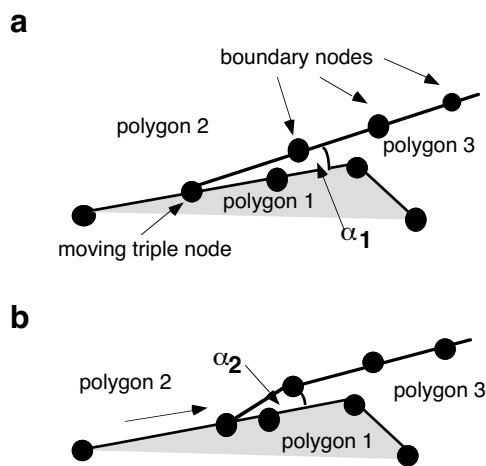


Figure 3.17 Schematic diagram illustrating the effect of the clean-up routine. (a) In the routine sharp angle between two grain boundaries (α_1) are recognized and (b) one node is moved along one grain boundary. The distance between the original node position and the new node position is chosen in such a way that the resultant enclosing angle $\alpha_2 > \text{MinAngle}$. The decision which node is moved along which boundary is random if all polygons are polygons of the same mineral species. If one of the polygons (e.g. polygon 1) has a different mineralogy than the other polygons involved, node is moved along the boundary between polygons of the same mineral species.

3.3 Analytical methods

To be able to interpret and compare microstructures, it is necessary to accurately describe the different elements of a microstructure, and ideally to quantify its characteristics. In the following, three new methods are described and applied to two simulated microstructures (Fig. 3.18).

3.3.1 Ratio low/high angle boundary length per unit area (R_{gbl})

Trimby et al. (1998) suggested that specific relationships between grain boundaries with different misorientation angles are characteristic for the dominance of processes such as rotational recrystallization, recovery or grain boundary migration. Accordingly, different combinations of active processes and variations in parameters are expected to influence the low to

high angle boundary length ratio. Here, a low angle boundary is defined as a boundary between two subgrains which exhibits a misorientation angle equal or below a specific *MisorientAngle* value (section 3.2.3.5). If we assume a *MisorientAngle* of 10° , the R_{gbI} is 1.54 and 0.51 for the two microstructures shown in Fig. 3.20.

This technique can not only be used to analyse results from numerical simulations. In rock samples the length of high and low angle boundaries can be determined automatically using the new analytical technique of electron backscatter diffraction (EBSD) (e.g. Trimby et al., 1998; Faul and Fitz Gerald, 1999; Fliervoet et al., 1999; Trimby and Proir, 1999; Trimby et al., 2000; Heidelbach et al., 2000) and optically with an accuracy of $\pm 2^\circ$ (Heilbronner and Pauli, 1993).

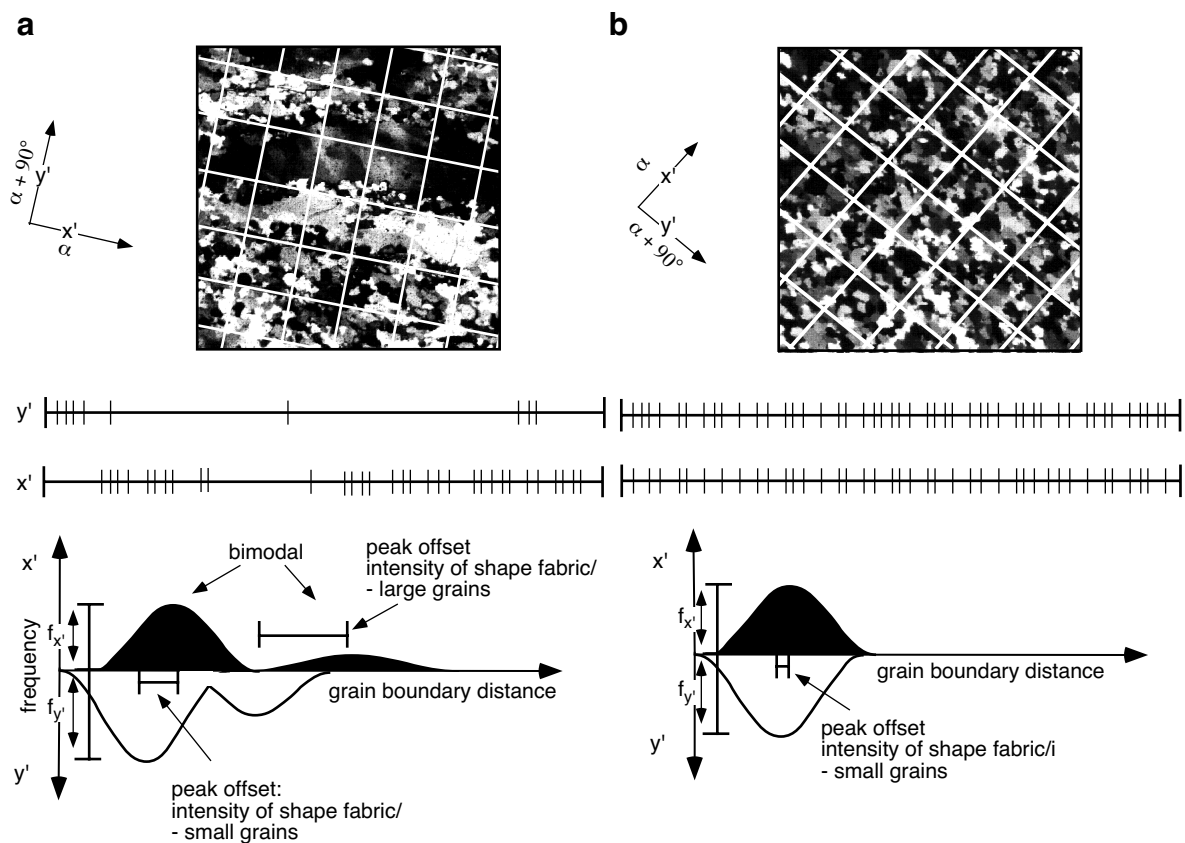


Figure 3.18 Illustration of the method to generate a grain boundary distribution plot. On top of a photomicrograph a grid of two perpendicular sets of parallel lines is drawn, whereby one set of lines is parallel to the x' and the other parallel to the y' direction. Directions are shown at side of diagram. Intersections of high angle grain boundaries with lines of analyses are marked and are shown below photomicrographs. The distances between markers are measured and recorded. Histograms of the grain boundary distances are generated, and put next to each other as shown on diagram. The resultant plot shows a distinct pattern characterizing the fabric of the analysed sample. Offsets between frequency peaks in the x' and y' direction give a quantitative measure of the shape fabric of the specific grain distance range. Another quantitative measure is the ratio of the highest frequencies in the two perpendicular directions F_{xy} which is defined as $f_{x'}/f_{y'}$. (a) Photomicrograph of partially recrystallized quartzite (Cap de Creus, Spain) crossed nicols; field of view = 1 mm; (b) photomicrograph of fine grained completely recrystallized quartzite (Cap de Creus, Spain) crossed nicols, field of view = 1 mm.

3.3.2 Grain boundary distance plots (gbd-plots)

The technique involves the measurement of the distance of high angle grain boundaries ($> \text{MisorientAngle}$) along sets of lines drawn parallel to α (x' -direction; parallel to the orientation of the long axis of the shape ellipse) and perpendicular to α (y' -direction). The angle α is calculated from the grain boundary orientation of a microstructure (Panozzo, 1983, 1984; section 3.2.4.3) (Fig. 3.18). The area of analysis should be a square, and orientation, spacing and length of lines identical in both directions. For the grain boundary distribution along each direction a histogram is drawn, whereby the values of grain boundary distances in the x' -direction are plotted upright and in the y' -direction upside-down. For both histograms the same histogram bin width and scaling is used. The combined plots show the degree of shape preferred orientation, the nature of the grains boundary distance distribution (e.g. multi-, bi- or unimodal) and the range and frequency of grain boundary distance lengths. The horizontal offset between peak frequencies in the x' and y' direction can be quantified and is a measure for the degree of a shape fabric. Another characteristic feature is the ratio F_{xy} between the number of elements of the highest frequency in the x and y direction. The corresponding gbd-plots for the microstructures shown in Fig. 3.20a are given in Fig. 3.20b.

3.3.3 Logarithmic plots of property value against ranked number of property

Since its original introduction by Mandelbrot (1967), the concept of fractals (power law distributions) has found wide applicability. In geology this concept is has been applied to different geological problems e.g. seismiscity, roughness of materials, fracture and fault patterns, extensional veins and grain shapes (e.g. Marsh, 1988; Kruhl, 1994 and papers therein; Carter and Winter, 1995; Johnston and McCaffrey, 1996; Giuseppe, 1997; Takahashi et al., 1998). A fractal or power law distribution signifies a scale-invariant structure in the property range where the fractal trend is present. Such scale invariant structures can be recognized in logarithmic plots of ranked number or cumulative number of property versus ranked property value (s). In such logarithmic plots a straight line indicates that the cumulative distribution $P(S > s)$, where $P(S > s)$ is the probability that a randomly selected property value will have a size S greater than s , is a power law. Besides recognizing a distribution as a fractal or power law distribution, the fractal dimension (power law exponent) is an appropriate means to characterize a fabric. A fractal set is defined according to

$$N_n = \frac{C}{r_n^D} \quad (\text{Eq. 3.34})$$

where N_n is the number of objects with a characteristic linear dimension r_n , C is a constant of proportionality and D is the fractal dimension. The fractal dimension can be an integer, in which case it is the equivalent to an Euclidean dimension. In order to determine D the following equation is used

$$D = \frac{\ln(N_{n+1} / N_n)}{\ln(r_{n+1} / r_n)} = \frac{\partial(\log(N_n))}{\partial(\log(r_n))} \quad (\text{Eq. 3.35})$$

In Fig. 3.19 the significance of D is illustrated in a number of examples (Turcotte, 1993). In a $\log N$ versus $\log r$ plot the fractal dimension signifies the slope of a straight line. The fractal dimension is high, if there are many small and few large fragments (Fig. 3. 19); it is low if there are relatively few small grains. In rocks fabrics fractal distributions have been recognized (e.g. Marsh, 1988; Takahashi et al., 1998). In his paper, Marsh (1988) showed that in igneous and metamorphic rocks, crystal size distribution analysis in terms of fractal or power law distributions is not only a valuable tool to quantitatively describe a crystal size distribution, but can yield information about the kinetics and dynamics of crystallization. Nucleation rates and growth rates can be determined using a combination of analysis of a crystal size distribution, theoretical considerations and understanding of the physics of responsible mechanisms. Accordingly, logarithmic plots of properties of microstructure, for example grain size distributions, could potentially be used to quantify involved processes, rates of recrystallization, and parameters such as grain boundary mobility. If in a plot of log rank number and property, the property is not a measure of length (one dimension) but a measure of area (2 dimensions), the obtained slope in the plot does not strictly correspond to the fractal dimension D as defined above. Therefore, the fractal dimension D^* is defined here as the slope in a plot of log rank number against measure of area e.g. grain size. The logarithmic plots of grain sizes of the two example meshes are shown in Fig. 3.20c.

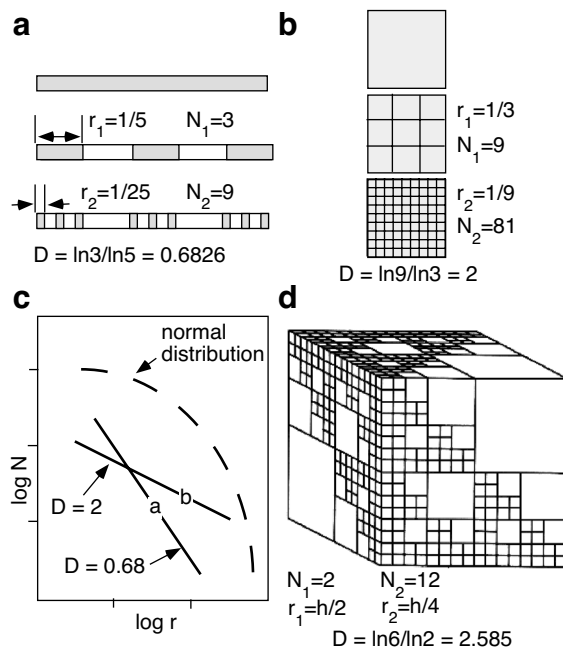


Fig. 19 Figure illustrating the concept of fractal/power law distributions and fractal dimensions. **(a)** Diagram showing a line segment of unit length that is divided into 5 equally-sized smaller segments. Two of these segments are retained. The resultant fractal dimension is $D = \ln 3 / \ln 5 = 0.6826$ (for used equation see text). **(b)** A unit cell is divided into 9 equally sized smaller squares, at order two all squares are again divided into 9 equal squares. The resultant fractal dimension is $D = \ln 9 / \ln 3 = 2$. **(c)** Schematic $\log N$ (ranked number) – $\log r$ (length) plot with fractal dimensions $D = 0.6826$ (see (a)) and $D = 2$ (see (b)) plotted. Dashed line signifies a normal distribution. **(d)** Representation of cubic cell fragmentation according to a fractal distribution. Note the similarity of the cube and the three dimensional appearance of microfabrics (modified after Turcotte, 1992).

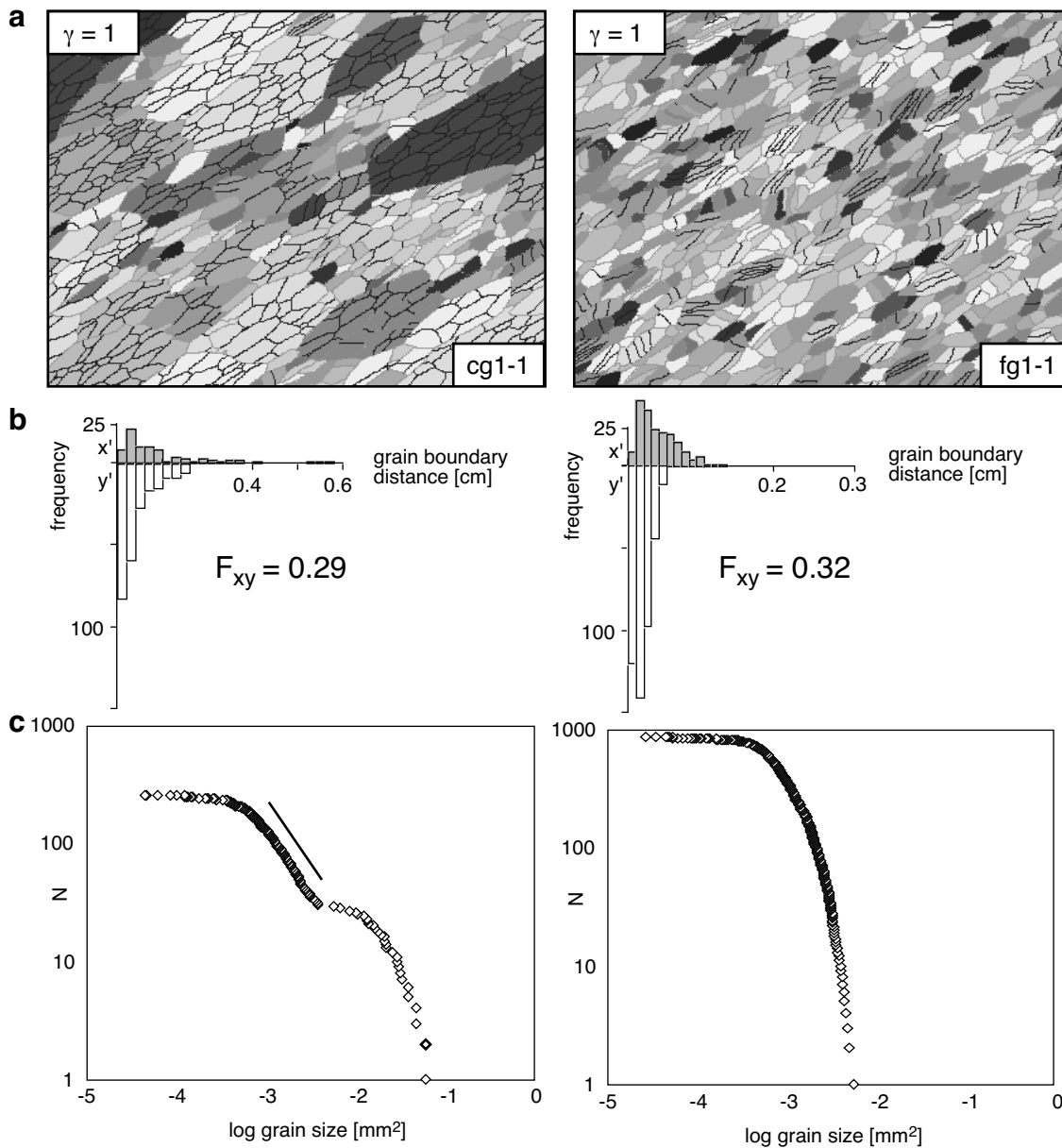


Figure 3.20 Diagrams showing the application of the three different methods of analyses which are proposed to be useful to quantitatively and qualitatively describe a microstructure. Two microstructures (results from simulations) are analysed with the three different techniques. (a) Microstructures; different grey colours signify different grains, dark boundaries low angle boundaries and light grey coloured boundaries high angle boundaries. Simulated simple shear strain (γ) is 1 for both examples. The example on the left hand side is an initially coarse grained monomineralic fabric (simulation run cg1-1) and on the right hand side a fine grained fabric (simulation run fg1-1). Simulation run nomenclature corresponds to that of Tab. 3.5 (end of chapter). (b) Grain boundary distance plots with corresponding ratios of peak frequencies in the x' direction and y' direction. (c) Logarithmic plots of grain size plotted against corresponding rank number. In the coarse grained microstructure a power law distribution is seen in parts of grain size range.

3.4. Simulations

3.4.1 Aim of numerical simulations

In chapter 2 it has been proposed that the shape fabric of a rock seen in discrete shear zones is strongly affected by the way dynamic recrystallization affects a microstructure during progressive deformation. Especially, the initial fabric in terms of the ratio of grain sizes of initial and recrystallized grains seemed to be important. Other possible influencing factors could be the grain boundary mobility and the characteristics of rotational recrystallization and recrystallization by nucleation. Twelve simulations were performed to test and develop a better understanding of the findings and interpretations provided in Chapter 2 and to investigate the validity of the developed model of dynamic recrystallization and used input parameters.

3.4.2 Setup of numerical simulations

3.4.2.1 Values identical to all simulations

In all 12 simulations a certain set of parameters were kept constant. These values were chosen in accordance to values provided from the literature. If no such values existed values were chosen to fit the general proposed relationship between different values. Values were primarily chosen to fit dynamic recrystallization at low to medium grade conditions ($T = 450^\circ$, $P = 3$ kbar) and deformation of wet quartz ($Fluid_Factor = 1$). At the same time, the calculation time for one individual experiment had to be reasonable (below 5 days). Used values are given in Tab. 3.3 (pg. 81).

The modelled type of deformation with BASIL was deformation with pistons at the upper and lower limit of the unit cell and plane strain, dextral simple shear ($W_n = 1$) with a displacement Δs in the x direction of 0.025 per time step (Fig. 3.21). This results in a strain increment $\Delta\gamma$ of 0.05. This value was chosen to ensure a balance between process discretization and computational calculation time. Perfect bonding between polygons, hence no slip along grains is assumed. To assure reasonable results the accuracy of output of the deformation program basil was regularly checked using the value display program SYBIL. The general flow behaviour of the simulated material was chosen to be Newtonian viscous. The commonly cited non-linear viscous behaviour of rocks (e.g. Carter, 1976; Schmid, 1976; Urai, 1983; Stöckert et al., 1999) is to some extent already modelled separately within the crystallographic lattice rotation routine (section 3.2.3.2). In this routine, the increase of the dislocation density with stress is already taken into account. It is therefore reasonable to allocate an n value of 1 for the general deformation of the material used in the viscous deformation routine BASIL (cf. section 3.2.3.1).

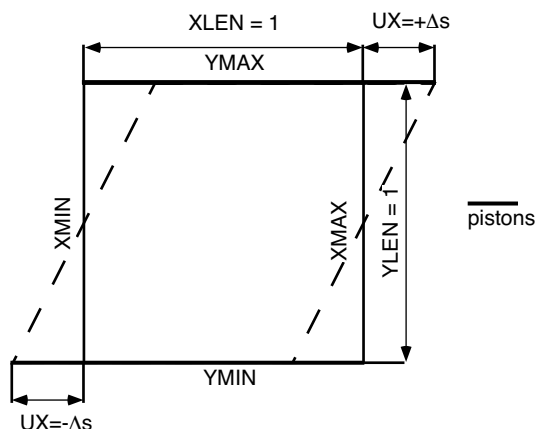


Figure 3.21 Illustration of simple shear deformation and the parameters specified in BASIL.

Values for *SwitchDistance* (=0.00625), *MinNodeSep* (=0.00625), *MaxNodeSep* (=0.03175), *MinAngle* (=9°) (Tab. 3.3) which affect the resolution of the mesh were chosen to result in a balance of a resolution as high as possible while keeping computational calculation sufficiently short.

To scale the values of the model to real world values several scaling factors had to be specified. The time scaling factor ($t_{scale} = 3.1536e^{10}$ s) and the chosen strain per time step ($\Delta\gamma = 0.05$; see above) result in a strain rate of $1.6 \cdot 10^{-12} \text{ s}^{-1}$. This is in accordance to strain rates of 10^{-10} s^{-1} and 10^{-15} s^{-1} which are suggested for midcrustal rocks (e.g. Pfiffner and Ramsay, 1982; Carter and Tsenn, 1987; Prior et al., 1990; Stöckert et al., 1999). The stress scaling factor was chosen to assure a reasonable viscosity range for the simulated rock (quartzite) which is between $3.15 \cdot 10^{18} \text{ Pa s}$ and $6.3 \cdot 10^{18} \text{ Pa s}$. This value corresponds to the range of proposed kinematic viscosity values for mid-crustal rocks 10^{16} Pa s to 10^{21} Pa s (Kirby, 1983; Carter and Tsenn, 1987; Evans and Kohlstedt, 1995; Clark and Royden, 2000). The length scaling factor l_{scale} is 10^{-3} and ensured the representation of fabric in the dimensions of a normal thin section (1 cm by 1 cm). The dislocation density factor ρ_{scale} (=10¹²) is chosen to result in a modelled dislocation density ranges between $1 \cdot 10^{10} \text{ m}^{-2}$ and $1 \cdot 10^{13} \text{ m}^{-2}$ corresponding to dislocation densities observed in undeformed and deformed rocks and metals (e.g. Hacker and Kirby, 1993; Gottstein and Shvindlermann, 1999; Stöckert et al., 1999). The lowest dislocation density value is corresponds to $\rho'_{nucl} = 0.01$.

The used critical resolved stress values (CRSS) which are used in ELLE_TBH are given for each slip system in Tab. 3.4. These values correspond to data for greenschist to lower amphibolite facies conditions provided by Hobbs (1985) and Jessell and Lister (1990). Constants *a* and *b* (Eq. 3.3) are 0.4 and 0.7, respectively.

The value for energy of dislocations ρ_{energy} ($7 \cdot 10^{-9} \text{ J/m}^2$) was chosen according to the range given by Hacker and Kirby (1993) and Gottstein and Shvindlermann (1999) (used in ELLE_SPLIT, ELLE_NUCLXX, ELLE_GBM).

Table 3.4 Critical Resolved Shear Strass

Slip number	Slip system	CRSS
1	BASAL a	5.00
2	PRISM c	11.00
3	PRISM a	6.00
4	PRISM c+a	1e ¹⁰
5	PRISM -c-a	1e ¹⁰
6	(2-1-1- 1) c+a2	9.50
7	(2-1-1- 1) c+a3	9.50
8	(2-1-1- 1) -c-a2	9.50
9	(2-1-1- 1) -c-a3	9.50
10	RHOMB a	15.00
11	RHOMB —a	15.00
12	RHOMB c+a	1e ¹⁰
13	RHOMB -c-a	1e ¹⁰

The orientation vector O of the subgrain boundaries (used in ELLE_SPLIT) was chosen to be crystallographically determined. It is chosen in such a way that "Splitting" occurs preferably parallel or perpendicular to the c-axis. This corresponds to observations of Lloyd et al. (1992) and Stöckert et al. (1999). The energy threshold value above which a grain has a probability to split Th_{split} is $2.4 \cdot 10^5 \text{ J/m}^2$. The area of newly created subgrains was between $3.12 \cdot 10^{-4} \text{ mm}^2$ (*MinArea*) and $1.25 \cdot 10^{-3} \text{ mm}^2$ (*MaxArea*) which is in the range of observed recrystallization grain sizes for quartz (e.g. Twiss, 1977; White, 1979a; Christie et al., 1980; Kronenberg and Tullis, 1984).

Constants c used in ELLE_NUCLXX (Eq. 3.7) is 1000.

The *MisorientAngle* used in ELLE_ROTXX, SHOWELLE; ELLE_STATS was set to be 10° according to values given for quartz (e.g. White, 1977; Lloyd et al., 1992; Trimby et al., 1998).

In ELLE_GBM the fraction d of *SwitchDistance* used to calculate D_{trial} is 0.01. The chosen value for surface energy Γ is $7 \cdot 10^{-2} \text{ J/m}^2$. This value is in accordance to the value range proposed ($0.01 - 1 \text{ J/m}^2$) for surface energy in rocks and metals (Urai et al. 1986 and references therein; Hacker and Kirby, 1993; Gottstein and Shvindlermann, 1999; Stöckert & Dyster, 2000). The influence of the crystallographic c-axis misorientation angle Π between adjacent grain or subgrains is chosen so that the crystallographic factor (*xx_factor*) is 0 at a c-axis misorientation angle of 0° , 0.1 at a misorientation of 10° and 0.99 at 20° , which corresponds to the general relationships observed in metals (Fig. 3.13). A_α is always 1; hence the surface energy is assumed to be isotropic with respect to the orientation of the boundary relative to the lattices of the crystals. The mobility is assumed to be isotropic, i.e. is not lattice orientation controlled. An isotropic nature of the grain boundary mobility is justified if the mobility is controlled by the transport rate across the boundary layer. In wet mineral aggregates this seems to be the case (Tullis and Yund, 1982; Bons et al., in press) and therefore this assumption is in accordance to the wet quartz model (*Fluid_Factor* = 1) in simulations. Constant d (Eq. 3.10) is 0.01 so that no computational and geometric problems arise.

Constants e and f used in ELLE_RECOVERY (Eq. 3.28) are 0.97 and 1000, respectively. RF_{base} is 0.95.

The base viscosity η_{base} used in ELLE_VISCOSITY is 1.

At the beginning of experiments the following Elle attribute values were pre-defined for all polygons: dislocation density = 0, viscosity = 1 and random Euler angles.

3.4.2.2 Values varied throughout simulations

Three parameters were varied in simulations (Tab. 3.5; end of chapter - pg. 125):

(a) initial fabric (R_ϕ): a coarse grained and fine grained monomineralic microstructure. An initially "coarse grained" microstructure has a mean ratio of initial grain size to numerical mean subgrain grain size R_ϕ of 48 and the initially "fine grained" microstructure a R_ϕ of 2.2.

(b) threshold value for recrystallization by nucleation (RX_{nuc}): two energy threshold values for recrystallization by nucleation i.e. $4.8 \cdot 10^5 \text{ Jm}^{-2}$ and $3.8 \cdot 10^5 \text{ Jm}^{-2}$. These two values were chosen to be in the general range of the proposed driving force magnitude for nucleation of new grains of Gottstein and Svindlerman (1999; p. 343).

(c) grain boundary mobility (*GBMob*): three values of grain boundary mobility i.e. $1 \cdot 10^{-12} \text{ m}^2\text{s}^{-1}\text{J}^{-1}$, $20 \cdot 10^{-12} \text{ m}^2\text{s}^{-1}\text{J}^{-1}$ and $40 \cdot 10^{-12} \text{ m}^2\text{s}^{-1}\text{J}^{-1}$. *GBMob* values were chosen in such a way that the resultant grain boundary migration rates are in the same order of magnitude range as those derived by Prior et al. (1990) for dynamic recrystallization of a quartz band in a low to medium grade pelite; given values are $1.2 \cdot 10^{-9} \mu\text{ms}^{-1}$ and $1.2 \cdot 10^{-11} \mu\text{ms}^{-1}$. For simplicity, we will call different R_ϕ coarse grained and fine grained, different RX_{nucl} values high and low, and *GBMob* values low, medium and high. A variety of movies that illustrate the fabric development are provided on the CD-Rom (Appendix F).

Tab. 3.3 Values used

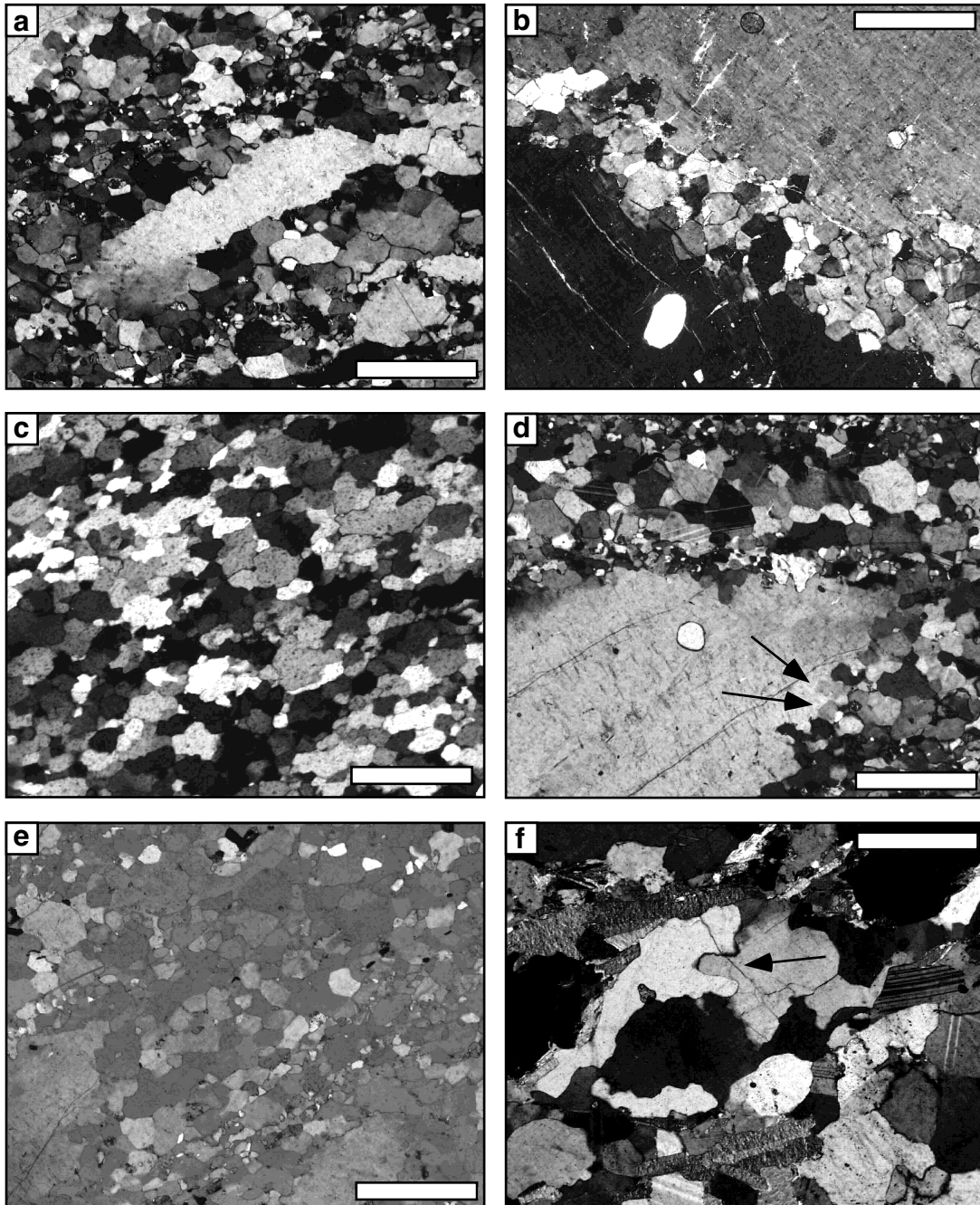
description and symbol	value	unit	literature
temperature T	450	°C	-
pressure P	3	kbar	-
Fluid_Factor	1	-	-
type of deformation W_n	1	-	-
flow behavior of material	Newtonian viscous		
displacement per time step Δs	0.025	-	-
strain per time step $\Delta \gamma$	0.05	-	-
strain rate	$1.6 \cdot 10^{-12}$	s^{-1}	Prior et al, 1990; Pfiffner & Ramsay, 1982
finite strain γ	2	-	-
sense of shear	dextral	-	-
<i>SwitchDistance</i>	$0.00625 \cdot 10^{-3}$	m^2	-
<i>MinNodeSep</i>	$0.00625 \cdot 10^{-3}$	m^2	-
<i>MaxNodeSep</i>	$0.03175 \cdot 10^{-3}$	m^2	-
<i>MinAngle</i>	9	°	-
time scaling factor t_{scale}	$3.1536e^{10}$ (1000a)	s	-
length scaling factor l_{scale}	10^{-3}	m	-
dislocation density scaling factor or ρ_{scale}	10^{13}	m^{-2}	Gottstein & Shvindlermann, 1999; Hacker & Kirby, 1993
stress scaling factor t_{scale}	10^8	Pa	-
dislocation density of new recrystallized grain ρ'_{nucl}	0.001	m^{-2}	
constant <i>a</i>	0.7	-	-
constant <i>b</i>	0.4	-	-
dislocation energy ρ_{energy}	$7 \cdot 10^{-9}$	Jm^{-2}	Hacker & Kirby, 1993
given vector for splitting direction <i>O</i>	parallel & perpendicular to c-axis	mm^2	Lloyd et al., 1992; Stöckert et al., 1999
SplitThreshold Th_{split}	$2.4 \cdot 10^5$	J/m^2	Gottstein & Shvindlermann, 1999
<i>MinArea</i>	$3.12 \cdot 10^{-4}$	mm^2	Twiss, 1977
<i>MaxArea</i>	$1.25 \cdot 10^{-3}$	mm^2	Twiss, 1977
constant <i>c</i>	1000	-	-
<i>MisorientAngle</i>	10	°	White, 1977; Lloyd et al. 1992; Stöckert et al., 1999
surface energy Γ	$7 \cdot 10^{-2}$	Jm^{-2}	Gottstein & Shvindlermann, 1999; Urai et al., 1986; Dyster & Stöckert, 2000
constant <i>d</i>	0.01	-	-
Boltzmann constant B	$1.3806503e10^{-23}$	JK^{-1}	-
activation energy H	$1.3806503e10^{-23}$	JK^{-1}	-
grain boundary activation energy QGBM	$1.3806503e10^{-23}$	Jmol^{-1}	-
Recovery_factor RF_{base}	0.95	-	-
constant <i>e</i>	0.97	-	-
constant <i>f</i>	1000	-	-
Base_viscosity η_{base}	$3.15 \cdot 10^{18}$	Pa s	Clark and Royden, 2000

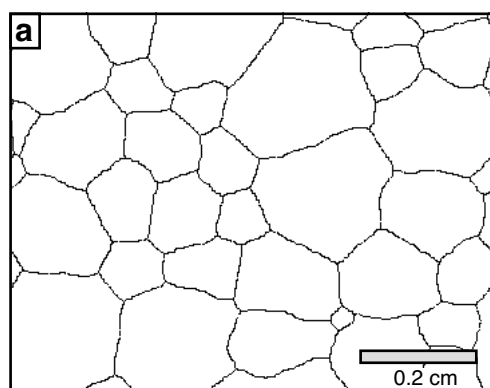
3.4.4 Results

3.4.4.1 General microstructural features observed in simulations

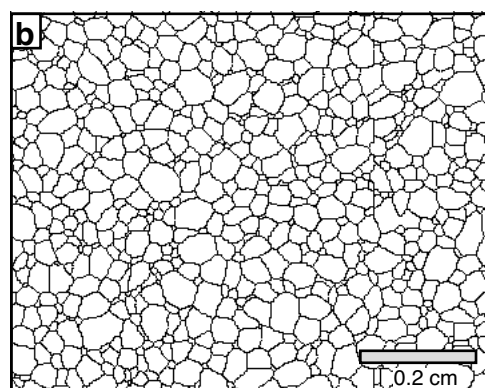
Simulated microstructures that developed during progressive deformation correspond to microstructures that are commonly attributed to dynamic recrystallization (e.g. Poirier and Nicolas, 1975; Guillopé and Poirier, 1979; Fitz Gerald et al., 1983; Means, 1983; Kronenberg and Tullis, 1984; Olsen and Kohlstedt, 1985; Urai et al., 1986; Jessell, 1987; Karato and Masuda, 1989; Dell'Angelo and Tullis, 1992; Lloyd et al., 1992; Hirth and Tullis, 1992; Takeshita et al., 1999; Shigematsu, 1999; Heidelbach et al., 2000). Such typical microstructures are shown in Fig. 3.22. In simulations, a bimodal grain size distribution is seen in initially coarse grained microstructures. A few large, strongly elongated grains that are surrounded by small grains remain even at a strain of 2. Small recrystallized grains develop predominately at the rim of large, old grains (Fig. 3.23c, cf. Fig. 3.22a) and trains of recrystallized grains cross-cut old, large grains are seen (Fig. 3.23d, cf. Fig. 3.22b). In initially fine grained fabrics a unimodal grain size distribution is common (Fig. 3.23e, Fig. 3.22c). In simulations with initially coarse grained microstructures domains of similarly oriented grains are observed at low recrystallization rates and low grain boundary mobility (Fig. 3.23f, Fig. 3.22e). Completely recrystallized microstructures were not achieved in any of the experiments (Fig. 23g), whereby completely recrystallized means that all grains have gone through at least one stage of either recrystallization by nucleation simulated by ELLE_NUCLXX or recrystallization by rotation simulated by ELLE_ROTXX. If *GBMob* is high, microstructures such as bulging grain boundaries develop in both initially fine and coarse grained microstructures (Fig. 3.23h, cf. Fig. 3.22f).

Figure 3.22 (opposite page) Photomicrographs of typical microstructure seen in rocks that have undergone dynamic recrystallization; scale bar = 0.5 mm; **(a)** Microstructure characterized by elongate grains with undulatory extinction and recrystallized grains surrounding the large, "old" grains, Qtz-Fsp mylonite, bimodal grain size distribution, Schirmacher Oasis, East Antarctica, crossed nicols. A similar microstructure is seen in Fig. 3.22c **(b)** Large grain cut by train of small recrystallized grains, Qtz-Fsp mylonite, Schirmacher Oasis, East Antarctica, crossed nicols. **(c)** Completely recrystallized quartzite, unimodal grain size distribution, Conceição do Rio Verde, Minas Gerais, Brasil (courtesy of S. ten Grotenhuis), crossed nicols. **(d)** Tip of a large, elongate, "relict" grain. Recrystallized grains are present at the rim of the large, "old" grain. Grain size of recrystallized grains are in the range of subgrains (arrows), Qtz-Fsp mylonite, Schirmacher Oasis, East Antarctica, crossed nicols. **(e)** Cluster of recrystallized grains with similar crystallographic orientation of Qtz-Fsp mylonite, Schirmacher Oasis, East Antarctica, crossed nicols and gypsum plate; **(f)** Irregular, bulging grain boundaries (arrow) typically attributed to originate from grain boundary migration recrystallization (e. g. Jessell, 1987), Qtz-Fsp mylonite, Schirmacher Oasis, East Antarctica, crossed nicols.

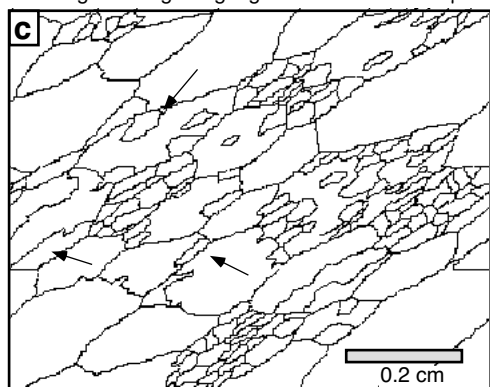




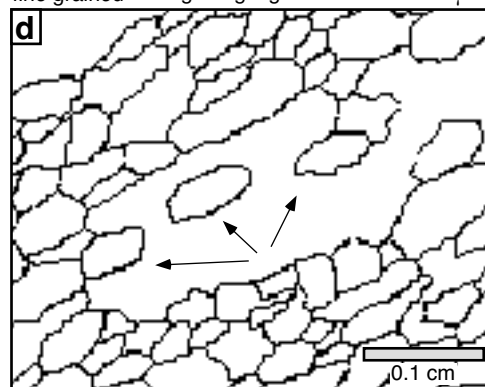
a coarse grained high angle grain boundaries $\gamma = 0$



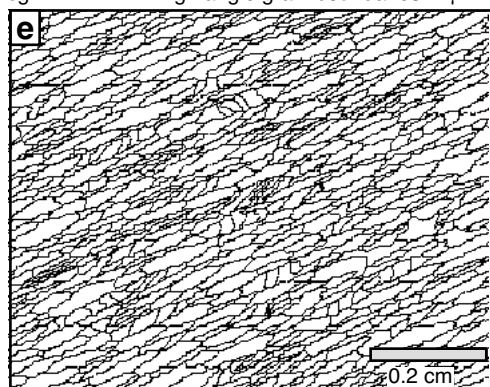
b fine grained high angle grain boundaries $\gamma = 0$



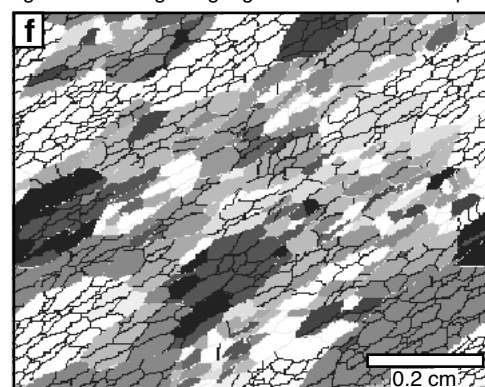
c cg1-1 high angle grain boundaries $\gamma = 2$



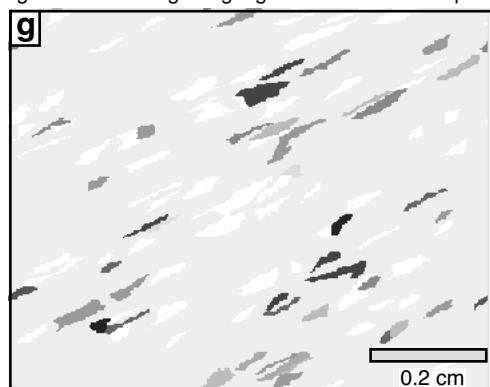
d cg2-3 high angle grain boundaries $\gamma = 1$



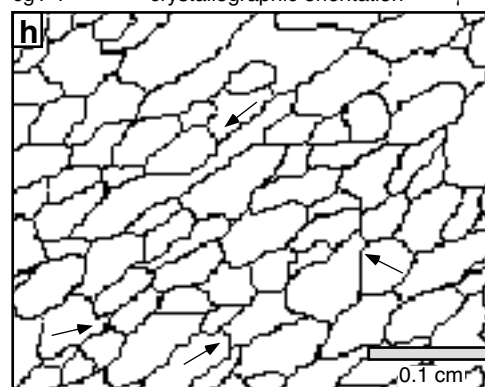
e fg1-1 high angle grain boundaries $\gamma = 2$



f cg1-1 crystallographic orientation $\gamma = 2$



g fg1-1 recrystallized grains $\gamma = 2$



h cg2-3 high angle grain boundaries $\gamma = 1$

Figure 3.23 (opposite page) Selected simulated microfabrics; simulation number (see Tab. 3. 2), attribute shown and finite strain are given below the diagrams. Scale bars given assume a unit cell width and height of 1 cm. **(a)** Initial fabric: coarse grained; only high angle boundaries are shown. **(b)** Initial fabric: fine grained; only high angle boundaries are shown, **(c)** Initially coarse grained fabric showing recrystallized grains at rims of large grains (core and mantle structures; arrows); bimodal grain size distribution; only high angle boundaries are shown. **(d)** Initially coarse grained fabric depicting a train of recrystallized grains running through grain at a similar angle as the orientation of the elongation of grains; only high angle boundaries are shown. **(e)** Uniform grain size distribution developed in an initially fine grained fabric; only high angle boundaries are shown. **(f)** Initially coarse grained fabric (same as depicted in **(c)**) showing the crystallographic orientation in grey scales; note clusters of similarly oriented recrystallized grains; different grey scale of grain boundaries signify different misorientation angles (dark $< 10^\circ$, light $> 10^\circ$). **(g)** Same microstructure as shown in **(e)**. Only grains shown in grey tones other than light grey are recrystallized. **(h)** Bulging grain boundaries typical for high grain boundary migration recrystallization. Initially coarse grained fabric. Small arrows point out such typical features; only high angle boundaries are shown.

The two initial fabric types are shown in Fig. 3.24 and results of all experiments are given Fig. 3.25. In none of the simulations a true steady state microstructure (Means, 1981) developed. This means that the characteristics of the microstructure such as the grain size, orientation of the long axes of grains still change with ongoing deformation at least up to a strain (γ) of 2. In simulations with an initial fine grained microstructure this change in the characteristics of the microstructure per time step is less pronounced than in initially coarse grained simulations.

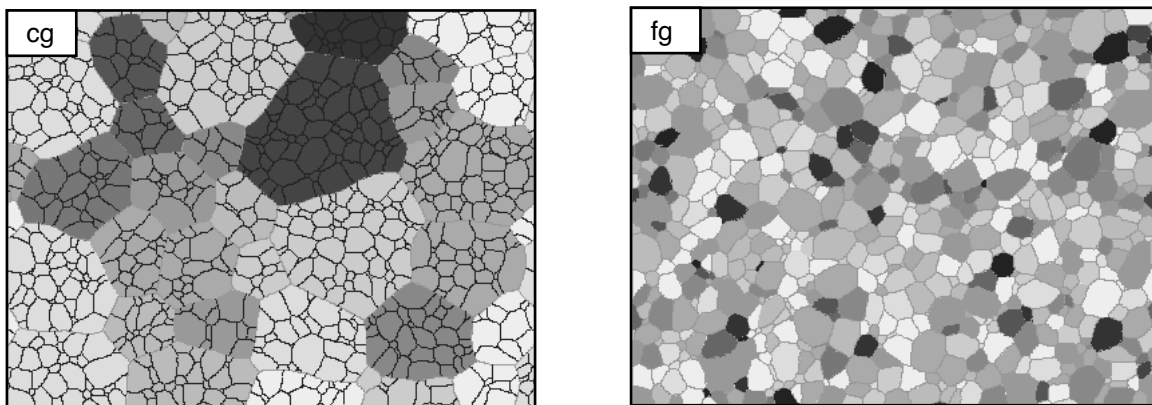
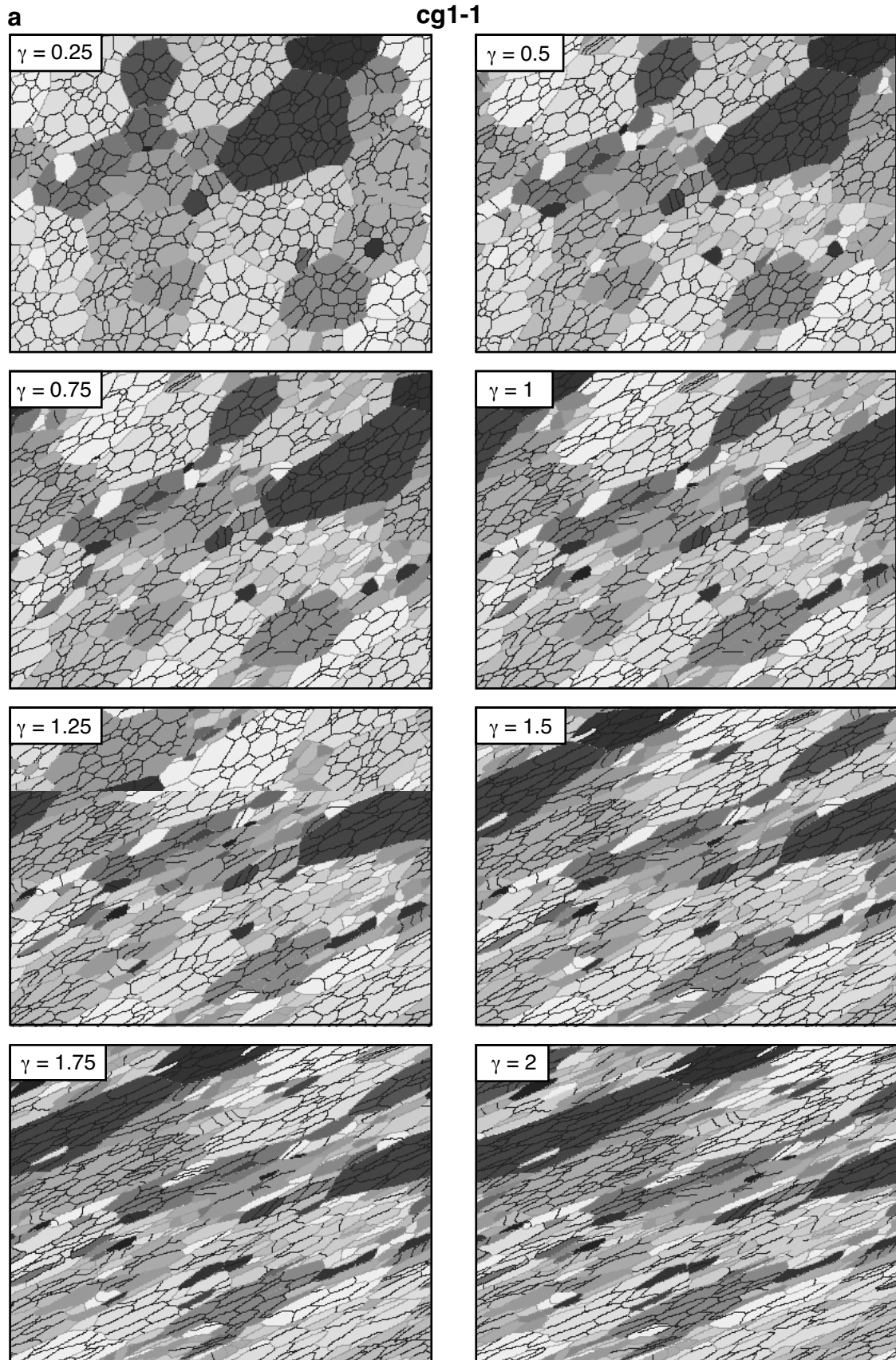
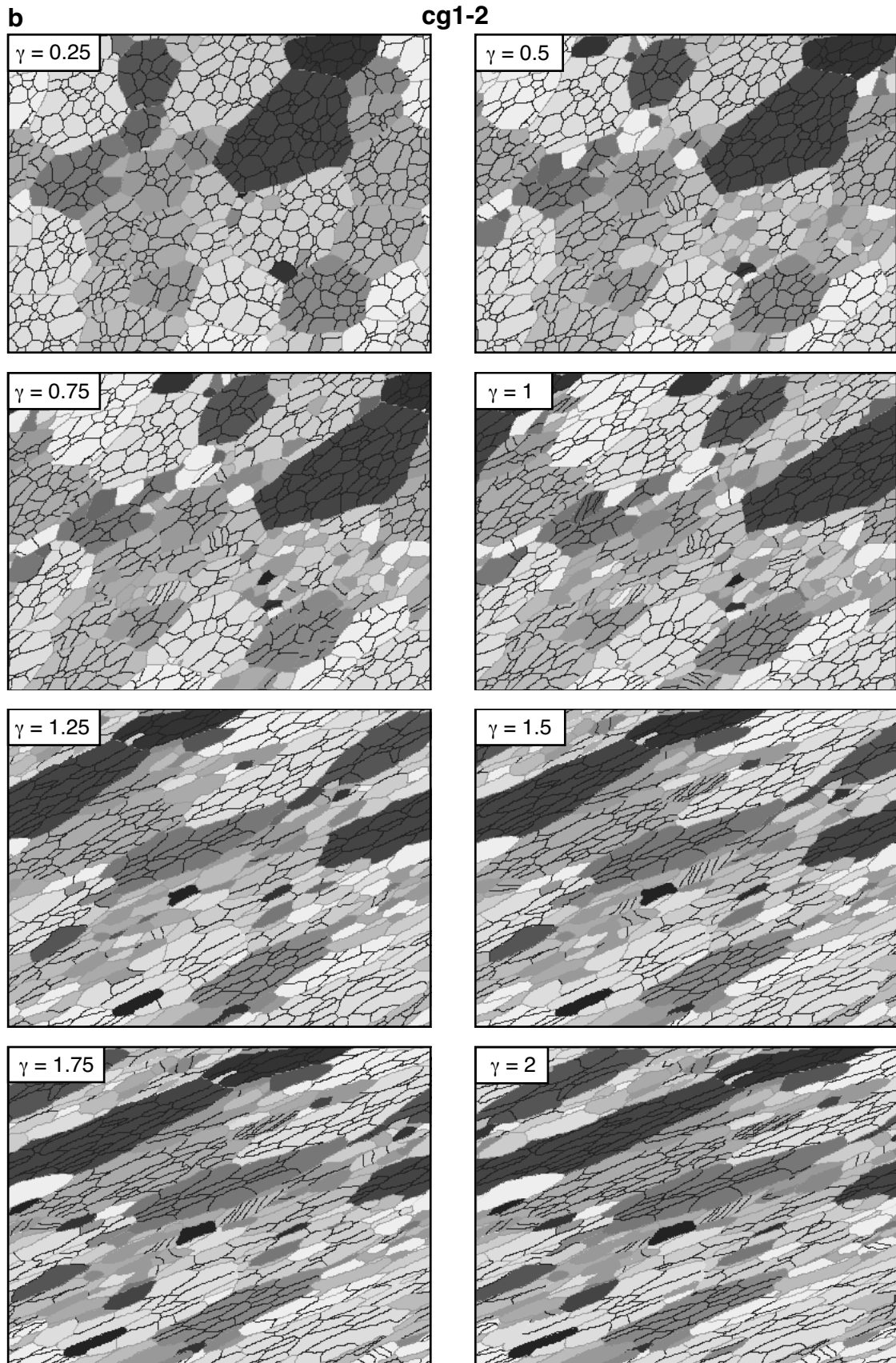
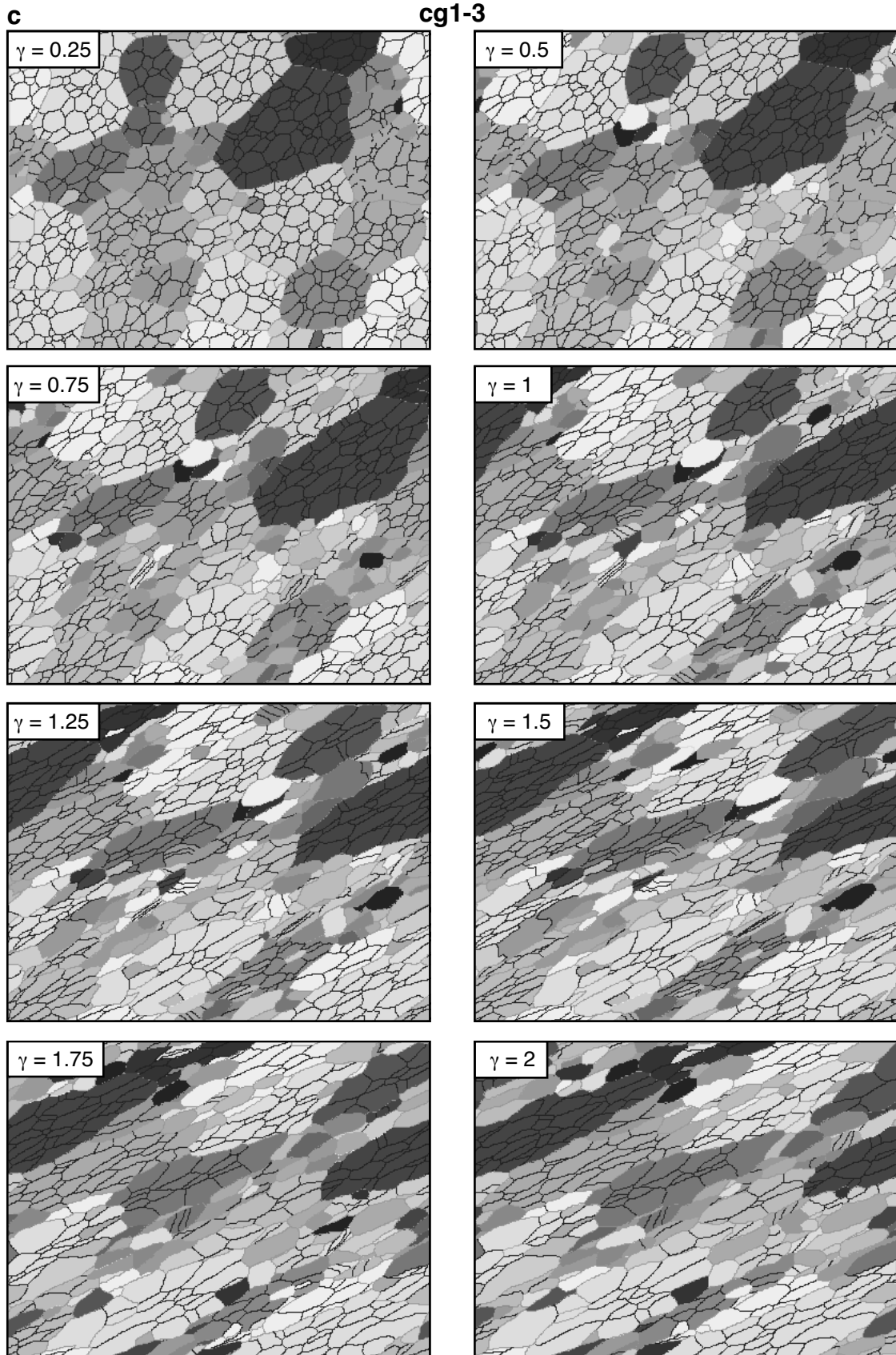


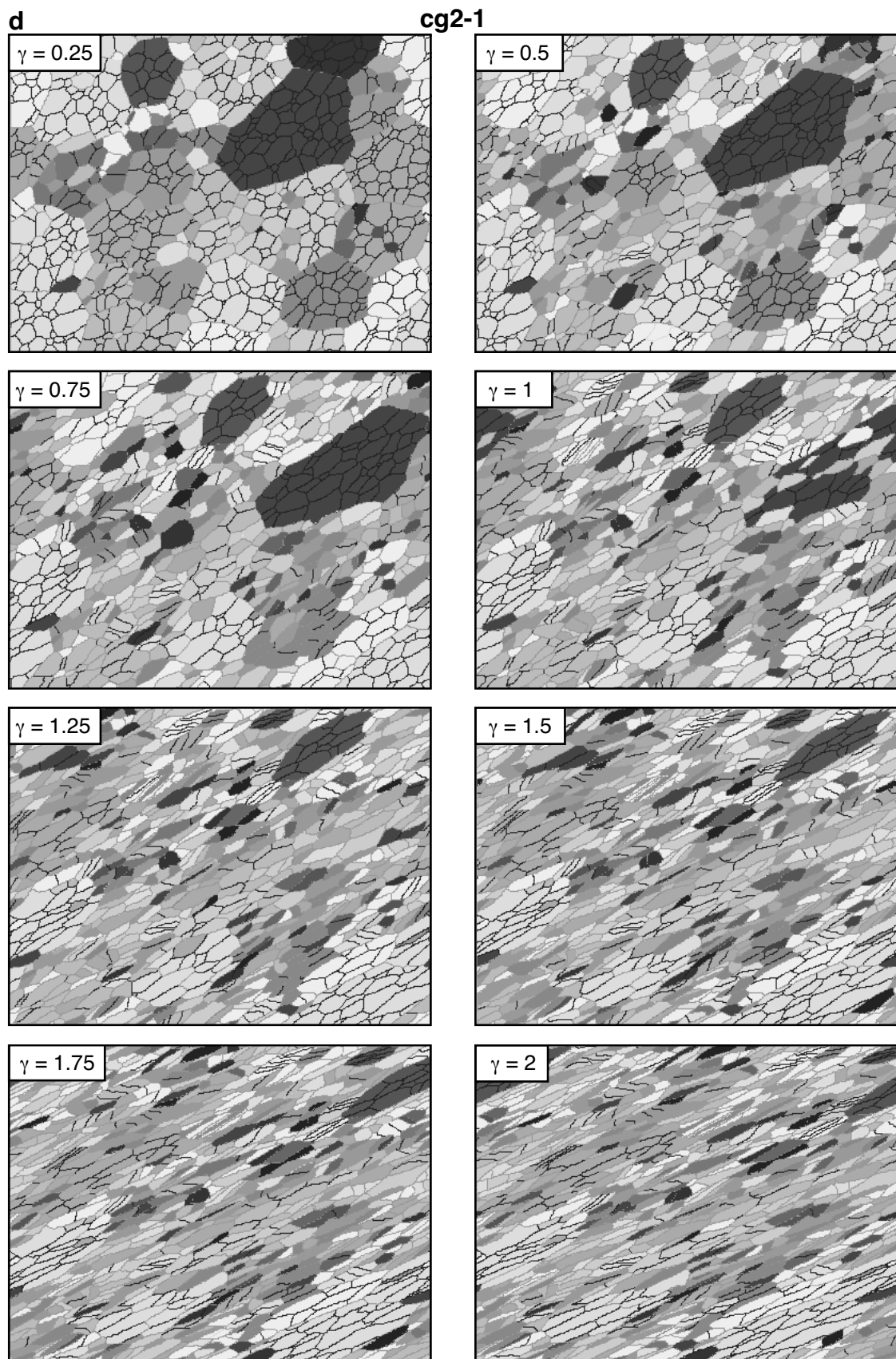
Figure 3.24 Representation of the two different initial fabrics used in simulations. **(a)** coarse grained; **(b)** fine grained. Different grey colours signify different grains, dark boundaries low angle boundaries and light grey coloured boundaries high angle boundaries. See movies in Appendix F (CD-Rom) for colour representation.

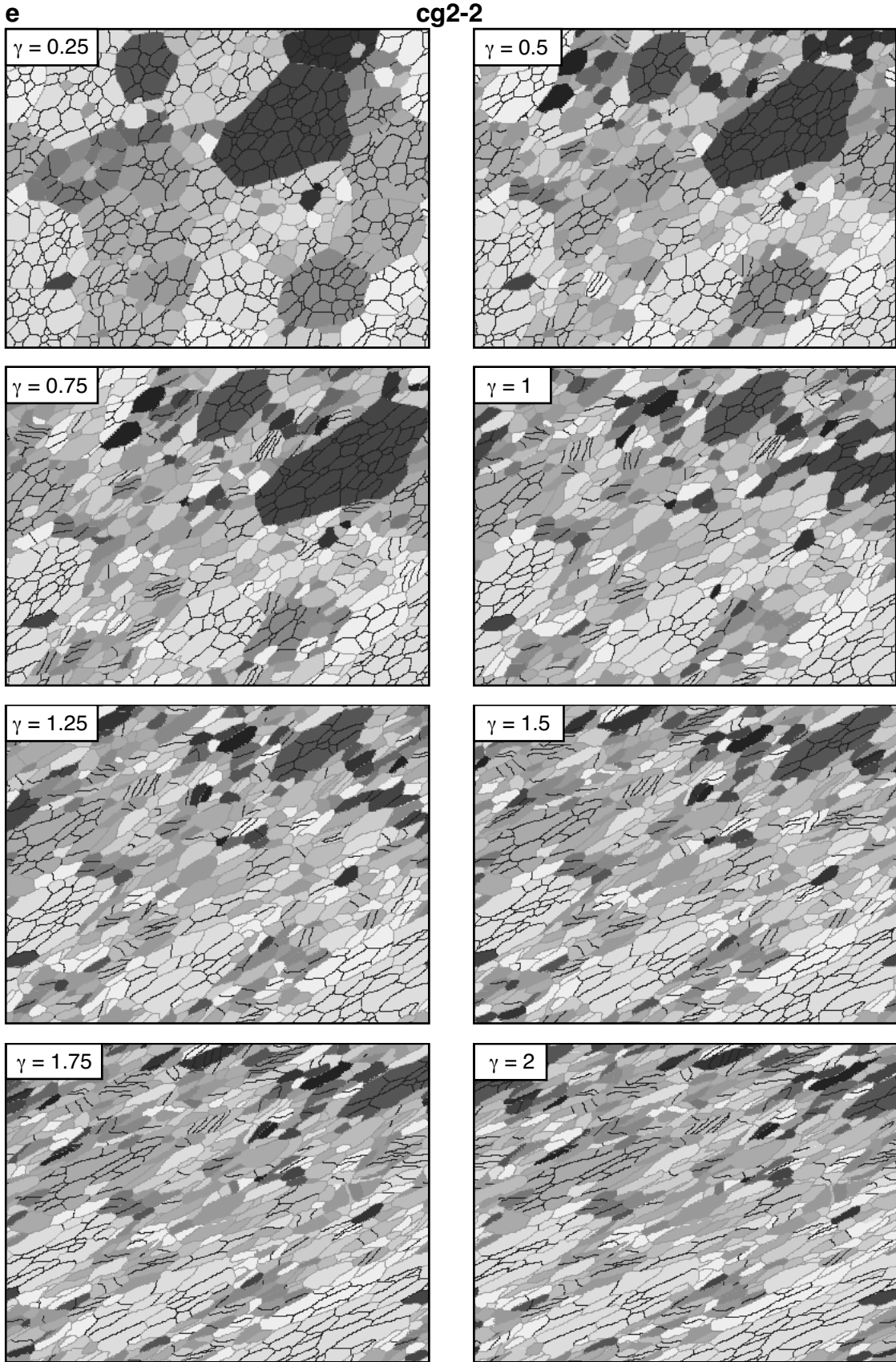
Figure 3.25 (next 12 pages) Results of the 12 simulation runs. Different grey colours signify different grains, dark boundaries low angle boundaries and light grey coloured boundaries high angle boundaries. The same files are shown in colour in the movie files of Appendix F (CD-Rom). For the nomenclature of simulation runs refer to Tab. 3.4. **(a)** cg1-1; **(b)** cg1-2; **(c)** cg1-3; **(d)** cg2-1; **(e)** cg2-2; **(f)** cg2-3; **(g)** fg1-1; **(h)** fg1-2; **(i)** fg1-3; **(j)** fg2-1; **(k)** fg2-2; **(l)** fg2-3. In none of the simulations a true steady state microstructure is seen. In simulations with an initial fine grained microstructure (fg-simulations) the change per time-step in the characteristics of the microstructure is less pronounced than in initial coarse grained simulations (cg-simulations). Simulations with high grain boundary mobility (last number of simulation nomenclature: 3, cf. Tab. 3.5; end of chapter - pg. 125) show large grain sizes and bulging boundaries. Simulations with a low threshold value for nucleation (first number of simulation nomenclature: 1, 2) exhibit a high amount of high angle boundaries (light grey coloured boundaries). In all simulations with an initial coarse grained microstructure (cg-simulations) subgrain develop preferably at the rim of large grains and at a strain of 2 still some large and strongly elongated grains remain.

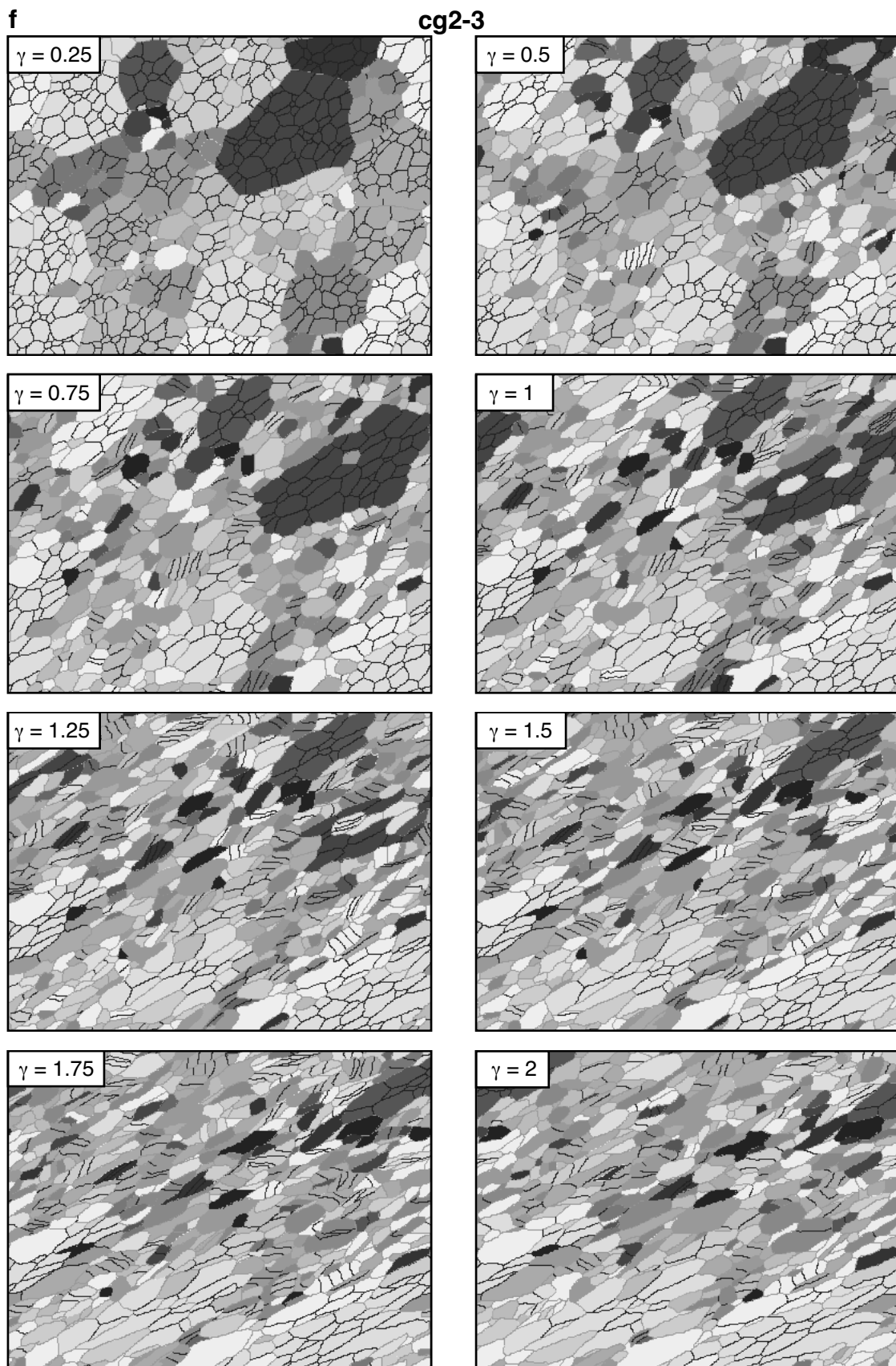


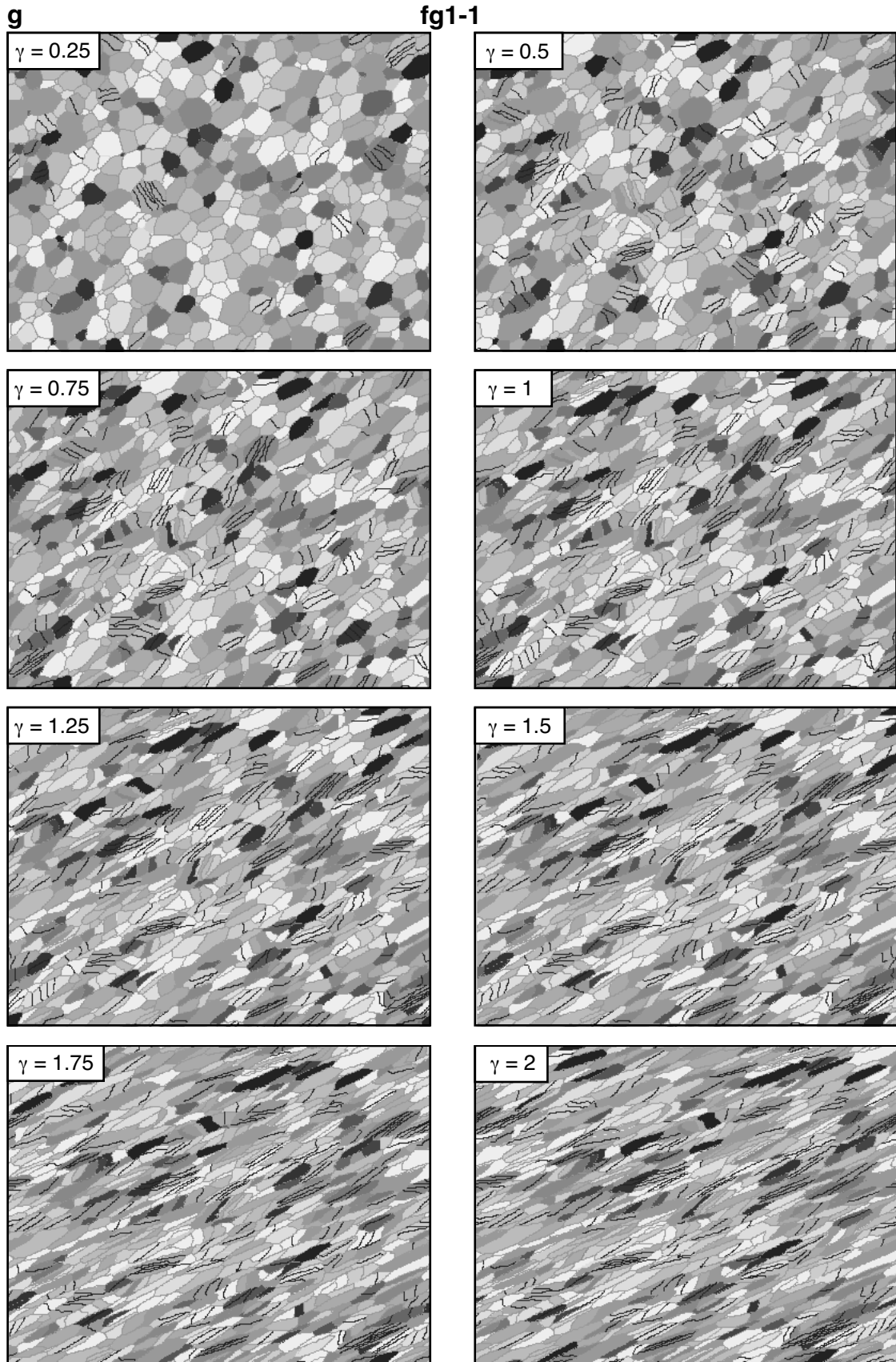






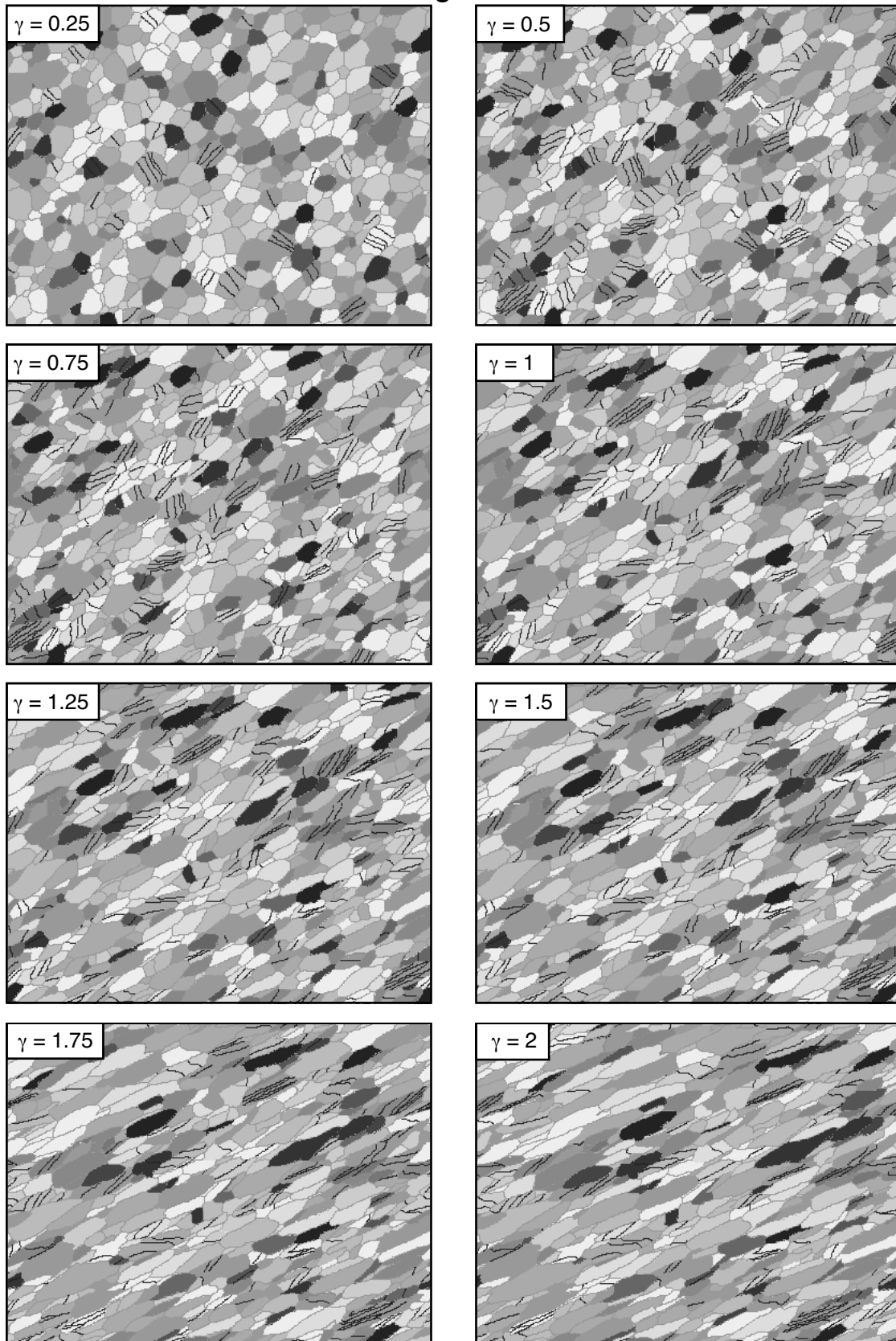






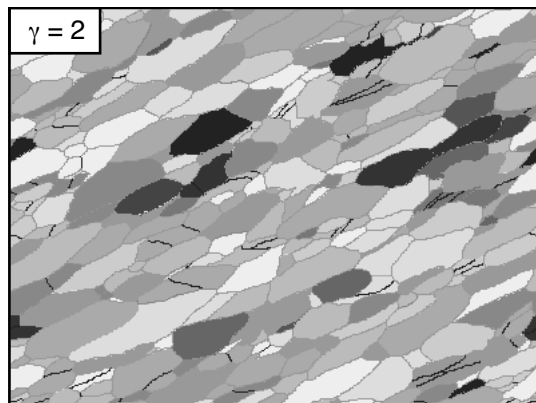
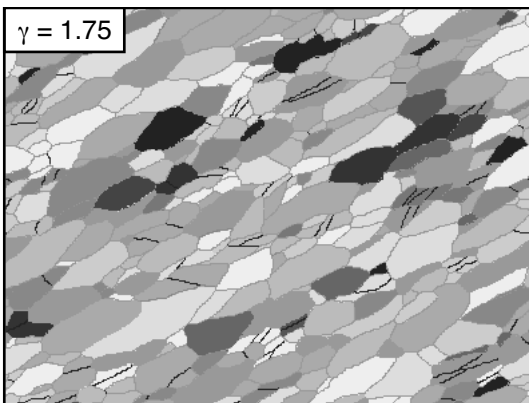
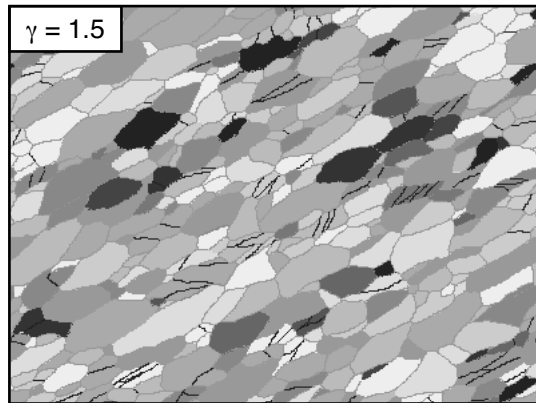
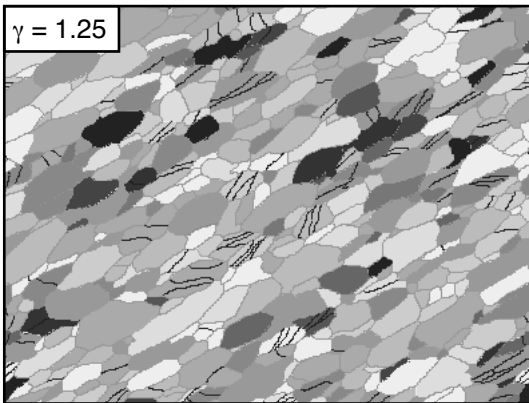
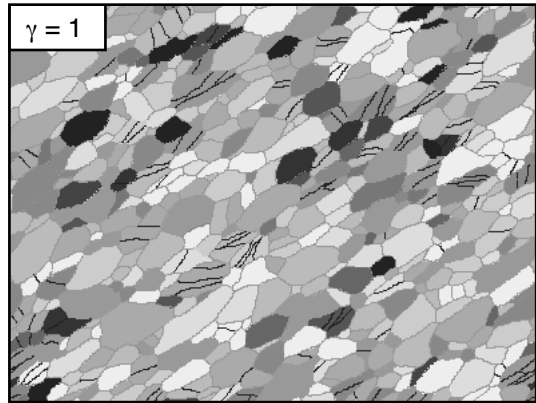
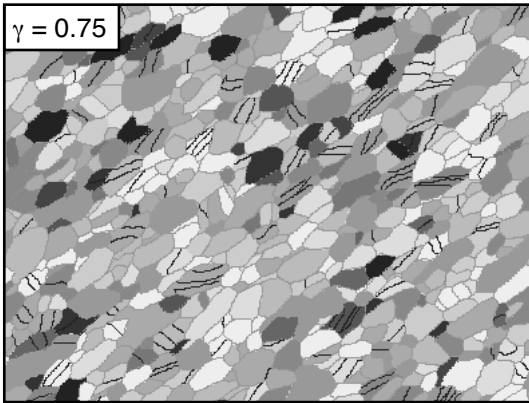
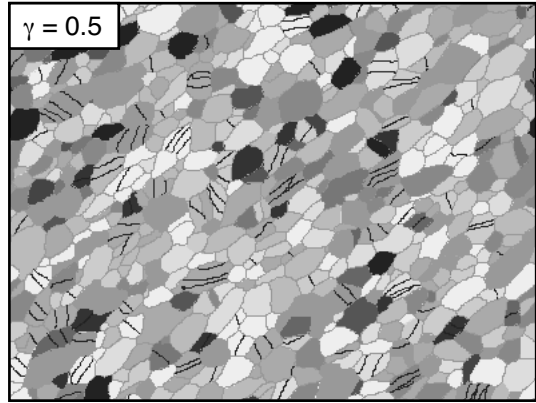
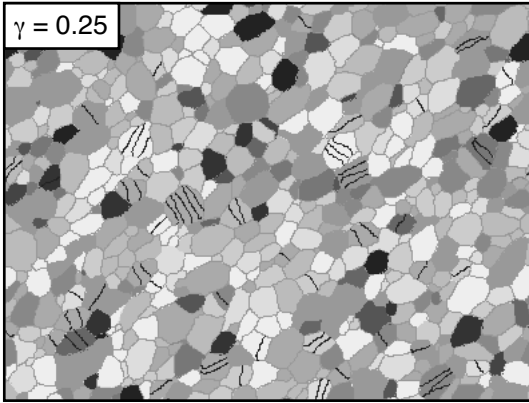
h

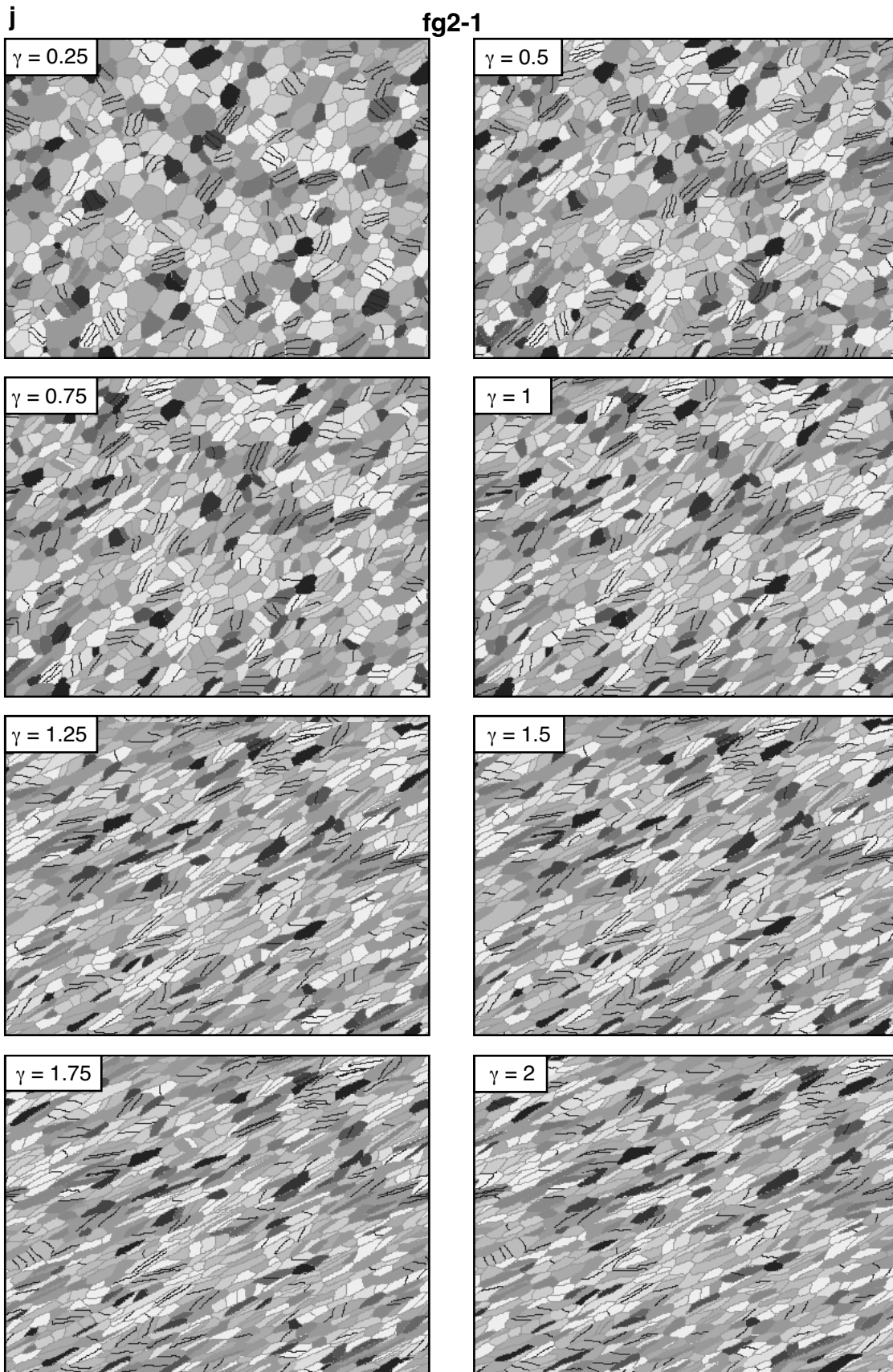
fg1-2



i

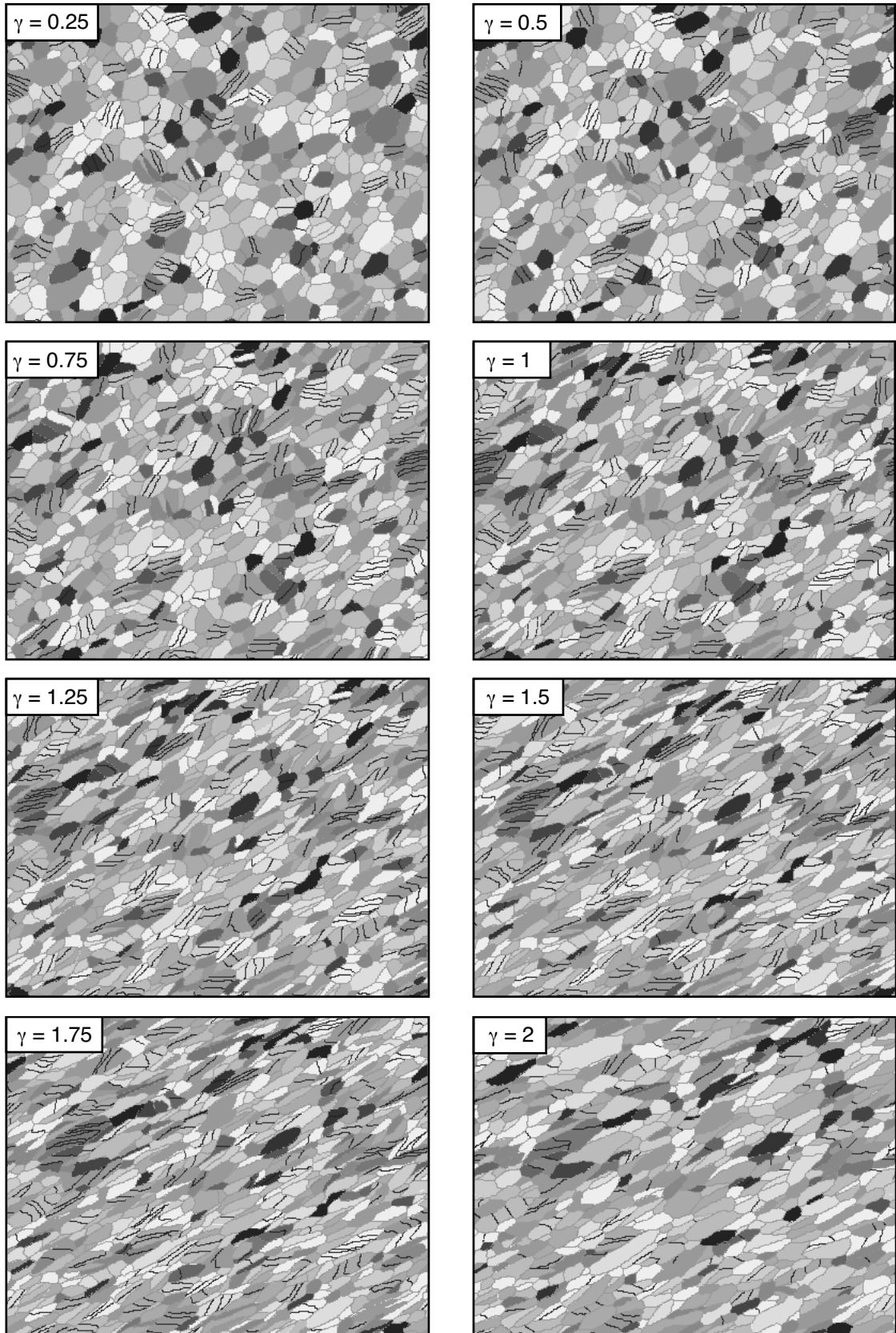
fg1-3

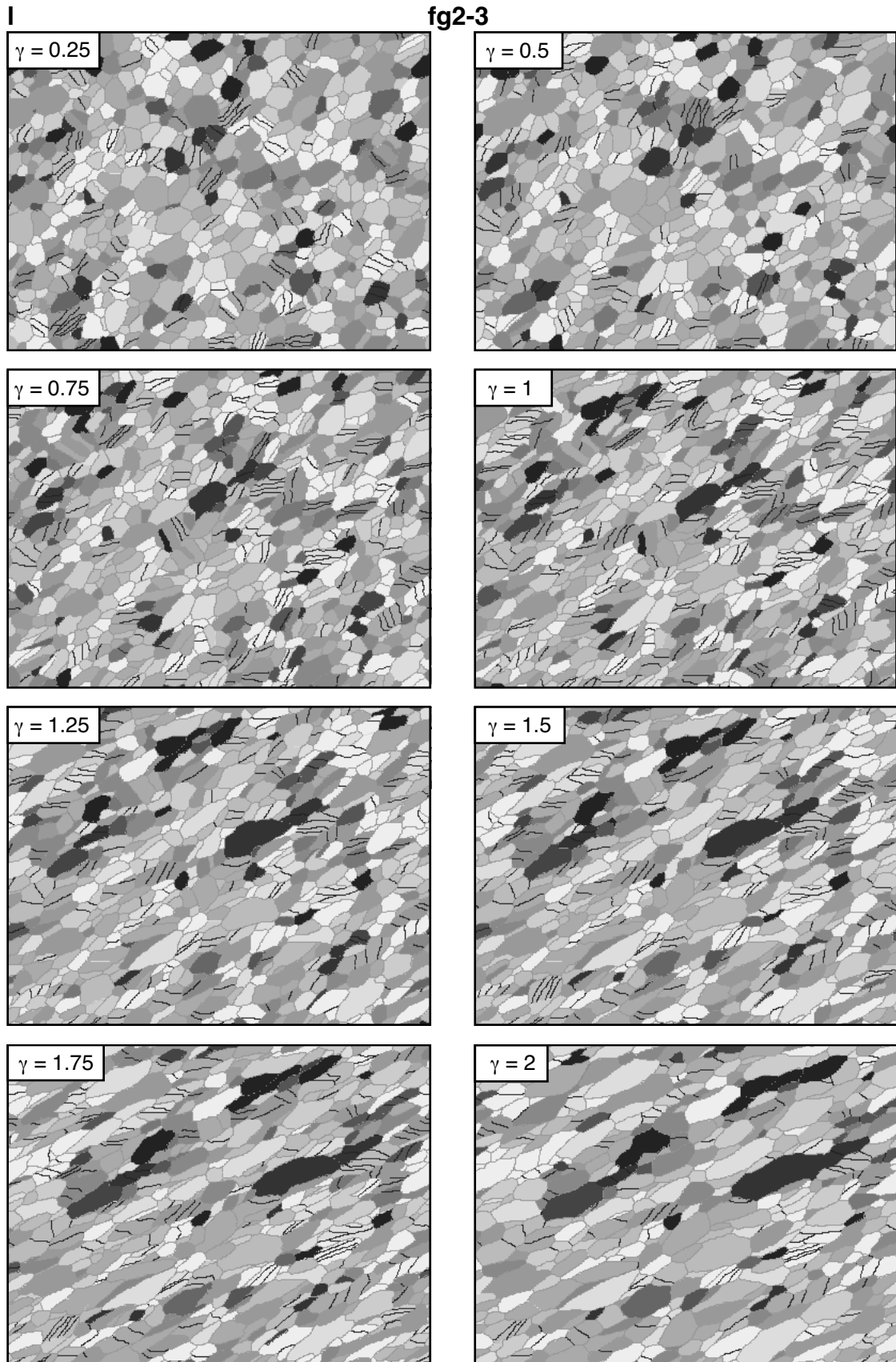




k

fg2-2





3.4.4.2 Detailed description of different fabric development with varying parameters

3.4.4.2.1 Grain shape and orientation of the principal axis

The grain shape in terms of aspect ratio R_a and orientation of the long principal axis of the ellipse α that characterizes the grain shape preferred orientation were calculated for each time step according to the method described by Panozzo (1983, 1984) (section 3.3.2). Undeformed, initial microstructures have a calculated ellipse aspect ratio R_a of 1.02. For comparison, values of the aspect ratio (R_e) and orientation β of the strain ellipsoid were calculated.

Low RX_{nucl} and high $GBMob$ show lower aspect ratios R_a in simulations than R_e of the strain ellipsoid (Fig. 3.26). In simulations with initially coarse grained fabrics α does not significantly deviate from β (Fig. 3.27a). In initially fine grained microstructures only slight differences between α and β are present (Fig. 3.27b). In none of the simulations a steady state foliation i.e. no change in orientation of the oblique foliation i.e. R_a with progressive deformation is observed (Fig. 3.27c).

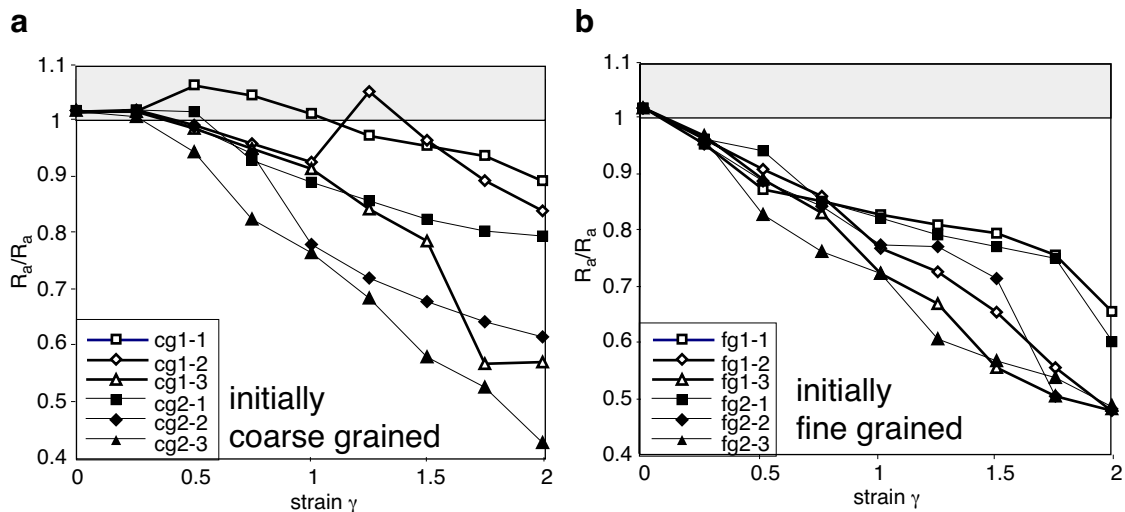


Figure 3.26 Graphs showing the change in aspect ratio of the ellipse calculated from simulated microfibrils using the method of Panozzo (1983, 1984). Calculated values from microstructures are normalized to the values of the ratio of longest and shortest axes of the corresponding strain ellipse. This means that if the normalized value is below 1, the calculated ratio of the aspect ratio of the microstructure is smaller than the aspect ratio of the strain ellipse. Hence, the shape fabric is weaker. (a) Simulations with initially coarse grained microstructure. (b) Simulations with initially fine grained microstructure.

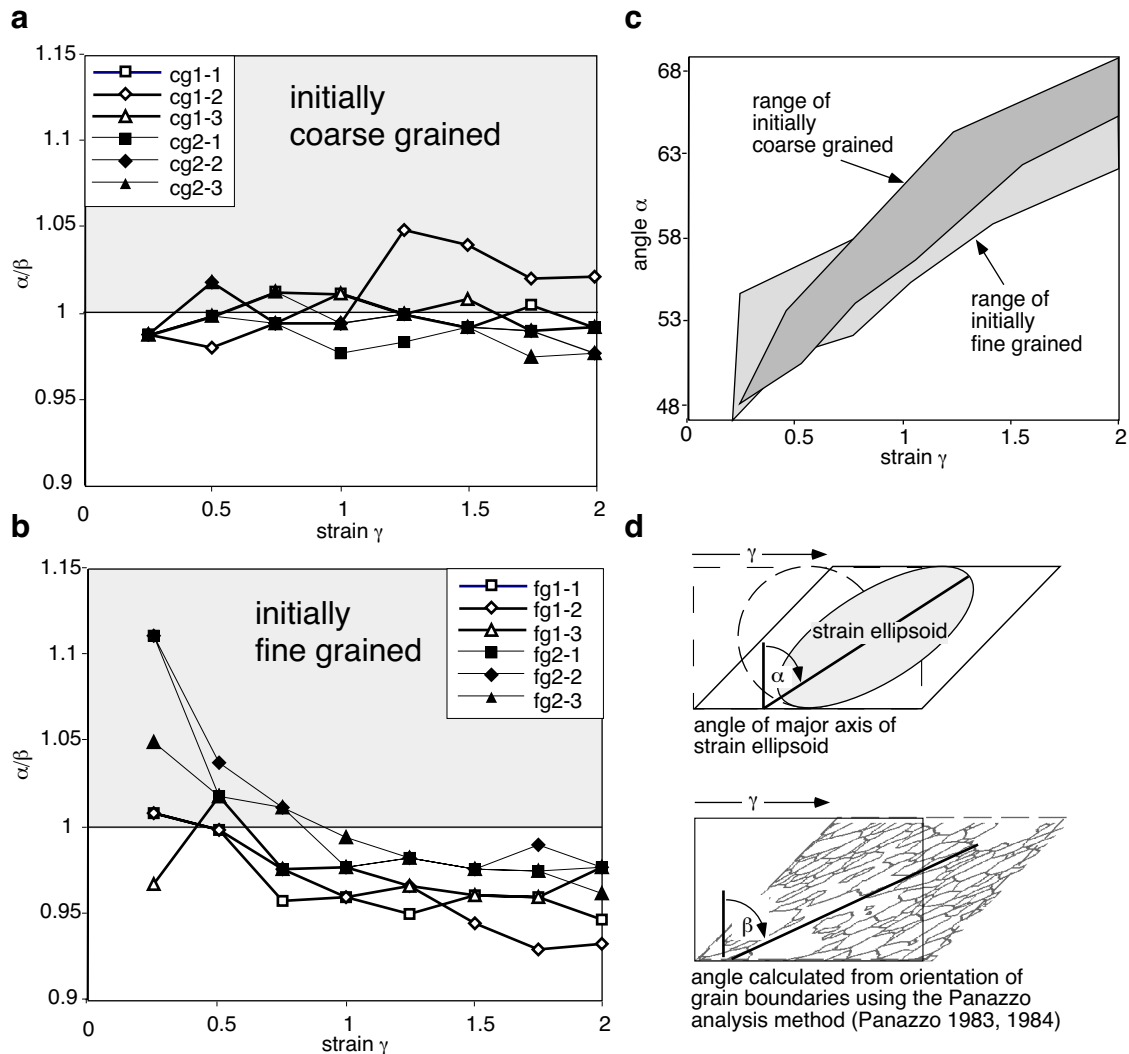


Figure 3.27 Change in orientation of the long axis of the shape ellipse calculated from simulated microfibrils using the method of Panazzo (1983, 1984) normalized to the calculated values orientation of the long axis of the strain ellipse (R_e). This means that if the normalized value is below 1, the $\alpha < \beta$ and therefore the orientation of the fabric is more „upright“ than expected from the orientation of the strain ellipse. (a) Simulations with initially coarse grained microstructure; no significant deviation from values of the strain ellipse. (b) Simulations with initially fine grained microstructure; at high strain lower values than values of the strain ellipse. In none of the simulations a steady state foliation (Means, 1981) is observed. (c) Graph illustrating the change in angle α with increasing strain for all experiments. (d) Representation of the definition of calculated angles of axes orientation with respect to shear boundaries.

3.4.4.2.2 Mean grain size and grain size distribution

In initially coarse grained fabrics, a constant mean grain size is achieved after a strain of about 1 if RX_{nucl} is low. At high RX_{nucl} only simulations with medium $GBMob$ exhibit a constant grain size (Fig. 3.28a). Initially fine grained fabrics show a constant mean grain size after a strain of 0.5 except for simulations with high $GBMob$ (Fig. 3.28b). The grain size increases with increasing strain in initially fine grained microstructures if high $GBMob$ is high.

The general pattern of grain size distribution is very similar in all experiments within one category of initial fabric (Fig. 29 and Fig. 30). In initially fine grained fabrics high $GBMob$ values result in a larger range of grain sizes. Grain size distributions of initial coarse grained fabrics are characterized by large number of small grains and a few remaining large grains. With increasing strain less and less large grains are present. This effect is most profound at low RX_{nucl} (Fig. 3.25, Fig. 3.29). In initially fine grained fabrics the grain size distribution are always unimodal (Fig. 3.25, Fig. 3.30) with a strong curtosis towards small grain sizes, whereby the most of the grains are small grained (Fig. 3.30).

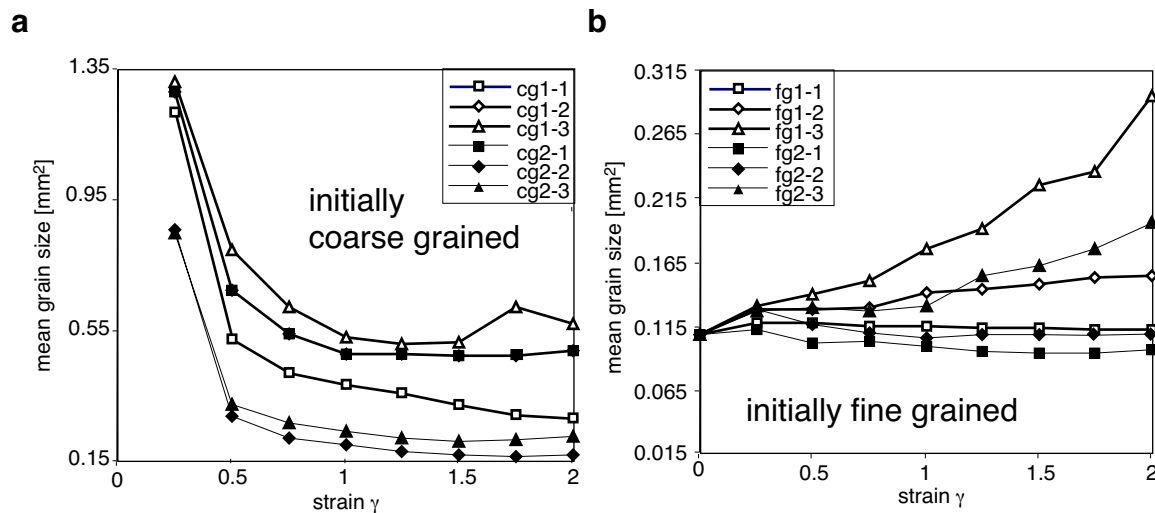


Figure 3.28 Change in mean grain size during progressive deformation. (a) Simulations with initially coarse grained microstructure. (b) Simulations with initially fine grained microstructure.

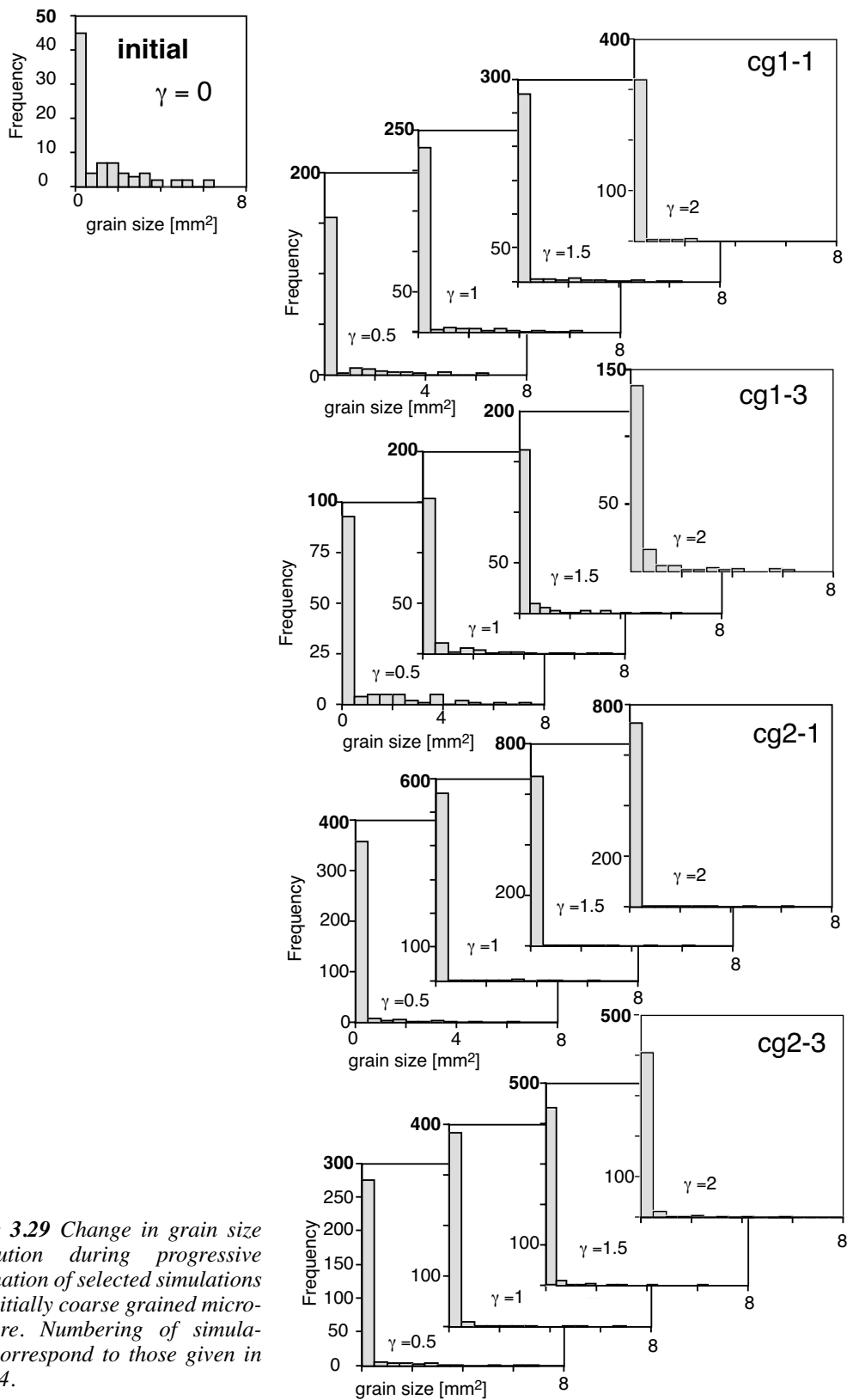


Figure 3.29 Change in grain size distribution during progressive deformation of selected simulations with initially coarse grained microstructure. Numbering of simulations correspond to those given in Tab. 3.4.

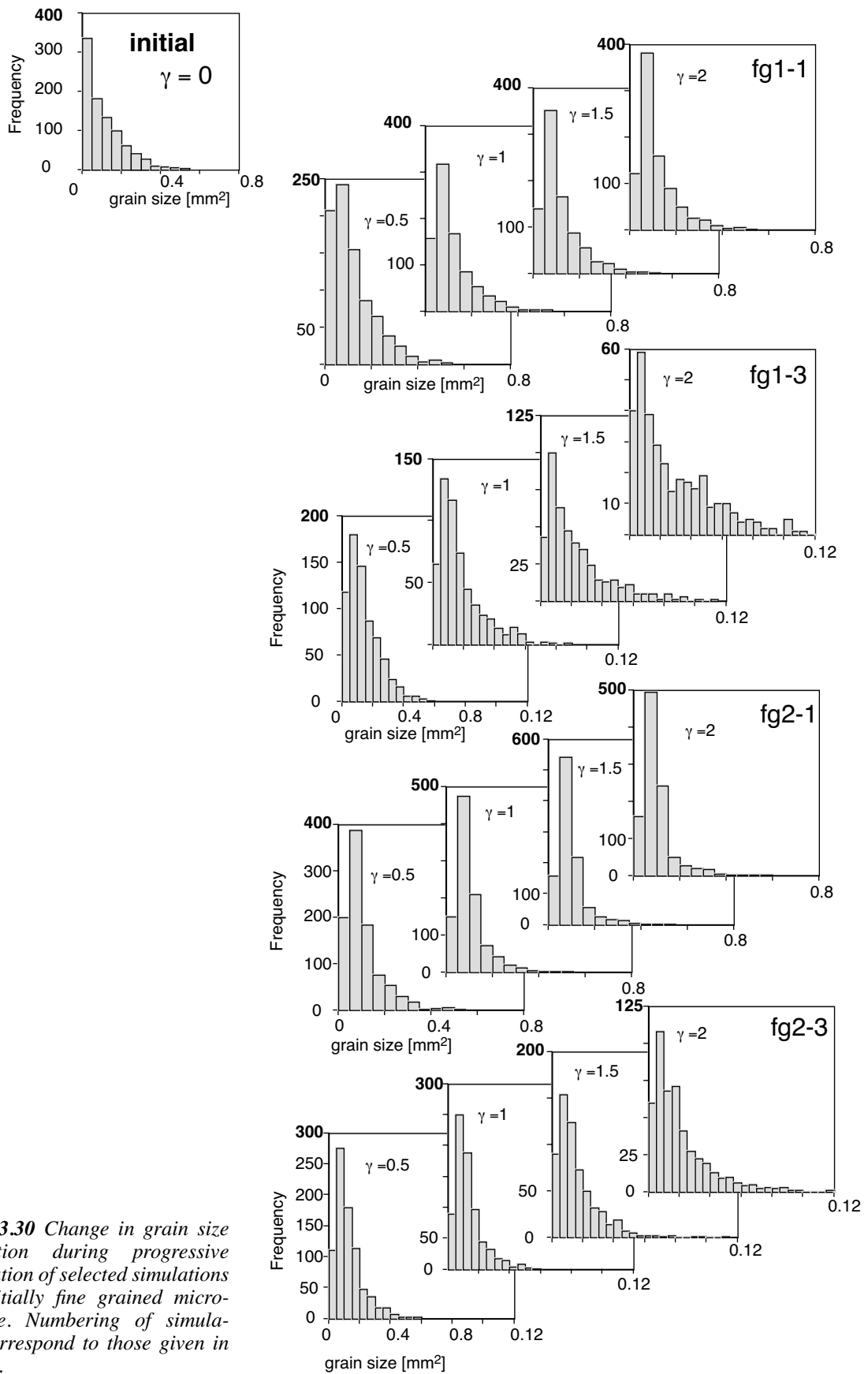


Figure 3.30 Change in grain size distribution during progressive deformation of selected simulations with initially fine grained microstructure. Numbering of simulations correspond to those given in Tab. 3.4.

3.4.4.2.3 Degree of recrystallization simulated by ELLE_ROTXX and ELLE_NUCLXX

The degree of recrystallization in the sense used here is the area fraction of grains that have recrystallized according to recrystallization by rotation (ELLE_ROTXX) and recrystallization by nucleation (ELLE_NUCLXX). The degree of recrystallization increases with increasing strain (Fig. 3.31). High *GBMob* result in low degrees of recrystallization. The highest values are seen for initially coarse grained fabrics and low threshold values for recrystallization by nucleation.

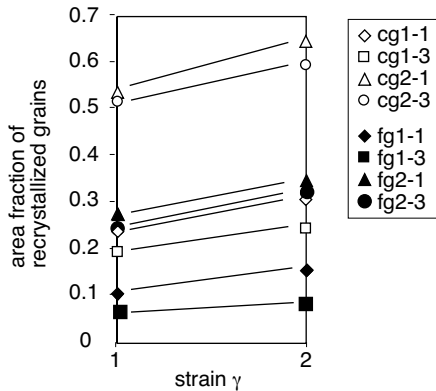


Figure 3.31 Degree of recrystallization with increasing finite strain for selected simulations. The degree of recrystallization is the area of grains which recrystallized either by rotation (ELLE_ROTXX) or by nucleation (ELLE_NUCLXX) with respect to the total area.

3.4.4.2.4 Total dislocation density and spatial distribution of dislocation densities

In all simulations the total dislocation density, which is the area weighted average dislocation density of all polygons, decreases with increasing strain. In simulations with low *GBMob* and low RX_{nucl} highest values are seen (Fig. 3.32a, Fig. 3.32b). The decrease in dislocation density during progressive deformation is most pronounced in experiments with high RX_{nucl} .

The spatial distribution of dislocation density and therefore of viscosity (cf. section 3.2.3.7) generally show bands of high and low dislocation density areas which are oriented parallel to the grain shape fabric of the microstructure. In experiments with low RX_{nucl} and high *GBMob* these bands are poorly developed (Fig. 3.33, Fig. 3.34). In the initially coarse grained fabric remnant large grains exhibit markedly lower dislocation densities than the surrounding fine grained matrix (Fig. 3.33, Fig. 3.34).

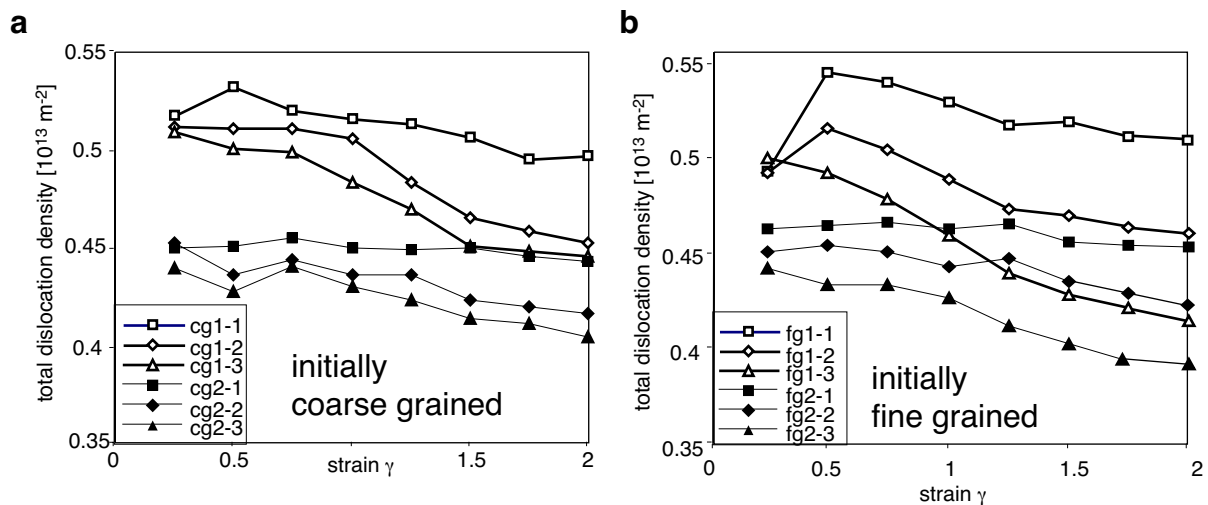


Figure 3.32 Change in total dislocation density during progressive deformation. The total dislocation density is the area weighted average dislocation density of all polygons. To calculate the total dislocation density. (a) Simulations with initially coarse grained microstructure. (b) Simulations with initially fine grained microstructure.

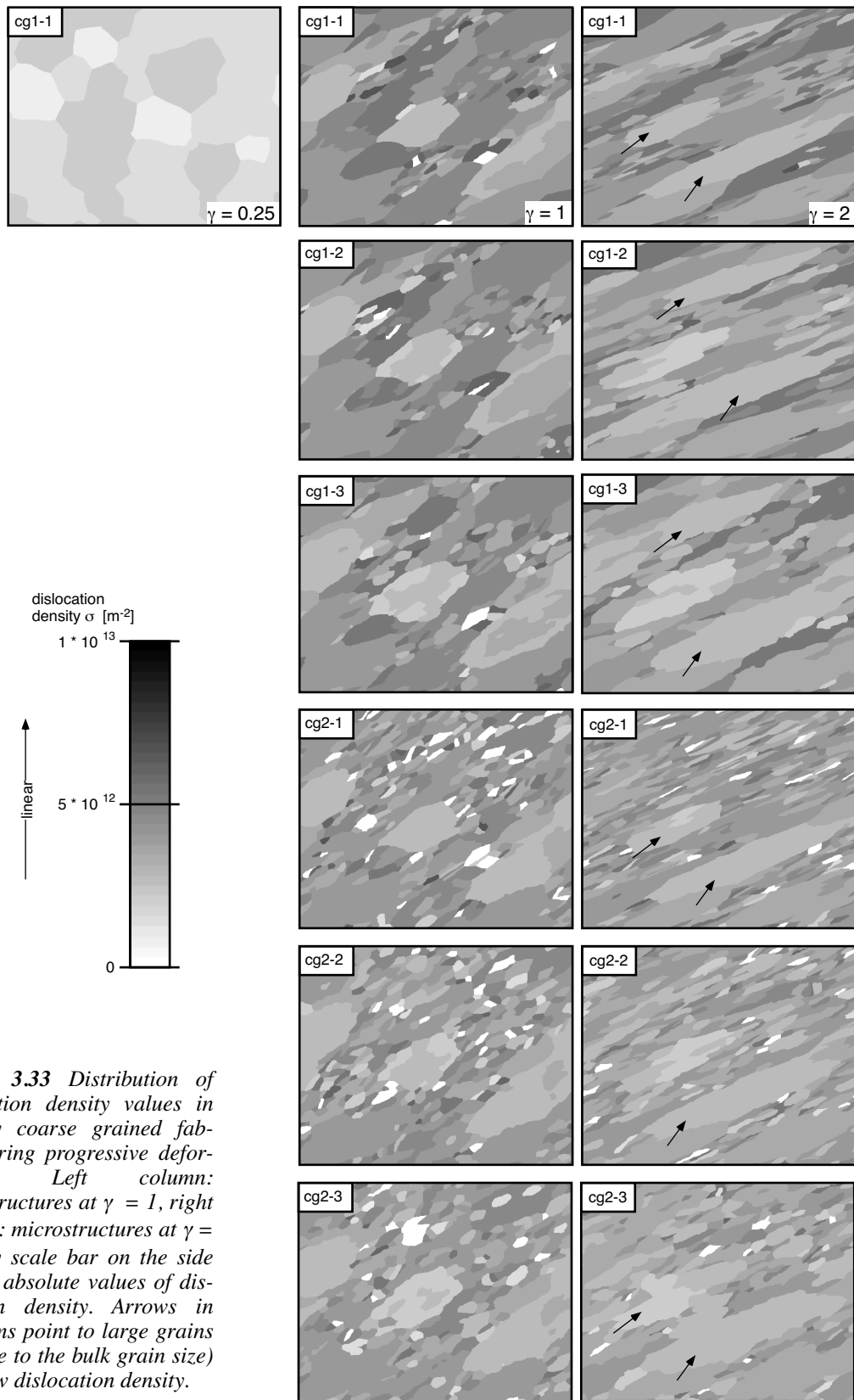


Figure 3.33 Distribution of dislocation density values in initially coarse grained fabrics during progressive deformation. Left column: microstructures at $\gamma = 1$, right column: microstructures at $\gamma = 2$. Grey scale bar on the side depicts absolute values of dislocation density. Arrows in diagrams point to large grains (relative to the bulk grain size) with low dislocation density.

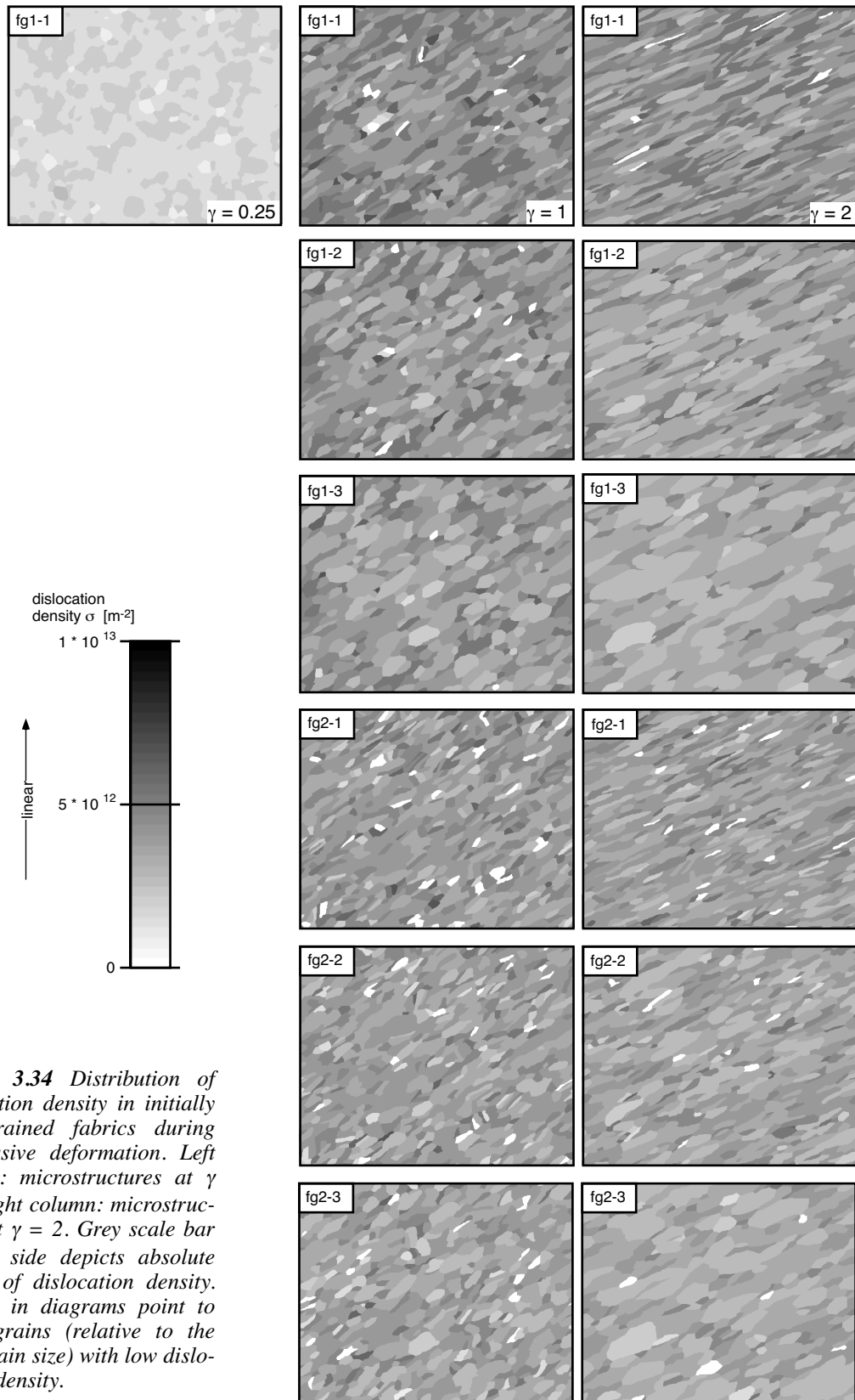


Figure 3.34 Distribution of dislocation density in initially fine grained fabrics during progressive deformation. Left column: microstructures at $\gamma = 1$, right column: microstructures at $\gamma = 2$. Grey scale bar on the side depicts absolute values of dislocation density. Arrows in diagrams point to large grains (relative to the bulk grain size) with low dislocation density.

3.4.4.2.5 Crystallographic orientation

A crystallographic preferred orientation develops in all experiments (Fig. 3.35 – Fig. 3.38). In many cases, a cross girdle of c-axes develops at medium to high strain ($1 < \gamma < 2$). Many grains align with the basal plane parallel to the flow plane. In initially fine grained fabrics the N-S orientation of the cross girdle becomes more pronounced with increasing strain (Fig. 3.37), and a single girdle develops. In initially coarse grained fabrics with high GBMob the crossed girdle is only weakly developed. In all experiment with an initial coarse grained fabric (Fig. 3.35, Fig. 3.36) "strings" of similarly oriented grain are seen which follow great circles. These are rotated subgrains of large, relict grains. Maxima of a-axes are weakly developed, whereby 2 maxima lie in the flow plane. A number of grains align with the a-direction parallel to the flow direction. Additionally, 4 weak maxima are seen at 60° degrees angle to the other maxima.

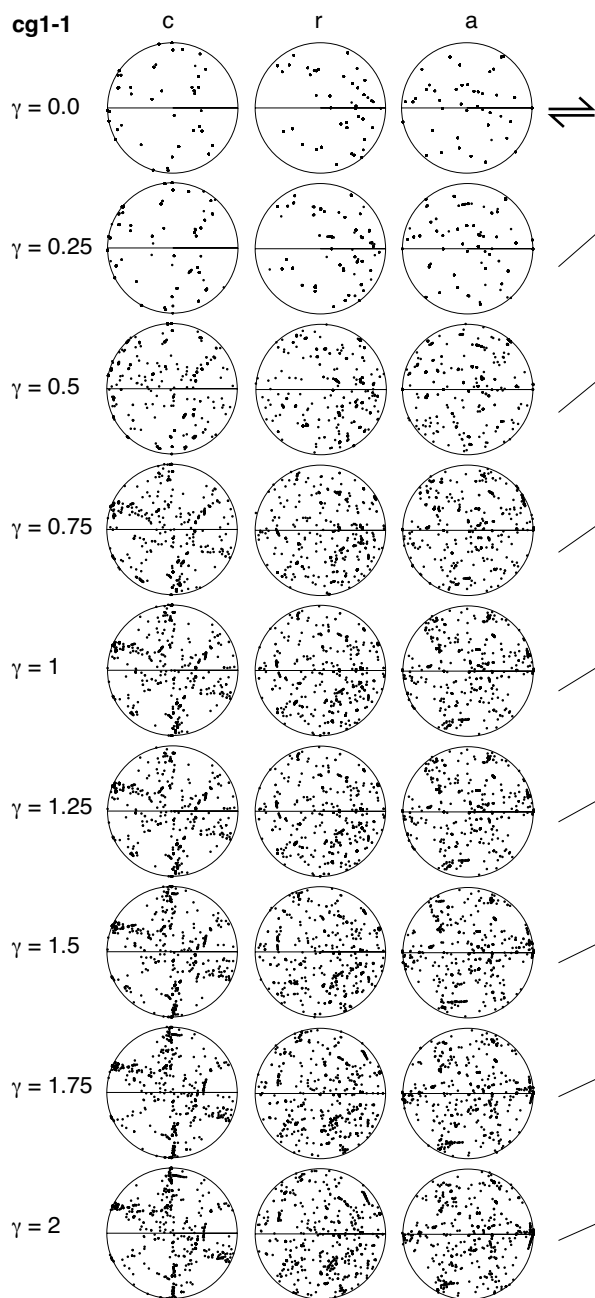


Figure 3.35 Crystallographic orientation of the c-, r- and a-axes during progressive deformation (simulation cg1-1). The shear plane is oriented E-W. For each stage the orientation of the line of maximum finite elongation is shown as a tick mark next to the lower hemisphere equal area projections. With progressive deformation a preferred crystallographic orientation of c-axes with a crossed girdle develops. At high strain clusters of c-axes following a great circle are seen. These are rotated subgrains of large remaining grains. Projections of a-axes show the development of 6 weakly developed maxima that are oriented 60° to each other.

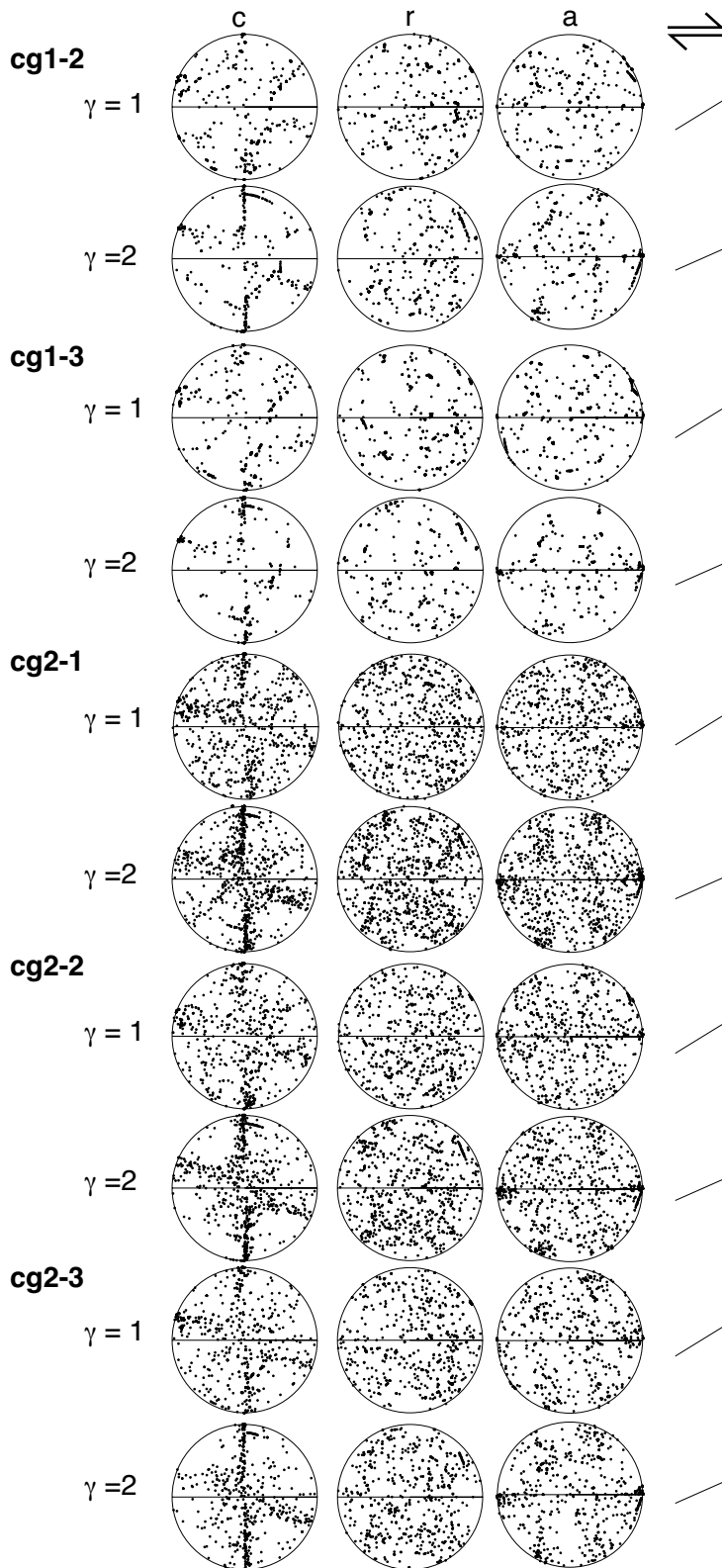


Figure 3.36 Crystallographic orientation of the *c*-, *r*- and *a*-axes during progressive deformation for simulations *cg1-2*, *cg1-3*, *cg2-1*, *cg2-2*, *cg2-3*. The shear plane is oriented E-W. For each stage the orientation of the line of maximum finite elongation is shown as a tick mark next to the lower hemisphere equal area projections. With progressive deformation a preferred crystallographic orientation of *c*-axes with a crossed girdle develops. At high strain clusters of *c*-axes following a great circle are seen. These are rotated subgrains of large remaining grains. These clusters and the crossed girdle configuration are only weakly developed in simulations with high GBMob (*cg1-3*, *cg2-3*). Projections of *a*-axes show in most cases the development of two main maxima on the horizontal. They are most pronounced for simulations *cg2-1* and *cg2-2*.

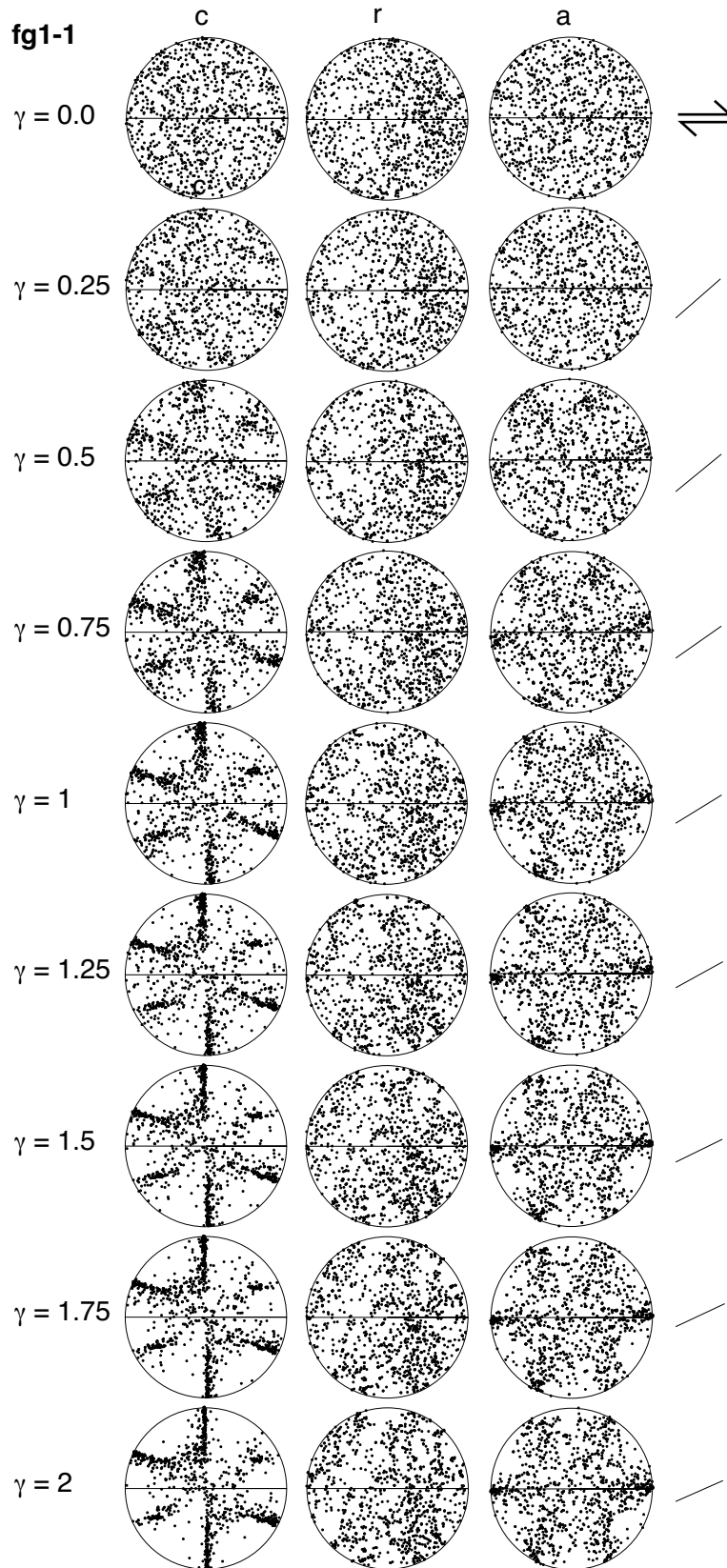


Figure 3.37 Crystallographic orientation of the c-, r- and a-axes during progressive deformation (simulation fg1-1). The shear plane is oriented E-W. For each stage the orientation of the line of maximum finite elongation is shown as a tick mark next to the lower hemisphere equal area projections. With progressive deformation a preferred crystallographic orientation of c-axes with a crossed girdle develops. There are also 2 noticeable maxima at an angle of 40-60° to the girdle maxima. Projections of a-axes show the development of 6 weakly developed maxima that are oriented 60° to each other, whereby the two maxima on the E-W line are most pronounced.

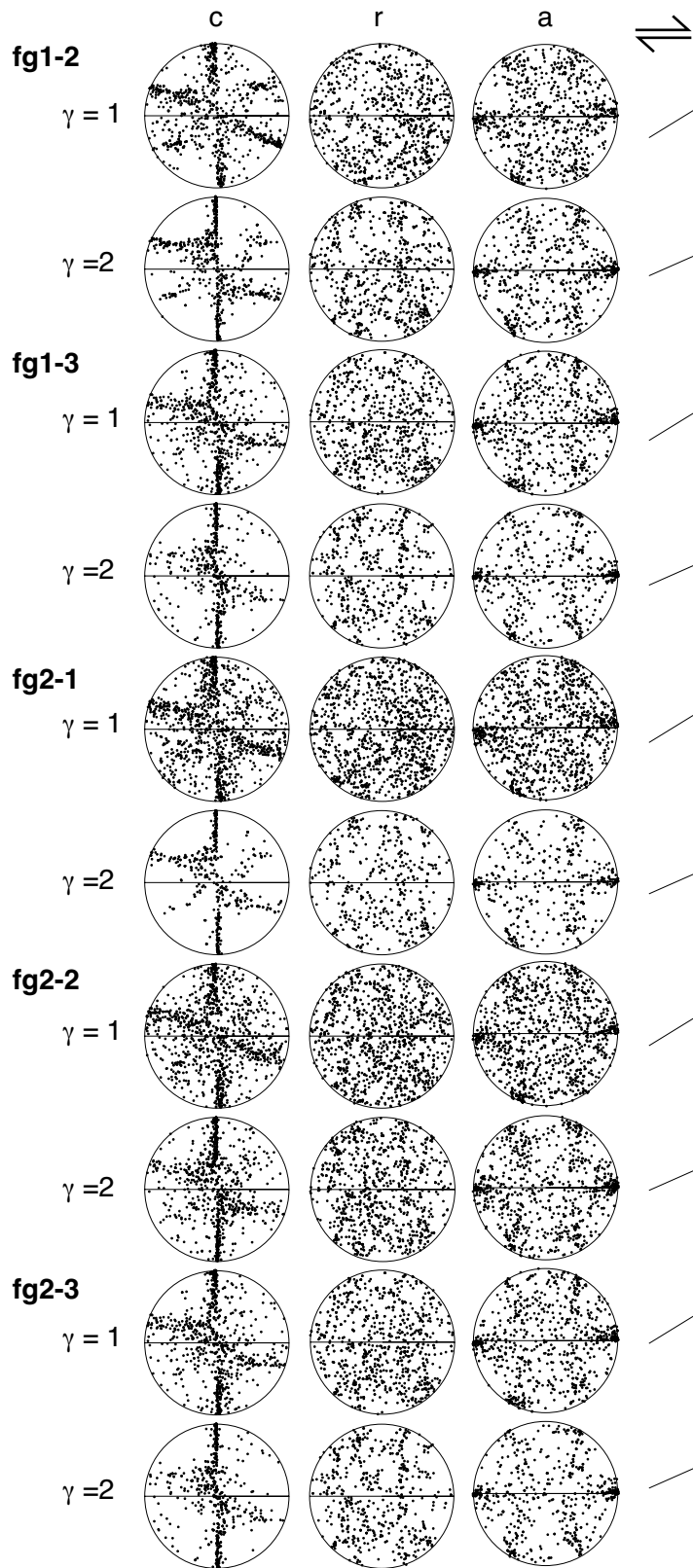


Figure 3.38 Crystallographic orientation of the *c*-, *r*- and *a*-axes during progressive deformation simulations fg1-2, fg1-3, fg2-1, fg2-2, fg2-3. The shear plane is E-W oriented. For each stage the orientation of the line of maximum finite elongation is shown as a tick mark next to the lower hemisphere equal area projections. With progressive deformation a preferred crystallographic orientation of *c*-axes with a crossed girdle develops. Here, clusters along the vertical are most pronounced. In simulations with high GBMob (cg1-3, cg2-3) the prominence of crystallographic axes projected along the N-S orientation is very pronounced. Projections of *a*-axes show the development of 6 weakly developed maxima that are oriented 60° to each other, whereby the two maxima on the E-W line are most pronounced.

3.4.4.2.6 Grain boundary hierarchy – absolute length and ratio of low ($<10^\circ$) and high angle boundary ($\geq 10^\circ$) lengths per unit area

The length of low angle boundaries remains quasi constant in experiments with low RX_{nucl} . In initially coarse grained fabrics the length of low angle boundaries is generally higher than in initially fine grained fabrics, and low angle boundary length show higher values with high RX_{nucl} than with low RX_{nucl} (Fig. 3.39).

The length of high angle boundaries increases with increasing strain in all experiments except at high $GBMob$ (Fig. 3.40). Simulations with high $GBMob$ show generally short total high angle boundary lengths. At low RX_{nucl} values are higher than at high RX_{nucl} if an initially coarse grained fabric is deformed. In initially fine grained fabrics, the high angle boundary length generally increases with increasing strain, except at high $GBMob$.

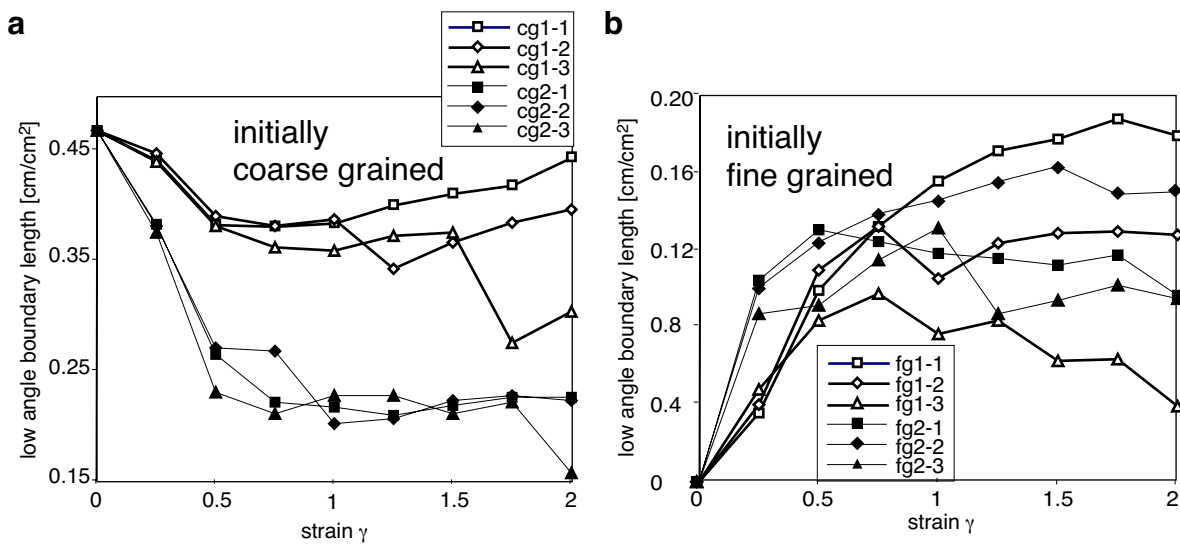


Figure 3.39 Total length of low angle boundaries with increasing strain. (a) Simulations with initially coarse grained microstructure. (b) Simulations with initially fine grained microstructure.

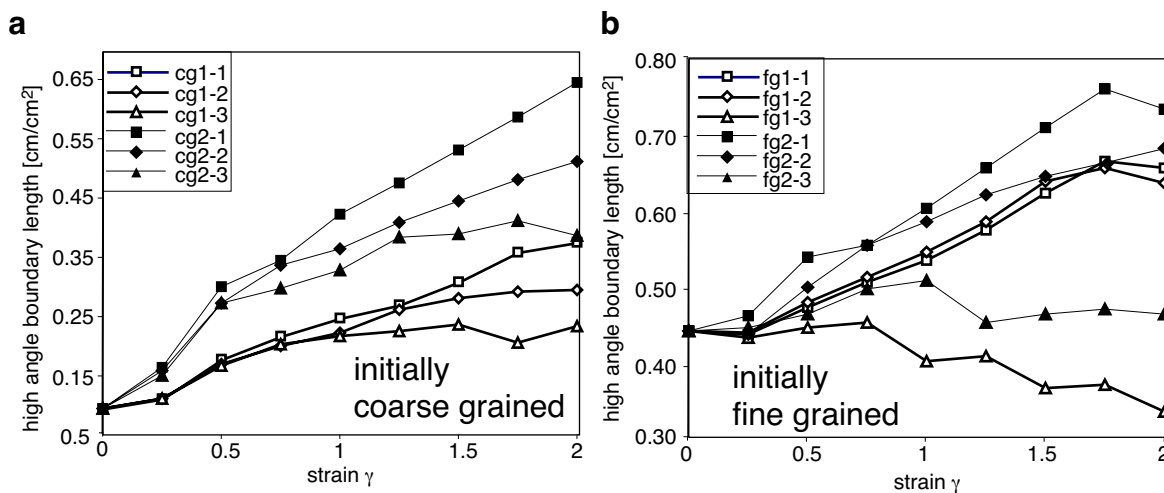


Figure 3.40 Total length of high angle boundaries with increasing strain. (a) Simulations with initially coarse grained microstructure. (b) Simulations with initially fine grained microstructure.

The ratio low to high angle boundary length (R_{gbl}) is in most experiments nearly constant for $\gamma > 1$ (Fig. 3.41). R_{gbl} is primarily dependent on the initial grain size of a microstructure. Initially coarse grained fabrics exhibit significantly higher values than initially fine grained fabrics. Additionally, R_{gbl} is strongly influenced on RX_{nucl} in initially coarse grained fabrics. Here, R_{gbl} values in experiments with high RX_{nucl} are above 1 and distinctively different (nearly one order of magnitude) to the values of simulations with low RX_{nucl} , which are significantly below 1 (Fig. 3.41a). In fine grained fabrics such a clear distinction cannot be made (Fig. 3.41b). $GBMob$ values do not influence R_{gbl} .

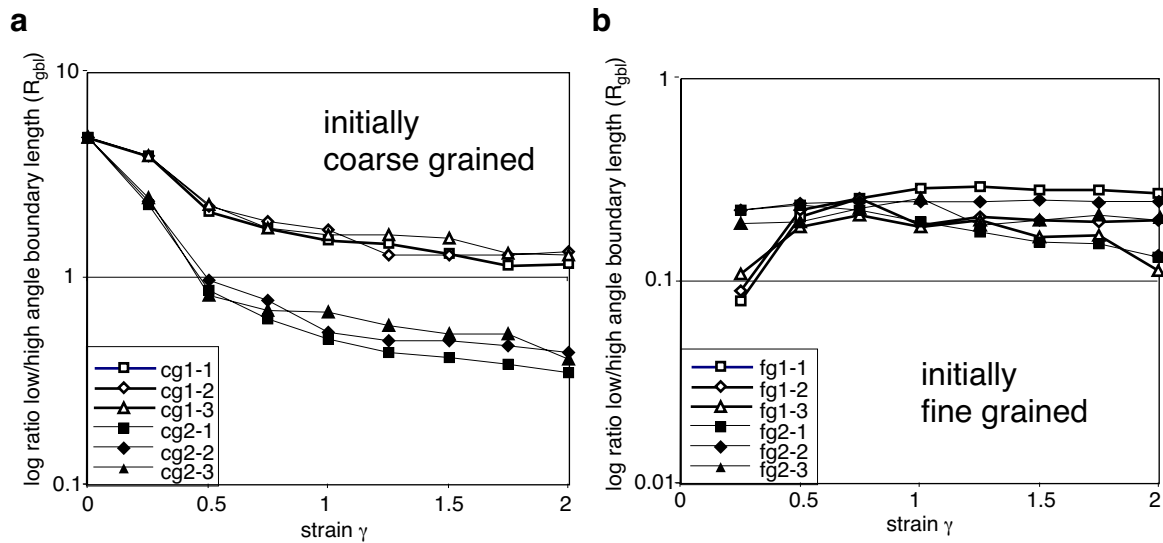


Figure 3.41 Change in the ratio of low to high angle length of high angle boundaries (R_{gbl}) with progressive deformation. (a) Simulations with initially coarse grained microstructure. (b) Simulations with initially fine grained microstructure.

3.4.4.2.7 Grain boundary distance plots

Grain boundary distance plots in the x' and y' direction of the simulated fabrics (gbd-plots) show similar features as those described in section 3.4.4.2.1 and 3.4.4.2.2 (Fig. 3.42, Fig. 3.43). However, these features are shown in one single plot and additional information is depicted. Gbd-plots show distinct patterns. These patterns are characterised by the number of frequency peaks, the individual and relative position of these peaks of both directions, the horizontal offset between peaks in both directions and the absolute and relative values of total frequencies per bin. In all experiments, patterns of low and high $GBMob$ are very similar for both high and low RX_{nucl} . Differences arise in the frequency of grain boundary distances. In all experiments the frequencies of distances in the y' direction is smaller in simulations with high $GBMob$ than with those with low $GBMob$. In most simulations with low $GBMob$ the highest frequency of grain boundary distances in the y' direction are seen in the lowest length range if $0.5 < \gamma < 2$. High $GBMob$ result the occurrence of peak frequencies in the second smallest bin. The shift of peak frequencies of y' direction grain boundary distances while peak frequencies

in the x' direction remain constant point to a marked shape fabric in simulations with low $GBMob$ with progressive deformation. In the x' direction the range of values increases with increasing strain and $GBMob$. Lower frequencies are seen at high RX_{nucl} than at low RX_{nucl} . For all experiments F_{xy} values depend on $GBMob$. At low $GBMob$ F_{xy} are low (0.08-0.11) and at high $GBMob$ high (0.18-0.21). A bimodal grain size distribution develops in the x' and y' direction in coarse grained fabrics, if $GBMob$ is high (Fig. 3.43). In initially fine grained fabrics only one distinct peak is present.

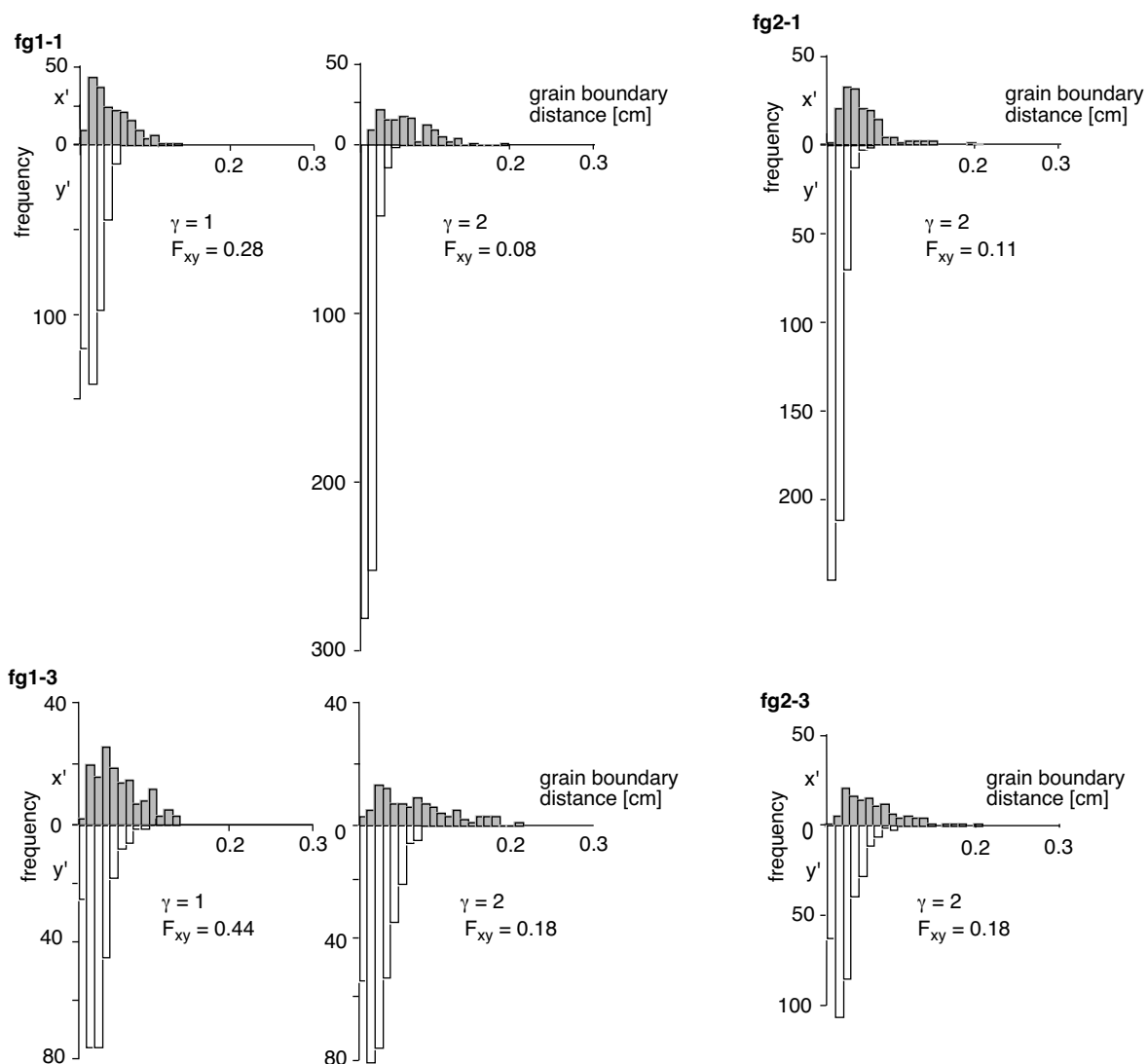


Figure 3.42 Graphs depicting the change in gbd plot pattern of selected initially fine grained fabrics with finite strain (for further details see text; section 3.3.2 and section 3.4.4.2.7). Additionally, the ratios of the peak frequencies in the x' and y' directions F_{xy} are given.

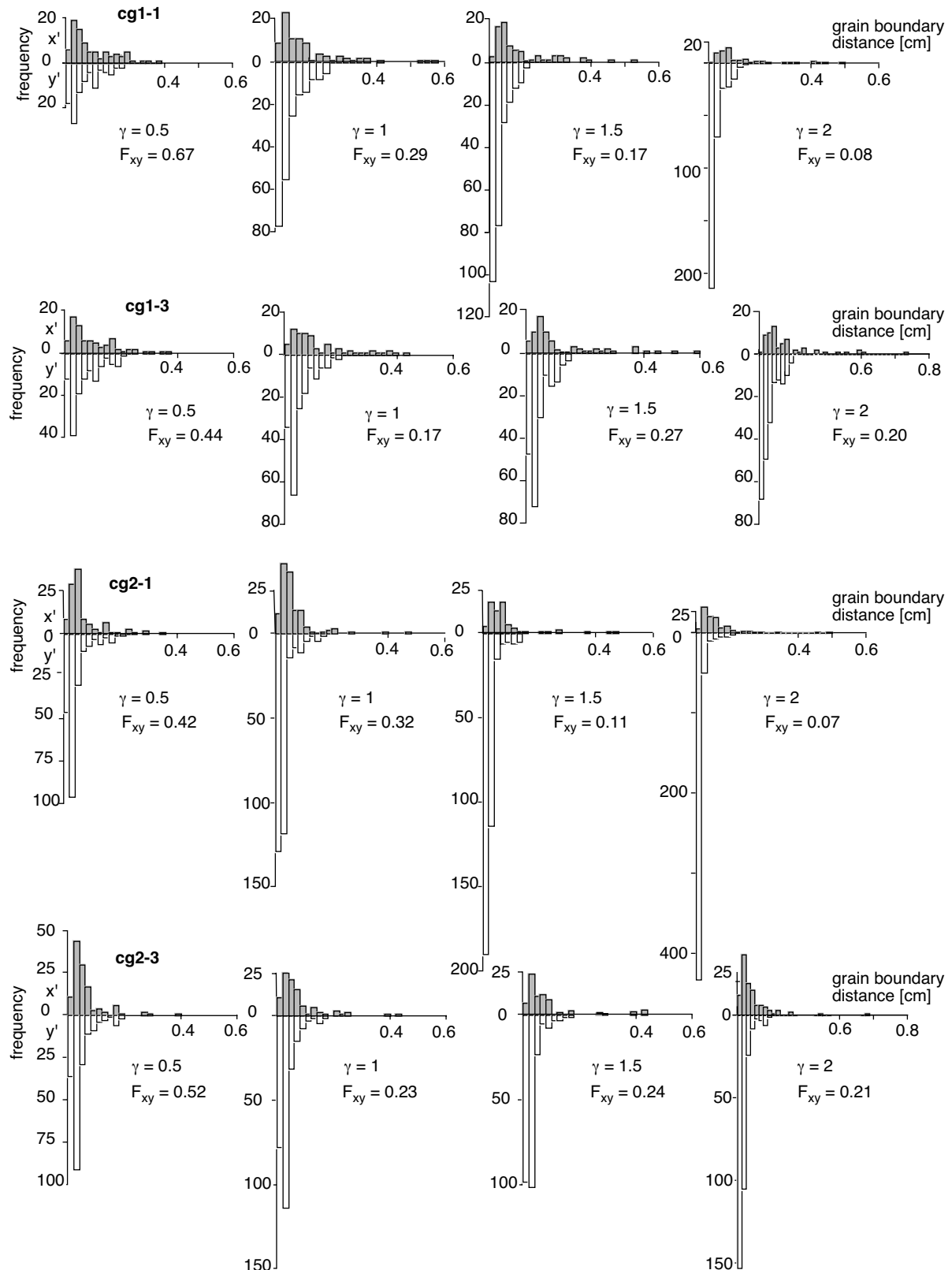


Figure 3.43 Graphs depicting the change in gbd plot pattern of selected initially coarse grained fabrics with finite strain (for further details see text; section 3.3.2 and section 3.4.4.2.7). Simulation runs with the same GBMob values show similar patterns regardless of the threshold values for recrystallization by nucleation. Additionally, the ratios of the peak frequencies in the x' and y' directions F_{xy} are given.

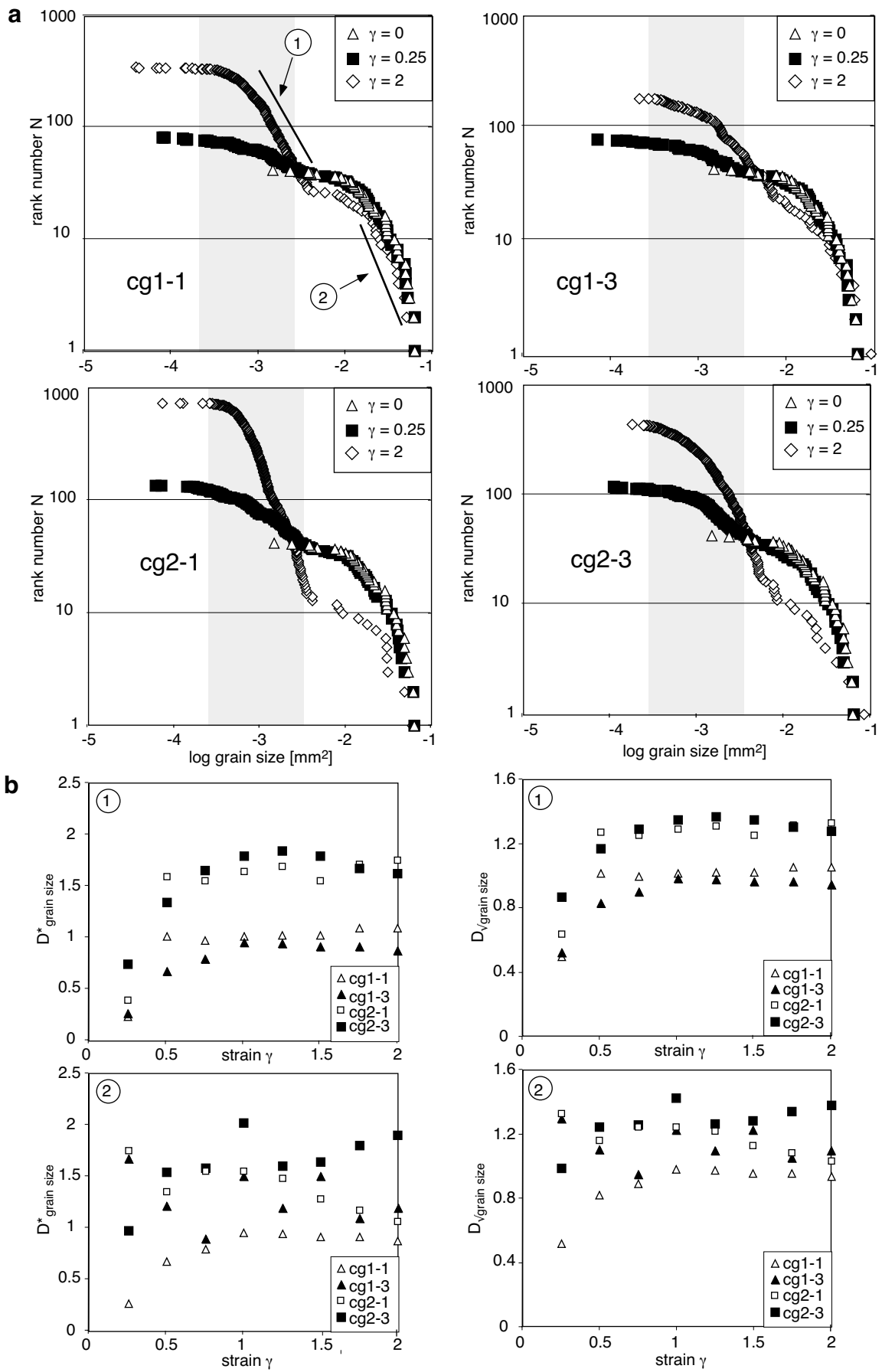


Figure 3.44 (opposite page) (a) Logarithmic plots of grain size against rank number N of selected simulations with initially coarse grained microstructure. Grey field signifies the range of initial size of subgrains ($MinArea < subgrain\ area < MaxArea$). (b) Measured fractal dimensions $D^*_{grain\ size}$ and $D_{sqrt(grain\ size)}$ against increasing strain. Numbers 1 and 2 (in circles) correspond to fractal trends as shown in (a).

3.4.4.2.8 Grain size distributions plotted in log-log diagrams

In two sets of fractal dimensions develop with increasing strain in initially coarse grained fabrics (Fig. 3.44). One fractal trend ((1) in Fig. 3.44a) is seen in a grain size range that closely corresponds to the range of allowed subgrain sizes ($MinArea < subgrain\ size < MaxArea$). In simulations with high $GBMob$ this range is extended to higher grain size values. The other fractal trend ((2) in Fig. 3.44) is seen in the grain size range of the initially coarse grains. At a grain sizes above 10^{-2} mm^2 the fractal dimension shows no trends (Fig. 3.44b). At low strain, the initial normal grain size distribution is distorted and the function exhibits no power law trends. In a grain size range of approximately $1 \cdot 10^{-3}$ to $5 \cdot 10^{-4} \text{ mm}^2$ ((1) in Fig 3.44) the fractal dimension is a function of RX_{nucl} . At low RX_{nucl} the fractal dimension is significantly higher than for high RX_{nucl} values (Fig. 3.44b). $GBMob$ does not influence the fractal dimensions.

In initially fine grained fabrics a normal grain size distribution is seen in all experiments (Fig. 3.45).

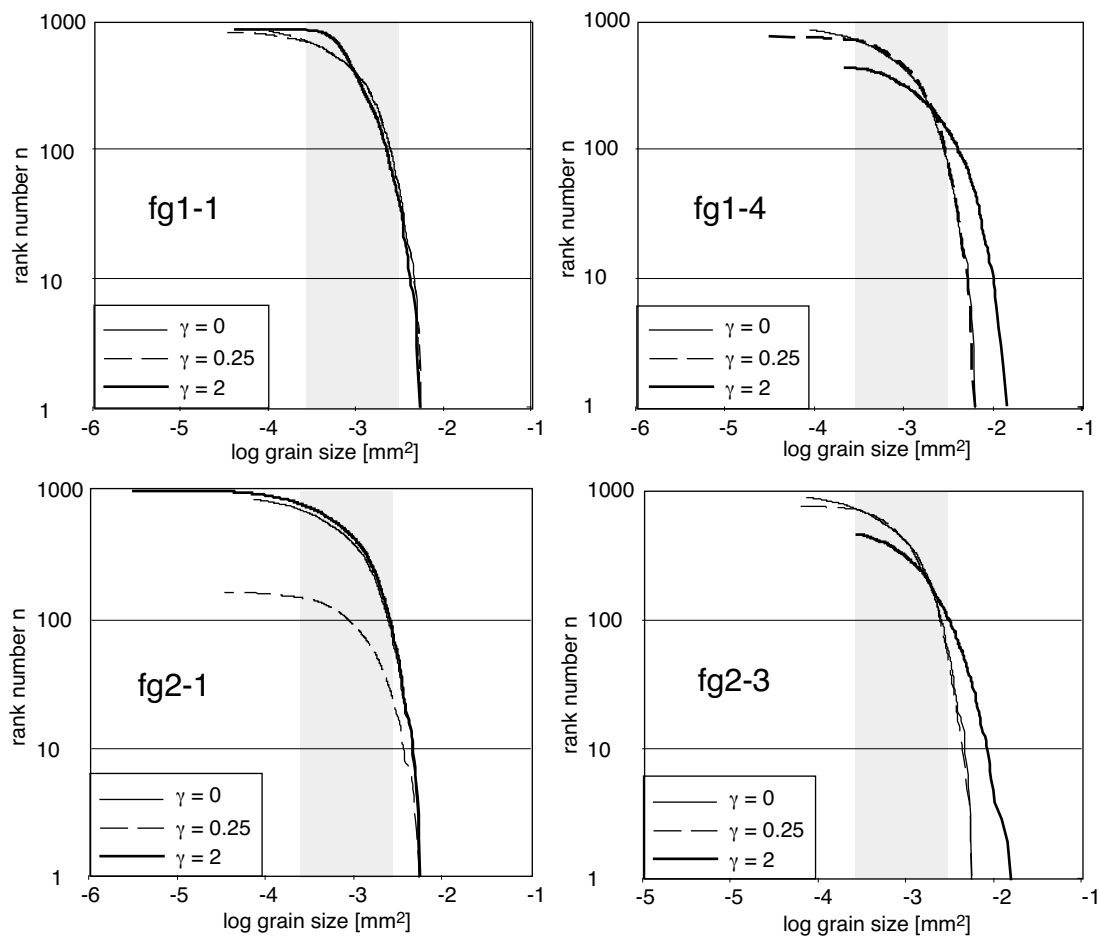


Figure 3.45 Logarithmic plots of grain size against rank number N of selected simulations with initially fine grained microstructure. Grey field signifies the range of initial size of subgrains. No straight line is seen in graphs, hence the grain size distribution is not a power law distribution.

3.4.5. Discussion of simulations

3.4.5.1 Microstructures indicative for initial fabric, values of RX_{nucl} and $GBMob$

Initially coarse grained microstructures show microstructure with a few large and elongated grains in a matrix of small recrystallized grains. Grain size distributions are power law functions in part of the grain size range. The ratio low/high angle boundaries is between 0.7 and 2. In all experiments, with initially coarse grained microstructures distinct gbd-plot patterns develop. They show several frequency peaks in the x' and y' directions whereas in initially fine grained microstructures only one distinct peak develops. The horizontal offset between peaks in the two perpendicular directions is large in coarse grained microstructures; hence a strong shape fabric is present. In fine grained microstructures, grain size distributions are unimodal and the ratio low/high angle boundaries is always below 0.4. Only a weak shape fabric develops.

High $GBMob$ generally result in low aspect ratios and increasing mean grain sizes with progressive deformation. High angle boundary lengths, total dislocation density values and viscosity are low and decrease with progressive deformation. In gbd-plots, F_{xy} increases with increasing $GBMob$. Here, distinct patterns develop with only a slight offset between frequency peaks in the x' and y' direction, hence a weak shape fabric. The decrease in total dislocation density and therefore viscosity during progressive deformation is most pronounced at high $GBMob$.

Low RX_{nucl} values result in large sizes, slow decrease total dislocation density and distinctly different R_{gbl} in initially coarse grained rocks. Fractal dimensions are higher in experiments with high RX_{nucl} than with low RX_{nucl} in initially coarse grained microstructures. In all experiments with low RX_{nucl} high frequencies are seen in gbd-plots.

3.4.5.2 Comparison of the microstructural development observed in simulations with natural examples and predictions from theory

3.4.5.2.1 Effect of initial fabric

As described above, in experiments to a finite strain of 2 the fabric development of a microstructure is significantly influenced by its initial grain size. In simulations of initially coarse grained microstructures strong shape fabrics develop (Fig. 3.25, Fig. 3.43), whereas in initially fine grained microstructures the shape fabric is weaker. Although in the model the microstructure is observed in the xy-plane and not in the yz-plane (cf. Fig. 3.5) as in Chapter 2, the general characteristics of the microstructural development can be extrapolated to the yz-plane. Low aspect ratios in the xy-plane correspond to low aspect ratios in the yz-plane if plane strain deformation is assumed and low viscosity ratios between different grains. If the latter assumption is true, also, the general characteristics of the grain size and grain boundary distance distributions can be assumed to be similar in both observation surfaces. Therefore, the findings of a strong effect of the ratio of initial to recrystallized grain size on fabric development seen in the field (Chapter 2) is supported by experiments.

3.4.5.2.2 Effect of grain boundary mobility values

In general, the effective mobility of a boundary is a function of temperature, whereby at higher temperatures the mobility increases (Eq. 3.11). Accordingly, fabrics seen in simulations at high grain boundary mobility should simulate fabrics seen in rocks undergoing deformation at higher metamorphic grade than those with low mobility values. In simulations with low

GBMob, microstructures closely resemble textures observed in low grade rocks. Typical features are aggregates of small, dynamically recrystallized grains with non-bulging boundaries around a weakly flattened, near-spherical, weakly undulose crystal core i.e. core and mantle structure (Passchier 1982; Passchier and Simpson, 1986). Large grains show subgrains in the same grain size range as small recrystallized grains (Regime I of Hirth and Tullis, 1992; Urai et al. 1986; Drury and Urai, 1999, Takeshita et al., 1999; Shigematsu, 1999; Heidelbach et al., 2000). With medium *GBMob* simulated fabrics generally correspond to microstructures seen in medium grade rocks which have undergone dynamic recrystallization. Typical features are flattened grains, undulose extinction, core and mantle structures with flattened grain as a core and irregular grain boundaries. These features are characteristic for low to medium temperatures. (Regime II of Hirth and Tullis, 1992; Urai et al., 1986; Drury and Urai, 1990). Large grain sizes, low aspect ratios, bulging grain boundaries and "left over grains" are seen in simulations with high *GBMob*. These microstructural features have been observed in high temperature microstructures in naturally deformed rocks (Jessell, 1987), amphibolite facies shear zones (Fig. 3.22) and high temperature experiments (Regime II of Hirth and Tullis, 1992; Drury et al., 1985; Urai et al., 1980, 1986). Accordingly, the value of low, medium and high grain boundary mobility seem to approximate reasonably well the effective mobility at greenschist, lower amphibolite and amphibolite facies rocks. It should be noted, though, that at lower strain rate the rate of recrystallization will decrease and therefore the dominance of grain boundary mobility will in relation increase; thus, at low strain rates similar microstructures to high grade mylonite may develop in low grade mylonites (Hirth and Tullis, 1992).

3.4.5.2.3 Effect of recrystallization rate in terms of recrystallization by nucleation and rotational recrystallization

Low values of RX_{nucl} result in a high degree of dynamic recrystallization (cf. section 3.4.4.2.3 and Fig. 3.31) and development of microstructural features attributed to the dominance of recrystallization by nucleation and rotational recrystallization. Such characteristic features are subgrain formation at the rim of large boundaries, few remaining large grains in initially coarse grain rocks and a unimodal grain size distribution in fine grained rocks. Similar features are described to be typical for high strain rate and low temperature (Regime I of Hirth and Tullis, 1992; Drury and Urai, 1990). Features observed at low RX_{nucl} values are expected to correspond to natural features developed at high strain rate because high strain rate result in the built up of high strain energy in grains, hence the recrystallization rate increases with increasing shear strain rate. This corresponds to simulated microstructures.

3.4.5.2.4 Crystallographic preferred orientation

It as been shown that the constituent mineral grains of plastically deformed materials commonly develop a crystallographic preferred orientation (see review of Law, 1990). Detailed analyses of quartz fabrics show that with progression in strain (shear zone boundary to shear zone centre), c-axes orientation develop from a random distribution to a cross girdle to a single girdle (e.g. Carreras et al., 1977; Simpson, 1983; Law, 1990 and references therein). In simulations, the random orientation of c-axis is only present at low strain. With increasing strain cross girdles develop whereby the basal plane is generally parallel to the flow plane and the a-axis orientation is parallel to the flow direction. This is similar to observations in nature (e.g. Carreras et al., 1977; Simpson 1983; Schmid and Casey, 1986; Law, 1990; Lloyd et al., 1992; Trimby et al., 1998; Stöckert & Duyster, 1999).

Observations in experiments with crystalline analogue material such as OCP (Ree, 1990) show that grains which are oriented with the basal plane subparallel to the shear direction, tend to deform without formation of subgrains and absence of recrystallization by rotation and by nucleation. A similar feature is seen in nature where grains that are in orientations where slip is easy may develop large subgrains in contrast to grains which are in orientations where slip is extremely difficult. These latter grains are characterized by enhanced subgrain formation and rotational recrystallization (Knipe and Law, 1987). The same feature is seen in simulations. In initially coarse grained fabrics, large, remaining grains exhibit markedly lower dislocation densities, hence lower stored strain energy, than the surrounding fine grained matrix (Fig. 3.33). These large grains show an initial preferred crystallographic orientation that is with the easy slip basal [a] plane subparallel to the flow plane (blue colours in euler_angle movies; Appendix F). They deformed easily, the rotation rates of the crystallographic axis were low and only few dislocations were built up during progressive deformation. Therefore, no rotational recrystallization of subgrains to grains at the rims of the large grains and no subgrain recrystallization by nucleation did occur.

Another feature observed both in rocks and simulations is the development of cluster of subgrains with c-axis orientations following a great circle (Fig. 3.35, Fig. 3.36; Lloyd and Freeman, 1994). In nature and simulations, these develop from progressive rotation of subgrains of large "parent" grains.

Although a high number of new grains with a random crystallographic orientation form during progressive deformation, a well defined crystallographic orientation develops in simulations with low RX_{nucl} . This points to a quick adjustment of the crystallographic orientation of these grains.

3.4.5.2.6 Dominance of certain processes involved in dynamic recrystallization

A general classification of recrystallization microstructures seen in rocks is based on the dominance of active mechanisms (e.g. Urai et al., 1986; Urai and Drury, 1990). These are (a) subgrain rotation microstructures and (b) grain boundary migration microstructures. Microstructures developing from subgrain rotation recrystallization are in general characterized by clusters of grains having similar orientation. Variations in orientation should proceed more or less smoothly across the cluster, or in an ABAB fashion as in microfolding. Local deviations from this smooth pattern of misorientation due to heterogeneously strained grains seems to be rather common. Recrystallized grain size should be more or less equal to the optically visible subgrain size (Urai et al., 1986).

Grain boundary migration microstructures often show irregular grain shapes. One grain bulges into the neighboring grain, and "old" grains are being consumed by new grains with low dislocation density (e.g. Urai et al., 1986; Jessell, 1987; Drury and Urai, 1990). These features correspond to the observed microstructures in simulations.

Typical subgrain rotation microstructures are seen in simulations with low $GBMob$ and low RX_{nucl} and grain boundary migration microstructures in simulations with high $GBMob$ values (cf. section 3.4.5.2.2).

Closely linked with the dominance of specific processes is the concept of a steady state microstructure (Means, 1981). Such a microstructure can only develop if effects of competing processes, for example, processes which reduce the mean grain size and those which results in an grain size increase are balanced according to the general relationship

$$(\delta A/\delta t)_{\text{process1}} + (\delta A/\delta t)_{\text{process2}} + \dots = 0 \quad (\text{Eq. 3.34})$$

Recrystallization by nucleation together with rotational recrystallization and grain boundary migration are such competing processes. Recrystallization by nucleation together with rotational recrystallization generally results in a reduction of grain size and increase in the numbers of grains. In contrast, grain boundary migration generally results in an increase in grain size, reduction of the number of grains and generation of round, bulging grain boundaries (e.g. Jessell, 1987). No steady state microstructure developed in the simulations. This could be due to the current limit of the simulations to a maximum finite strain of two. Probably higher strain than that simulated ($\gamma = 2$) is needed to develop a steady state microstructure.

3.4.5.3 Implication of results of simulations for the interpretation of microstructures in rocks

3.4.5.3.1 Dynamic recrystallization microstructures: Result of several concurrent processes

As stated above, recrystallization by nucleation together with rotational recrystallization and grain boundary migration are competing processes. In most simulations the effect of one the processes dominate the microstructural development and accordingly microstructural characteristics change with progressive deformation. In all simulations the modelled concurrent processes are "active", but microstructures are dominated by the effects of specific processes according to the values of associated parameters such as *GBMob*. In some cases, the effects of less dominant processes will be largely obliterated by the dominant process, although the less dominant process still influences the microstructure. This should be taken into account when interpreting microstructures in terms of active processes.

3.4.5.3.2 Use of detailed analyses of grain size distributions

The fact that fractal dimensions of grain size distributions in simulations with high RX_{nucl} are higher than those with low RX_{nucl} (Fig. 3.44) could be used as an indicator for RX_{nucl} values, rates of recrystallization and dominance of processes. To refine the use of the value of the fractal dimensions, a larger number of experiments need to be performed.

3.4.5.3.3 Use of dynamic recrystallization grain size as an indicator for stress

Recrystallized grain size can be used as a measure of stress (e.g. Twiss, 1977; Christie et al., 1980; Kronenberg and Tullis, 1984). In these studies, it is assumed that the recrystallized grain size is exclusively related to the imposed stress. However, Urai et al. (1986) already pointed out that the use of recrystallized grain size as a measure for flow stress can be complicated. The size of recrystallized grains produced by different mechanisms, e.g. rotational recrystallization and grain boundary migration may be different at the same flow stress (Poirier and Guillopé, 1979; Guillope and Poirier, 1979). As has been shown in simulations, the temperature dependence of grain boundary mobility has a direct effect on the recrystallized grain size. This is in accordance with experimental results of de Bresser et al. (1998) and considerations of Derby and Ashby (1987). Therefore, to derive flow stress values from recrystallized grain size, the temperature dependence of the grain size has to be taken into account. Further simulations may be helpful to quantify the temperature dependence of recrystallized grain size.

3.4.5.3.4 Flow laws and shear zone formation

In all simulations the total dislocation density and viscosity decrease with increasing strain. This supports the suggestion of Tullis and Yund (1985) and Rutter (1999) who attribute shear zone formation to the onset of dynamic recrystallization. Once dynamic recrystallization starts to take place in a rock, the rock becomes softer i.e. strain softening occurs. As a result strain is localized in this area and a shear zone develops. Experiments show that the flow laws of a monomineralic rock are affected by parameter values with respect to the rate and mode of dynamic recrystallization. High *GBMob* results in a pronounced decrease of the total dislocation density and therefore viscosity with progressive deformation. Accordingly, at medium to high temperature conditions strain localization would be expected to be more common than at low grade conditions. Additional sets of simulations are needed to confirm this preliminary result.

3.5 Discussion of numerical model and analytical techniques

3.5.1 The Numerical model

3.5.1.1 Validity of the model

In the previous sections, it has been shown that microstructures developed in simulations resemble those seen in rocks. Additionally, differences in the microstructural development due to different parameter values fit well with predictions derived from observations in nature and experiments. This suggests that the numerical model for dynamic recrystallization can adequately simulate the development of microstructures in rocks that undergo dynamic recrystallization. Consequently, algorithms describing the effect of an individual process on a microstructure seem to be a good approximation to effects of the corresponding process active in nature and values of parameters seem to correspond with true physical values. Additionally, the relative effects of different processes seem to be corresponding to natural relationships. The division of the flow law of dislocation creep in one part related to the work term of the Taylor Bishop Hill code and in one part related to the passive viscous deformation results in decrease in viscosity as expected from theory. Hence, this division is assumed to be suitable to simulated dislocation creep.

The fit of results of simulation with microstructures observed in rocks suggests that the method of discretization of a complex system of interacting, concurrent processes to a set of successive processes active in small time and length intervals (Eq. 3.1) can be used to model such a complex system.

3.5.1.2 Implications for geological processes and parameters assuming the validity of the model

In the model, it is assumed that the dislocation density is positively related to the work term calculated in the Taylor-Bishop-Hill code. The relationship between dislocation density and the work needed to deform a crystal along certain slip planes seems to be a good approximation to nature as simulated and natural microstructures correspond with each other. Especially, the preferred recrystallization at rims of large grains supports the assumptions made. According to this, in rocks a similar relationship between imposed stress, accumulation of new dislocations and retained, previously accumulated dislocations would be expected.

The algorithm of the movement of nodes due to the combination of surface energy and energy due to dislocations seems to be appropriate to model natural grain boundary migration (see also test experiments described in Appendix C3). Thus, the values of the energies involved seem to be well chosen. Microstructures developed in simulations with low $GBMob$ and low RX_{nucl} show typical microstructures for greenschist facies conditions. Therefore, these values may be relevant to low grade conditions. Therefore, the lowest $GBMob$ ($1 \cdot 10^{-12} \text{ m}^2\text{s}^{-1}\text{J}^{-1}$) seem to be a good approximation for the effective grain boundary mobility M at greenschist facies conditions. The other two $GBMob$ values seem to adequately describe M for lower amphibolite and amphibolite facies conditions. Another set of experiments with adequate CRSS valid for higher grade conditions have to be performed to confirm this preliminary result.

Different threshold values for recrystallization by nucleation (ELLE_NUCLXX), hence the dominance of ELLE_NUCLXX, affect the microstructural development of a fabric in characteristic ways. Nevertheless, these effects are hard to delineate with conventional microstructural techniques and might not have been recognized before in analyses of natural microstructures. Further research in this direction may yield new indicative microstructures to determine the importance of this process in rock samples.

3.5.1.3 Possible use of the numerical model for further investigations

With this new model, it is now possible to systematically investigate the effect of different mechanism on a microstructure and the interaction between different processes. Additionally, extrinsic and intrinsic parameters can be changed in simulations. We have now a tool to forward model a microstructure, perform analyses and compare results with natural samples and interpret observed microstructures accordingly. Direct comparison of simulated microstructures and those developed in experimentally deformed samples is possible as the range of possible strain in simulations and rock experiments are similar. Additionally, new analytical techniques can be developed, as in simulations a large database (e.g. complete set of grain size, crystallographic orientation, dislocation density, viscosity, misorientation between grains etc.) is provided with which new techniques can be readily tested. It should be noted that all along, validity tests should be performed (similar to those test described in Appendix C3) to ensure the validity of simulations.

3.5.2 Analytical techniques

The three new analytical techniques (R_{gbl} -plots, gbd-plots, grain size distribution analyses; section 3.3) proved to be suited to (a) compare observed microstructures in detailed, (b) describe microstructures quantitatively. Additionally, these technique could potentially be used to derive parameter values and to delineate dominance of processes involved.

The ratio of low/high angle boundary lengths (R_{gbl}) can be used to distinguish between microstructures with different initially fabrics and low and high RX_{nucl} in coarse grained fabrics. Further investigation of parameters e.g. threshold values for subgrain formation or CRSS may yield indicative R_{gbl} values for specific parameter values.

Grain boundary distance-plots are easily generated with image analysis techniques (e.g. macro in NIH-Image). Such plots provide the geologist with a good presentation of the fabric of a rock that show, at one glance, several pieces of information. Application of gbd-plots to simulated microstructures show that distinct gbd-plot patterns and F_{xy} values are indicative for

specific *GBMob*. Comparison of gbd-plots of simulated microstructures and natural examples may help to derive relative grain boundary mobility and threshold values for recrystallization by nucleation. In order to do so, it is necessary to normalize the grain boundary distance values. This could be done by normalizing the distances to the total length of grid lines used.

Gbd-plots are not restricted to microstructural analyses of mylonites only. They could also be used in igneous geology to characterize flow fabrics and crystal distributions in layered sequences. In these cases, perpendicular sets of analysis lines could, for instance, be chosen to be perpendicular and parallel to the magma chamber wall or settling front. Characteristic gbd-plot patterns in combination with theoretical considerations might yield insights in flow and crystal settling mechanisms. In metamorphic petrology, this technique could be used to get a picture of the spatial distribution of different mineral species, which could in turn be applied to diffusion models etc.. Here, analysis line orientations could be perpendicular and parallel to a contact aureole, different rock type boundaries or corona around a specific phase. Further research is needed to test the applicability of the technique and its value for fabric analysis in different geological disciplines.

Fractal dimensions of the observed power law grain size distributions in initially coarse grained fabrics seem to change systematically with different RX_{nucl} values. Therefore, it is suggested that analyses of properties such as grain size in terms of power law distributions may be used to quantify a microstructure if a power law distribution is present. Characteristics such as the fractal dimensions and intercept values may yield information about the relative dominance of different processes and may even be used to quantify certain parameter values (e.g. Marsh, 1988). Further research involving numerical modelling coupled with analysis of natural samples is needed to evaluate and establish the use of the characteristics of power law distributions, together with physical and theoretical concepts to quantitatively describe microstructures, delineate active mechanisms and quantify parameter values.

3.6 Conclusion

In this Chapter a new modelling technique was expanded, tested and applied to the geological problem posed in Chapter 2. Simulated microstructures resemble characteristic microstructural features observed in rocks and experimentally deformed rock samples.

Results from simulations and the findings and interpretation provided in Chapter 2 correspond with each other. The initial fabric of a rock significantly influences the mode at which recrystallization changes a microstructure and in this way strongly affects the development of a shape fabric. In fine grained monomineralic rocks only a weak shape fabrics and in coarse grained rock types strong shape fabric commonly develop. Therefore, the intensity of a shape fabric cannot directly be used to infer the intensity of strain.

Simulations with the numerical modelling system Elle proved to be useful to delineate microstructures typical for certain sets of parameter values and active mechanisms. Low grain numbers, low aspect ratios, large grain size, low fractal dimensions of grain sizes and high low/high angle boundary length ratios point to high grain boundary mobility values and dominance of grain boundary migration. Low threshold values for recrystallization by nucleation result in large grain numbers and low low/high angle boundary length ratios in initially coarse grained (high ratio of initial to recrystallized grain size) fabrics.

New analytical techniques such as the ratio of low/high angle boundaries, grain boundary distance plots and logarithmic plots of grain size distribution represent tools with which it is possible to accurately and quantitatively describe a microstructure. Further development of these techniques may result in tools with which it is possible to determine parameter values and the dominance of active processes.

Simulations indicate that the general assumption on which the numerical system Elle is based seems to be valid. A system of discretization of concurrent, interacting processes into distinct individual processes can be used to model the complex microstructural development of a rock.

With the numerical model developed to simulate dynamic recrystallization it is now possible to investigate the evolution of a microfabric in a systematic manner. In this model, processes can be turned off and on, parameter, temperature, pressure, strain rates varied and different initial fabric used. Accordingly, the influence of specific processes and a large set of variables can be studied and results compared to rock samples. The existing structure of the model allows to supplement the currently existing set of process algorithms with new process algorithms. By implementing new algorithms for processes, underlying concepts of these algorithms can be tested and if necessary modified. Simulations with a specific set of parameter values and active processes may result in the recognition of indicative microstructural characteristics, which can then be used to interpret natural microstructures.

A combination of numerical modelling, analysis of natural and experimentally deformed samples in combination with new quantitative analysis techniques will considerably improve our understanding of the coupling and dominance of different processes, and the influence of different parameters on an evolving microstructure. New insights from such a study have a potential to enable the geologist to describe and interpret microstructures in a quantitative manner and to recognize microstructures indicative for specific set of active processes and parameters.

Acknowledgments

S. P. wishes to thank the members of the Earth Science Department at Monash University, Australia for making facilities available used for this study. Special thanks to Lynn Evans and Mark Jessell for their continuous support not only during my stay in Australia but also in Germany via email. Cameron Blackwood (Monash University, Melbourne) is thanked for his assistance in setting up the computers and Vroni Tenzler (Graz) for helpful discussions regarding BASIL. This work was partly funded by the Deutsches Akademisches Auslandsamt Deutschland.

Tab. 3.2 Routine abbreviations and explanations

routine abbreviation	description of routine
BASIL	finite element code for viscous deformation
SYBIL	display program for BASIL output
ELLE_TBH	lattice rotation and workterm coupled with dislocation density calculation
ELLE_SPLIT	subgrain formation
ELLE_NUCLXX	recrystallization by nucleation
ELLE_ROTXX	rotational recrystallization
ELLE_GBM	grain boundary migration
ELLE_RECOVERY	annihilation of dislocations
ELLE_VISCOSITY	calculation of viscosity according to dislocation density and fluid activity
SHOWELLE	display program for Elle data files
ELLE_STATS	statistics of data derived from Elle data file
ELLE_CHECKANGLE	clean-up of computationally problematic mesh geometries

Tab. 3.5 Parameters changed

Abbrev.	initial fabric type	ratio of initial to recrystallized grain size R_ϕ (mean value)	minimum threshold for RX_{nucl} [Jm^{-2}]	grain boundary mobility $GBMob$ [$m^2 s^{-1}J^{-1}$]
cg1-1	coarse grained	48	$4.8 \cdot 10^5$	$1 \cdot 10^{-12}$
cg1-2	coarse grained	48	$4.8 \cdot 10^5$	$20 \cdot 10^{-12}$
cg1-3	coarse grained	48	$4.8 \cdot 10^5$	$40 \cdot 10^{-12}$
cg2-1	coarse grained	48	$3.8 \cdot 10^5$	$1 \cdot 10^{-12}$
cg2-2	coarse grained	48	$3.8 \cdot 10^5$	$20 \cdot 10^{-12}$
cg2-3	coarse grained	48	$3.8 \cdot 10^5$	$40 \cdot 10^{-12}$
fg1-1	fine grained	2.2	$4.8 \cdot 10^5$	$1 \cdot 10^{-12}$
fg1-2	fine grained	2.2	$4.8 \cdot 10^5$	$20 \cdot 10^{-12}$
fg1-3	fine grained	2.2	$4.8 \cdot 10^5$	$40 \cdot 10^{-12}$
fg2-1	fine grained	2.2	$3.8 \cdot 10^5$	$1 \cdot 10^{-12}$
fg2-2	fine grained	2.2	$3.8 \cdot 10^5$	$20 \cdot 10^{-12}$
fg2-3	fine grained	2.2	$3.8 \cdot 10^5$	$40 \cdot 10^{-12}$

Tab. 3.1 Symbols used

a	constant in ELLE_TBH	-	r_n	linear dimension of a fractal set	-
A	area of grain	m^2	RF'_{base}	recovery factor (material dependent) in ELLE_GBM	-
$Elle_area$	dimensionless area of polygon stored in Elle file	-	RF	effective recovery factor in ELLE_GBM	-
$Min\ Angle$	Minimum angle allowed in between boundary segments	$^\circ$	R_a	aspect ratio of ellipse calculated from orientation of grain boundaries	-
$MisorientAngle$	angle below which polygon boundaries are regarded as subgrain boundaries	$^\circ$	R_e	aspect ratio of strain ellipse	-
$MinArea$	minimum area of new subgrain	mm^2	R_{gbl}	ratio low/high angle boundary length per unit area	-
$MaxArea$	maximum area of new subgrain	mm^2	RX	energy threshold value for recrystallization by nucleation in ELLE_GBM	Jm^{-2}
$initial-Area$	area of polygon before node movement	m^2	RX_{nucl}	initial energy threshold value for recrystallization by nucleation (material dependent) in ELLE_GBM	Jm^{-2}
$newArea$	area of polygon after node movement	m^2	R_ϕ	ratio of initial to recrystallized grain size	-
A_{XX}	anisotropy of surface energy due to tilt angle between adjacent grains	-	M	grain boundary mobility in general sense	$m^2 s^{-1} J^{-1}$
A_α	anisotropy of surface energy due to crystallographic orientation of boundary in ELLE_GBM	-	M_0	base grain boundary mobility specific to a mineral species	$m^2 s^{-1} J^{-1}$
b	constant in ELLE_TBH	-	$Min-NodeSep$	minimum node separation	-
B	Boltzmann constant	JK^{-1}	$Max-NodeSep$	maximum node separation	-
$ b $	magnitude of the Burgers vector	-	$Switch-Distance$	maximum distance between joint triple nodes	-
c	constant in ELLE_NUCLXX	-	t	time	s
CRSS	critical resolved shear stress used in ELLE_TBH	-	t_{scale}	time scaling factor	-
C	constant of proportionality of a fractal set	-	T	temperature	$^\circ C$
d	factor used to calculated distance for trial displacement	-	Th_{split}	energy threshold for splitting in ELLE_GBM	Jm^{-2}
D	fractal dimension	-	r	radius of a sphere	m
D	chosen displacement for node movement in ELLE_GBM	m	V	molar volume of phase	$molcm^{-3}$
D_{trial}	trial displacement of node used in ELLE_GBM	m	v	velocity of grain boundary migration - general	ms^{-1}
e	constant in ELLE_RECOVERY	-	v_m	mean velocity of a dislocation segment	ms^{-1}
$ework$	work term in ELLE_TBH	-	v_{node}	velocity of node movement in ELLE_GBM	ms^{-1}
E_{stored}	strain energy stored in grain	Jm^{-2}	W_n	kinematic vorticity number	-
E_ρ	energy due to dislocation density in ELLE_GBM	Jm^{-2}	xx_factor	crystallographic misorientation factor in ELLE_GBM	-
$E_\rho(polygon)$	energy of a polygon due to dislocation density in ELLE_GBM	Jm^{-2}	α	angle between the long principal axis of the calculated ellipse and the shear plane	$^\circ$
$E_\rho(initial)$	initial energy of a polygon due to dislocation density in ELLE_GBM	Jm^{-2}	β	angle between the long principal axis of the strain ellipse and the shear plane	$^\circ$
$E_\rho(new)$	new energy of a polygon due to dislocation density in ELLE_GBM	Jm^{-2}	Δs	displacement per time step	-
$E_{\rho-trial}$	trial energy due to dislocation density in ELLE_GBM	Jm^{-2}	$\Delta\gamma$	strain per step	-
E_ϕ	overall surface energy in ELLE_GBM	Jm^{-2}	δ	critical misorientation angle- general	-
E_{trial}	trial energy in ELLE_GBM	Jm^{-2}	Π	tilt angle of c-axis of adjacent crystals in ELLE_GBM	-
E_{length}	surface energy due to length of boundary in ELLE_GBM	Jm^{-2}	ϵ	surface energy of phase (Gibbs-Thompson equation)	-
f	constant in ELLE_RECOVERY	-	$\dot{\epsilon}$	strain rate	s^{-1}
F	driving force	Jm^{-3}	$\dot{\gamma}_i$	finite strain	-
$Fluid_Factor$	factor describing the presence of H ₂ O at grain boundary	-	κ	frequency of obstacle jumps	s^{-1}
$F(\rho)$	available energy for subgrain formation	Jm^{-2}	ρ	density of mobile dislocations	m^{-2}
F_{xy}	ratio of number of values in the highest frequency bins of histograms of x-direction and y-direction of gbd-plots	-	ρ'	dislocation density of a polygon stored in Elle data file	m^{-2}
gbd-plots	grain boundary distance plots	-	$\rho'(initial)$	initial dislocation density of a polygon	m^{-2}
ΔG	Gibbs free energy of activation for by-passing of an obstacle	Jm^{-2}	$\rho'(new)$	new dislocation density of a polygon	m^{-2}
$GBMob$	grain boundary mobility in ELLE_GBM	$m^2 s^{-1} J^{-1}$	ρ_{energy}	dislocation energy	Jm^{-2}
$GBMob_0$	base grain boundary mobility in ELLE_GBM	$m^2 s^{-1} J^{-1}$	ρ'_{nucl}	dislocation density of newly nucleated grain	m^{-2}
H	activation energy	Jm^{-2}	ρ_{scale}	dislocation density scaling factor	m^{-2}
i	chemical component	-	τ_{scale}	stress scaling factor	Pa
l	length of boundary segment in ELLE_GBM	m	Γ	surface energy	Jm^{-2}
l_{scale}	length scaling factor	m	Γ_i	isotropic surface energy	Jm^{-2}
n	stress exponent of power law flow	-	Γ_a	anisotropic surface energy	Jm^{-2}
N_n	number of objects of fractal set	-	η	viscosity	$Pa s$
O	given vector for splitting direction in ELLE_GBM	-	η_{base}	base viscosity	$Pa s$
p	chosen vector for node displacement used in ELLE_GBM	-	μ	chemical potential	-
p_{trial}	random vector for trial walks used in ELLE_GBM	-	ζ	geometric factor (Gibbs-Thompson equation)	-
P	pressure	$kbar$	φ	tilt angle between two adjacent grains	i
P_{action}	probability function in ELLE_GBM	-	ν	frequency of obstacle jumps	s^{-1}
$QGBM$	grain boundary activation energy	$Jmol^{-1}$	σ	stress	Pa
			σ_b	grain boundary energy due to tilt angle between boundaries - general	Jm^{-2}

Chapter 4

Are polymers suitable rock-analogs?

Abstract

To evaluate if a polymer is suitable for analog modeling it is essential to know the rheological properties of the material. Polymers used in analog modeling exhibit a complex rheological behavior only part of which has been taken into account in most modeling studies. The mechanical behavior is strongly dependent on strain rate and temperature, and is characterized by specific dependencies of the storage and loss moduli, related to the elasticity and viscosity, on the deformation rate (frequency). We present a set of new data from measurements with an oscillatory parallel-disk rheometer obtaining the storage and loss moduli at a broad range of frequencies and strains. Investigated materials are polydimethylsiloxane (PDMS), mixtures of PDMS and BaSO₄ (filler), Rhodorsil Gomme and mixtures of Rhodorsil Gomme and plasticine, all commonly used in analog experiments. Our results show that mixtures of plasticine and Rhodorsil Gomme exhibit a dependence of the rheological properties with strain and therefore these mixtures are problematic for analog modeling. For mixtures of PDMS and BaSO₄, the significance of the elastic component increases with increasing filler content, accordingly these mixtures have a limited application for modeling of viscous deformation. Pure PDMS and Rhodorsil Gomme exhibit Newtonian flow behavior at strain rates commonly used in analog modeling.

4.1 Introduction

Polymers (e.g. Polydimethylsiloxane (PDMS)) and polymers with fillers (e.g. bouncing or silicone putties) in combination with other materials (e.g. sand) have been extensively used for analog modeling in geosciences for decades. Polymers have been applied in experiments modeling the development of small-scale structures in ductile shear zones (e.g. Ghosh and Sen Gupta, 1973; Fernandez et al., 1983; Ildefonse et al., 1992a, 1992b; Passchier and Sokoutis, 1993), medium-scale structures such as boudinage or mullions (e.g. Ramberg, 1955; Ghosh and Ramberg, 1976; Sokoutis, 1987; Kobberger and Zulauf, 1995) and strain variation in layers of different rheology (e.g. Treagus and Sokoutis, 1992), and large scale fold and fault structures (e.g. Dixon and Summers, 1985; Brun et al., 1994). In large-scale experiments polymers are commonly used to represent the ductile lower crust. Polymers are also used to model rising plumes, convection, magmatic fabric developments, and emplacement of igneous bodies (e.g. Whitehead and Luther, 1975; Nataf et al., 1984; Roman-Berdiel et al., 1995; Anma, 1997; Anma and Sokoutis, 1997; Donnadiou and Merle, 1998).

Several papers have been published in the geological literature which specifically or in parts investigate the physical properties of polymeric liquids and related materials (e.g. McClay, 1979; Dixon and Summers, 1985, 1986; Weijermars, 1986; Sokoutis, 1987; Treagus and Sokoutis, 1992; Kobberger and Zulauf, 1995). McClay (1976) and Kobberger and Zulauf (1995) performed constant strain rate, plane strain compression tests and concluded that the mechanical behavior of different types of plasticine is complex, but that after a certain amount of strain it is linear viscoelastic. Dixon and Summers (1985, 1986) used an annular shear rig to obtain rheological properties of a silicone putty. They have shown that the mechanical behavior of the silicone putty and the plasticine cannot be fully described by flow laws which are used to describe rock deformation (power-law flow, Newtonian flow, Bingham flow behavior). Sokoutis (1987) and Sokoutis and Treagus (1992) used a capillary (extrusion) viscometer and a concentric cylinder (Couette) viscometer. Weijermars (1986) performed additional measurements with a Stokes (falling-ball) viscometer and a Weissenberg cone and plate rheometer, for the investigation of the viscosity of polymeric analog materials (plasticine, Rhodorsil Gomme, polymers and mixtures). They reported changes in viscosity with strain rate. In all these studies no other rheological properties than effective viscosity were measured.

Geologists performing analog modeling need comprehensive information about the rheological character of a material to evaluate its suitability as a rock analog. However, the knowledge of the rheological properties of analog materials in the geological literature is strongly restricted to analyses of effective viscosity without specification of any other rheological quantities. Quantities such as the loss and storage moduli especially when determined in a broad range of deformation rates allow to determine the rheological character of a material (Nelson and Dealy, 1993).

We performed a series of rheological measurements on several commonly used polymers. Our results show that the mechanical behavior is complex and that some commonly used polymers are in fact problematic as analog materials for rocks.

In Tab. 4.1 (end of chapter) used symbols are listed

4.2 Structure and deformation of polymeric liquids

4.2.1 Structure and mechanical behavior of polymeric liquids

Polymeric materials used for analog modeling belong to the so-called thermoplastics. These are characterized by flexible linear chain-like macromolecules, which are formed by chemical binding of a number of small molecules (monomers). The polymer chains, when sufficiently long, are entangled and assume complex three dimensional structures. The mean form of the three dimensional structure can be characterized as a soft ellipsoid, the size of which is chain length dependent. In an undeformed system, the chains assume an equilibrium state with random orientation of their long axes (Winter et al., 1993). During deformation chains can reorient with their long axes preferentially directed towards the drawing direction, can straighten and finally can glide past each other (Fig. 4.1). When deformation ceases, chains tend to "relax" to their equilibrium state both by a form retraction and by a randomization of orientation. Therefore, polymers behave like an elastic material when a high stress is applied for a short time (less than the chain relaxation time) but like a viscous material when a low stress is applied for a long time (longer than the chain relaxation time). For a constant imposed strain, the initial elastic response is gradually converted into permanent viscous deformation and the associated stress decays with time (Maxwell model).

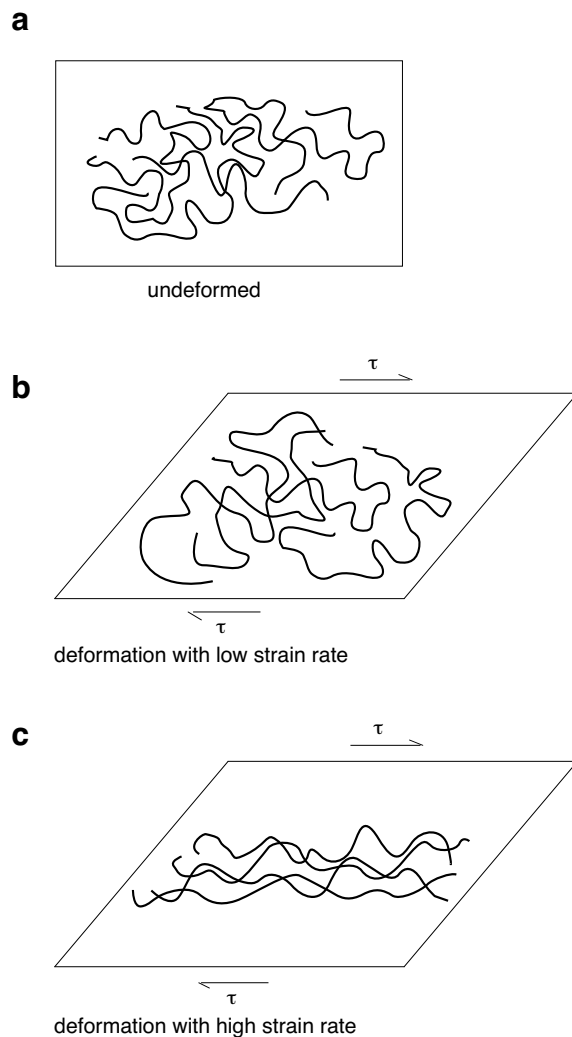


Figure 4.1 Sketch of chains of a polymeric liquid in (a) undeformed equilibrium state, (b) deformed state at low deformation rate relative to relaxation time of polymer chains, (c) deformed state at high deformation rate relative to relaxation time of polymer chains.

Such behavior is termed viscoelastic as it is characterized by a combination of elastic deformation and viscous flow. An important feature of viscoelastic materials is the time-dependence of rheological properties (Askeland, 1990).

At a certain range of deformation rates time-independent rheological properties may be observed for a given material but there certainly exists a range where the material will show time-dependent properties. Besides this time-dependence, properties of viscoelastic materials can be strain-independent, "linear" or strain-dependent, "non-linear". The term linear viscoelastic is used when during testing the material remains in equilibrium state and the rheological properties are not influenced by the conditions of testing, hence rheological properties are strain-independent. The term non-linear viscoelastic is used when the material structure is altered under observed conditions and consequently rheological properties are strain-dependent (Fig. 4.1).

4.2.2 Viscoelastic properties of polymers

4.3.2.1 Linear viscoelastic behavior

The properties of linear viscoelastic materials are usually described by the storage G' and loss G'' moduli, whereby the storage and loss moduli are representative for the elastic and viscous component, respectively (Nelson and Dealy, 1993).

These material properties are usually determined by applying sinusoidal shear strain of amplitude γ_0 and frequency ω to a sample. The shear strain as a function of time is

$$\gamma(t) = \gamma_0 \sin(\omega t) \quad (\text{Eq. 4.1})$$

and the corresponding shear strain rate

$$\dot{\gamma}(t) = \gamma_0 \omega \cos(\omega t) \quad (\text{Eq. 4.2})$$

If the response is linear, the resulting shear stress will also be sinusoidal but can be shifted in phase as follows

$$\sigma(t) = \sigma_0 \sin(\omega t + \delta) \quad (\text{Eq. 4.3})$$

where δ is the phase shift angle and σ_0 is the stress amplitude (Nelson and Dealy, 1993; Jeffrey Giacomini and Dealy, 1993). The phase angle δ can be regarded as characterizing the distribution of the deformation energy into the two fractions: (1) the energy stored in the system as an elastic deformation and (2) the energy lost irreversibly. For purely elastic behavior δ is zero, and the ratio between shear stress and strain is constant in time. For viscous behavior $\delta = \pi/2$ and the ratio between the shear stress and strain rate is constant (Fig 4.2).

The shear stress is usually written as a trigonometric identity as follows

$$\sigma(t) = \gamma_0 [G' \sin(\omega t) + G'' \cos(\omega t)] \quad (\text{Eq. 4.4})$$

and d as

$$\tan \delta = \frac{G''}{G'} \quad (\text{Eq. 4.5})$$

where $G'(\omega)$ is the storage modulus and $G''(\omega)$ is the loss modulus. In a simple viscoelastic system both moduli are functions of frequency with a characteristic behavior, which is linked to the relaxation time of the structural units e.g. the polymer chains. An example of such behavior is illustrated schematically in Figure 4.3. In such a diagram a plateau of G' and a low G'/G'' ratio ($G' \gg G''$) are both characteristic for elastic behavior (Hookean).

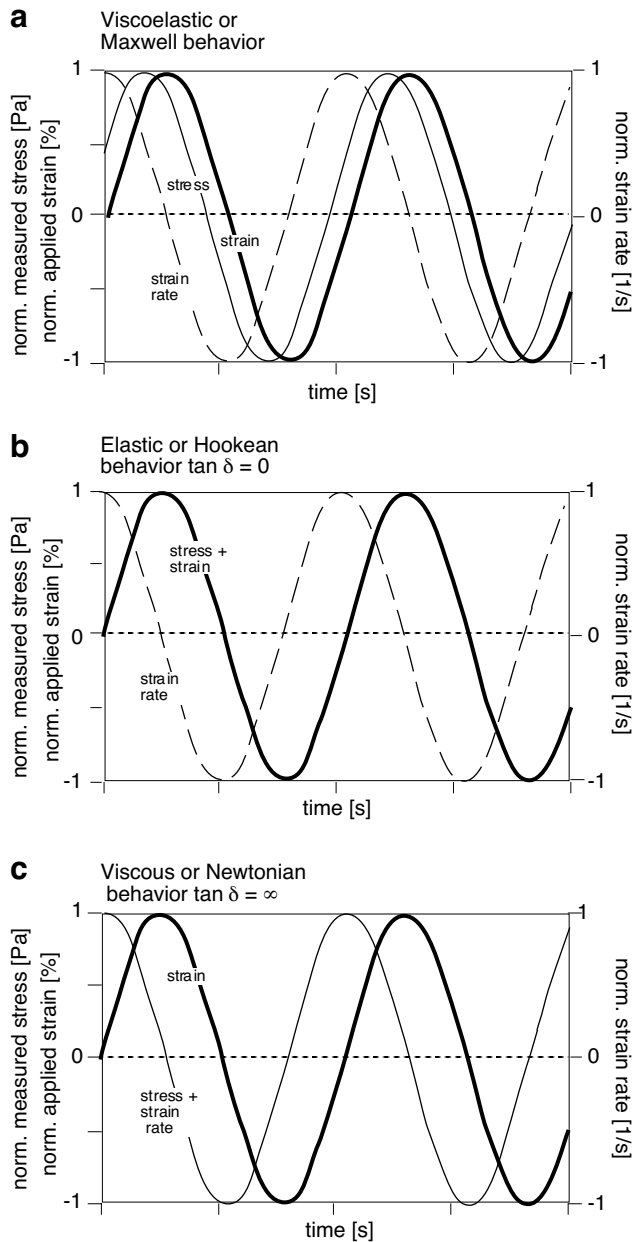


Figure 4.2 Graph to illustrate the applied sinusoidal strain and strain rate and resulting stress. **(a)** Viscoelastic or Maxwell behavior; resulting stress is not in phase with the applied strain or strain rate. **(b)** Elastic or Hookean behavior; resulting stress is in phase with the applied strain. **(c)** Viscous or Newtonian behavior; resulting stress is in phase with the strain rate.

The elastic shear modulus describing the material properties in this range is given by

$$G_0 = \lim_{\omega \rightarrow \infty} G'(\omega) \tag{Eq. 4.6}$$

In the frequency range where $G'' \gg G'$ and where G' and G'' obey the characteristic proportionalities to ω^2 and ω , respectively, flow behavior is viscous (Newtonian). Here the system can be characterized by the complex viscosity $\eta^*(\omega)$ given by

$$\eta^*(\omega) = \frac{\sqrt{G'^2 + G''^2}}{\omega} \tag{Eq. 4.7}$$

(Winter et al., 1993). The complex viscosity $\eta^*(\omega)$ is equal to the kinematic viscosity η only if $G'' \gg G'$. Only in this range, the viscosity is a meaningful material property and the complex viscosity can then approach the value of the zero shear viscosity

$$\eta_0 = \lim_{\omega \rightarrow 0} G''(\omega) / \omega \tag{Eq. 4.8}$$

The intermediate cross-over region between the two limiting types of behavior (elastic and viscous) can be regarded as typically viscoelastic (Maxwell). The point at which G' and G'' cross each other determines the place (ω_r) on the frequency scale which is related to the relaxation time τ of the structural units constituting the system, ($\tau=1/\omega_r$). Assuming a simple Maxwell model, the maximum of G'' and intersection of the functions of $\log(G')$ and $\log(G'')$ vs. $\log(\omega)$ always occur at the same frequency.

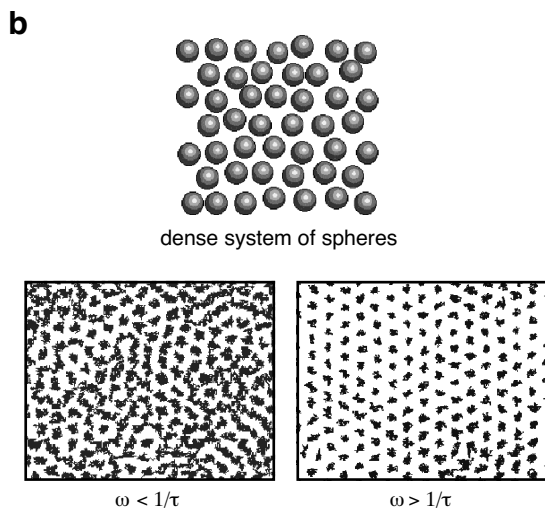
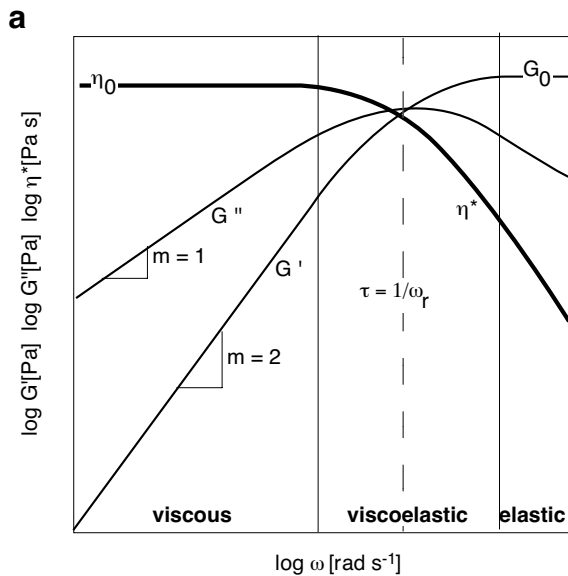


Figure 4.3 Representation of typical rheological properties of linear viscoelastic material; (a) plot of log frequency (ω), against log storage modulus (G') and loss modulus (G''); different fields signify different mechanical behavior, determined by the relation between G' and G'' . Viscous behavior is characterised by $G'' \gg G'$ and slopes of G'' and G' of 1 and 2 respectively. Elastic behavior is characterised by $G' \gg G''$ and by a constant value for G' . Viscoelastic field is between the elastic and viscous field. $\eta^* [Pa]$ is the complex viscosity; (b) representation of centre paths of particles in a simple model (dense system of spheres) corresponding to low ($\omega < 1/\tau$) and high ($\omega > 1/\tau$) deformation rate.

Fig. 4.3b gives an example of a possible structural interpretation of the mechanically observed relaxation which can be considered for molecular or colloidal systems. For a dense system of spheres which can be regarded as representing molecules or particles there is a solid-like state at higher and a liquid-like state at low frequencies. In the high frequency regime, they indicate only vibrational motions and quasi localized positions of particles between the neighbors, whereas, at low frequencies displacements exceeding particle sizes make the system viscous - changing neighbors becomes possible. According to such a model, the relaxation is related to the position correlation of particles and the mechanical response can be considered as a Fourier transform of the position autocorrelation function with the characteristic relaxation time necessary for particles to escape from the surroundings of the initial neighbors.

4.2.2.2 Non-linear viscoelastic behavior

In non-linear viscoelastic materials increasing deformation amplitude i.e. finite strain at a constant frequency leads to structural changes, for example, chain orientation and extension, which influence the material properties. In such cases, the stress-response becomes non-sinusoidal, therefore the property definitions for G' , G'' and d are not meaningful for such a response (Jeffrey Giacomini and Dealy, 1993). Other methods of analysis as those discussed here are required in order to characterize such non-linear viscoelastic behavior.

4.2.3 Relation of G' and G'' to shear modulus and coefficient of viscosity

In geological literature it is common to describe the viscous and elastic behavior of rocks in terms of the coefficient of viscosity (η), which relates the shear strain rate to shear stress, and the shear modulus (G), which relates elastic shear strain to shear stress.

$$\eta = \frac{\sigma(t)}{\dot{\gamma}} \quad (\text{Eq. 4.9})$$

$$G = \frac{\sigma(t)}{\gamma(t)} \quad (\text{Eq. 4.10})$$

Using the equations (2 - 7) the coefficient of viscosity η and the shear modulus G can be rewritten in terms of G' and G''

$$\eta = \frac{G''}{\omega} \quad (\text{Eq. 4.11})$$

$$G = G' \quad (\text{Eq. 4.12})$$

The coefficient of viscosity η may only be used in ranges where the material exhibits viscous behavior ($\tan \delta \rightarrow \infty$). The shear modulus G can only be used for elastic behavior ($\tan \delta \rightarrow 0$). Therefore, to describe the rheological behavior of rocks either the viscosity or the shear modulus is an appropriate quantity.

4.2.4 Typical rheological behavior of polymeric liquids and polymeric liquids with fillers

In complex systems like polymers, structural units of considerably different size i.e. monomers and polymer chains relax with rates which differ by many orders of magnitude. Therefore, the observed frequency dependencies of G' and G'' indicate more than one relaxation region as illustrated in Fig. 4.4. The figure shows a typical example of viscoelastic behavior of a melt of a polyisoprene sample with linear chains of the molecular weight $M_w=130000$ (Pakula et al., 1996). The two different relaxation ranges observed for the polymer melt at low and high frequencies correspond to structural rearrangements concerning two different structural units i.e. monomers and polymers, respectively. The ranges characteristic to viscous and elastic response appear now at various deformation rates and correspond to different size scales in the examined system. Further complication of the structure, for example by introduction of fillers, can lead to creation of new structural scales and new relaxation processes with relaxation times which will depend on particle size and the structure that particles form in the matrix (Gohr et al., 1999). Such additional relaxation can shift the regions of typical deformation behavior (viscous, elastic and viscoelastic) of the material to different deformation rates.

The examples given above show that details of viscoelastic and consequently rheological response of polymeric materials can be strongly influenced both qualitatively and quantitatively. In complex polymers with a broad chain length distribution or with fillers with a broad particle size distribution regions may exist where, for example, $G'' > G'$, the slope of G'' is not equal to 1, and the viscosity is a function of the strain rate. For such behavior the relation between shear stress and strain rate is often empirically described by a power-law function.

$$\dot{\gamma} = k\sigma^n \quad (\text{Eq. 4.13})$$

where k is a constant and n the power-law index. A constant power-law index (n) for a range of strain rates is achieved if the slopes of the functions of $\log(G'')$ and $\log(G')$ vs. $\log(\omega)$ are both constant.

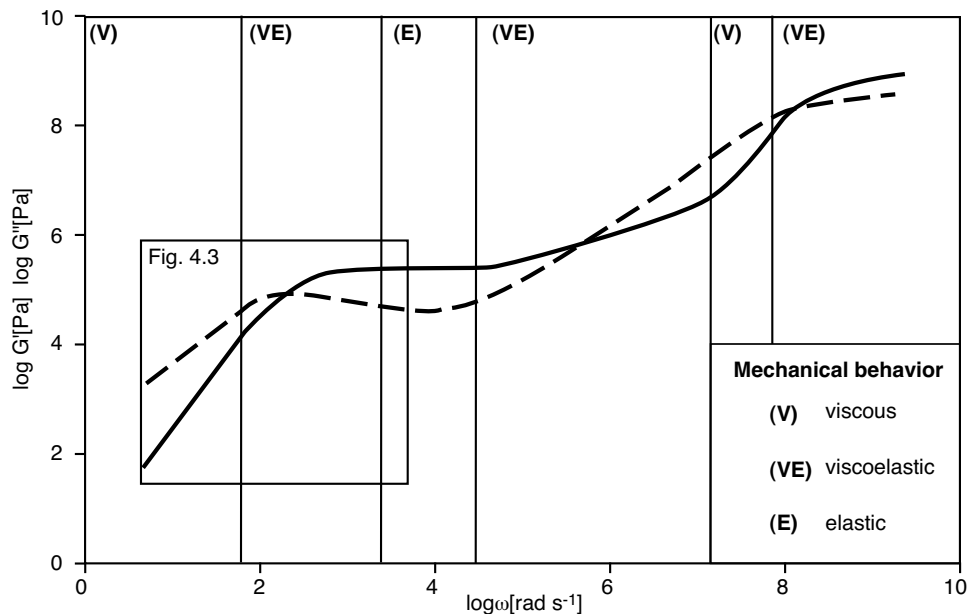


Figure 4.4 Typical example of results characterizing the viscoelastic behavior of a melt of a polyisoprene sample (M_w 130000) with linear chains.

In polymers the power-law behavior is due to specific superposition of various molecular or supramolecular relaxation processes whereas in rocks the power-law behavior is considered as associated with dislocation creep or relaxation. Hence, in polymers and rocks two structurally different mechanisms result in a similar macroscopic behavior.

4.3 Rheological measurements

A number of polymers that are commonly used in geological experiments have been tested. The first step in the rheological characterization of polymeric liquids and similar materials is the determination if the material is linear or non-linear viscoelastic. This is done by deriving G' , G'' and η^* at a constant frequency but varying applied strain. The material is linear viscoelastic only if the values of G' , G'' and η^* are constant in the applied strain range. The second step is to derive G' , G'' and η^* at a range of frequencies.

4.3.1 Method

For measurements we used an oscillatory parallel-disk rheometer (Rheometric RMS 800). The rheometer cell consists of two equally sized parallel disks (Fig. 4.5) of radius $R = 6.5$ mm and the distance between the disks $d = 1.5$ mm. The sample is put between the two plates. At a given frequency of the sinusoidal strain the phase angle δ and the amplitude of the stress response $\sigma(t)$ are measured.

The rheometer has a limited range of frequencies (10^{-3} - 10^2 rad/s) that can be applied. To obtain values for G' and G'' over a wider range of frequencies a so-called master curve is constructed. To do this, measurements are performed at different temperatures and are later shifted along the frequency scale to positions supposed as corresponding to the behavior at a chosen reference temperature T_{ref} according to

$$G'(\omega, T_{ref}) = G'(a_T \cdot \omega_m, T_m) \quad (\text{Eq. 4.14})$$

$$G''(\omega, T_{ref}) = G''(a_T \cdot \omega_m, T_m) \quad (\text{Eq. 4.15})$$

The value of the shift factor a_T is calculated with

$$\log(a_T) = \log(\omega(T_m)) - \log(\omega(T_{ref})) \quad (\text{Eq. 4.16})$$

where T_m is the temperature and ω_m the frequency at which measurements were performed (Winter et al., 1993). The procedure works well for melts of amorphous polymers in which temperature independent structure and temperature independent relaxation spectrum can be assumed.

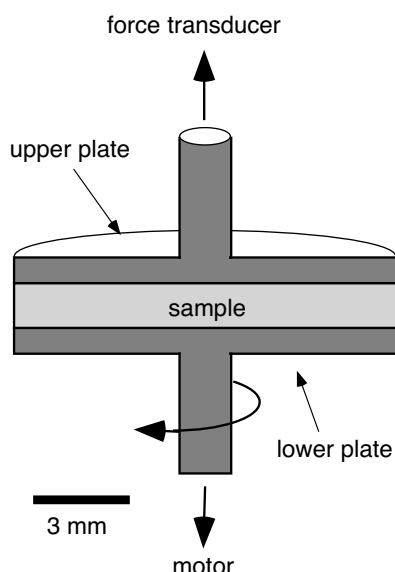


Figure 4.5 Sketch of parallel-disk rheometer geometry. The fluid (polymer) is sheared between an oscillating lower and upper disk. Strain is applied with a certain amplitude and frequency and resulting stress is measured.

4.3.2 Results

4.3.2.1 PDMS and mixtures of PDMS and BaSO₄

PDMS (trade name: SGM 36; produced by Dow Corning, UK) is a transparent polymer with a density of 965 kgm^{-3} (Weijermars, 1986).

To determine if PDMS is linear or non-linear viscoelastic measurement of rheological properties as a function of finite strain at constant strain rate were performed (Fig. 4.6) and revealed a linear viscoelastic flow behavior. Figure 4.7a shows the temperature dependence of the rheological properties for pure PDMS. Figure 4.7b illustrates the calculated master curve of PDMS for a reference temperature of 20°C . The mastercurve for PDMS shows that at 20°C , at strain rates below $5 \cdot 10^{-1} \text{ s}^{-1}$ the slope of G'' is 1 and that of G' is 2, indicating viscous flow behavior. In this range of strain rates the complex viscosity represents a meaningful value which is $3 \cdot 10^4 \text{ Pa s}$. For strain rates between $5 \cdot 10^{-1} \text{ s}^{-1}$ and 13 s^{-1} $G'' > G'$.

Rheological data for 3 different mixtures of PDMS with the filler material BaSO₄ (25 wt%, 33 wt%, 50 wt%) are given in Fig. 4.8. For increasing filler content the values of G' and G'' increase. For mixtures with 33 wt% and 50 wt% BaSO₄ $G' > G''$ at the range of measured strain rates, indicating viscoelastic behavior with a high elastic component. The mixture with 25 wt% BaSO₄ has a G' - G'' crossover at a strain rate of 16 s^{-1} . Below this value G'' is larger than G' . Below a strain rate of 1 s^{-1} the slopes of G' and G'' have a constant value, indicating power-law behavior. The viscosity decreases from $1 \cdot 10^5 \text{ Pa s}$ at a strain rate of $4.3 \cdot 10^{-2} \text{ s}^{-1}$ to $3 \cdot 10^4 \text{ Pa s}$ at a strain rate of 1 s^{-1} . This corresponds to a power-law index (n-value) of 1.23.

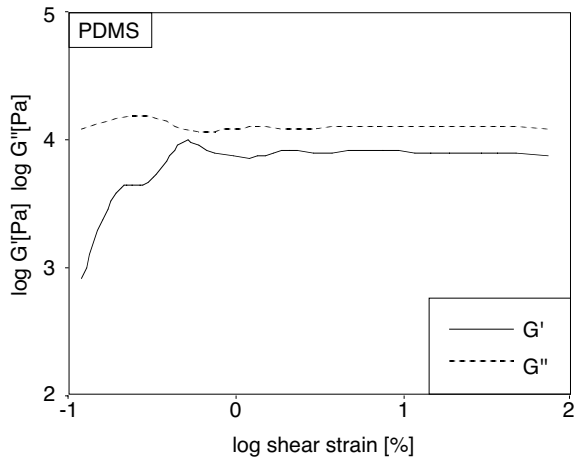


Figure 4.6 Plot of finite shear strain versus G' and G'' for PDMS, confirming its linear viscoelastic flow behavior.

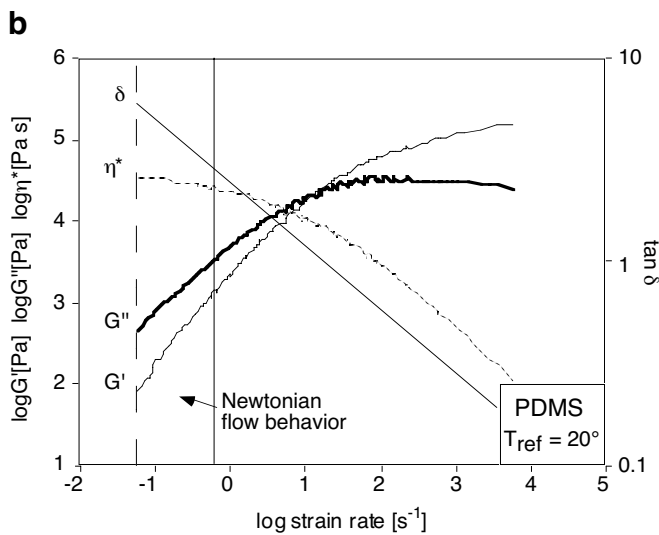
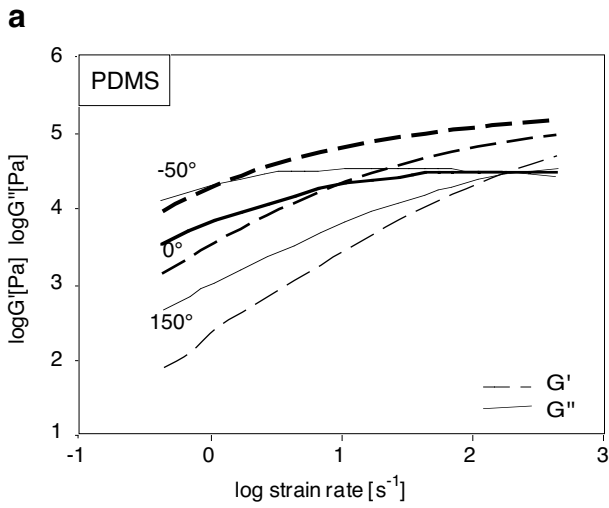


Figure 4.7 Rheological data of PDMS; (a) plot of strain rate versus G' and G'' measured at different temperatures; (b) mastercurve for 20°C, showing G' , G'' , η^* and $\tan \delta$, below a strain rate of 0.5 s^{-1} PDMS shows viscous (Newtonian) flow behavior.

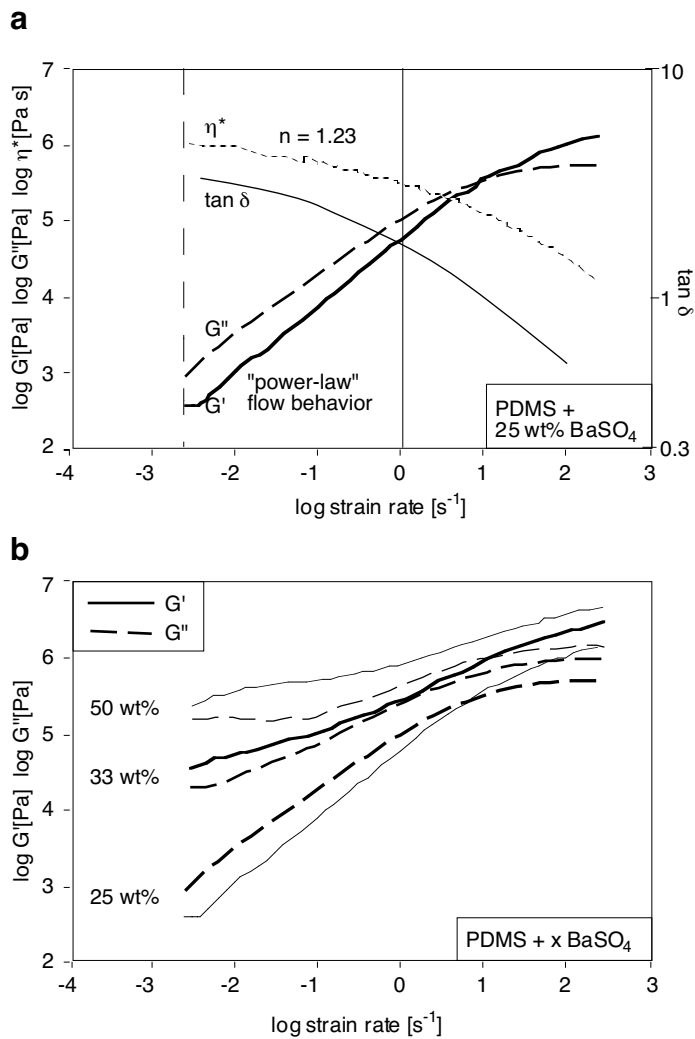


Figure 4.8 Rheological measurements of three mixtures of PDMS and BaSO₄; **(a)** results for PDMS with 25 wt% BaSO₄, plot shows strain rate versus G' , G'' , η^* and tan δ . This material shows power-law behavior below a strain rate of 16 s⁻¹; **(b)** results for PDMS with 33 wt% and 50 wt% BaSO₄, plot shows shear strain rate versus G' , G'' . Both materials behave viscoelastic with a high elastic component.

4.3.2.2 Rhodorsil Gomme

The mastercurve for Rhodorsil Gomme (pinkish opaque bouncing putty, Société des Chimiques Rhône-Poulenc (France)) at T_{ref} of 20°C is shown in Figure 4.9. Three strain rate ranges with distinctly different mechanical behavior can be distinguished. Below a strain rate of $1 \cdot 10^2 \text{ s}^{-1}$ the slope of G'' is 1 and that of G' is 2 and $G'' > G'$, i.e. the material is in the viscous behavior range. The complex viscosity η^* in this range is $8 \cdot 10^3 \text{ Pa s}$. Between $1 \cdot 10^2 \text{ s}^{-1}$ and $2 \cdot 10^3 \text{ s}^{-1}$ the slopes of both G' and G'' are not constant; this is the viscoelastic range. The cross-over of G' and G'' occurs at a strain rate of $2.7 \cdot 10^2 \text{ s}^{-1}$. Above a strain rate of $2 \cdot 10^3 \text{ s}^{-1}$ G' approaches a plateau at $5 \cdot 10^5 \text{ Pa}$ in the elastic range.

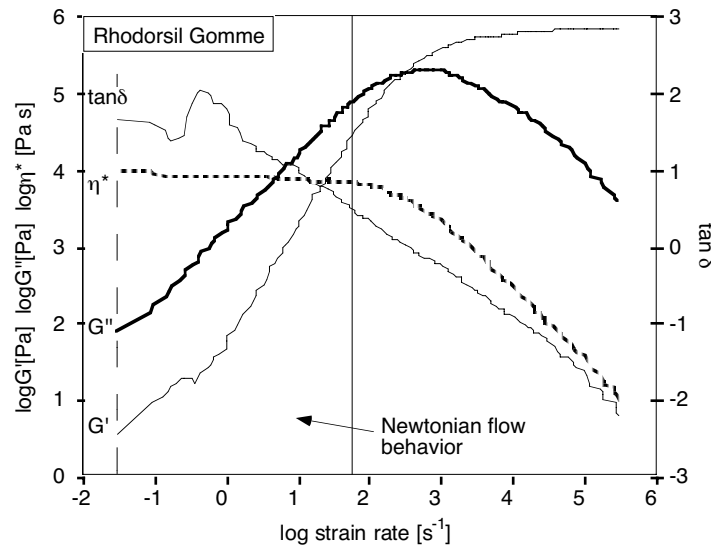


Figure 4.9 Mastercurve of Rhodorsil Gomme, showing G' , G'' , η^* and $\tan \delta$ versus strain rate. Rhodorsil Gomme behaves viscously below a strain rate of $1 \cdot 10^2 \text{ s}^{-1}$.

4.3.2.3 Mixtures Rhodorsil Gomme and white plastilina

Figure 4.10 depicts strain percentage versus G' and G'' at different frequencies for 2 different mixtures of white plasticine (PI; Swedish version of Harebutt's Plasticine (McClay, 1976)) and Rhodorsil Gomme (RG) (32wt% PI/68wt% RG, 50wt% PI/50wt% RG, 75wt% PI/25wt% RG). The mixture of 32wt% PI/68wt% RG exhibits constant values of G' and G'' with increasing finite strain, thus this mixture is linear viscoelastic. Figure 4.11 depicts the corresponding mastercurve. Below a strain rate of 26 s^{-1} the slopes of G'' and G' are constant, but not equal to 1 and 2, respectively. The calculated n -value assuming power law flow is 1.25. Above a strain rate of $5 \cdot 10^3 \text{ s}^{-1}$ the mechanical behavior is elastic. For mixtures of 50wt% PI/50wt% RG and 75wt% PI/25wt% RG values of G' and G'' are not constant with increasing finite strain and therefore the material is non-linear viscoelastic.

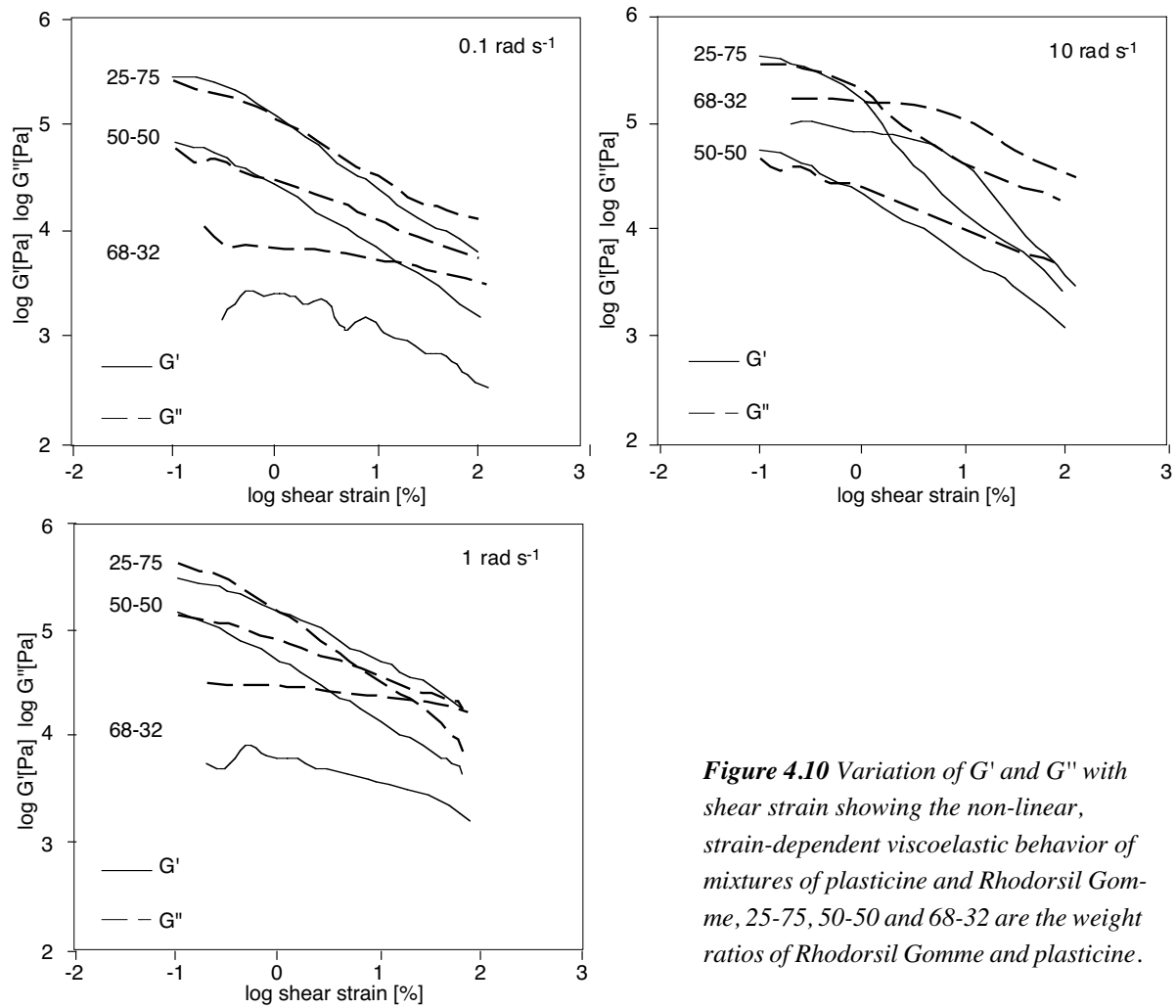


Figure 4.10 Variation of G' and G'' with shear strain showing the non-linear, strain-dependent viscoelastic behavior of mixtures of plasticine and Rhodorsil Gomme, 25-75, 50-50 and 68-32 are the weight ratios of Rhodorsil Gomme and plasticine.

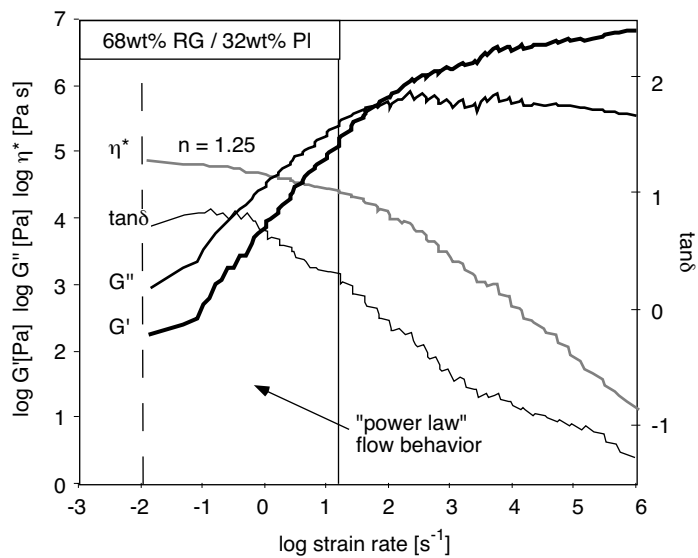


Figure 4.11 Mastercurve of the mixture of 32 wt% Plastilina and 68 wt% Rhodorsil Gomme, showing G' , G'' , η^* and $\tan \delta$ versus strain rate. The mixture behaves like a power law material below a strain rate of 26 s^{-1} .

4.3.3 Comparison of results with existing data

Our data for PDMS closely resemble those given by Weijermars (1986) (Fig. 4.12) and confirm a Newtonian flow behavior below a strain rate of around $5 \cdot 10^{-1} \text{ s}^{-1}$ at room temperature (20–25°C). Between strain rates of $2 \cdot 10^{-1} \text{ s}^{-1}$ and 13 s^{-1} the flow behavior is viscoelastic, whereby $G'' > G'$. Above a strain rate of 13 s^{-1} no viscous flow is present as $G' > G''$. Our data additionally show that the mechanical behavior of PDMS changes significantly with temperature (Fig. 4.7). Treagus and Sokoutis (1992) measured the viscosity of PDMS mixed with 23wt% BaSO₄ at strain rates between $6 \cdot 10^{-3} \text{ s}^{-1}$ and $1 \cdot 10^{-1} \text{ s}^{-1}$ (Fig. 4.12). Their finding of a non-Newtonian flow behavior for this mixture is confirmed by our data for a mixture of PDMS and 25wt% BaSO₄. The power-law index (n) for the mixture with 25 wt% BaSO₄ is 1.23, which is slightly above the n-value of 1.1 for the mixture investigated by Treagus and Sokoutis (1992).

Viscosity measurements of Rhodorsil Gomme have been performed by Weijermars (1986) and Sokoutis (1987) (Fig. 4.12). Our data for Rhodorsil Gomme confirm the Newtonian flow behavior below a strain rate of $1 \cdot 10^2 \text{ s}^{-1}$, as concluded from these measurements. The viscosity determined from our data is $8 \cdot 10^3 \text{ Pa s}$, in contrast to the value of $3 \cdot 10^4 \text{ Pa s}$ from earlier measurements (Weijermars, 1986; Sokoutis, 1987). Above a strain rate of $1 \cdot 10^2 \text{ s}^{-1}$ the material shows viscoelastic behavior and above $2 \cdot 10^3 \text{ s}^{-1}$ elastic behavior. Earlier measurements were not performed in the latter range.

Our data for mixtures of white plasticine and Rhodorsil Gomme do not confirm comparable data of Weijermars (1986) and Sokoutis (1987). Our findings show that these materials are non-linear viscoelastic (Fig. 4.10), and therefore viscosity is not a meaningful rheological property.

McClay (1976) and Kobberger and Zulauf (1995) measured the rheological properties of several types of plasticine and a mixture of plasticine and oil using a uniaxial compression apparatus. They investigated the response of the different materials at constant strain rate and a range of finite strains and used measured values only at a finite strain at which a constant stress response was seen to derive the power-law exponent of the materials. With this procedure they assured linear viscoelastic behavior of the investigated materials. Therefore, the derived power-law exponents are meaningful for the specific range of strain percentage. Dixon and Summers (1985, 1986) investigated the rheological properties of a silicon putty with an annular shear rig. The plots (Fig. 10; Dixon and Summers, 1985) of time versus shear strain clearly show the time-dependent response of the material and therefore the significance of the elastic component in the rheological behavior of the material. Nevertheless, it is not clear whether the material is linear or non-linear viscoelastic.

Weijermars (1986) measured the viscosity of several mixtures of Rhodorsil Gomme and BaSO₄ with different ratios of the filler to matrix. The purpose of this work was (a) to derive power-law exponents for the different mixtures and (b) a function to predict the power-law exponent of mixtures of Newtonian polymers and filler material. As shown by our data for mixtures of PDMS and BaSO₄ (Fig. 4.8) mixtures with a filler content of 33 and 50 wt% are characterized by higher storage moduli than loss moduli. Therefore, mixtures of polymeric liquids and fillers do not necessarily flow viscously. If $G' > G''$ derived power-law exponents are meaningless. Hence, the general function given by Weijermars (1986) should not be used.

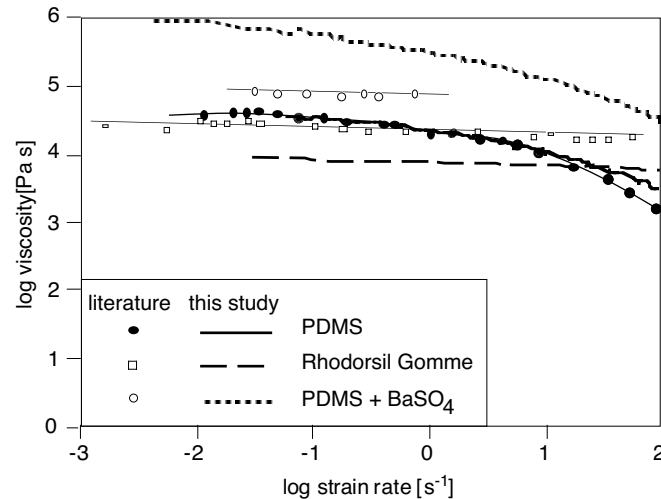


Figure 4.12 Stress-strain rate plot of existing data from literature. PDMS and Rhodorsil Gomme from Weijermars (1986) and Sokoutis (1987), PDMS with 23 wt% BaSO₄ from Treagus and Sokoutis (1992) and the data for PDMS, Rhodorsil Gomme and PDMS with 25 wt% BaSO₄ from this study.

4.4 Implications for the use of polymers and related materials as rock analogs

Analogues are used as scaled-down models of rocks. Their rheological properties should closely fit the requirements of scaling. This should not be checked only according to viscosity but by a complete rheological investigation of material properties. A modern analysis of polymers must include the determination of the storage and loss moduli.

First of all, the rheological behavior at a range of strains at a given strain rate should be known in order to determine if the material is linear or non-linear viscoelastic. If it is non-linear viscoelastic the behavior of the material strongly depends on its deformation history. Therefore, the behavior of these materials is unpredictable. If the material is linear viscoelastic the next step is to determine the values for the storage and loss moduli. The relation of these two moduli is an expression of the different types of linear viscoelastic behavior. If the value of the loss modulus is below the value of the storage modulus viscosity, measurements are not meaningful as the elastic behavior dominates. For polymers the rheological behavior is strongly dependent on strain rate and temperature. Therefore, it is necessary to know the rheological properties of a material exactly at experimental conditions.

As the rheological properties of polymers depend on the relaxation time of the structural units, mixing of polymers with different chain lengths or addition of filler may result in materials with rheological properties very different from those of the endmembers. Therefore, it should be possible to create materials with properties favorable for analog modeling of rocks.

4.5 Conclusions

The knowledge of the effective viscosity alone is not sufficient to fully describe the rheological properties of polymers and related materials. The values of the storage and loss moduli are necessary to evaluate the suitability of a polymer for analog modeling. First of all, the properties as a function of the finite strain must be known in order to determine if the material linear or non-linear viscoelastic. If the properties are not constant with increasing finite strain, a mate-

rial is non-linear viscoelastic. In this case, its use as a rock-analog is problematic as the material properties (i.e. viscosity, storage and loss moduli) are a function of the deformation history. Examples for non-linear viscoelastic materials are mixtures of Rhodorsil Gomme and Plastilina used by Passchier and Sokoutis (1993).

If a material is linear viscoelastic the values of the storage and loss moduli as a function of strain rate determine the mechanical behavior at specific strain rates. Three types of mechanical behavior can be distinguished:

- 1) elastic (Hookean) behavior
- 2) viscoelastic (Maxwell) behavior
- 3) viscous (Newtonian) behavior

Our results reveal that commonly used analog materials can only be used to model viscous deformation at specific strain rates. The upper limit for viscous deformation modeling is $5 \cdot 10^{-1} \text{ s}^{-1}$ for PDMS and is $1 \cdot 10^2 \text{ s}^{-1}$ for Rhodorsil Gomme. To model power law behavior of rocks mixtures of PDMS and BaSO_4 with a BaSO_4 content below approximately 30 wt% and mixtures of Rhodorsil Gomme and plastilina with a plastilina content of 32 wt% can be used at strain rates below 1 s^{-1} and 26 s^{-1} , respectively. The power law exponent (n-value) for a mixture of PDMS and BaSO_4 with a BaSO_4 content of 30 wt% is 1.23 and for a mixture of Rhodorsil Gomme and plastilina with a plastilina content of 32 wt% it is 1.25. For mixtures with a BaSO_4 content above 30 wt% (mixture PDMS/ BaSO_4) the elastic component dominates.

These results show that exclusive measurements of viscosity are not sufficient to determine the mechanical behavior of a material and therefore to assess its suitability for specific analog modeling requirements.

Acknowledgements

A. Hanewald is thanked for the rheology measurements. We thank O. Pawlig for helpful discussions.

Table 4.1 Symbols used

a_T	shift factor for calculation of mastercurve	
G'	storage modulus	Pa
G''	loss modulus	Pa
G_0	elastic shear modulus	Pa
G	shear modulus	Pa
k	constant	
n	power law exponent	
T_{ref}	reference temperature for the calculation of mastercurve	°C
T_m	experimental temperature for the calculation of mastercurve	°C
δ	phase shift angle	
γ	shear strain	
$\dot{\gamma}$	shear strain rate	s ⁻¹
γ_0	shear strain amplitude	
η	kinematic viscosity	Pas
η^*	zero shear viscosity	Pas
η_0	phase shift angle	Pas
ω	frequency	rads ⁻¹
ω_m	experimental frequency	rads ⁻¹
ω_r	frequency where $G' = G''$	rads ⁻¹
σ	shear stress	
σ	shear stress amplitude	
τ	relaxation time	s

Chapter 5

A New Apparatus for Controlled General Flow Modeling of Analog Materials

Abstract

We present a new deformation apparatus to model homogeneous deformation in general flow regimes, in which all combinations of simple shear parallel to the xy-plane and pure shear parallel to the x-, y- and z-axes can be realized. With this apparatus it is possible to control the kinematic vorticity number of monoclinic flow during progressive deformation. The user defines the type of deformation by a set of parameters such as kinematic vorticity number, strain rate and duration of the experiment. The apparatus consists of a set of mobile pistons on a low friction sole and is open at the top. All pistons are flexible to ensure homogeneity of deformation in a major part of the sample. The corners of the box are connected to four sliding carriages, which themselves are sliding on another set of four carriages positioned at right angles to the first set. This set-up and the controlled movement of the sliding carriages allow the user to model any type of monoclinic transtension and transpression. A computer program controls six stepping motors used to move the different carriages simultaneously and accurately. In the apparatus materials with a viscosity range of 10^3 to 10^6 Pa s can be used. A set of pilot experiments investigating the rotation of mica fish in different general regimes is presented as an example for the use of this apparatus.

5.1 Introduction

Research in recent years has shown that many shear zones cannot be explained with a simple shear model but that combinations of simple and pure shear are likely to represent the true character of flow in natural shear zones. Therefore, non-coaxial monoclinic and/or triclinic shear zones have been the focus of a lot of recent work including both analytical and numerical studies (e.g. Ghosh and Ramberg, 1976; Sanderson and Marchini, 1984; Weijermars, 1991, 1993, 1997; Robin and Cruden, 1994; Jezek et al., 1996; Dewey et al., 1998 and reference therein; Fossen and Tikoff, 1998; Passchier, 1998), field studies (e.g. Druguet et al.; 1997; Tikoff and Greene, 1997; Krabbendam and Dewey, 1998) and analog modeling (e.g. Giesekus, 1962; Weijermars, 1998; Cruden and Robin, 1999; Griera and Carreras, 1999). However, the effect of different flow geometries on the development of structural elements within and at the boundaries of shear zones is still unclear. Data from the field and field-derived samples are the most important source of information on shear zones. Nevertheless, small-scale structures in shear zones can only be correctly interpreted if their development is modeled under controlled conditions. An important complementary tool to field data and analytical work is experimental rock deformation (e.g. Price and Torok, 1989; Tullis and Yund, 1985) and analog modeling

using paraffin wax (e.g. Abbassi and Mancktelow, 1990; Grujic, 1993), modeling clay and bouncing putties (e.g. Ramberg, 1955; Ghosh and Ramberg, 1976) and crystalline materials (e.g. Bons and Urai, 1995). Analog modeling using viscous materials such as polymers and bouncing putties offers the opportunity to investigate the development of structural elements such as folds, shear sense indicators and stretching lineations in 3D during progressive deformation up to relatively high finite strain. Several deformation machines have been designed to model flow in shear zones using analog materials; these are used to model simple shear flow (e.g. Robertson and Acrivos, 1970; Price and Torok, 1989), “circular” simple shear or Couette flow (e.g. Passchier and Sokoutis, 1993) and general flow i.e. combinations of pure and simple shear (e.g. Giesekus, 1962; Weijermars, 1998; Cruden and Robin, 1999; Griera and Carreras, 1999). We designed an apparatus in which flow is homogeneous over a large part of the sample. In this apparatus it is possible to control strain rates along three perpendicular directions and therefore all types of shear zones in monoclinic flow such as transpression and transtension (Fig. 5.1) can be modeled. Extending and contracting flexible walls of the deformation box are used to obtain homogeneous deformation. The described apparatus, therefore, offers the possibility to perform progressive homogeneous deformation at a chosen constant or changing strain rate and kinematic vorticity number W_n (Means et al., 1980) during progressive deformation in monoclinic flow. Obviously, a large number of controlled inhomogeneous flow types and histories can also be modeled. A general description of the new apparatus, its possibilities and limitations, suitable materials and experimental procedure is presented here. A set of pilot experiments is described to illustrate the scope of the apparatus.

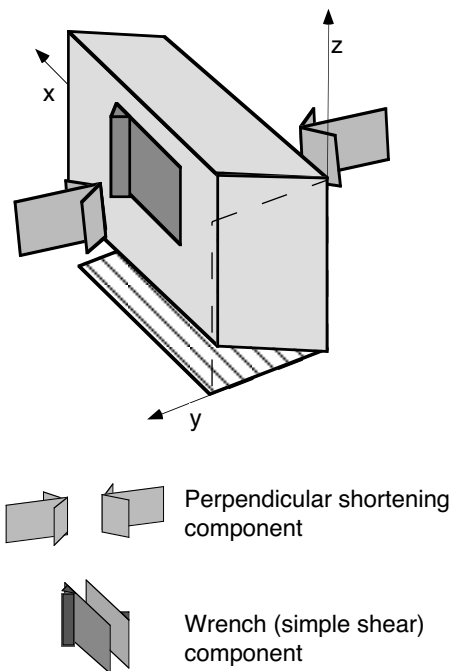


Figure 5.1 Illustration of homogeneous transpression (Sanderson and Marchini, 1984) as combination of simple shear (wrench) component and simultaneous coaxial shortening component perpendicular to vertical shear plane. Example here is in plane strain (modified from Sanderson and Marchini, 1984).

5.2 Description of the apparatus

The apparatus assembly consists of four main parts: the deformation apparatus, a computer, a power driver subsystem and a camera placed 50 cm above the deformation apparatus (Fig. 5.2 and Fig. 5.3).

The deformation apparatus consists of a four-sided deformation box that contains the sample and which we describe in an x - y - z reference frame (Fig. 5.2a). Two opposing sides are always parallel to the x -direction and the two other sides can rotate about the z -axis. The walls of the box are constructed from 1 cm x 12 cm Plexiglas segments (30 on the sides parallel to the x -direction, 20 on the other two sides) which are connected with flexible plastic to corrugated deformable pistons. Every second Plexiglas piece is connected at its back (side facing away from inner part of the box) to two metal springs. This construction ensures homogeneous contraction and extension of the walls. The range of the length of the sides parallel to the x -direction is between 15 and 30 cm and of the other two sides between 5 and 20 cm. The springs are connected to four aluminum plates (P) at the corners of the deformation box. A sheet made of 0.35 mm thick elastic latex forms the bottom of the deformation box. Its corners are fixed to the four aluminum plates (P). This construction results in a deformation box which slides with low friction on the basal plate and which is open at the top. Each one of the four aluminum plates (P) is attached to a sliding carriage (C1). These four sliding carriages are arranged two by two at each long side of the box, parallel to the x -direction. The sliding carriages themselves sit on two PVC boards (B1) which are parallel to the long side of the box and attached to another set of four sliding carriages (C2) oriented parallel to the y -direction. These sliding carriages (C2) are themselves attached to a 1 m x 1 m basal plate (B2). The contraction or extension of the flexible sides of the deformation box is controlled by six stepping motors (M). Four motors drive the movement of the corners of the box (P) in the x -direction via shafts and are fixed to the two PVC boards (B1). Two other motors are attached with shafts to the basal plate (B2) and control movement in the y -direction. This configuration of motors and sliding carriages is chosen to meet two requirements. On the one hand, the center of the deformation box has to remain in one place so that objects of interest in the deforming sample do not move with respect to the camera (Fig. 5.3); on the other hand, all possible monoclinic flow types should be attainable. For simple shear, motors M1, M2, M3 and M4 move the corners of the deformation box at the same constant velocity but in different directions; M1 and M4 in the one direction and M2 and M3 in the opposite (Fig. 5.4). For pure shear M1 and M3 drive their corners of the deformation box in the x -direction and M2 and M4 move their corners in the y -direction. M5 and M6 control movement in the y -direction, and their velocity is determined by the velocity of the other 4 motors (Fig. 5.4) if flow is to be plane strain. Deformation in monoclinic flow at a constant kinematic vorticity number requires movement to be transmitted by all motors and recalculation of the velocity generated by the six motors for each time step since the ratio of pure and simple shear is constantly changing during progressive deformation if the kinematic vorticity number W_n is to remain constant. Corresponding particle paths (Ramberg, 1975) or flow lines (Fig. 5.4) are shown for the coordinate system used here since the geometry of the flow lines is characteristic for each flow type (Passchier, 1998).

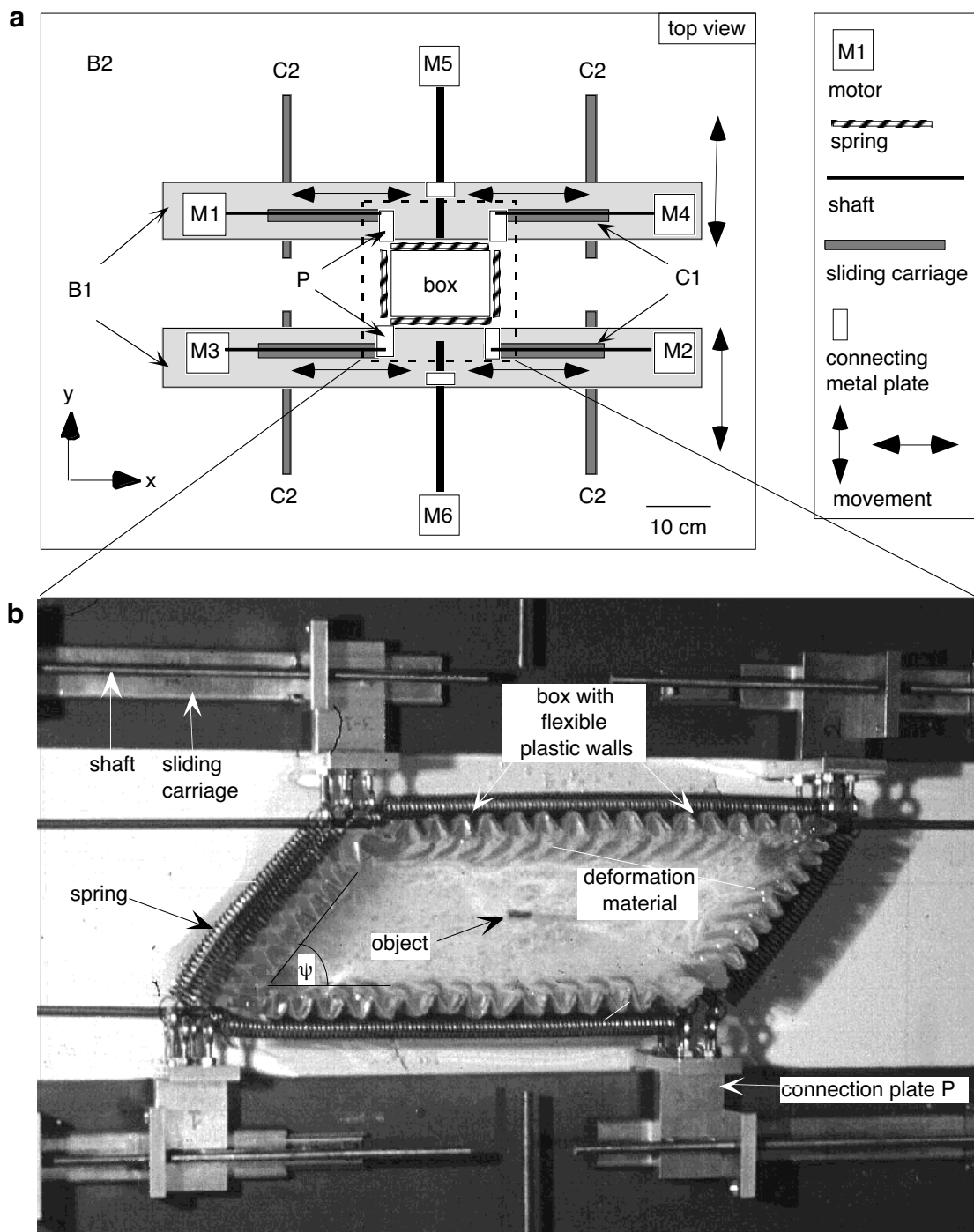


Figure 5.2 (a) Schematic drawing of deformation apparatus (view from top) where x and y are along symmetry axes of apparatus. $B1$ are PVC boards, $B2$ is base plate, $C1$ is a set of 4 sliding carriages parallel to x -direction, $C2$ a set of 4 sliding carriages parallel to y -direction, P connecting aluminum plates and $M1 - M6$ are motors. **(b)** Close-up of deformation box with flexible walls (view from the top). Angle ψ is angle between sides of deformation box.

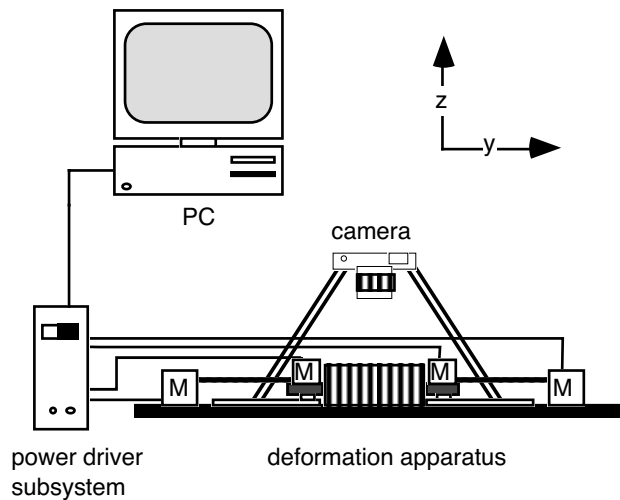


Figure 5.3 General set-up of apparatus; y and z are along symmetry axes of apparatus.

A control panel allows the user to set specific parameters, such as the kinematic vorticity number and strain rate along a specific axis and duration of the experiment. Each second signals are passed on from the PC to the stepping motors via the power driver subsystem. The rotation angle per step is 1.8° with an accuracy of 0.05° . The velocity range is 1-10000 steps/s, which result in 0.005-50 rotations/s and a displacement of 0.005-50 mm/s. The range of possible displacement rates guarantees an accurate control of the movement of the four sides of the box, bulk strain rate and progressive deformation type. The maximum shear strain that can be reached with our apparatus is restricted by the geometry of the shear box. For one experimental run, the maximum attainable R_{xy} value defined as the strain axis ratio in the xy -plane, is 10 in simple shear and 4 in pure shear. Corresponding maximum finite shear strain γ for simple shear is 3, and for pure shear the maximum k -value is 2. In other flow types an R_{xy} of at least 4 can always be obtained. In practice, this means that the maximum duration of one experimental run achieving maximum finite shear strain is 180 min. Higher finite strains than the values mentioned above can be achieved with our machine, but only by running series of experiments. After each experimental run the precise orientation of the object is measured and photographed. After returning the box to the starting position the object is placed in the corresponding measured orientation and another experimental run under the same conditions as the previous run can be carried out. This technique is particularly useful when studying one or a few rigid objects (cf. Passchier and Simpson, 1986).

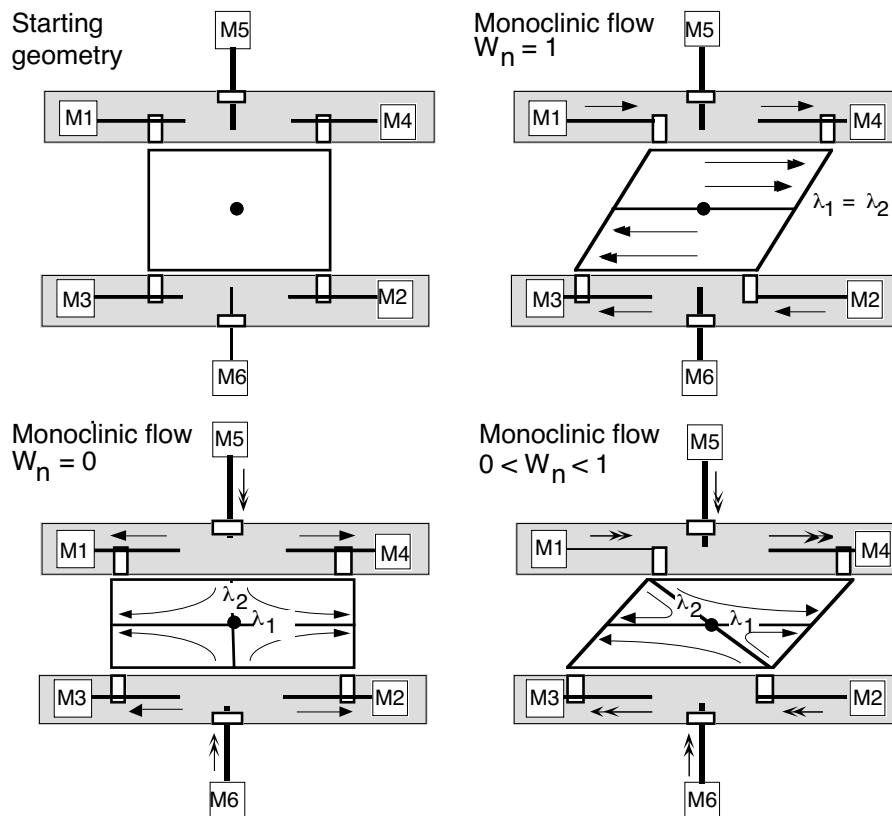


Figure 5.4 Schematic diagrams illustrating different flow types in shear box (see Fig. 5.2). Arrows indicate direction of movement of pistons and specific parts in reference frame of machine; arrows with bold arrowheads signify constant velocity; double arrow heads indicate continuously changing velocity. Longer arrow indicates higher velocity. Within the deformation box, bold lines signify flow apophyses (λ_1 and λ_2) and thin lines trace particle paths where small arrowheads point in direction of particle movement. Black dot is center of the reference frame. M1- M6 are motors. Figure is not to scale.

5.3 Experimental materials

The range of suitable analog materials for our apparatus is restricted by two factors: leakage at the bottom of the deformation box and strength of the stepping motors. Leakage problems of the deformation box limits suitable materials to those with viscosities at least 10^3 Pa s. The strength of the motors limits suitable materials to those with viscosities lower than or equal to 10^6 Pa s, leaving a viscosity range of $10^3 - 10^6$ Pa s. This means that most crystalline analog materials, as well as paraffin wax cannot be deformed in our apparatus. Polymers such as Polydimethylsiloxane (PDMS; trade name. SGM 36; produced by Dow Corning, UK; density 0.965gcm^{-3}), Rhodorsil Gomme (pinkish opaque bouncing putty; produced by the Société des Chimiques Rhône-Poulenc, France) and mixtures of Rhodorsil Gomme and Plastilina (Swedish version of Harbutt's Plasticine; McClay, 1976) are ideally suitable for use in our shear box. For the first tests which were performed to establish the properties of this shear box and for pilot experiments we used PDMS and Rhodorsil Gomme. The low behavior of both materials is Newtonian for strain rates below 10^{-1} s^{-1} (Fig. 5.5). At room temperature viscosities of PDMS and Rhodorsil Gomme are $5.0 \cdot 10^4$ Pa s and $2.9 \cdot 10^4$ Pa s (Weijermars, 1986), respectively. A major advantage of PDMS over other materials commonly used in geological modeling is its

transparency. Furthermore, it is non-toxic and relatively cheap. The flow behavior of Plastilina is highly non-Newtonian (Fig. 5.5) with $n = 7.5$ (Weijermars, 1986) where n is the stress exponent of power law flow.

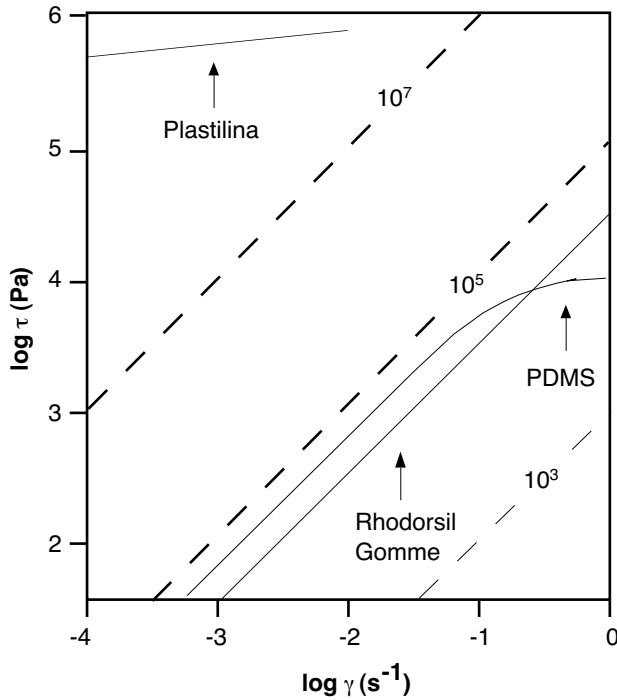


Figure 5.5 Graph illustrating shear stress and shear strain rate of some materials suitable for use in apparatus (modified from Weijermars, 1986). Thin diagonal lines represent viscosity contours in Pa s. See text for discussion

5.4 Types of flow modeled by new apparatus

In order to discuss the flow types that can be modeled with the new apparatus we use the terminology of Passchier (1998) to describe monoclinic flow. Passchier (1998) defined monoclinic flow using the instantaneous stretching axes (ISA), defined as vectors a_I , a_{II} and a_{III} , where a_I , a_{II} and a_{III} are the magnitudes of stretching rates of material lines instantaneously parallel to the ISA. The vorticity vector w is parallel to a_I ; w , the vorticity, is the sum of the angular velocity of material lines instantaneously parallel to a_{II} and a_{III} (Passchier 1997). Any type of monoclinic flow can now be described by the four numbers w , a_I , a_{II} and a_{III} . Alternatively, three normalized numbers W_n , A_n and T_n can be defined which describe the geometry of monoclinic flow completely.

These numbers are defined as the sectional kinematic vorticity number

$$W_n = w / (a_{II} - a_{III}) ,$$

the sectional kinematic dilatancy number (representing the instantaneous area change in the x - y plane during progressive deformation)

$$A_n = (a_{II} + a_{III}) / (a_{II} - a_{III}) ,$$

and the sectional kinematic extrusion number (representing the shortening or extension in the z -direction)

$$T_n = a_I / (a_{II} - a_{III}).$$

In addition, a kinematic volume change number can be defined as

$$V_n = T_n + A_n$$

In our case V_n is approximately zero because of the incompressibility of the sample materials under our experimental conditions, and therefore $T_n = -A_n$. This means that all possible monoclinic flow types at $V_n = 0$ can be depicted in a plane plotting W_n against A_n or T_n (Fig. 5.6).

Up to three non-rotating material lines can be defined in monoclinic flow, the flow eigenvectors or apophyses. For our apparatus eigenvector l_3 is always parallel to the z -axis of our reference frame and λ_1 is always parallel to the x -axis. The third eigenvector l_2 coincides with l_1 in simple shear flow, and otherwise l_2 is situated somewhere in the xy -plane. Two different main groups of monoclinic model shear regimes can be defined for shear boxes of this type, based on the magnitude of l_1 and l_2 . If $\|l_1\| > \|l_2\|$ the shear zone is of group 1, if $\|l_1\| < \|l_2\|$ it is of group 2 (Fig. 5.6). Material lines parallel to the flow apophyses can be either instantaneously extending, shortening or not changing in length.

When there is no stretching or shortening along l_3 (plane strain flow), A_n and T_n are zero. Material lines parallel to either l_1 or l_2 are not deforming when

$$A_n^2 + W_n^2 = 1 \text{ (Passchier 1991a, 1997),}$$

and these situations are represented by the circular curves in Fig. 5.6. All types of flow shown in Fig. 5.6 can be modeled with our apparatus.

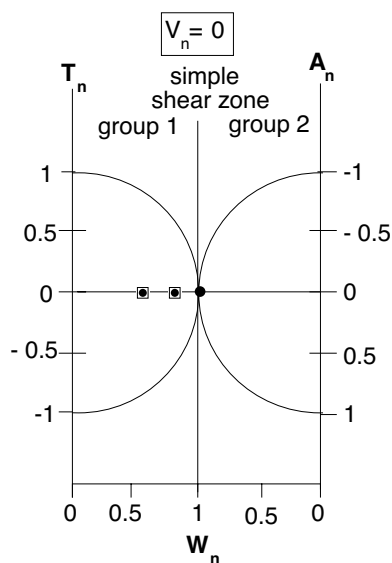


Figure 5.6 Representation of all types of homogeneous constant-volume monoclinic flow (modified from Passchier, 1998). W_n is sectional kinematic vorticity number, A_n is the sectional kinematic dilatancy number, T_n is sectional kinematic extrusion number. V_n , kinematic volume change number is 0. With apparatus it is possible to model all shear zone types in this graph; open squares represent test experiments and black dots represent pilot experiments.

5.5 Flow tests and boundary conditions

In order to test flow conditions that can be obtained in the shear box, we (a) checked the flow patterns in the shear box using particle paths, (b) obtained the distribution of R_{xy} throughout the sample and (c) investigated the rotation rate of a sphere in simple shear flow.

To check the flow patterns several experimental runs were performed with different kinematic vorticity numbers and strain rates. We then compared flow lines observed in the matrix material with flow lines predicted by theory (Ramberg, 1975) and the movement of particle in the central area of the box. The shear box was filled with PDMS. After a few hours of settling carbon powder was sprinkled on top of the material. An additional 5 mm thick layer of PDMS was then put on top of the carbon powder. Again a few hours of settling were needed to ensure a flat surface which is necessary to observe the exact movement of the marker particles. All experiments were performed with a dextral shear sense.

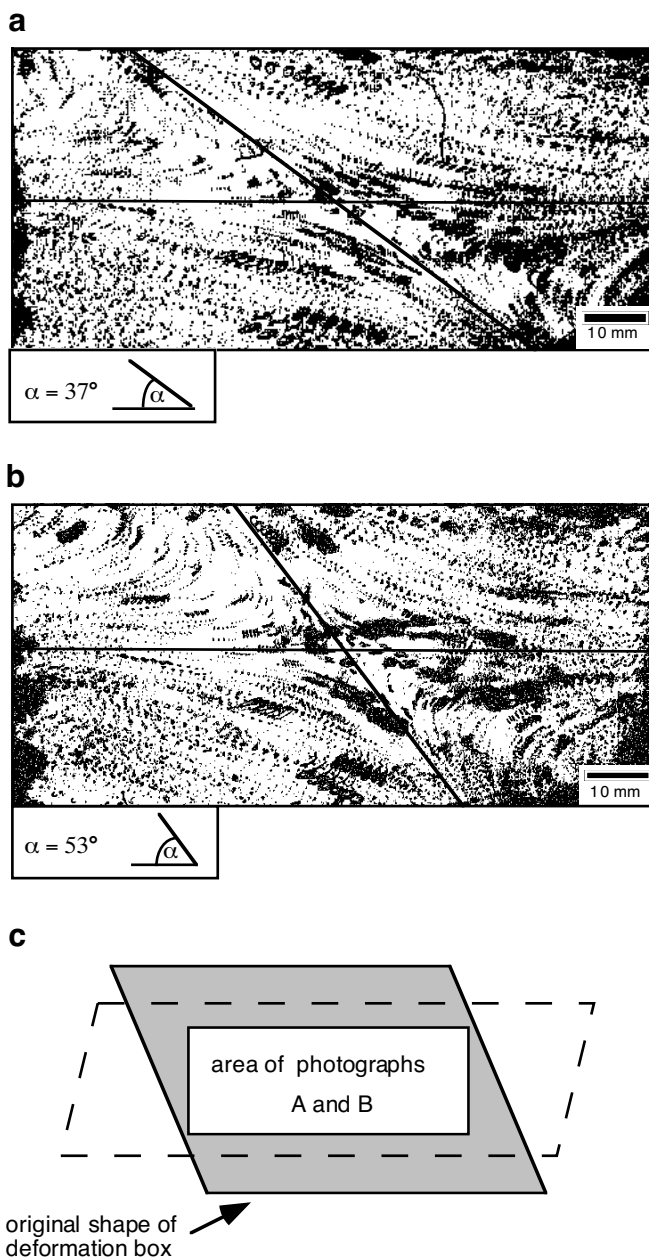


Figure 5.7 Diagrams illustrating particle paths within matrix material PDMS during progressive deformation at $W_n = 0.8$ (a) and at $W_n = 0.6$ (b). Series of photographs taken during the test experiments were stacked onto each other in order to determine the flow pattern during progressive deformation. Insets in (a) and (b) show the theoretical acute angle α between two flow apophyses (see Fig. 5.4) during progressive deformation. (c) Position of area photographed during deformation (white box) inside the deformation box. Original shape of the deformation box is shown in gray and final shape is shown by dashed line.

For the experiments, the initial dimensions of the shear box were 150 x 100 mm and the angle ψ between the sides (Fig. 5.2b) was 135° at the beginning of each experiment. The test experiments presented here were performed at a constant kinematic vorticity number (W_n) of 0.8 and 0.6, a strain rate in the x-direction of $3.3 \cdot 10^{-4} \text{ s}^{-1}$, and plane strain flow ($T_n = A_n = 0$). Photographs were stacked on top of each other in order to determine the flow pattern (ten Brink, 1996; Weijermars, 1998). The acute angle α between the two flow apophyses (Fig. 5.4) during homogeneous deformation can be expressed as $\alpha = \arccos W_n$ for plane strain flow (Bobyarchick, 1986; Passchier, 1986). At $W_n = 0.8$ the angle α is 36.9° and at $W_n = 0.6$ it is 53.1° . The observed values in the test experiments are $37 \pm 0.5^\circ$ at $W_n = 0.8$ (Fig. 5.7a) and $53 \pm 0.5^\circ$ at $W_n = 0.6$ (Fig. 5.7b). This demonstrates that the apparatus is well suited to model homogeneous flow in monoclinic shear zones. The experiments also indicate that the flow pattern is constant in time, as particle paths do not intersect during progressive deformation (Fig. 5.7). Hence, time independent plane strain flow is realized in at least part of the apparatus.

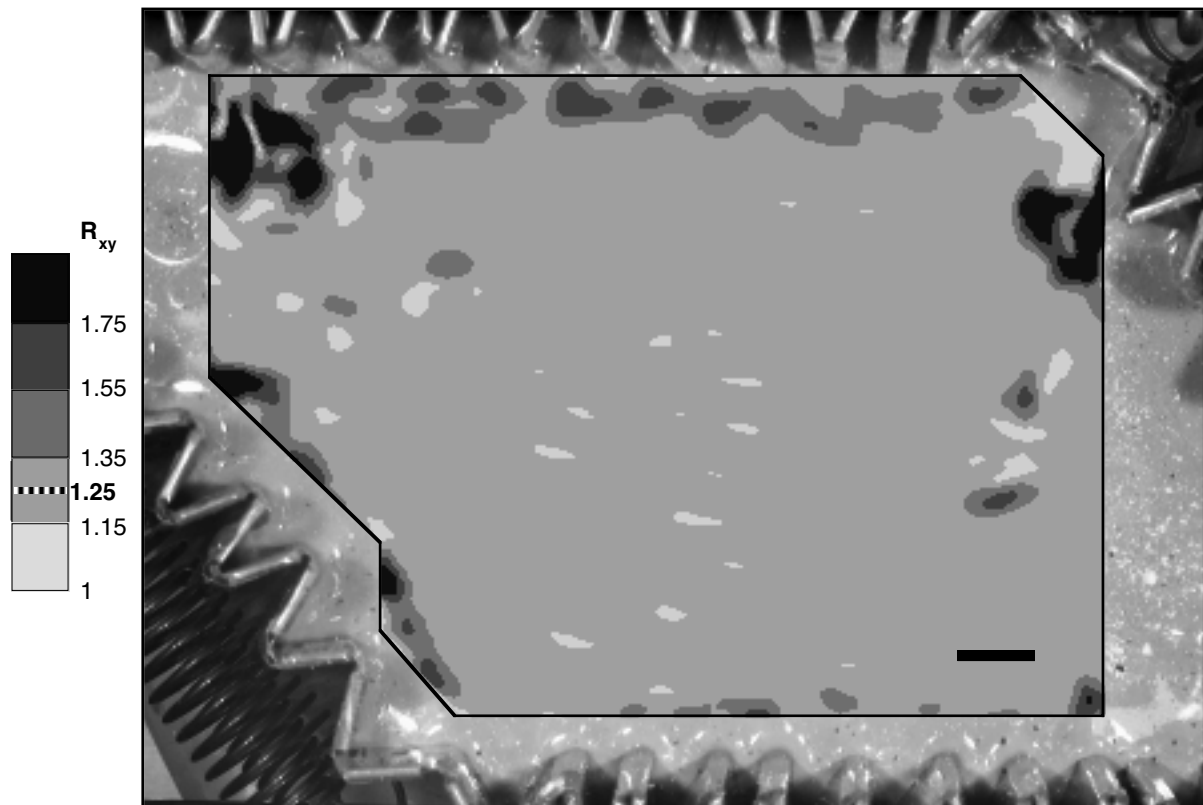


Figure 5.8 Photograph of deformation box. Inset represents distribution of R_{xy} values over analyzed area of a sample. Inset was generated using pattern matching program PatMatch (Bons and Jessell, 1995). Different gray shades represent different ranges of R_{xy} values. Dashed line in legend represents theoretical value of R_{xy} ($R_{xy} = 1.25$) and at same time measured average of analyzed area (excluding narrow zone close to pistons). Most part of analyzed area exhibits R_{xy} values which correspond to theoretical value of R_{xy} . Note that on upper left corner and on upper right side reflections cause significant errors in PatMatch routine because the program cannot identify patterns in reflected areas. Experimental conditions are: $W_n = 0.6$, stretching rate in x-direction is $3.3 \cdot 10^{-4} \text{ s}^{-1}$ and sample material is Rhodorsil Gomme. Scale bar = 1 cm.

To quantify the area of homogeneous deformation in the sample we performed a number of plane strain test experiments with different vorticities ($W_n = 0.8, 0.6$), strain rates (stretching rate of the x-axis: $2.0 \cdot 10^{-4} \text{ s}^{-1}$, $3.3 \cdot 10^{-4} \text{ s}^{-1}$, $4.7 \cdot 10^{-4} \text{ s}^{-1}$) and matrix materials (PDMS, Rhodorsil Gomme). The preparation and procedure of the experimental runs was identical to that described for the other test experiments (see above). We used the computer program PatMatch (Bons and Jessell, 1995), which performs strain analysis by analyzing displacements between two images to obtain the distribution of R_{xy} within a deformed sample. Results reveal that a large area of the samples deform homogeneously and the R_{xy} values closely correspond to theoretical values (Fig. 5.8). Only in a narrow zone adjacent to the corrugated walls inhomogeneous flow occurs. The width of this zone depends on the viscosity of the matrix material and is independent of the kinematic vorticity number and strain rate (within the accuracy of our measurements). For PDMS the width of the zone with inhomogeneous flow is 0.8 to 1.3 cm measured from the tips of the corrugated wall; for Rhodorsil Gomme this width is 0.6 to 1.1 cm.

A third set of experiments investigated the behavior of a rigid sphere in plane strain simple shear flow at a simple shear strain rate of $1 \cdot 10^{-3} \text{ s}^{-1}$ up to a finite strain g of 2. We inserted a Plexiglas sphere with a diameter of 0.8 cm in the middle of the deformation box and took a number of consecutive photos during progressive deformation. Figure 5.9 shows the change in orientation of the sphere (θ) against simple shear strain (γ) observed in the experiment and the theoretical values of rotation (Ghosh and Ramberg, 1976). Experimental values show good agreement with theoretical values.

The flow tests presented above are all in plane strain ($A_n = T_n = 0$), where the specimen surface remains flat. Under these conditions a large volume of homogeneous flow can be obtained. In experiments with extrusion of material parallel to the z-axis ($A_n \neq 0$ and $T_n \neq 0$) the rigidity of the pistons in the z-direction causes the sample surface to attain a parabolic shape, which has an effect on the flow homogeneity. Accordingly, any user of our apparatus working at $T_n \neq 0$ should test the effect of boundary conditions for the specific experimental set-up used.

Leakage of material with a viscosity of $5.0 \cdot 10^4 \text{ Pa s}$ out of the deformation box is less than 0.5 vol.% during one experimental run if the experimental duration is less than 4 hrs. Leakage does not exceed 1 vol. % in 24 hrs if the sample material (viscosity: $5.0 \cdot 10^4 \text{ Pa s}$) is left in the deformation box without performing experiments.

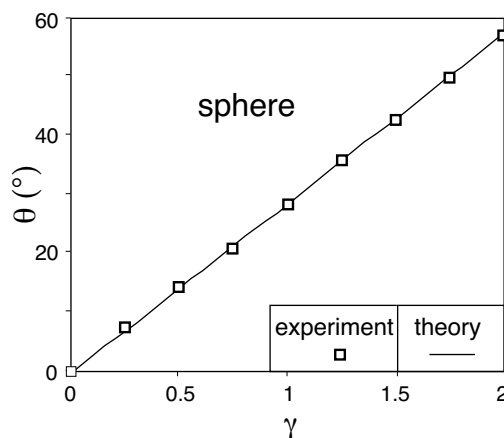


Figure 5.9 Graph illustrating the change in orientation of rigid sphere as a function of shear strain in simple shear flow ($W_n = 1$). Solid line represents theoretical values (after Ghosh and Ramberg, 1976) and squares represent experimental values.

5.6 Pilot experiments: Rotation of mica-fish in plane strain

As an example of the practical application of our apparatus, we present the modeling of mica-fish. Mica-fish are commonly observed in mylonites and their asymmetrical form and the stair-stepping of their tails are often used to determine shear sense (Lister and Snoke, 1984; Passchier and Trouw, 1996). Study of natural mica-fish show that in the plane parallel to the stretching lineation and perpendicular to the foliation, their shape is predominantly monoclinic. All studied examples lie with their long axis tilted $2^\circ - 40^\circ$ with respect to the inferred flow plane (ten Grotenhuis and Passchier, 1999). This could mean that mica fish are in a stable irrotational position with respect to the apophyses of bulk flow for at least a part of their evolution. In addition, it is not clear to what extent object shape, flow partitioning, W_n or other factors influence the development of mica-fish. Our deformation apparatus is suitable to study kinematic aspects of the development of such mica-fish.

Analytical work of Ghosh and Ramberg (1976) shows that in two dimensional homogeneous flow with a particular kinematic vorticity number, the rate of rotation of a rigid elliptical particle in a Newtonian viscous fluid varies in a systematic manner depending on the orientation and the axial ratio (R_{ob}) of the inclusion. This means that the orientation of the particle is a function of the initial angle, the aspect ratio of the particle and strain. Up to now, experiments investigating the rotation of rigid objects in homogeneous flow were mainly restricted to simple shear (Ghosh and Ramberg, 1976; ten Brink, 1996). With our apparatus, we can expand such work to homogeneous monoclinic flow experiments.

To investigate the effect of object shape on the rotation behavior we performed experiments with a monoclinic object in a Newtonian viscous fluid (PDMS). The object is made of rigid India rubber and has a long side A of 10 mm, a short side B of 7 mm and height h of 16 mm (Fig 5.10).

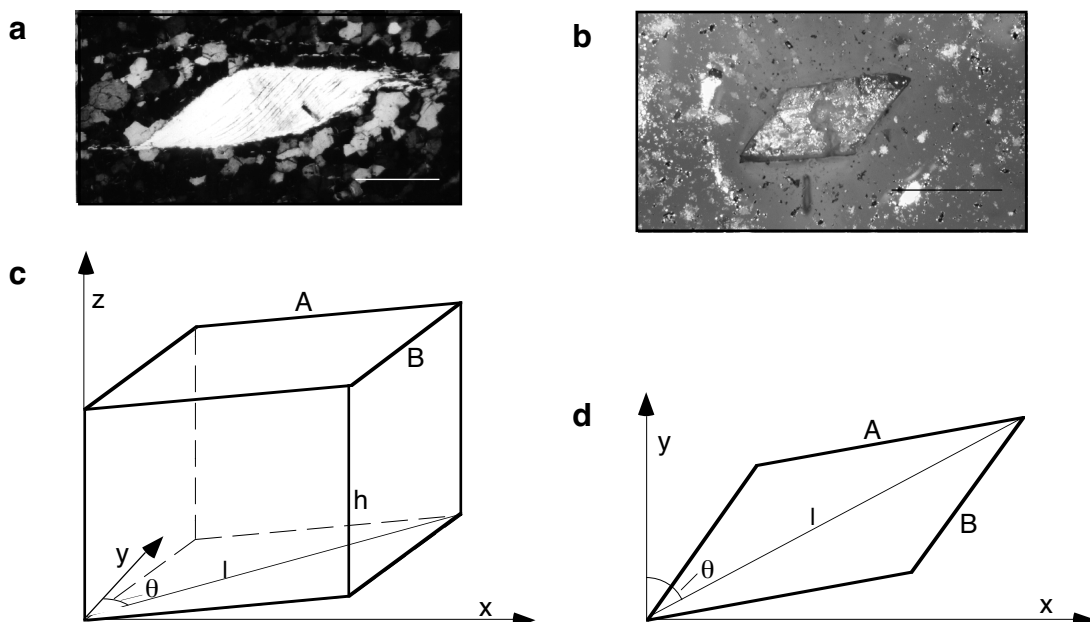


Figure 5.10 (a) Natural example of muscovite mica-fish (Ribeira belt, Brazil); crossed polars, scale bar = 1 mm. (b) Photograph of the object used in the experiments, inserted in its matrix (PDMS); scale bar = 10 mm. (c) Schematic three-dimensional drawing of rigid monoclinic object used as an analog for a mica fish; x, y and z correspond to reference frame of apparatus, h is height, l longest axis of the object and θ the angle between longest axis (l) and y-axis of reference frame. (d) Schematic drawing of AB-plane of object.

The angle between A and B is 135° . The aspect ratio of the object (R_{ob}) in the xy-plane is three. The angle θ is between the long axis of the object and the y-direction of the reference frame. Angles are measured clockwise. A and B are parallel to the z-axis. The object is placed in the middle of the box with its top 5 mm below the surface of the PDMS and parallel to the y-direction, $\theta_0 = 0^\circ$. The experiments model plane strain monoclinic flow ($T_n = 0$) with a kinematic vorticity number (W_n) of 1 (simple shear flow), 0.8 and 0.6 (Fig. 5.6). In the simple shear experiment the simple shear strain rate is $1 \cdot 10^{-3} \text{ s}^{-1}$ and the final shear strain g is 3. For the flow experiments at $W_n = 0.8$ and $W_n = 0.6$ the stretching rate along the x-axis is held constant at $3.3 \cdot 10^{-4} \text{ s}^{-1}$. After one experimental run the maximum R_{xy} value reached was 3.58 at $W_n = 0.8$ and 2.68 at $W_n = 0.6$. For the experiments with $W_n = 0.8$ and 0.6 seven consecutive runs were performed.

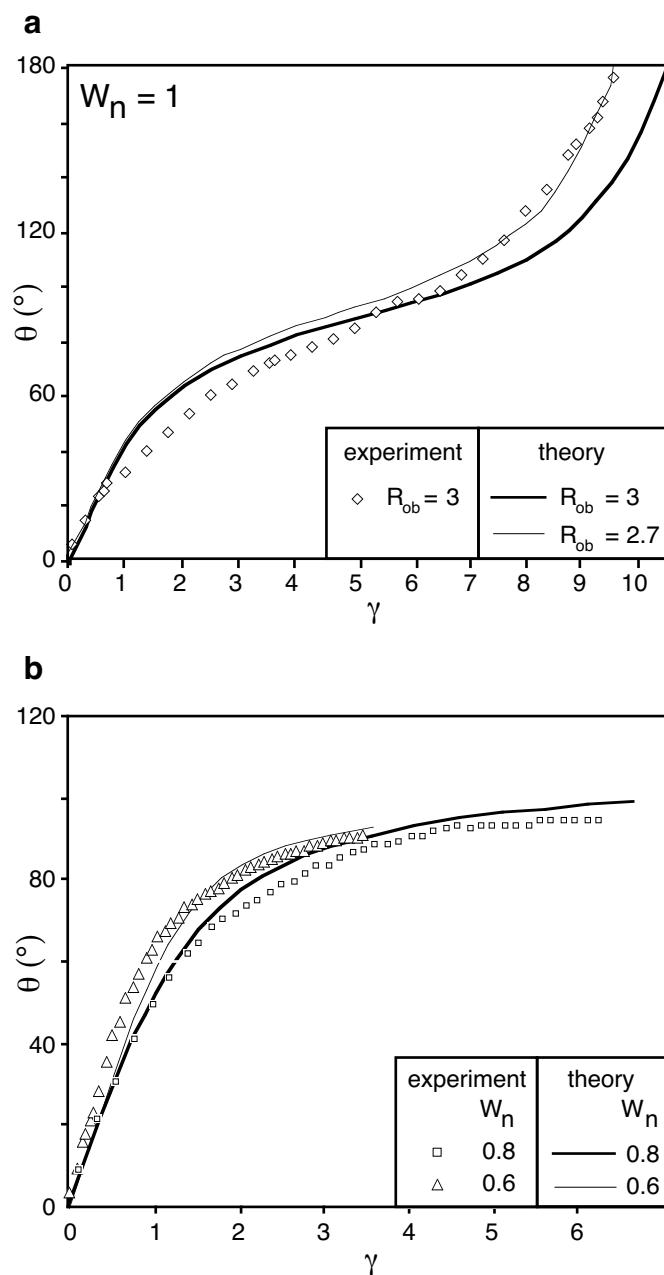


Figure 5.11 (a) Graph illustrating change in orientation of rigid monoclinic object (θ) as a function of simple shear component of strain in monoclinic flow with $W_n = 1$. Solid line represents theoretical values (after Ghosh and Ramberg, 1976) and symbols experimental values. R_{ob} is aspect ratio of object. **(b)** Graph illustrating the change in orientation of rigid monoclinic object (θ) with aspect ratio of 3 as function of simple shear strain in monoclinic flow with $W_n = 0.8$ and 0.6. Solid lines represent theoretical values (after Ghosh and Ramberg, 1976) and symbols represent experimental values.

Figure 5.11 shows the experimental results and the theoretical orientation of the long axis for ellipses with $R_{ob} = 3$ against the simple shear component of strain (γ) for $W_n = 1$, $W_n = 0.8$ and $W_n = 0.6$ (equation 11 - 13 in Ghosh and Ramberg, 1976). We chose to plot the simple shear component of strain (γ) and not R_{xy} in Figure 5.11 because γ increases linearly with progressive deformation. It should be noted that the highest γ value for one experimental run was 1.08 at $W_n = 0.8$ and 0.61 at $W_n = 0.6$.

The experiments show a deviation in the orientation of the lozenge object from theoretical values for ellipses. In simple shear the rotation curves of the object and the theoretical curve of an ellipse with $R_{ob} = 3$ differ considerably (Fig. 5.11a). The theoretical curve for an ellipse of $R_{ob} = 2.7$ fits the experimental results better with regards to the amount of shear strain necessary for a 180° rotation of the object but the shape of the curves (θ versus γ) is systematically different (Fig. 5.11a). In monoclinic flow with $W_n = 0.8$ and $W_n = 0.6$ experimental results show that the object attains a semi-stable position (Fig. 5.11a). This position is 95° at $W_n = 0.8$ and 90° at $W_n = 0.6$ (Fig. 5.11b). Theory predicts 5° higher values for the semi-stable position of an ellipse of $R_{ob} = 3$ in both experimental flow types. Theoretical values for an ellipsoid with $R_{ob} = 2.7$ show even stronger deviations from experimental results. We suggest that the observed deviation from theory is due to the shape of the rigid object. Both the axial ratio of an object and its shape i.e. elliptical, rectangular, or lozenge-shaped influence the behavior of such an object in monoclinic flow.

Nevertheless, the preferred orientation (θ) of mica-fish in nature is 50° to 88° using the reference frame of the experiments. Therefore, monoclinic flow with a kinematic vorticity number smaller than 1 cannot be the only explanation for the orientation of mica fish in shear zones and further experiments are needed to explain the behavior of these structures.

5.7 Conclusions

The newly developed apparatus described in this paper can combine simple and pure shear independently and simultaneously and allows the modeling of structures in all types of homogeneous monoclinic flow, as illustrated in Passchier (1998). Test and pilot experiments show that flow in the apparatus is homogeneous in plane strain except for a small zone along the pistons and that particle paths, R_{xy} and rotation rates of spheres are comparable to theoretical values in monoclinic shear zones. Limitations of the apparatus are the maximum finite strain of one experimental run, availability of suitable analog materials, and the limited range of attainable strain rates. For one experimental run, the maximum strain axis ratio in the xy-plane R_{xy} is at least 4 for all types of monoclinic flow that can be modeled in the machine. The set-up of the apparatus and technical limitations restrict suitable materials to those with a viscosity in the range of 10^3 to 10^6 Pa s. The attainable range of strain rate is strongly dependent on the analog material used.

Acknowledgements

A. Klügel (Max-Planck-Institute for Geochemistry, Mainz, Germany) is thanked for his support during the construction of the apparatus. D. Sokoutis and G. Mulugeta (University of Uppsala, Sweden) are acknowledged for making samples of Plastilina available. We would like to thank A. R. Cruden and R. Weijermars for their helpful reviews and Paul Bons for constructive discussions.

Chapter 6

Influence of rheology and vorticity on fabric development of populations of rigid objects during progressive plane strain deformation

Abstract

The influence of vorticity and rheology of matrix material on the development of shape preferred orientation of populations of rigid objects is experimentally studied. Experiments in plane strain monoclinic flow with kinematic vorticity numbers (W_n) of 1, 0.8 and 0.6 were performed to model the fabric development of two populations of rigid objects with object aspect ratios of 2 and 3. Objects were dispersed in a Newtonian and a non-Newtonian, power-law matrix material. At the high object aspect ratio the shape preferred orientation of a population of rigid objects is strongly influenced by W_n and the material properties of the matrix. Deformation of a power law matrix material and low W_n results in a stronger fabric than of a linear viscous matrix and high W_n . Strain localization coupled with particle interaction plays a significant role in the development of a shape preferred orientation. High strain simple shear zones separate trains of rigid objects which are surrounded by low strain zones with W_n lower than the W_n of the applied flow type. In fabrics involving populations of objects with low aspect the rheology of the matrix materials does not systematic influence the intensity of the shape preferred orientation.

6.1 Introduction

Rigid inclusions and matrix systems form an important class of structures that are used for structural and kinematic analysis. One of these structures is the shape preferred orientation of a population of elongate rigid objects. Commonly observed examples are populations of mm-scale feldspar laths dispersed in granitic melt or crystal mesh, amphiboles in a fine grained feldspar-mica matrix, kyanite in a quartz-mica matrix, dm-scale mafic enclaves in a felsic intrusive rock (e.g. Ildefonse et al., 1990 and references therein; Bouchéz 1997 and references therein) or obducted, km-scale ultramafic bodies in a predominantly sedimentary sequence. The shape preferred orientation (SPO) of populations of rigid objects describes the relative frequency of different object orientations. Data on finite strain and type of flow can potentially be derived from characteristics of the shape preferred orientation.

Several parameters determine the SPO of a population of rigid objects. These are the shape of the individual objects, type of flow, finite strain, slip at the object surface, rheology of matrix material and density of the object population. The basis for the understanding of the behaviour of a population of objects during progressive deformation is knowledge of the behaviour of an individual isolated object in a deforming matrix. The influence of the shape of

a rigid object on its rotation rate has been investigated using theoretical models based on the work of Jeffery (1922). These models (e.g. Bhattacharyya, 1966; Gay 1966, 1968; Rees, 1968, 1979; Reed and Tryggvason, 1974; Ghosh and Ramberg, 1976; Ferguson, 1979; Jezek et al., 1994) consider the rotation of an isolated axisymmetric ellipsoidal rigid object embedded in a deforming viscous Newtonian fluid. In a Newtonian matrix individual objects rotate cyclically and therefore exhibit multiple revolutions during bulk straining. In a non-Newtonian matrix orbits of single ellipsoidal, non-spherical objects are not closed but drift towards a final position (Ferguson, 1979). Nevertheless, Jeffery's model which assumes a viscous Newtonian matrix material is still likely to yield an acceptable approximation except for very high strains (Ferguson, 1979). Analytical work has shown that in two dimensional homogeneous flow the rate of rotation of a rigid elliptical object in a Newtonian viscous fluid varies in a systematic manner depending on the kinematic vorticity number of deformation (Means et al., 1980), the orientation of the long axis of the object, slip at the object-matrix interface and the axial ratio (R_{ob}) of the inclusion (Ghosh and Ramberg, 1976; Odonne, 1994; Pennacchioni, 2000).

The shape fabric evolution of a population of rigid neighbouring objects dispersed in a deforming matrix has been investigated experimentally (Fernandez, 1987; Ildefonse, 1992a, 1992b; Ildefonse and Mancktelow, 1993; Arbaret et al., 1997; Fernandez and Fernandez-Catuxo, 1997) and analytically (e.g. Jezek et al., 1994, 1996; Masuda et al., 1995b). Experimental work has shown that mechanical interaction between rigid objects, perturbations of flow next to rigid objects and therefore the density of a population profoundly affect the developing fabric. As analytical solutions for the influence of the latter parameters on the SPO are so far lacking, analytical work can only in parts be applied to SPO seen in rocks. Due to experimental and mathematical restrictions, most analytical and experimental investigations consider usually only a Newtonian viscous matrix rheology and end-members in progressive deformation types i.e. simple and pure shear. For example, experimental studies of the effect of particle interactions and density of object populations were exclusively performed for pure and for simple shear (e.g. Ildefonse et al., 1992a, 1992b; Fernandez 1987); experiments using a non-Newtonian matrix materials were only done in simple shear (Ildefonse and Mancktelow 1993).

In contrast to experimental and theoretical investigations, deforming rocks commonly follow non-Newtonian power-law flow (e.g. Carter, 1976, Schmid, 1976; Urai, 1983; Kirby and Kronenberg, 1987; Passchier and Trouw, 1996) and deformation may deviate from simple shear and pure shear in a significant way (Passchier, 1987; Vissers, 1989; Masuda et al., 1995b; Wallis, 1995; Beam and Fischer, 1999; Jiang, 1999).

In this study, the effect of different combinations of pure and simple shear, matrix rheology, object aspect ratio, particle interaction and resultant flow perturbation on the development of shape preferred orientation of a population of rigid objects during progressive deformation is investigated.

6.2 Experimental setup

Experiments were performed in a two dimensional shear zone using a new apparatus with which it is possible to model homogeneous deformation in plane strain monoclinic regimes (Chapter 5). In experiments, populations of 34 individual objects made of India rubber were inserted with a random orientation in the deformation box. The initial distance between two neighbouring objects was between 0.2 to 1.5 the length of its long axis.

The initial dimension of the shear box was 150 x 100 x 100 mm and the angle ψ between the long (parallel to the x-direction) and short side (parallel to the y-direction) of the shear box was 135° at the beginning of each experiment (Fig. 6.1). Experiments were performed at a constant kinematic vorticity number W_n with no extension or shortening in the z-direction of the shear box. The shear sense in all experiments was dextral.

Three parameters were varied in experiments. Aspect ratios of individual rigid objects (R_{ob}) in the xy-plane (Fig. 6.1) were either three (6 mm x 2 mm) or two (5 mm x 2.5 mm), the matrix material was either Newtonian linear viscoelastic (Polydimethylsiloxane (PDMS)) or non-Newtonian, non-linear viscous with a power law exponent of 1.23 (mixture of PDMS and 25 wt% BaSO₄). The kinematic vorticity number was varied between 1 (simple shear), 0.8 and 0.6. Rheological properties of both matrix materials are provided and discussed in detail in Chapter 4.

Experiments at $W_n = 1$ were performed with a simple shear strain rate of $1 \cdot 10^{-3} \text{ s}^{-1}$. In experiments with $W_n = 0.8$ and $W_n = 0.6$ the stretching rate along the x-axis was held constant at $3.3 \cdot 10^{-4} \text{ s}^{-1}$. At the end of a first run, the position and orientation of the objects was recorded and at the beginning of the second run each one of the objects was inserted with the recorded orientation and position. Finite simple shear strains that were achieved were 4.6 ($W_n = 1$), 2.6 ($W_n = 0.8$) and 1.1 ($W_n = 0.6$). In terms of the axial ratios of the finite strain ellipse (R_{xy}) these values correspond to 22.7, 9.5 and 3.4, respectively (Tab. 6.1).

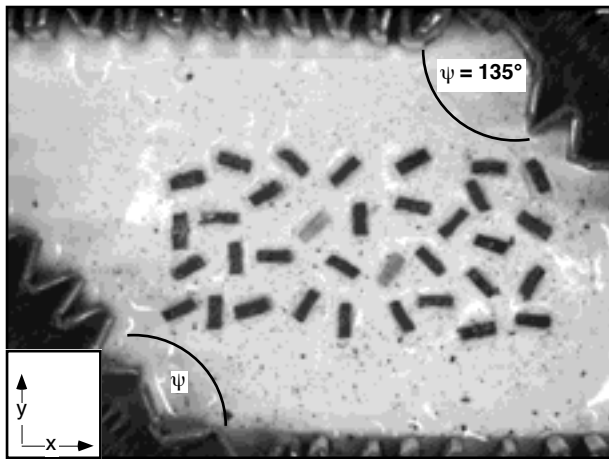


Figure 6.1 Photograph of initial fabric of experiments and definition of the reference frame (x , y , z direction) of the shear box; the x axis is parallel to long sides of box, the y axis is perpendicular to the x axis and lies in the plane of the upper surface of sample. Observations are made in the xy -plane. Angle ψ is initial angle between long and short sides of deformation box. Shown is the starting configuration of the object population with aspect $R_{ob} = 3$. The matrix material is the non-Newtonian material (Polydimethylsiloxane with 25 wt% BaSO₄). Small particles of different color and size were randomly dispersed on the surface of the sample for flow analyses with the program PatMatch (Bons and Jessell, 1995).

Table 6.1 Experimental conditions

Type of deformation	plane strain deformation
W_n	1, 0.8, 0.6
Initial dimensions [mm]	150 x 100 x 100 mm
Initial angle β	135°
Finite simple shear strain of one experiment (two stages)	4.6 ($W_n=1$), 2.6 ($W_n=0.8$), 1.1 ($W_n=0.6$)
R_{xy} of one experiment (2 stages)	22.7 ($W_n=1$), 9.5 ($W_n=0.8$), 3.4 ($W_n=0.8$)
Simple shear strain rate [s^{-1}] ($W_n=1$)	$1 \cdot 10^{-3} s^{-1}$
Stretching rate along x-axis [s^{-1}] ($W_n=0.8, 0.6$)	$3.3 \cdot 10^{-4} s^{-1}$
Matrix material	a) PDMS, linear Newtonian viscous, $\eta = 3 \cdot 10^4$ Pa s b) PDMS + 25% BaSO ₄ , non-linear non-Newtonian viscous, power law behavior, stress exponent = 1.23
Object material	rigid India rubber
Object dimensions [mm]	6 mm x 2 mm, 5 mm x 2.5 mm
Initial number of objects	34

6.3 Analytical Methods

Analyses of experiments consisted of (1) a comparison of the measured SPO as a function of R_{xy} , W_n and finite strain and the corresponding analytically predicted SPO using the formulas provided by Ghosh and Ramberg (1976), (2) measurement of the mean orientation of the long axis of objects with the x-direction of the shear zone and (3) investigation of flow characteristics.

Equations of Ghosh and Ramberg (1976) were applied to the starting object populations to obtain the analytically predicted SPO development. These equations were derived for elliptical inclusions in a Newtonian viscous matrix, while in experiments objects are rectangular. They can, however, be used here as experiments by ten Brink (1996) have shown that rectangular objects rotate at approximately the same rate as elliptical objects with a similar axial ratio.

The shape preferred orientation of a fabric can be quantified using the statistical concentration parameter (κ) of a von Mises distribution (Masuda et al., 1999) and angle β of the mean orientation of the long axis of objects with the x-direction of the shear zone. The von Mises distribution is commonly referred to as the equivalent to a normal distribution that is specifically suitable to statistically evaluate orientation data. The concentration parameter k is proportional to the normalized length (R) of the mean resultant vector of the oriented data, here the orientations of the long axis of the objects. R ranges from 0 to 1 whereas κ ranges from 0 (no alignment) to infinity (perfect alignment). Using κ is preferred for its larger range of values (for more details see Appendix B). The angle β is the angle between the x-axis and the mean resultant vector of all object orientations. It has been assumed by some workers that β corresponds to the orientation α of the maximum finite stretching axis (e.g. Fernandez, 1987; Ildefonso et al., 1992a).

The distribution of deformation within the samples was measured using the program PatMatch, which employs the pattern-matching method of Bons and Jessell (1995). This program measures the displacement field between two stages of deformation to derive various deformation parameters, such as the distribution of absolute finite strain (R_{xy}) and deformation of an initial grid of perpendicular closely spaced lines within a deformed sample.

6.4 Experimental results

In experiments with rigid objects of $R_{ob} = 3$ three main features are observed (Fig. 6.2): (a) in all experiments there is a pronounced discrepancy between analytically predicted and experimental κ values, particularly in experiments with non-Newtonian matrix material and non-simple shear deformation; (b) the intensity of SPO increases with decreasing W_n and (c) κ is higher for a non-Newtonian, power law matrix material than for a Newtonian matrix.

Significant strain localization during deformation was observed in all experiments (Fig. 6.3). High strain simple shear zones (high R_{xy}) anastomose and low strain zones develop close to the rigid objects. Trains of objects, bounded by shear zones, had a width of 1.2 to 1.6 times the longest axis of the rigid objects. Individual high strain zones remained stable for part of the progressive deformation history (Fig. 6.4).

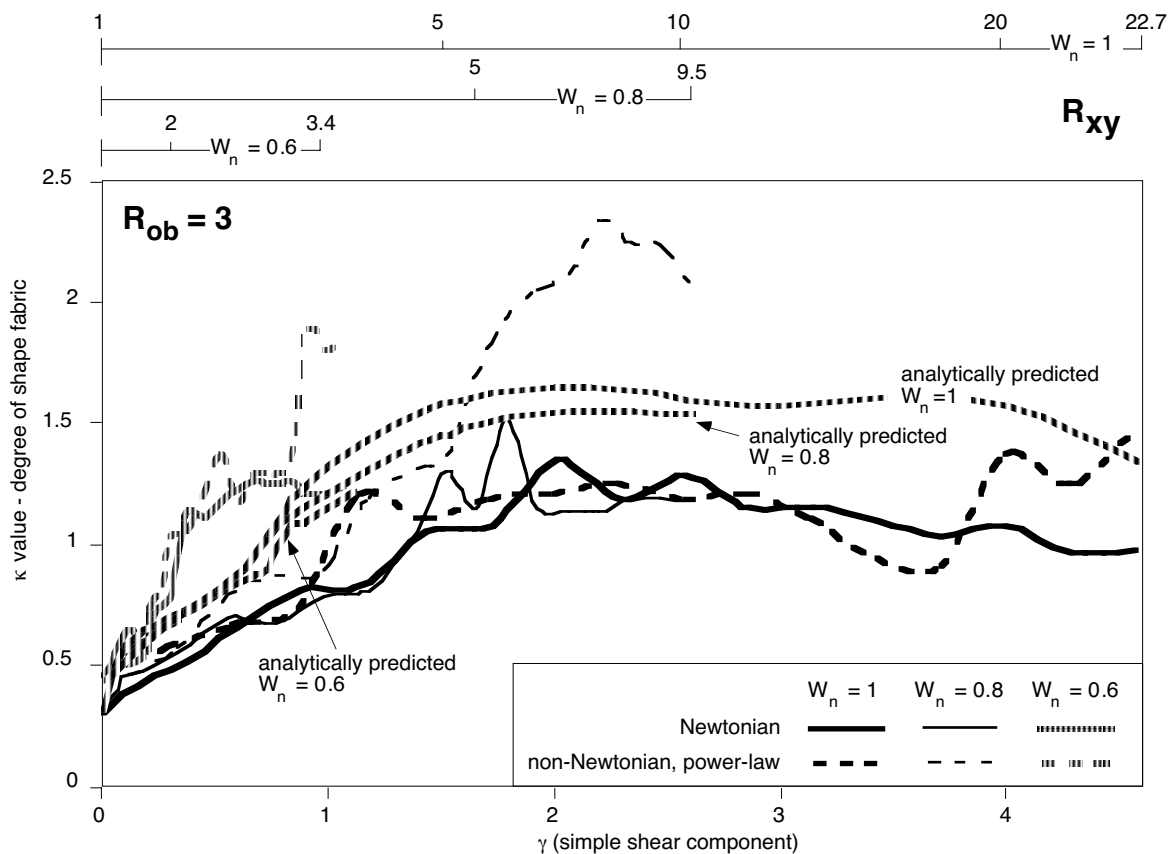


Figure 6.2 Results of experiments with a population of objects with $R_{ob} = 3$ plotting the degree of shape preferred orientation (concentration parameter κ of a von Mises distribution) as a function of magnitude of the simple shear strain γ . Corresponding R_{xy} values are given at top of diagram. Depicted are measured κ values and analytically predicted values (Ghosh and Ramberg, 1976).

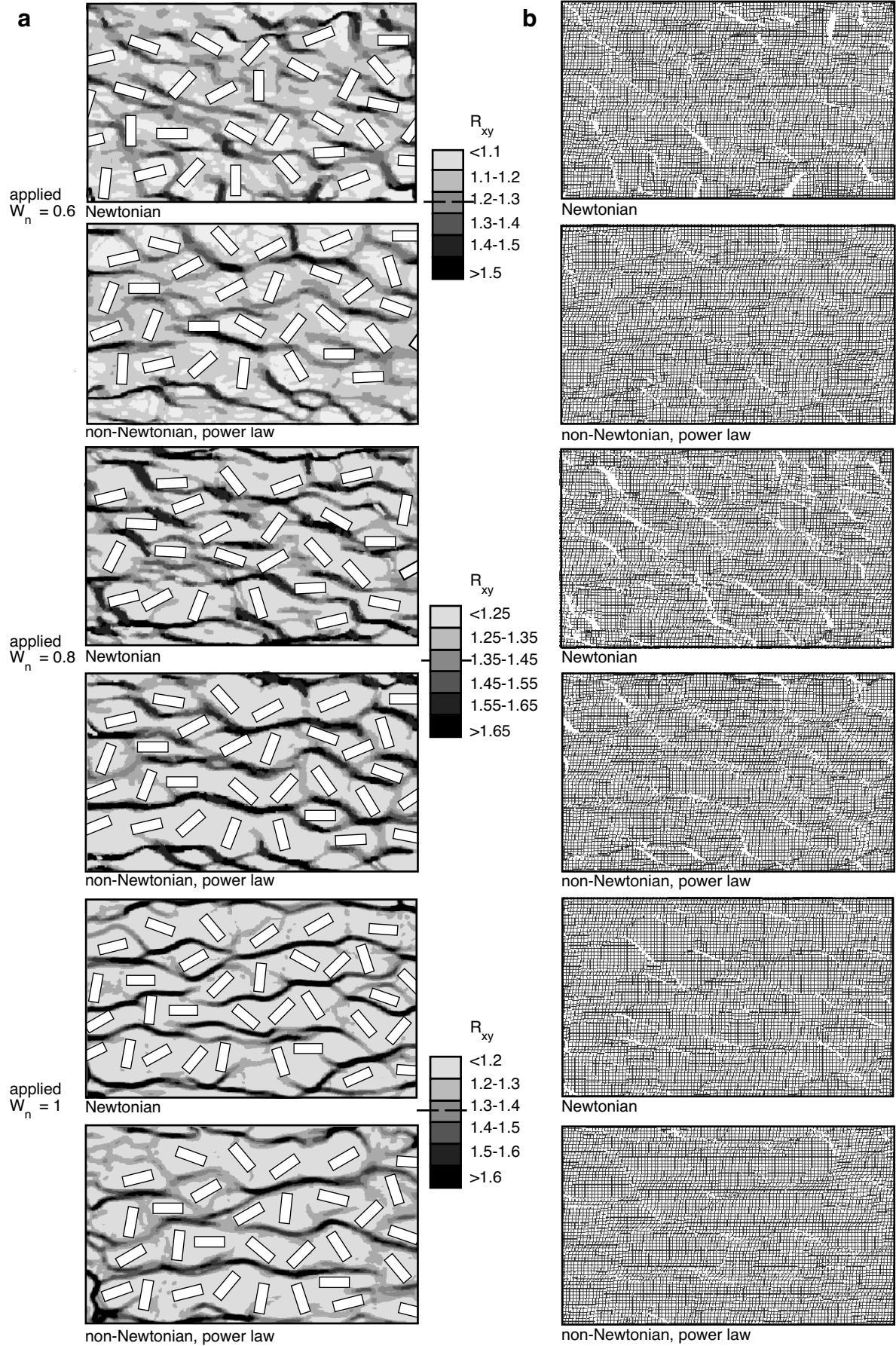


Figure 6.3 (opposite side) Flow analyses of experiments with population with $R_{ob} = 3$ for 3 different W_n and 2 matrix materials. Long sides of the rectangles are parallel to the long sides of deformation box (cf. Fig. 6.1). (a) Gray scale plots of R_{xy} . High strain zones appear as dark bands (high R_{xy}), light zones have low R_{xy} values. Rectangular boxes show position and orientation of objects. Dashed lines in legend represent the applied R_{xy} . In non-Newtonian, power law matrix material high strain shear zones extend over larger distances and separate trails of objects positioned in low strain areas. With increasing W_n high strain shear zones show an higher angle to the long sides of the deformation box. (b) Deformation of originally rectangular grid generated by the program Pat-Match (Bons and Jessell, 1995). In deformed grid simple shear zones appear dark due to tilt of grid lines. Pure shear zones show rectangles. White areas are due to problems of program to find patterns in deformed sample.

The geometry of anastomosing shear zones closely resembles the pattern of an anastomosing disjunctive foliation with cleavage domains and microlithons (e.g. Stephens et al. 1979). With an increasing amount of pure shear component, high strain zones at a high angle to the shear zone (C'-shear band orientation; Berthé et al. 1979) become more abundant. Deformed grids (Fig. 6.3b) show that strain partitioning is coupled with partitioning of pure and simple shear components during progressive deformation.

High strain zones exhibit simple shear deformation and low strain zones in between high strain zones show pure shear dominated deformation. In non-Newtonian matrix material high strain zones are slightly anastomosing and extend in some cases over the whole model. In the Newtonian matrix material high strain zones are less pronounced, less discrete and shorter than in the non-Newtonian material. Angle β is always smaller than α (Fig. 6.5). The difference between β and α is largest for the Newtonian matrix, where β can even become slightly negative. It is therefore not realistic to consider β equal to α ; if β is negative this could lead to erroneous shear sense interpretation.

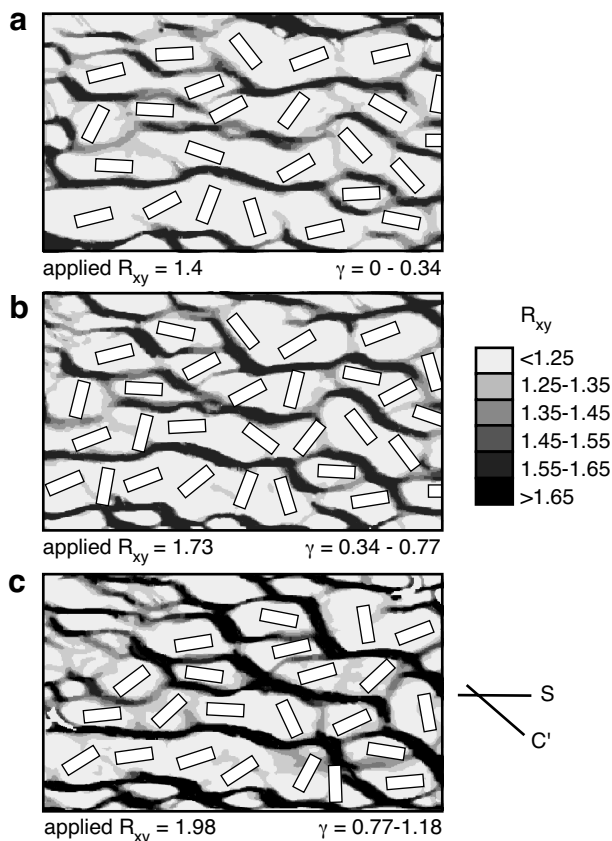


Figure 6.4 Gray scale plots of R_{xy} in experiments with population of $R_{ob} = 3$ for three strain intervals during progressive deformation at $W_n = 0.8$. The matrix material is non-Newtonian (PDMS + 25wt% $BaSO_4$). Rectangular boxes show the position and orientation of objects. (a) Simple shear strain $\gamma = 0 - 0.34$; (b) $\gamma = 0.34 - 0.77$; (c) $\gamma = 0.77 - 1.18$. During progressive deformation the position of high strain shear zone remains largely constant. Shear bands oblique to the shear plane i.e. C' shear band orientation develop. Note that the axial ratio R_{xy} of the strain ellipse increases non-linearly with increasing simple shear strain γ .

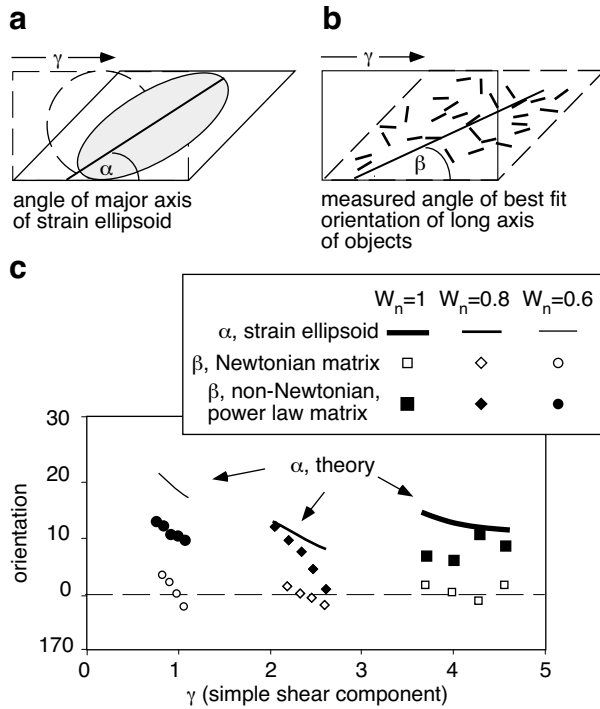
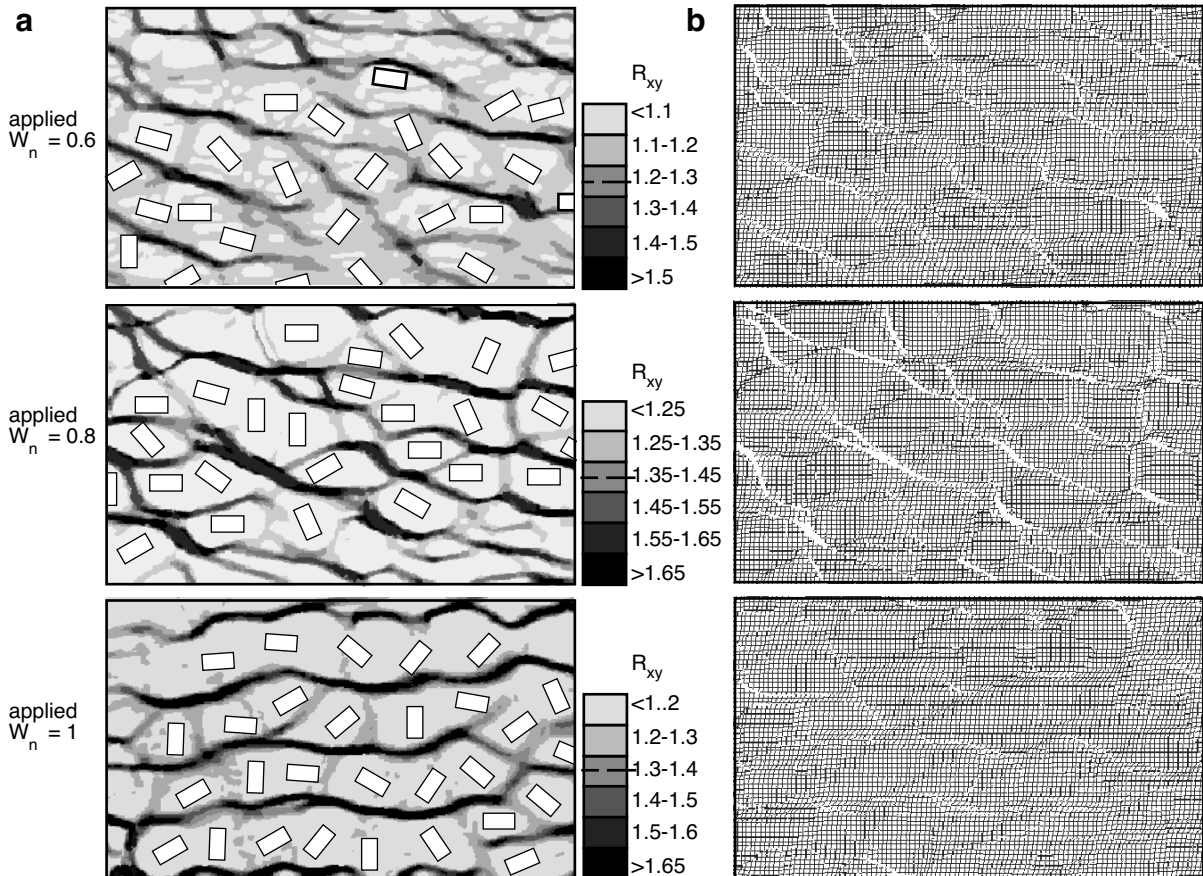
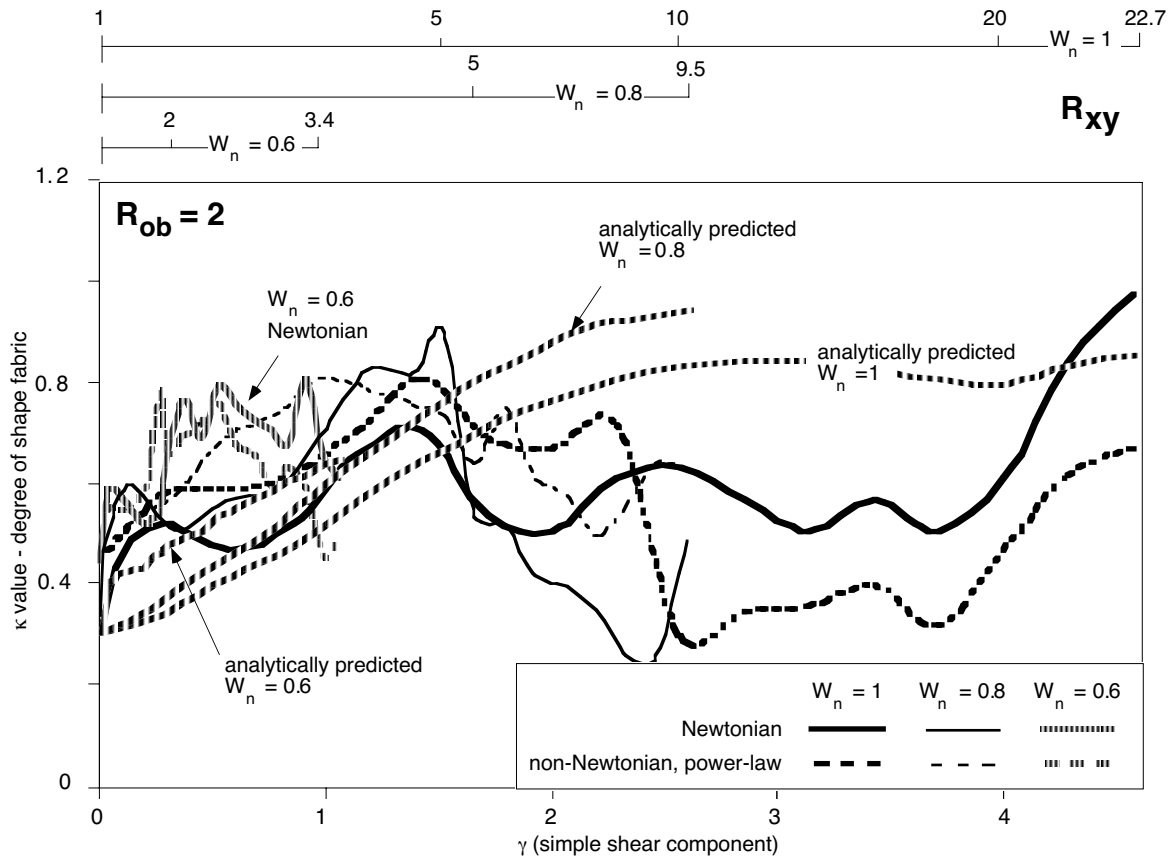


Figure 6.5 Diagram illustrating the change in orientation of the mean orientation of a population of rigid objects with $R_{ob} = 3$ during progressive deformation in comparison with orientation of the long axis of the strain ellipsoid. (a) Angle α is the angle between the long axis of the strain ellipse and the x-axis. (b) Angle β is angle between the mean of the orientation of the objects and the x-axis. (c) Graph showing angles α and β as a function of the simple shear component of finite strain.

Experiments with objects populations of $R_{ob} = 2$ (Fig. 6.6) show (a) a highly variable SPO intensity i.e. highly variable κ values during progressive deformation, (b) a slight increase in SPO intensity i.e. κ values with decreasing W_n , (c) minor discrepancy between analytically predicted and experimental SPO intensity and (d) only in parts of the deformation path higher SPO intensities in non-Newtonian matrix material than in the Newtonian matrix. High strain zones are present in both matrix materials. These are shorter and anastomose more strongly than high strain zones in experiments with $R_{ob} = 3$ (Fig. 6.7a). Similar to experiments $R_{ob} = 3$, low strain zones i.e. low R_{xy} values are seen close to rigid objects. High strain zones which are at an high angle to the shear direction become increasingly abundant with decreasing applied W_n . Partitioning of W_n in simple shear and pure shear dominated zones increases with decreasing applied W_n (Fig. 6.7b). In experiments with object populations of $R_{ob} = 2$ it is not possible to determine a meaningful value of β as SPO intensities are too weak.

Figure 6.6 (opposite side - top) Results of experiments with a population of objects with $R_{ob} = 2$ plotting the intensity of shape preferred orientation (concentration parameter κ of a von Mises distribution.) as a function of magnitude of the simple shear strain γ . Corresponding R_{xy} values are given at top of diagram. Depicted are measured κ values and analytically predicted values (Ghosh and Ramberg, 1976).

Figure 6.7 (opposite side - bottom) Representation of the distribution of R_{xy} and the corresponding deformed grids as calculated using PatMatch (Bons and Jessell, 1995) for experiments of rigid particles with $R_{ob} = 2$. The matrix material is non-Newtonian, power law matrix material (PDMS + 25wt% BaSO₄). (a) Gray scale plots of R_{xy} ; high strain zones appear dark and low strain zones light. Dashed lines in legend represents the applied value of R_{xy} for the specific deformation type. Rectangular boxes show the position and orientation of particles. With decreasing W_n the orientation of the high strain shear zones show an increasing angle to the shear zone boundary and a shortening of the length of individual bands. (b) Corresponding deformed grids; in the deformed grid simple shear zones appear dark due to tilt of grid lines. Pure shear zones show rectangles. White areas signify that the program had problems to find the corresponding pattern in deformed sample.



6.5 Discussion

Our experiments confirm the predictions from analytical solutions that (a) populations with high aspect ratios and (b) a high pure shear component of flow of the matrix material result in a high intensity of the shape preferred orientation. Additionally, results show that for populations with an object ratio of 3 the intensity of SPO is higher in a non-Newtonian, power law than in Newtonian matrix material.

From analytical solutions (Ghosh and Ramberg, 1976, Jezek et al., 1996) it is known, that rotation rates of objects oriented with their long axis close to the shear plane are low if deformation is pure shear dominated and if the object aspect ratio is high. In experiments, at high strain, the summed rotational behaviour of individual elongate objects of the object population with high object ratios results in a high shape preferred orientation, whereby the mean orientation of the longest axis of the objects forms at small angle with the shear plane. Populations of objects with low aspect ratios ($R_{ob} = 2$) produce low SPO intensities (low κ values) in all experiments. In experiments, pure shear dominated zones with low R_{xy} values are close to rigid objects and high strain simple shear zones characterized by high R_{xy} value anastomose around objects. During progressive deformation, an object initially oriented at a high angle to the shear plane is likely to be close to a high strain simple shear zone; hence, it will rotate with a high rotation rate towards the shear plane. An object which is oriented at a low angle to the shear plane, is most likely to be positioned within a low strain, low W_n zone; hence, its rotation rate will be slow and it will tend to remain with its long axis at an low angle to the shear plane during progressive deformation. The partitioning of rotation rates of objects is more pronounced for populations of high object aspect ratios than low object aspect ratios. This explains why population of rigid objects of $R_{ob} = 3$ show a higher degree of SPO (high κ values) than those with low aspect ratios. In experiments with a matrix material with a non-Newtonian, power law flow behaviour, the partitioning between high strain simple shear and low strain pure shear dominated zones is most pronounced. Therefore, in such materials the intensities of SPO is higher than in Newtonian material. With decreasing kinematic vorticity number, the area of low strain, low W_n increases; hence, the intensity of SPO increases.

The pattern of strain and W_n partitioning has important implications for the development of shear zones, shear bands and of shape fabrics in general and the applicability of flow type analyses in terms of kinematic vorticity number. Localized shear zones extending over large areas are likely to develop in rocks characterized by non-Newtonian, power law rheology and competence heterogeneities. Within shear zones, abundant shear bands oblique to the shear zone boundary are most likely to develop if the type of deformation is pure shear dominated i.e. low applied kinematic vorticity number. Experiments suggest that the abundance of shear bands and their orientations could be used to determine the type of deformation in terms of kinematic vorticity number. This observation supports the work of Passchier (1991b) who proposed that so-called ECC-fabrics (extensional crenulation cleavage; Platt, 1979; White, 1979b; Platt and Vissers, 1980) can develop more easily in stretching shear zones than shear zones with bulk simple shear flow.

Kinematic vorticity number analyses using for example porphyroclasts are generally performed in a localized volume of rock (Passchier, 1987; Vissers, 1989; Masuda et al., 1995, Wallis, 1995; Beam and Fisher, 1999). Commonly the result of this analysis is extrapolated to the bulk deformation of the whole rock. Our experiments show that W_n may locally deviate significantly from the bulk applied W_n . Therefore, extrapolation of analyses performed in a

specific volume of rock can be extrapolated to the deformation of a larger volume of rock only with caution. Especially in rocks in which the matrix exhibits non-Newtonian, power law rheology, locally derived kinematic vorticity numbers may yield erroneous values with respect to the true overall deformation type. Even in Newtonian matrix materials, locally derived W_n values will commonly yield wrong values with respect to the bulk deformation type. This problem may be solved by looking for foliation and aggregate and mineral lineation, or for fabric distribution in a rock. Partitioning as described above gives rise to strong gradients in fabric. Measurements in several representative parts of such a fabric may give more accurate results.

When comparing and applying experimental results to real rocks it should be noted that for rocks deforming in a ductile regime, a non-Newtonian flow behaviour with a stress exponent between 2 and 5 has been proposed (Kirby and Kronenberg, 1987). Hence, effects attributed to the non-linearity of the rheology of the matrix material are expected to be more pronounced in nature.

Experiments investigating the effect of the density of a population of rigid objects on the fabric development in different types of deformation and matrix materials were not in the scope of this paper and still remain to be performed and analysed.

6.6 Conclusion

Analogue modelling of shape fabric development of a population of rigid objects dispersed in a viscous matrix show that the shape preferred orientation is a function of (a) shape of rigid objects, (b) the type of flow and (c) the rheological properties of the matrix material. Populations with object aspect ratios of 3 can be used for kinematic analyses i.e. determination of type of deformation and shear sense, and strain analyses. Analyses of the shape preferred orientation of populations with object aspect ratios of 2 may yield wrong results in terms of shear sense and the intensity of shape preferred orientation is not an indicator of finite strain or type of deformation.

The intensity of the developed shape preferred orientation increases with an increase in pure shear component. In a matrix material with non-Newtonian, power-law flow behaviour the intensity of the shape preferred orientation is higher than in a Newtonian viscous material. In both matrix materials high strain simple shear zones i.e. shear bands develop. Adjacent are low strain pure shear dominated zones i.e. microlithons, that are characterized by relatively stable similarly orientated trains of rigid objects oriented at low angles to the shear plane. Partitioning between high strain simple shear and low strain zones pure shear dominated flow is most pronounced in the non-Newtonian, power-law material. Therefore, in such materials kinematic vorticity analyses on the scale of partitioning may not necessarily represent the kinematic vorticity of bulk flow.

Acknowledgements

Special thanks to Ralf Halama (University of Mainz) for his assistance during experiments.

Chapter 7

Experimental modeling of viscous inclusions in a circular high strain shear rig

Implications for the interpretation of shape fabrics and deformed enclaves

Abstract

Deformation experiments with initially spherical and prolate viscous inclusions suspended in a viscous Newtonian matrix in a circular high strain shear rig provide insights in the shape development of inclusions in high strain shear zones during progressive deformation. Inclusions with a specific viscosity ratio with respect to the matrix material show distinct types of three-dimensional shape development. For instance, at a high viscosity ratio between matrix and inclusion a pulsating ellipsoid develops, which both continuously rotates and changes its shape from a sphere to an ellipsoid and back to a sphere. Experiments show that the shape of an inclusions which has a viscosity different to the matrix material cannot be taken as a reliable indicator for neither finite strain nor the type of strain in terms of plane, constrictional or flattening strain. The viscosity ratio between inclusion and matrix depends on the flow laws of the matrix and inclusion materials, shear stress, strain rate and finite strain. In shear zones, in which strain rates are heterogeneous from boundary to centre the complexities of the factors viscosity contrast and power law flow result in a large number of possible shape developments of inclusions such as mafic enclaves or mineral aggregates.

7.1 Introduction

Rocks are in most cases inhomogeneous on several scales of observation and can often be described as inclusions dispersed in a homogeneous matrix material. Examples of such inclusions are aggregates of recrystallized feldspar and mica in a matrix of predominately quartz, clusters of sillimanite laths in a matrix of quartz, feldspar and mica, oolithes in a matrix of fine grained calcite and pebbles in a conglomerate. Corresponding features in felsic or mafic igneous rock are mafic or felsic enclaves, xenoliths and mineral aggregates consisting of specific minerals e.g. tourmaline-quartz-feldspar (Tobisch and Williams, 1998 and references therein).

During deformation such inclusions deform and develop deformation structures such as aggregate lineations and oblate, planar or prolate shaped objects. These features provide an important tool for structural analyses as shape changes of inclusions carry information of the geometry and history of deformation of the host rock. Therefore, for over 100 years, shape fabrics and associated linear fabrics have been used to determine the presence and direction of tec-

tonic transport (e.g. Shackelton and Ries, 1984; Ellis and Watkinson, 1987; Shackelton, 1993; Peterson and Robinson, 1993), to determine the type of deformation in terms of plane, constrictional and flattening strain (e.g. McLelland, 1984; Wenk, 1998; Tobisch and Williams, 1998) and transtension and transpression (e.g. Druguet et al., 1997; Tikoff and Greene, 1997; Fossen and Tikoff, 1998; Schulmann et al., 1997; Krabbendam and Dewey, 1998; Tikoff and Fossen, 1999), and to perform strain analysis (e.g. Shimamoto and Ikeda, 1976; Fry, 1979; Ramsay and Huber, 1983 and references therein; Lisle et al., 1983; Paterson, 1983 and references therein; Lisle, 1985).

Problems in the interpretation of shape fabrics arise from the common assumption that as a first approximation an inclusion is a passive, deformable object with a viscosity equal to that of the matrix material. Hence, characteristics of deformation i.e. finite strain and type of deformation, derived from the shape of the inclusion is often directly correlated with the characteristics of deformation of the host rock. However, in nature the viscosity of inclusion and matrix commonly differ from each other and therefore matrix and inclusion deform not homogeneously. The changes in shape of an inclusion cannot be directly related to the deformation of the bulk rock as the change in three-dimensional shape of an inclusion during progressive deformation depends strongly on the viscosity contrast between an inclusion and host rock. This dependency of shape development and viscosity ratio of inclusion and matrix material has already been subject of several studies and has been applied to geological problems by a number of authors (Gay, 1968a, 1968b, 1976; Gay and Fripp, 1976; Bilby et al., 1975, 1976; Lisle et al., 1983; Lisle, 1985; Paterson, 1983; Freeman, 1985, 1987; Freeman and Lisle, 1987; Weijermars, 1993, 1997; reviews in Treagus and Lan, 2000). Eshelby (1957) put forward 5 equations describing the motion of an isolated ellipsoidal inclusion in a matrix of contrasting viscosity, given the viscosity contrast, rate of deformation and vorticity (the irrotational and rotational components of the flow applied to the enclosing matrix). Later, analytical work (e.g. Lisle et al., 1983; Lisle, 1985; Freeman, 1985, 1987; Freeman and Lisle, 1987; Weijermars, 1993, 1997) largely extended the models of Eshelby (1957) and drew attention to possible misinterpretation of inclusion shapes as direct indicators of the shape and orientation of the strain ellipse.

A number of analogue experiments were performed which investigate the shape development of viscous inclusions dispersed in a viscous matrix during progressive deformation. Ralison (1984) and Bentley and Leal (1986) performed experiments modeling oil drops in a more viscous oil, Ghosh and Sengupta (1973) looked at the shape of viscous inclusions in low strain deformation, Passchier and Sokoutis (1993) and ten Brink and Passchier (1995) at the development of mantled porphyroclasts, and Treagus et al. (1996) and Treagus and Lan (2000) at the changing shape of square objects.

Despite the mentioned work and the usefulness of shape fabrics to characterize deformation in rocks, the shape development of inclusions dispersed in a matrix is still incompletely understood. For instance, Weijermars (1993, 1997) predicted for inclusions with a viscosity contrast of inclusion to matrix of 2 to 5 a pulsating shape development i.e. continuous change between sphere and ellipsoid during progressive simple shear plane strain deformation. In contrast, analytical solutions of other authors e.g. Freeman (1985, 1987), Freeman and Lisle (1987) predict continuous stretching of an inclusion during progressive deformation under the

same conditions. Specific phenomena related to inclusions dispersed in a matrix are still only in parts understood; one exemplary phenomena is the large variety of observed inclusion shapes present in one individual shear zone within different lithologies and with a progression in strain.

We decided to improve the understanding of the shape development of viscous inclusions dispersed in a homogeneous matrix by carrying out experiments focussing on dependence of the shape development and rotation of a single inclusion in a circular (Couette flow) shear zone with respect to finite strain, strain rate and rheology of matrix and inclusion material. This work extends the investigations carried out by Passchier and Sokoutis (1993) and ten Brink and Passchier (1995) to deforming internally homogeneous inclusions which exhibit viscosity ratios between inclusion and matrix which are realistic for rocks. In the first part of the paper (section 7.2 and section 7.3) we present, analyse and discuss results of analogue experiments. In the second part (section 7.4 and section 7.5), we discuss implications of the experimental results on the interpretation of shape fabrics observed in rocks.

7.2 Experimental method

7.2.1 General outline

To be able to model high strain deformation we use an apparatus which can model non-coaxial circular Couette flow i.e. flow within a cylindrical plane strain shear zone. This has the advantage that the shear zone has no beginning or end and therefore very high strain values can be reached. The apparatus is a modification of the viscometer used by Passchier and Sokoutis (1993). An inner cylinder, which rests on a sharp point to minimise friction, is setup in an upright position within a fixed transparent outer cylinder (Fig. 7.1a). The rotation of the inner cylinder around its vertical axis results in circular simple shear flow between the outer and inner cylinder. A rotor is attached to the inner cylinder and rotation is achieved by suspending two weights which are attached to the rotor by ropes.

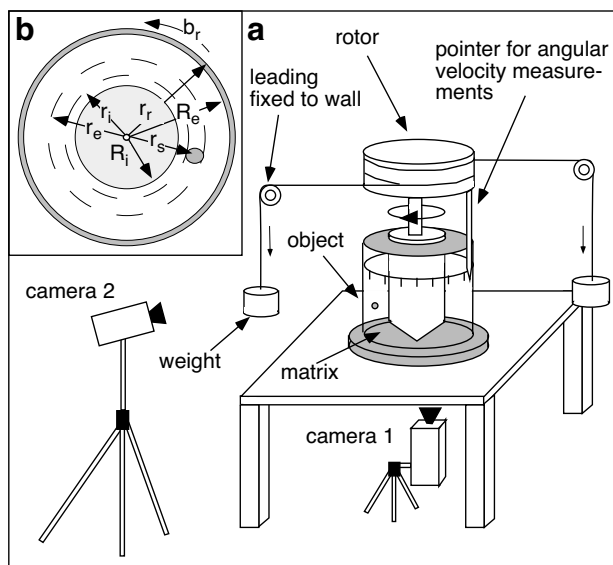


Figure 7.1 (a) Sketch of the apparatus used for analogue modeling. Note that different objects are not in scale. Camera 1 monitors the shape development of the object through the transparent floor of the apparatus and camera 2 through the transparent outer cylinder. The supporting frame for the rotor was left out to allow better representation of the shear chamber; (b) schematic drawing of the rotational shear zone of the apparatus and abbreviations used in calculations. Used abbreviations are given in Tab. 7.1 (end of chapter).

To allow 3D-monitoring during experiments the wall and floor of the apparatus are transparent. To perform experiments, a transparent material is filled in the space between the two cylinders to a height of 8-10 cm and spherical and prolate ellipsoidal inclusions are inserted in the matrix at a depth of 3 cm. Non-spherical inclusions are placed with their long axis in the plane parallel to the floor of the deformation apparatus and at different angles to the tangent of the curvature of the cylinders (cf Fig. 7.4). The inclusions themselves are marked by two perpendicular coloured marker lines to allow analysis of rotation of the inclusion during deformation. In experiments the inner radius of the outer cylinder (R_e ; Fig. 7.1b; Tab. 7.1 - end of chapter) is 85 mm while the radius of the inner cylinder (R_i) can be varied between 35 mm, 50 mm and 68 mm. The different radii of the inner cylinders result in different width of the shear zone and curvature of the shear surface. Bulk weight suspended from the rope attached to the rotor is between 0.025 kg to 2.25 kg on each side. Experiments lasted from 1 minute to a few hours, depending on the viscosity of the matrix, strain rate and finite shear strain. In several cases the experiment was interrupted to rewind the rope on the rotor.

7.2.2 Experimental Materials

7.2.2.1 Materials used

We used three different non-toxic and transparent linear viscous (Newtonian) matrix materials, two of which are also used as inclusion materials. Material PDMS is the polymer Polydimethylsiloxane (trade name: SGM 36; purchased from Dow Corning, GB) with a viscosity of $3.3 \cdot 10^4$ Pa s (at 25 °C) and is used as both matrix and inclusion material; the matrix and inclusion material PDMS/200 Fluid is a mixture of two different polymers (PDMS and 200 Fluid 30 000cs; the latter was purchased from Drawin, Germany) with a viscosity of $2.9 \cdot 10^4$ Pa s (at 25 °C) and material AK is a silicon oil (trade name: AK 50 000; purchased from Wacker, Germany) with a viscosity of 50 Pa s and is exclusively used as matrix material. Two additional materials were used for viscous inclusions; material RG which is made of pure Rhodorsil Gomme and RG68/PI32 which is a mixture of 32wt% white Plastilina (PI) and 68 wt% Rhodorsil Gomme (RG). Rhodorsil Gomme (produced by the Societe des Chemiqués Rhone-Poulenc, France) is a pinkish opaque bouncing putty with a Newtonian flow behaviour and a viscosity of $9 \cdot 10^3$ Pa s (at 25 °C). Plastilina is a Swedish version of Harbutt's Plastiline (McClay 1976) and its flow behaviour is non-linear viscoelastic. The mixture of the RG68/PI32 exhibits a slight non-Newtonian, power law viscoelastic flow behaviour with a power law stress exponent n of 1.25. It exhibits a viscosity of 5.5 to $6 \cdot 10^4$ Pa s in the range of performed experimental strain rates. Note that the properties given above apply exclusively to shear strain rates between 10^{-4} to 10 s $^{-1}$.

Several workers investigated the rheological properties of most of the used materials (McClay, 1976; Weijermars, 1986; Koyi, 1988) in terms of kinematic viscosity. Nevertheless, it is common that there are rheological differences between batches of material even if obtained from the same suppliers. We, therefore, measured the viscosity of the used materials at different strain rates and temperatures using a rotational viscosimeter (Brookfield Digital Viscometer; Model DV II+) and a torsional rheometer Rheometric RMS 800. Results obtained by the latter apparatus are discussed in detail in Chapter 4. Figure 7.2a depicts the measured properties of the different materials used. In general, the viscosity of used materials decreases nonlinearly with decreasing temperature (e.g. PDMS and PDMS/200 Fluid, Fig. 7.2b).

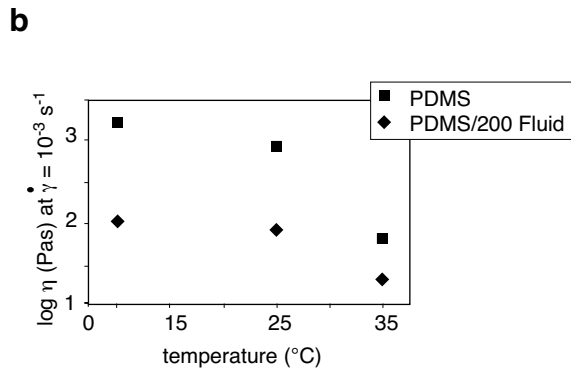
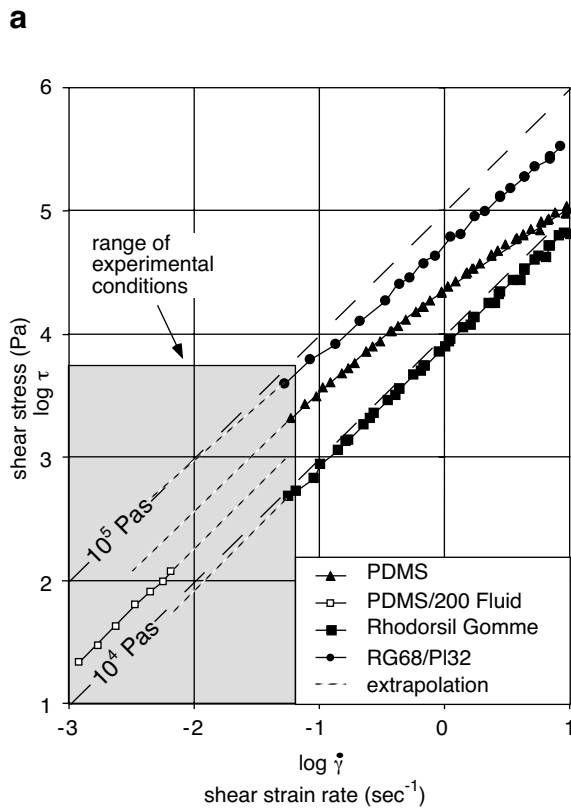


Figure 7.2 Graphs illustrating the kinematic viscosity of used analogue materials; (a) log shear stress (τ) to log shear strain rate ($\dot{\gamma}$) for used materials except AK, dashed (long dashes) diagonal lines represent viscosity contours in Pa s, a line of slope 1 signifies Newtonian flow behavior, dashed (short dashes) lines signify extrapolation of data; (b) temperature dependence of the viscosity of PDMS and PDMS/200 Fluid.

To assure constant rheological properties of materials during all experiments we performed experiments at temperatures between 23 °C and 25 °C. This results in a maximum viscosity error of 50 Pa s.

For the analyses of our experiments we define a viscosity ratio $\eta_{(i/m)}$ as the ratio of the viscosity of the inclusion and the viscosity of the matrix at the applied shear stress τ . The viscosity of PDMS, PDMS/Fluid, AK and RG are constant at different shear due to Newtonian flow behaviour, whereas the viscosity of RG68/PI32 slightly changes with shear stress as the flow law of the inclusion material is non-Newtonian (cf. Fig. 7.2a). Errors in the calculation of $\eta_{(i/m)}$ due to temperature variations and errors in the viscosity measurements are between 5% for the combinations of viscous Newtonian materials and 10% for combinations involving the non-Newtonian, power law flow material RG68/PI32.

7.2.2.2. Characteristics of materials deforming according to power law flow

Power law materials (e.g. RG68/PI32) are characterized by the equation

$$\dot{\gamma}_{(t)} = k\tau_{(t)}^n \quad (\text{Eq. 7.1})$$

where $\dot{\gamma}_{(t)}$ is the shear strain rate at time t , $\tau_{(t)}$ the shear stress at time t , k a constant and n the stress exponent. The effective viscosity $\eta_{(t)}$ at time t during deformation is a function of stress and strain rate. The latter relationship is expressed in

$$\eta_{(t)} = \frac{\tau_{(t)}}{\dot{\gamma}_{(t)}} \quad (\text{Eq. 7.2})$$

If we combine equations 1 and 2, the effective viscosity at time t is defined by

$$\eta_{(t)} = \frac{1}{k}\tau_{(t)}^{1-n} \quad (\text{Eq. 7.3})$$

According to Eq. 7.3 a power law material with an n -value > 1 shows a power law decrease in effective viscosity with increasing shear stress. The higher the n -value the more rapid is the decrease in effective viscosity with increasing shear stress. Therefore, an inclusion that deforms according to power law flow exhibits different effective viscosities if deformed at different shear stress values.

7.2.3 Analysis of experiments

To allow a quantitative analysis of the shape development and rotation of inserted viscous inclusions shear strain rate and shear stress have to be known during experiments. Shear strain rate and shear stress in a rotational shear zone are not homogeneous across the shear zone (i.e. between the two cylinders); both increase from the outer to inner part of the shear zone (see Fig. 2: Masuda et al., 1995a). Shear strain rate at a certain point in the shear zone depends on the position of this point with respect to the centre of rotation. We adopt the formulas put forward by Masuda et al. (1995a) to calculate the shear strain rate (Eq. 7.4) and shear stress (Eq. 7.5) in the rotational shear zone. We consider it a sufficient approximation to use those equations which are exclusively applicable to Newtonian materials, as in our experiments the matrix, i.e. more than 99.8 vol% of deformed material exhibit Newtonian flow behaviour. Influence of the inclusion on this behaviour is within our range of measurement error. Used equations (after Masuda et al., 1995) are for the the shear strain rate

$$\dot{\gamma} = \frac{-2(\Omega_i - \Omega_e)}{\frac{1}{R_i^2} - \frac{1}{R_e^2}} \frac{1}{r^2} \quad (\text{Eq. 7.4})$$

and for the shear stress

$$\tau = \eta \dot{\gamma} = \frac{-2(\Omega_i - \Omega_e) \eta}{\frac{1}{R_i^2} - \frac{1}{R_e^2}} \frac{1}{r^2} \quad (\text{Eq. 7.5})$$

where Ω_i the angular velocity of the inner cylinder, Ω_e the angular velocity of the outer cylinder (in our case = 0), η the viscosity of the matrix material, R_i the radius of the inner cylinder (35 mm, 50 mm, 68 mm) and R_e the radius of the outer cylinder (85 mm). The variable r represents the distance of the inserted inclusion from the centre of rotation (Fig. 7.1b). Shear strain rates are between 10^{-4} s^{-1} and 7 s^{-1} and shear stress values range between 5 and 7000 Pa. We used the centre of the inclusion as a reference point. Inaccuracy in the measurement of true r and the simplification in using the centre of the inclusion as a reference point results in shear stress and shear strain rate calculation errors of up to 5%. The accuracy of the calculation of the viscosity of an inclusion material is in the range of 2% - 5%.

The angular velocity of the inner cylinder Ω_i is calculated according to

$$\Omega_i = \frac{b_r}{r_r t} \quad (\text{Eq. 7.6})$$

where b_r is the distance along the circle with radius r_r (Fig. 7.1b), and t the elapsed time necessary to move the distance b_r .

To fully describe the shape development of an ellipsoid at least three values describing the axes of the ellipsoid are necessary. As we assume constant volume in our experiments the number of necessary values is reduced to 2; these are two aspect ratios of the principal axis of the inclusion i.e. aspect ratio of axis a and b ($R_{(a/b)}$), a and c ($R_{(a/c)}$) or c and b ($R_{(c/b)}$) where a is longer than b and c (cf. Fig. 7.4). Due to the curved nature of the shear surface deforming objects can exhibit curved axes (cf. Fig. 7.4a).

Data show that deformation stabilizes at strains above 0.06. Observations on the changing shape of inclusions were collected during the stable deformation leg. Monitoring and documentation of the development and evolution of the different inclusions was done by sets of digital photographs or slides that were taken throughout the experiment and subsequently analysed. Measurements of the aspect ratios of the inclusions during experiments is performed with an accuracy of 5%. The shape development of inclusions during deformation are reproducible in the range of measurement errors (Fig. 7.3).

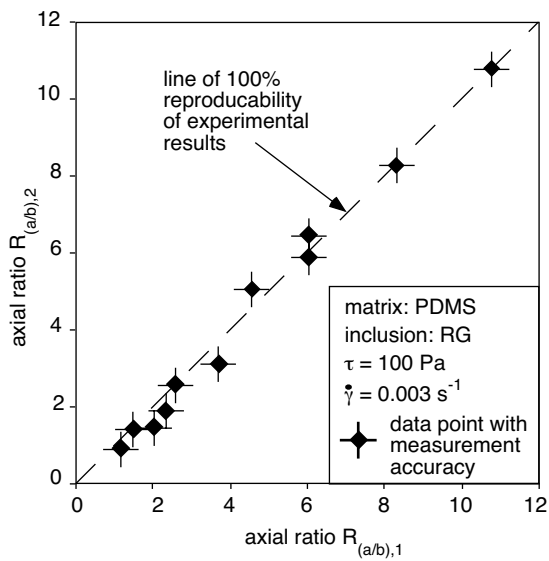


Figure 7.3 Diagram depicting the aspect ratio $R_{(ab)}$ of inclusions deformed in two experimental runs (1 and 2) plotted against each other. Experimental conditions and materials used are identical for both runs. Values of the axial ratios are identical for both experiments in the range of measurement accuracy; accordingly, experimental results are reproducible.

7.2.4 Reference frames

To accurately describe the position and orientation of an inclusion with respect to the apparatus and shear zone boundaries we use two reference frames. These are (a) a polar coordinate system centred at the centre of rotation, and (b) an inner cartesian coordinate system with its origin at the centre of the inclusion. The polar coordinate system is defined by r_s , which is the line between the centre of rotation and the centre of the inclusion, and h_s which lies in the plane of the shear zone surface and is parallel to the vertical axes of both cylinders, and an angle β which is the angle between r_{si} i.e. the line between the initial position P_i of the center of the inclusion and the centre of rotation and r_{sy} (Fig. 7.4).

The inner cartesian reference frame (Fig. 7.4) is defined by three axes; T_s which is the tangent to the curvature of the shear zone surface at the current position P_γ , r_s which is line between the shear zone surface at position P_γ and the centre of rotation and h_s which lies in the plane of the shear zone surface and is parallel to the vertical axes of both cylinders connecting position P_γ and the floor. All three axes r_s , T_s and h_s are perpendicular to each other. At an infinitely small increment T_s represents axis x of the shear zone as commonly used in the geological literature (e.g. Twiss and Moores, 1992; Passchier and Trouw, 1996) which parallel to the shear direction, r_s axis y which is normal to axis x, hence T_s , and h_s axis z which perpendicular to the xy, hence $T_s r_s$ -plane (Fig. 7.4c, Fig. 7.4d). Prolate objects are inserted with their ab-plane parallel to the $T_s r_s$ -plane i.e. xy-plane of the shear zone and axis c parallel to h_s . We define α as the angle between the orientation of the tangent T_a to the longest axis a of an inserted initially prolate ellipsoid and T_s .

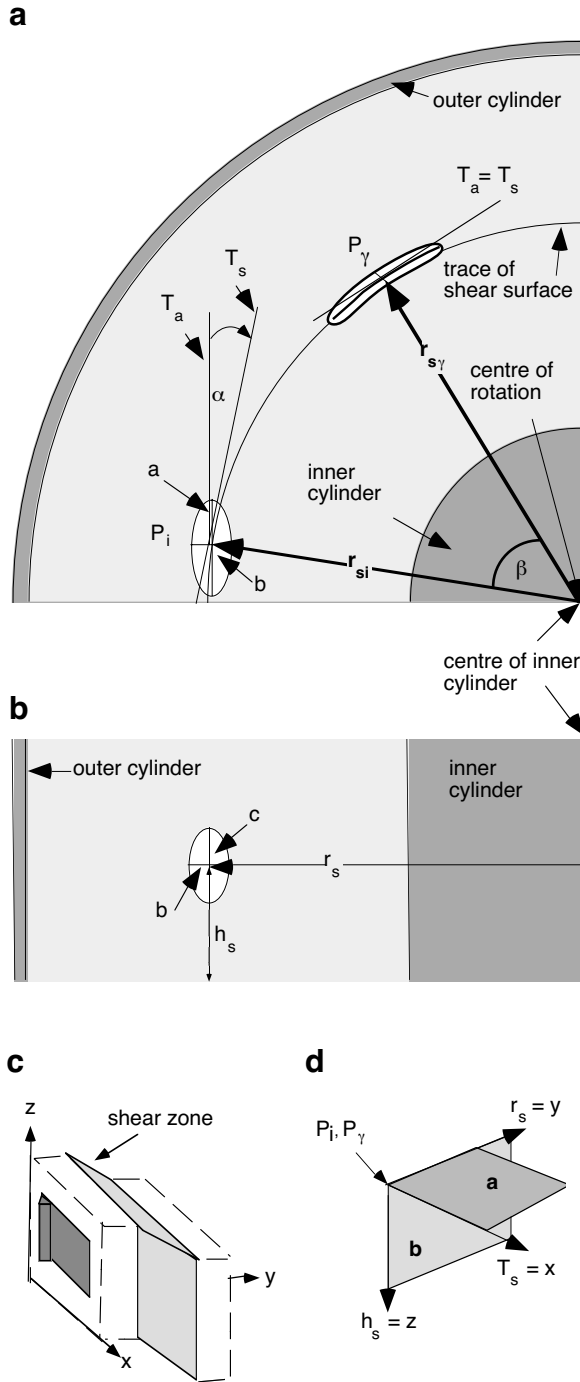


Figure 7.4 Schematic diagram depicting the two reference frames used in the analyses of experiments. See text for detailed explanation of the two reference frame and Tab. 7.1 for abbreviations; symbols *a*, *b* and *c* are the 3 perpendicular axis of an inclusion. **(a)** View from top or bottom of the apparatus; bold, thick lines and arrows depict elements of the polar coordinate system; **(b)** view parallel to trace of the radius of the apparatus; **(c)** geological shear zone nomenclature; **(d)** representation of inner cartesian reference frame; planes illustrated in **(a)**, **(b)** and the corresponding orientation of axis as defined under **(c)**.

7.3 Experimental results

7.3.1 Types of shape development of inclusions during progressive deformation

Inclusions exhibit three different general types of shape development. These we categorise as follows (Fig. 7.5):

type 1: rotating rigid sphere or rotating rigid ellipsoid

type 2: permanently stretching ellipsoid divided to type 2a, type 2b and type 2c subgroups

type 3: pulsating ellipsoid

Aspect ratios of rotating rigid spheres and ellipsoids are constant during progressive deformation (Fig. 7.5). Permanently stretching ellipsoids permanently change their aspect ratio during progressive deformation. Those that develop from a sphere stretch continuously (a increases, b decreases, c remains constant in length) and axes a, b, c are parallel to T_s , r_s , h_s of the shear zone. Those that develop from an initially prolate inclusion that was inserted at an angle to the shear surface rotate and change shape simultaneously until a is parallel to T_s , that is a between T_a and T_s is 0. If the initial angle a is smaller than 90° the long axis a decreases and b increases in length, and c remains constant both in orientation and length. If the angle is larger than 90° the ellipsoid rotates into the shear surface and a increases continuously, while b decreases and c remains constant in length. When the orientation of a approaches parallelism to T_s rotation ceases and inclusion shape development is characterized by an increase of a (parallel to T_s), decrease of b (parallel to r_s), while c remains constant in length (parallel to h_s) (Fig. 7.5, Fig. 7.6a). Accordingly, an initially prolate shaped inclusion which is inserted in the matrix at an angle smaller than 90° to the shear surface can first deform to a sphere i.e. the linear shape is lost and then reassume an ellipsoidal shape (Fig. 7.5, Fig. 7.6b). At very high strain, folding of the inclusion may occur (Fig. 7.5b). Fig. 7.7 shows the non-linear dependence of the aspect ratio $R_{(a/b)}$ and bulk strain for inclusions with $\eta_{(i/m)}$ of 0.27 (RG), 1 (PDMS) and 1.8 to 2 (RG68/PI32), which were dispersed in a PDMS matrix. Inclusions with $\eta_{(i/m)} < 1$ plot on the left hand side, $\eta_{(i/m)} = 1$ on and $\eta_{(i/m)} > 1$ on the right hand side of the curve of the theoretical aspect ratios of the strain ellipsoid. Plotted in a Flinn diagram (Flinn 1978) three subgroups can be distinguished; values of subgroup (2a) generally plot in the flattening field ($\eta_{(i/m)} = 0.27$, RG), subgroup (2b) on the plane strain line ($\eta_{(i/m)} = 1$, PDMS) and subgroup (2c) in the constrictional field ($\eta_{(i/m)} = 1.8-2$, RG68/PL32) (Fig. 7.8).

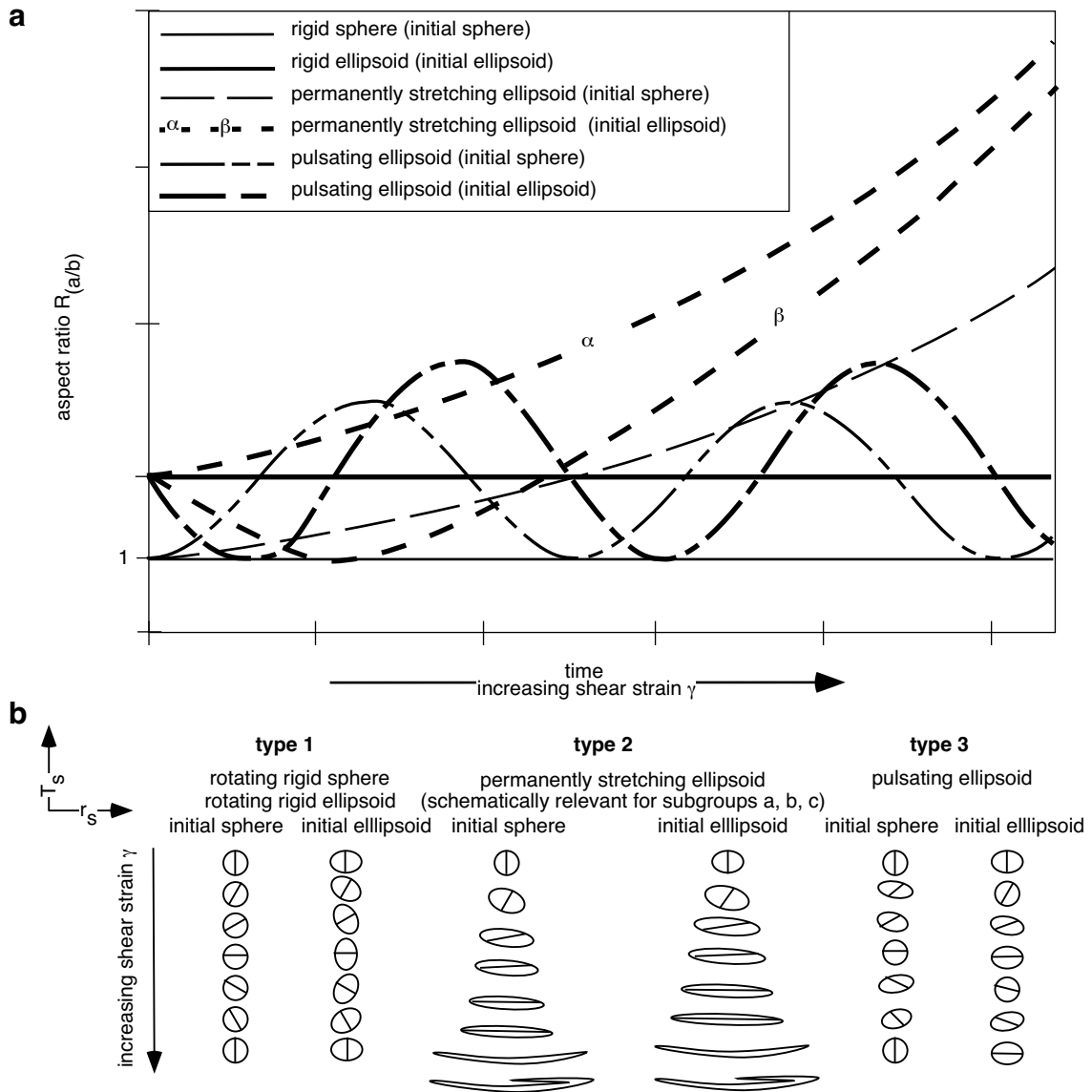


Figure 7.5 Schematic graphs depicting for the different types of inclusion shape development; **(a)** graph schematically plotting aspect ratio $R_{(a/b)}$ against increasing shear strain which corresponds to a progression in the duration of experiments; **(b)** representation of the different types of shape development during progressive deformation in the xy -plane of the shear zone i.e plane parallel to the floor of the apparatus.

Pulsating ellipsoids rotate into and out of the flow surface and periodically shorten to a sphere and lengthen to an ellipsoid in a pulsating manner (Fig. 7.5, Fig. 7.6c). This pulsating behaviour is only observed in experiments with AK as a matrix and PDMS ($\eta_{(i/m)} = 660$), RG ($\eta_{(i/m)} = 180$) and PDMS/Fluid ($\eta_{(i/m)} = 580$) as inclusions. The higher the viscosity contrast, the longer the pulsation period and the smaller the change in maximum aspect ratios (Fig. 7.9a). Plotted on a Flinn diagram, values for these inclusion materials plot in the constrictional field or on the line defining plane strain (Fig. 7.9b).

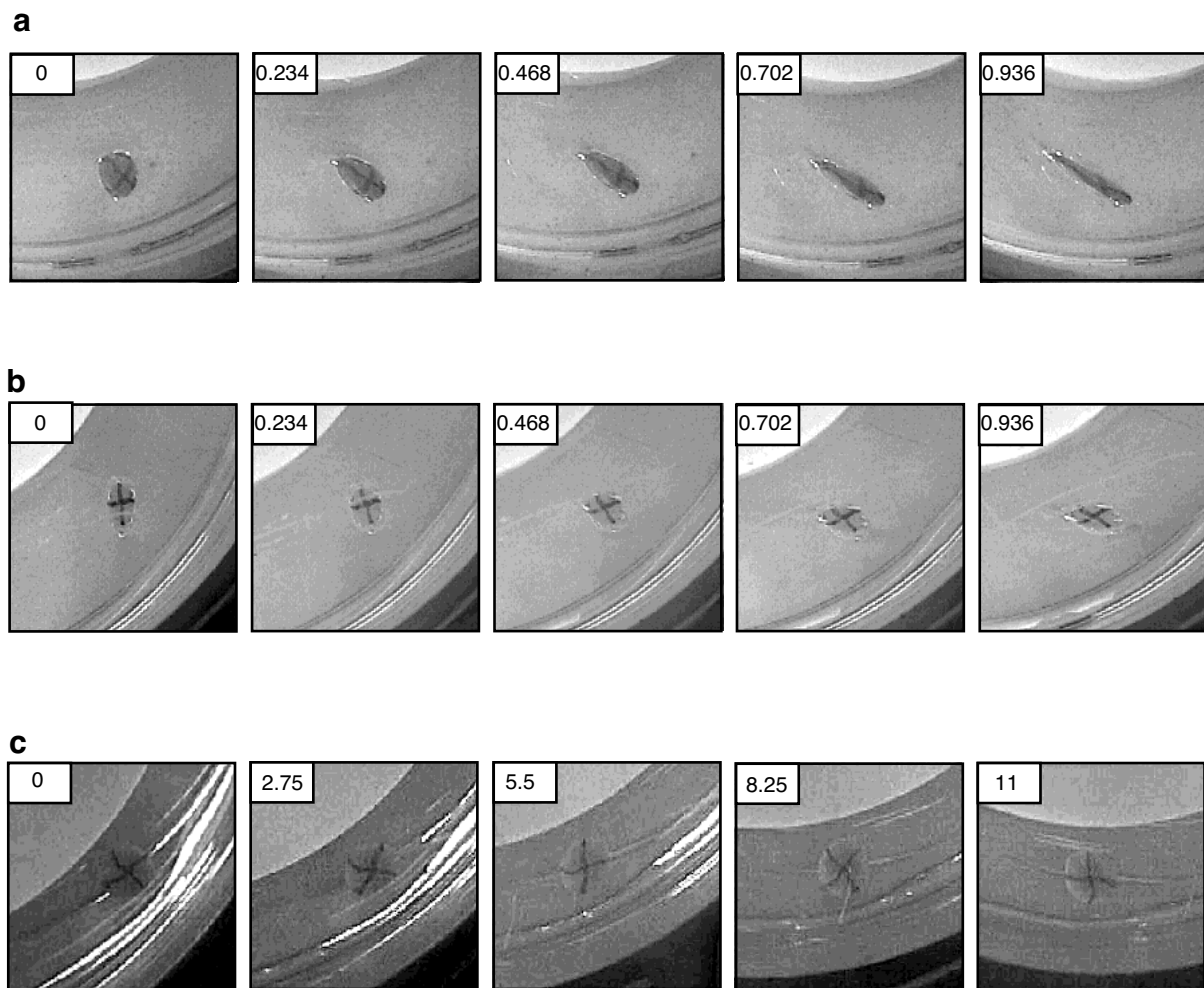


Figure 6 Series of photographs depicting the different types of shape development during progressive deformation; (a) permanently stretching ellipsoid, initial sphere. Experimental conditions are: shear strain rate: 0.0026 s^{-1} , inclusion material: RG, matrix material: PDMS, time interval between pictures: 90 s; (b) permanently stretching ellipsoid, initial ellipsoid at angle to shear zone boundary. Experimental conditions are: shear strain rate: 0.0026 s^{-1} , inclusion material: RG68/Pl32, matrix material: PDMS, time interval between pictures: 90 s; (c) pulsating ellipsoid: Experimental conditions are: shear strain rate: 0.275 s^{-1} , inclusion material: RG, matrix material: Ak, time interval between pictures: 10 s. Photographs are taken perpendicular to the $r_s T_s$ plane (cf. Fig. 7.4) of the shear zone, numbers given as insets in pictures correspond to simple shear strain values.

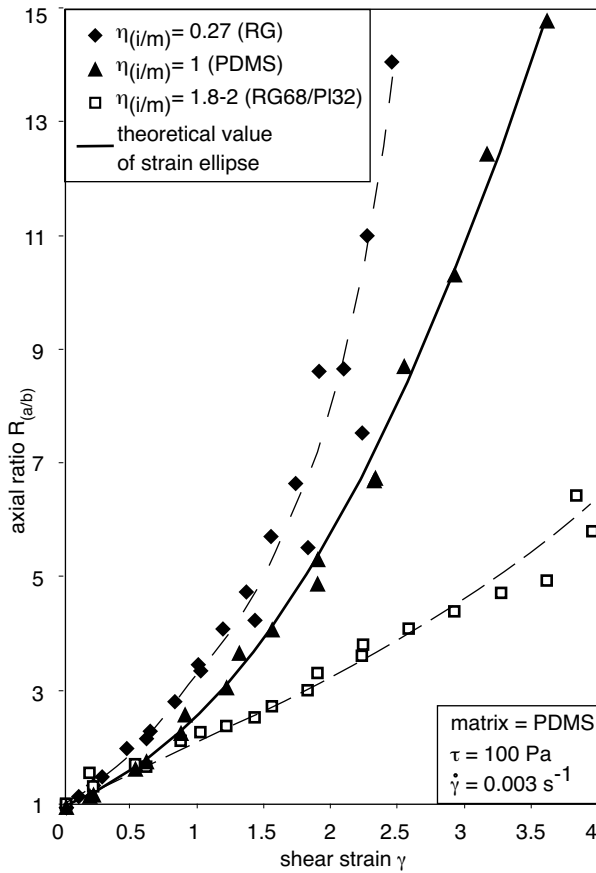


Figure 7.7 Diagram depicting the non-linear dependence of the aspect ratio $R_{(a/b)}$ of inclusion exhibiting different viscosity ratios (0.27, 1, 1.8-2) and shear strain; additionally, the theoretical aspect ratios of the strain ellipsoid is shown; note that except for a viscosity contrast of 1, several experiments were performed and plotted on the diagram.

To evaluate whether or not the pulsating nature of the inclusions is an artefact of the circular shear zone model, we performed experiments with two inner cylinders with different radii ($R_i = 35$ mm, $R_i = 68$ mm) which produce two different curvatures of the shear surface. In both cases experiments show the same type of inclusion shape development (pulsating ellipsoid) and the same period of pulsation in terms of finite strain. If the pulsating shape development type were a result of the curvature of the shear zone, differences in the period of pulsation would be expected. We therefore believe that this type of shape development is not caused by the curvature of the shear surface and represents a true shape development type that occurs if a viscous inclusion dispersed in a viscous matrix deforms.

Figure 7.10 shows the dependence of the different types of shape development (for definition see above) on the viscosity ratio between inclusion and matrix assuming perfect bonding between matrix and inclusion. Permanently stretching spheres or ellipsoids develop if $h_{(i/m)}$ is between 1 and at least 2; pulsating spheres develop at $180 < \eta_{(i/m)} < 660$ and rotating rigid spheres or ellipsoids occur at $\eta_{(i/m)} < 1200$.

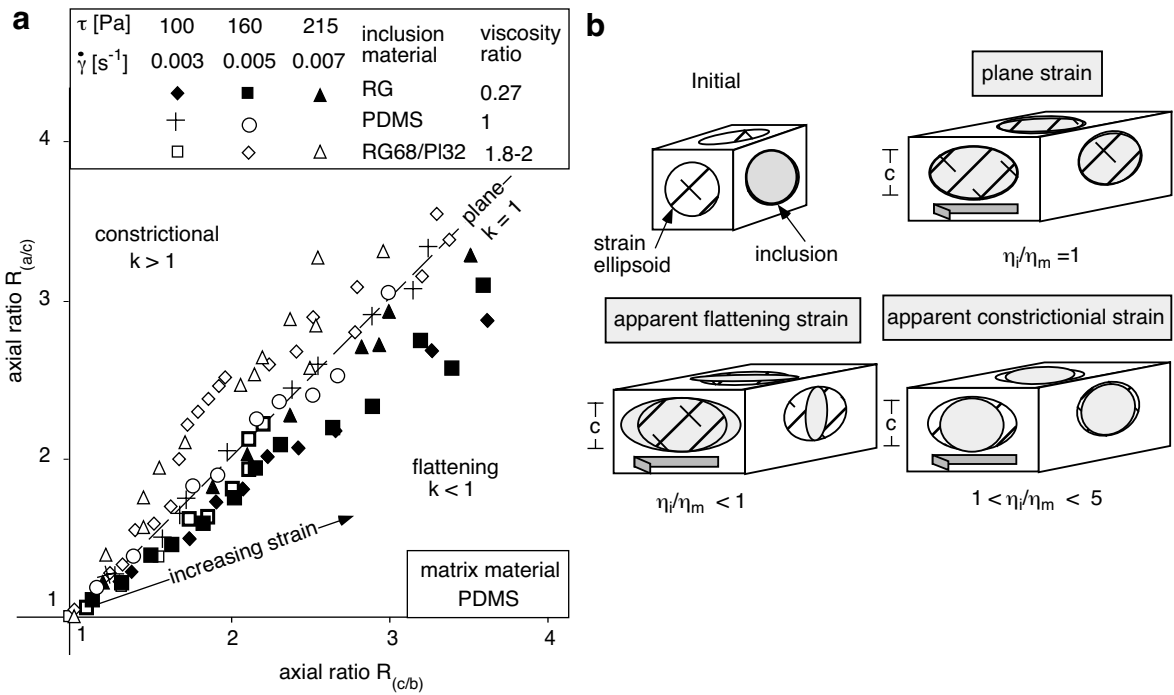


Figure 7.8 (a) Diagram depicting the aspect ratios of inclusions of viscosity ratios of 0.27, 1 and 1.8-2 plotted in a Flinn diagram (Flinn, 1978); inclusions of viscosity ratios of 0.27 plot in the flattening field, inclusions of viscosity ratios of 1 on the plane strain line and inclusions of viscosity ratios of 1.8-2 generally plot in the constrictional field in the range of measurement errors; **(b)** schematic representation of the discrepancy between the shape of the true strain ellipsoid and the shape of inclusions at different viscosity ratios; note, that the axis c of the inclusion always remains constant.

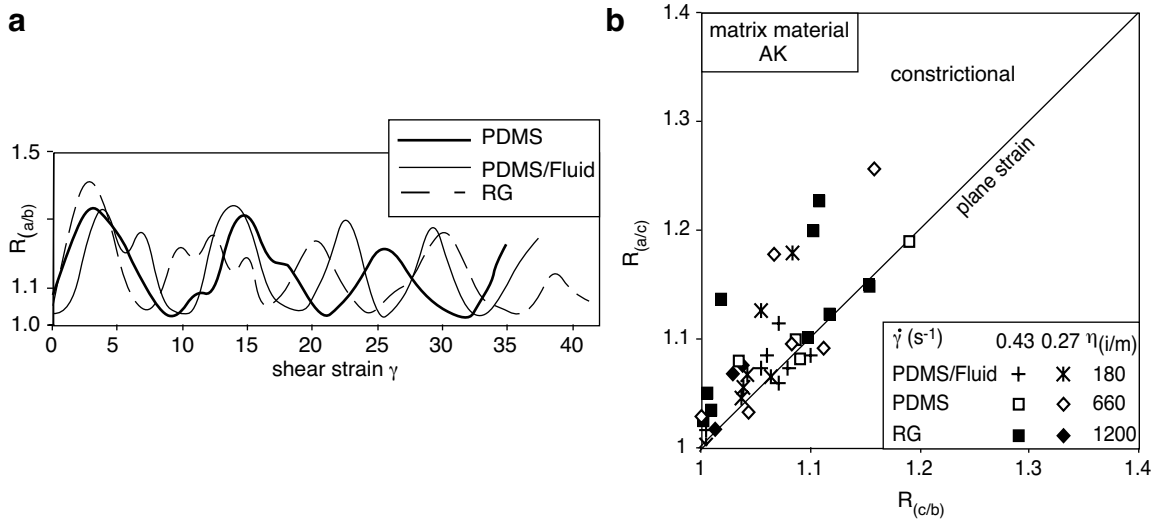


Figure 7.9 Graphs illustrating the character of pulsating ellipsoids. **(a)** Plot of $R_{(a/b)}$ against strain for three different inclusion of three different viscosity ratios (180, 660, 1200). The higher the viscosity contrast the longer the pulsation period and the smaller the change in aspect ratios; **(b)** Flinn diagram with values of inclusions of experiments using AK as the matrix material.

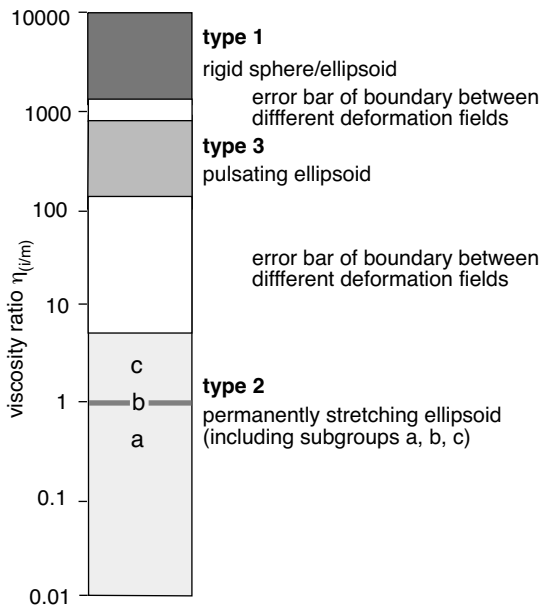


Figure 7.10 Plot summarizing experimental results relating viscosity ratio to the type of inclusion shape development; symbols a, b and c correspond to subgroups of shape development type 2 (permanently stretching ellipsoid); white boxes are error bars; for further details see text.

7.3.2 Rotation rate of rigid inclusions

The dependence of rotation velocity of a rigid object i.e. inclusions exhibiting type 1 shape development on shear strain rate, aspect ratio and orientation of the long axis of the object relative to the shear plane in two dimensions in viscous flow has already been discussed by Jeffery (1922). Theoretically, in simple shear viscous flow the velocity of rotation i.e. rotation rate of a rigid elliptical inclusion exhibiting a high bonding between matrix and inclusion is given

$$\dot{\Phi} = \dot{\gamma} \frac{(R^2 \cos^2 \phi + \sin^2 \phi)}{R^2 + 1} \tag{Eq. 7.7}$$

(Jeffery, 1922), where $\dot{\gamma}$ is the simple shear strain rate, $\dot{\Phi}$ the angle between the long axis of the ellipsoid and the normal to the flow i.e. shear surface and R the axial ratio of the inclusion. In words, this equation shows that the rotation rate of a non-spherical inclusion is strongly dependent on the angle of the maximum elongation axis to the shear surface. If we consider deformation in three dimensions, Eq. 7.7 is only relevant if the principal inclusion axes a and b are in the xy-plane of the shear zone (cf. Fig. 7.4c for shear zone nomenclature). When an inclusion lies with its long axis parallel to the flow surface, the rotation rate has a minimum value, and when the long axis is perpendicular to the flow surface it has a maximum value. The variation in rotation rate is also proportional to the aspect ratio of the inclusion; with increasing aspect ratio the difference between the minimum and maximum rotation rate increases (Jeffery, 1922). Despite the fact that Jeffery’s equations refer to a planar shear zone, the experimental results closely fit the theoretical values within 5% deviation, as long as long axis of the inclusion is a fifth or less of shear zone. Inclusions which are significantly larger exhibit during

parts of the deformation path higher and lower rotation rates than theoretical values. This phenomenon is attributed to the shear strain rate gradient across the shear zone width and the change in flow patterns with different shear zone width to object diameter ratios (ten Brink, 1996).

7.3.3. Inhomogeneity of internal deformation of deforming viscous inclusions

We observed some degree of inhomogeneity in the internal deformation of inclusions. These slight inhomogeneities are shown by the inhomogeneous deformation of the marker stripes (cf. section 7.2.1). In general, deformation of an inclusion observed on the *xy*-plane is stronger at the rim than in the centre and marker stripes deform to sigmoidal shapes as a result of these heterogeneities (cf. Passchier and Sokoutis, 1993). In inclusion material RG68/PI32 these heterogeneities may lead to viscosity difference within the inclusion. This effect is estimated to influence the viscosity by less than 1%; therefore these effects are not considered in the calculation of $\eta_{(i/m)}$.

7.3.4 Discussion of experimental results

Experiments show that there is a general relationship between the type of inclusion shape development, the apparent type of deformation in the sense of flattening, constrictional and plane strain, shear stress, shear strain rate and material properties. The subdivision of inclusion shape development type 2 (cf. section 7.3.1) i.e. permanently stretching ellipsoid or spheroid can be explained by the effect of viscosity ratio on the shape development of an inclusion. Subgroup type 2a occurs if the viscosity ratio is also below 1 i.e. the inclusion is less competent than the matrix. This type of shape development behaviour was already predicted by Freeman and Lisle (1987) and is supported by our experiments. At a viscosity ratio of 1 (subgroup type 2b) the apparent strain type shown on the Flinn diagram is plane strain i.e. the same as the true strain type. If the viscosity ratio is just slightly higher than 1 (subgroup type 2c) (e.g. RG68/PI32 inclusion in PDMS) the resultant apparent deformation type is constrictional ($k > 1$) (Fig. 7.8). This behaviour has also been predicted by Freeman and Lisle (1987). Freeman and Lisle (1987), though, did not predict a shape development type that we call a pulsating ellipsoid (inclusion shape development type 3). Means et al. (1980) showed already that pulsating strain should exist in nature. Weijermars (1993, 1997) investigated analytically the effect of pulsating strains on the shape development of viscous inclusions dispersed in a viscous matrix of differing viscosities. Weijermars (1993, 1997) predicted that a pulsating shape development of a viscous inclusion should be most noticeable at a viscosity ratio between 1 and 5. Results show that up to a viscosity ratio of 2 the shape development type is not pulsating but that of a permanently stretching sphere or ellipsoid. Only at $\eta_{(i/m)}$ of 180 to 660 a pulsating behaviour of an inclusion is seen. We suggest that in our experiments no pulsating strains as defined by Weijermars (1993, 1997) exist, but attribute the pulsating nature of inclusions shape development to the effect of a stress gradient, changes in rotation rate with the deformation of the inclusion and a bow-tie flow pattern around the viscous inclusion (ten Brink and Passchier, 1992; Passchier, 1993; Passchier, 1994; Passchier et al., 1994). The exact flow pattern around an object is dependent on the boundary conditions (Bons et al., 1997) and the degree of coherence between object and embedding matrix (Pennacchioni et al., 2000). Following results of Bons et al.

(1997) and Pennacchioni et al. (2000) we suggest that the flow pattern is generally speaking bow-tie shaped if the shape development type is a pulsating ellipsoid. An effect of such a bow-type flow pattern are stress concentrations at protruding corners (ten Brink and Passchier, 1995; ten Brink, 1996) which lead to changes in the shape of the inclusion i.e. the aspect ratio. At the same time the object rotates at a rate which is determined by the changing aspect ratio (cf. Ea. 7.7) and due to this rotation the flow pattern is effected and stress concentrations result in further deformation of the inclusion (Fig. 7.11).

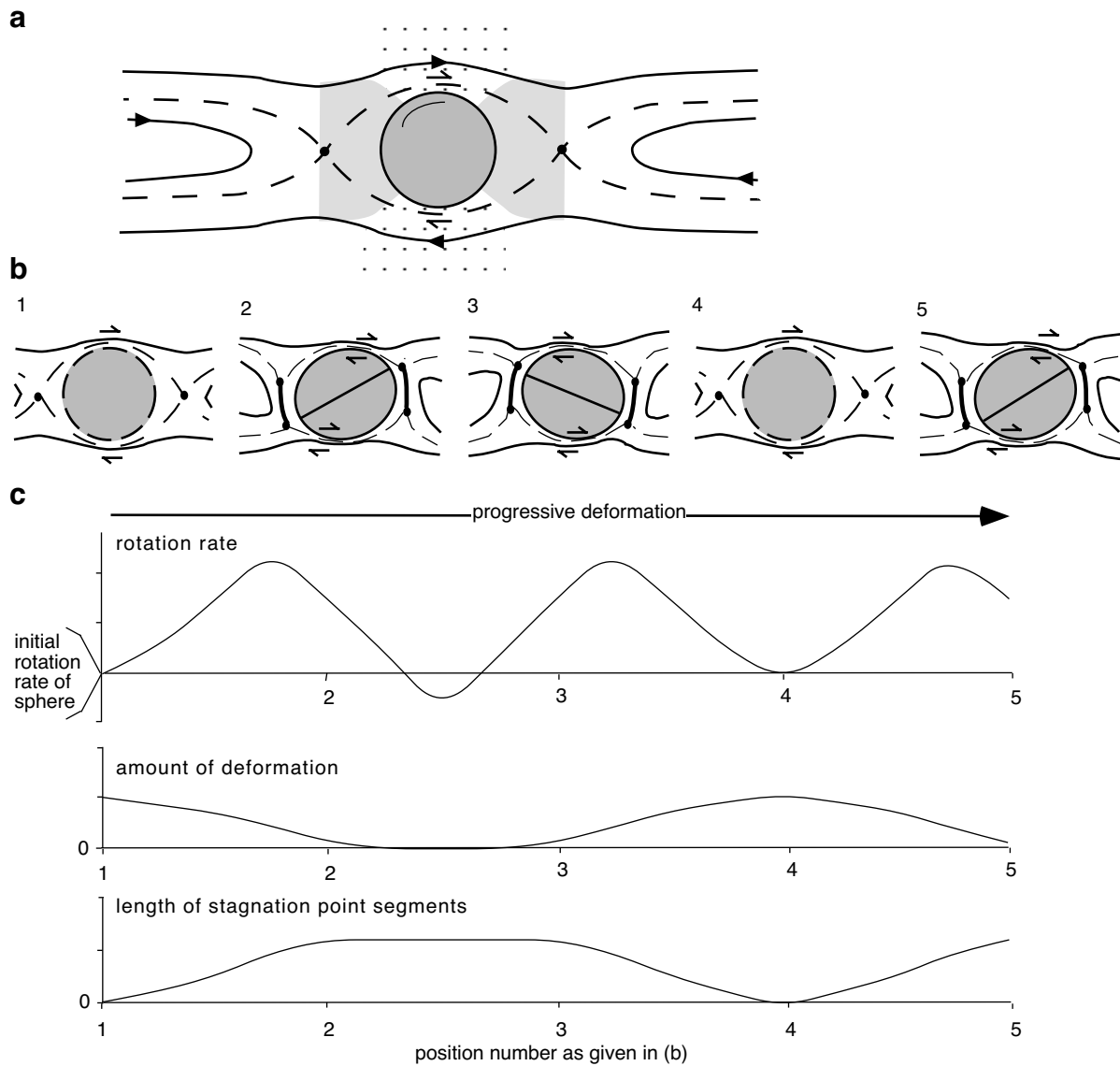


Figure 7.11 Illustration of the pulsating behavior seen at high viscosity ratios of 180 to at least 660; (a) stream-line pattern past a highly viscous sphere during simple shear far-field deformation, flow is characterized by a bow-tie shaped separatrix (dashed lines); flow lines are depicted as lines with arrows; fields of reduced (dark shading) and increased shear stress (stippled) are distinguished (modified after ten Brink;1996, p. 98); (b) interpretation of one pulsation cycle; diagram shows the development of a sphere (position 1) to an ellipsoid (position 2), rotation of ellipsoid (position 3), deformation to a sphere (position 4) and to an ellipsoid again (position 5); solid lines are flow lines, dashed lines and heavy dots are separatrices and stagnation points, respectively; heavy lines indicate line segments of stagnation points; (c) schematic graphs showing the change in rotation rate, amount of deformation and length of stagnation segments during progressive deformation; in the latter zero signifies the presence of two points of stagnation as seen in position 1 and position 4.

The results presented here are only in parts in agreement with earlier experiments performed by Passchier and Sokoutis (1993). In fact, in Chapter 4 it have shown that the materials c, d and e used by Passchier and Sokoutis (1993) are not suitable to model the effect of viscosity contrast between matrix and inclusion on the shape development of an inclusion; they are non-linear viscoelastic with a dominantly elastic mechanical behaviour. The main difference between our experimental results and those of Passchier and Sokoutis (1993) is that they observed an additional shape development type which is characterized by the deformation of a viscous sphere to a slightly elongate shape, the shape of which remains subsequently unchanged (Fig. 7.4 in Passchier and Sokoutis, 1993). This type of shape development was only observed in the materials described above and may therefore only be relevant to materials with a non-viscoelastic mechanical behaviour that is dominated by the elastic component.

7.4 Validity of experimental results for natural examples

To interpret shape fabrics observed in rocks in the light of the presented experimental results the limitations of the extrapolation of experimental results to natural examples must be taken into account. Important issues are whether the experiments can be directly extrapolated to rocks, whether viscosity, flow laws and viscosity ratios observed in rocks are in the same range as those used in experiments, whether the type of deformation with respect to homo- and heterogeneity are different in experiments and rocks and whether the nature of the bonding between matrix and inclusion are similar between experiments and geological examples.

7.4.1 Scaling of experimental models

In order to be able to link experimental results to deformation in rock, we need to completely describe the mechanical relationship of our analogue scale model and prototype i.e example in nature which should be modeled. To do this we need three independent scale factors for length (λ), time (Γ) and mass (μ) (e.g. Twiss and Moores, 1992). We define these factors by

$$\mu = \frac{m_m}{m_p}$$

$$\Gamma = \frac{t_m}{t_p}$$

$$\lambda = \frac{l_m}{l_p} \quad (\text{Eq. 7.8a, 7.8b, 7.8c})$$

where subscripts m and p refer to the model and prototype, respectively, and l is length, t is time and m is the mass of the material in geometrically similar volumes of the model and prototype. In our experiments l_m is 40-150 cm, t_m is approximately 10^{-6} and 10^{-5} a and m_m is 1, while we estimate l_p to be 150 to 6000 cm, t_p of $10^5 - 10^6$ a and m_p to be equal to 2.7. According to these scale factors the viscosity range modeled by our experiments ($10^1 - 10^6$ Pa) can be applied to prototype rocks with a viscosity of 10^{12} to 10^{19} .

Applied strain rates of 10^{-1} to 10^{-4} s^{-1} refer to strain rates of 10^{-9} to 10^{-14} s^{-1} in the prototype. These values for deformation of the prototype generally correspond to viscosity and strain rate values expected in rocks of the continental lithosphere (e.g. Kirby, 1983; Carter and Tsenn, 1987; Evans and Kohlstedt, 1995; Clark and Royden, 2000).

7.4.2 Homogeneity of deformation

In our experiments we only consider the behaviour of one single inclusion within a large volume of homogeneously deforming matrix. To interpret experimental results we have to be aware of the fact that inclusions which are close together can influence each others' deformation behaviour. Object interaction and flow perturbations have been shown to be significant for the rotational behavior of a rigid object dispersed in a Newtonian matrix by Ildefonse et al. (1992a, 1992b) and Fernandez (1987).

7.4.3 Bonding between inclusion and matrix

Odonne (1994), Ildefonse and Mancktelow (1993) and Pennacchioni et al. (2000) already pointed out that the degree of bonding between matrix and inclusion has a strong effect on the shape development and rotation of an inclusion. At a high degree of bonding, a viscous inclusion is directly affected by deformation in the matrix and changes its shape accordingly. In our experiments, rigid objects rotate with the predicted rotation rate calculated for inclusions with high bonding between matrix and inclusion; accordingly the bonding between the inclusion and matrix must be high. Lack of bonding, such as detachment and sliding along the interface of matrix and inclusion results in non-deformation of a viscous inclusion. If there is only some degree of bonding i.e. the detachment between matrix and inclusion is only seen at part of the surface between inclusion and matrix, a viscous inclusions can still be deformed, whereby the rate of deformation and the type of shape development will be different to the rate and shape development at 100% bonding. The apparent type of shape development will be similar to an inclusion of higher viscosity ratio at perfect bonding. In nature features such as pressure shadows, growth of fibres and deflection of foliation developing adjacent to an inclusion directly point to a low degree of bonding. In this case the low bonding has to be taken into account when extrapolating experimental results to fabrics seen in such a rock.

7.4.4 Viscosity, flow laws and viscosity ratios observed in rocks

To be able to extrapolate experimental results to rocks, it is necessary to review commonly observed viscosity ratios between inclusion and matrix and flow laws in rocks. In crystalline rocks flow laws are mechanism-dependent and several different flow laws have been proposed for different deformation mechanisms whereby rheological properties of rock which consists of several minerals are highly dependent on temperature and rock composition (e.g. Kirby, 1983; Tsenn and Carter, 1987). If mechanisms such as dislocation creep, dislocation glide, subgrain rotation and dynamic recrystallization, which commonly dominate deformation under greenschist and amphibolite facies conditions determine the rheological behaviour of the whole rock n values of 2 to 5 are expected (e.g. Carter, 1976; Schmid, 1976; Urai, 1983). However, mechanisms such as grain boundary sliding and those which are diffusion accommodated e.g. pressure solution are inferred to be Newtonian (Passchier and Trouw, 1996 and references

therein). Viscosities of rocks at mid to lower crustal levels are generally expected in the range of 10^{12} to 10^{19} Pa s (e.g. Carter and Tsenn, 1987), whereby rocks deforming at the same PT conditions are expected to exhibit viscosity ratios between 10^{-3} to 10^3 (Carter and Tsenn, 1987; Evans and Kohlstedt, 1995).

7.5 Application of experimental results on the interpretation of the shape and orientation of inclusions observed in rocks

In the following discussion, we assume perfect bonding between matrix and inclusion in nature and experiment. Otherwise considerations as outlined above must be taken into account when interpreting shape fabrics in rocks.

7.5.1 Predicted shape development of inclusions in deformed rocks

The shape of a deformed inclusion is only equal to the shape of the finite strain ellipse of the deformed host rock, if (a) the rheological properties of enclave and host-rock were equal during deformation (i.e. if deformation was homogeneous) and (b) if the enclave was spherical in shape before deformation. In low grade rocks this latter prerequisite is often fulfilled while in intrusive rock the initial shape of an inclusion is variable. Work by for example Williams and Tobisch (1994) and Vernon et al. (1988) suggest that deformation of inclusions during emplacement of the rock can lead to non-spherical enclave shapes. The statistical mean of a population of inclusions in an undeformed part of a studied intrusion can give an approximation for mean original shape of such enclaves. Tourmaline-quartz-feldspar aggregates, though, are commonly spherical if undeformed.

If the viscosity of the object and the embedding matrix differ from each other, analyses of strain and deformation type must be performed in the light of the viscosity ratio of object and inclusion. According to our experimental results four different scenarios must be considered.

- 1) viscosity ratio is significantly higher than 1200
- 2) viscosity ratio is between 5 and 1200
- 3) viscosity ratio is between 1 and 5
- 4) viscosity ratio is below 1

In nature it is difficult to determine whether an inclusion deformed at the same rate as the host rock, but deflection of foliation may be a good indicator for a viscosity ratio which is not equal to 1. In general, it is unlikely that the rate of deformation of an enclave, fossil or oolite and their corresponding host rock are identical as the composition and texture differ by definition. For instance, mafic enclaves which are finer grained and richer in mica than the host rock are likely to be softer than the host rock (Rutter, 1999).

7.5.2 Use of the three dimensional shape of a inclusion for quantitative structural analyses

Strain analyses which do not consider the viscosity ratio of objects and matrix will result in a number of misinterpretations if the viscosity ratio is not equal to 1. In the case of scenario (1) (cf. section 7.5.1) strain analysis is meaningless as the shape of the inclusion is not affected by deformation; in case of scenario (2) and (3) finite strain will be underestimated; in case of scenario (4) the apparent shape of the inclusion will lead to an overestimation of the finite strain. For instance, imagine a calcsilicate nodule embedded in a quartzitic gneiss is deformed in simple shear. The viscosity contrast during medium grade deformation would be expected to be above 1.5 and the expected shape development type would be a pulsating ellipsoid. In the field the geologist would be aware that the inclusion and matrix deformed, but applying strain analysis in this case would be bound to result in a vast underestimation of the finite strain.

Strain geometries in terms of flattening, constrictional and plane strain deformation can be determined from inclusions under certain circumstances. In scenario (1) application of analysis will result in unreasonable results as the shape of the inclusion exclusively depends on its shape before deformation. In scenario (2) and (3) the shape development is pulsating and permanently stretching, respectively. Analyses will lead to an overestimation of the constrictional strain type component. In case of scenario (4) interpretation of the apparent shape of the inclusion will lead to an overestimation of the flattening component. Examples from literature (e.g. Tobisch and Williams, 1998; Wenk, 1998; Olding, 1984) show that in most cases the strain type derived from strain analyses of mafic enclaves is either plane or flattening strain while in adjacent less strained areas the deformation type is plane or only weak flattening. Does this change of strain type reflect a true change in the nature of strain type in high strain zones or is it an artefact of the viscosity contrast between enclaves and matrix? As stated above (section 7.4.1.) mafic enclaves are expected to be softer than surrounding granitic material, hence such enclaves should exhibit an apparent flattening strain and therefore the true type of deformation cannot be directly derived from such rock types. Following geometric considerations (e.g. Weijermars 1992), in such cases the strain type is likely to have been plane strain throughout the whole rock body.

Recent work by Tikoff and Greene (1997), Fossen and Tikoff (1998) and Tikoff and Fossen (1999) connect the nature and orientation of the planar and linear shape fabric with a set of different transpressional and transtensional deformation regimes. In these papers, throughout the entire deformation history the type of fabric is discussed assuming no viscosity contrast between the matrix and inclusions that form planar and linear fabrics in the rock. As shown by our experiments, both the orientation of a linear and planar fabric in terms of axis aspect ratios is strongly dependent on the viscosity ratio between inclusion and matrix and finite strain. Although presented experiments were performed under identical boundary conditions (circular plane strain deformation) the type and orientation of the shape fabric in terms of its linear and planar components vary significantly depending on the viscosity ratio. At a high viscosity contrast i.e. the inclusion is significantly more competent than the matrix, the inclusion will not deform at all. The orientation of the lineation is only to a limited extent a function of the type of deformation and finite strain. If the deformation type is simple shear plane strain, only a strongly elongate object may assume a stable position for significant parts of the deformation path (Ghosh and Ramberg, 1976). If the viscosity ratio is close to 1 the shape develop-

ment type is in a general sense a permanently stretching ellipsoid. Irrespective of the exact viscosity ratio between inclusion and matrix the orientation of the longest axis of the inclusion will give a good idea of the deformation type, whereas the strain type derived from the shape fabrics may deviate significantly from the true finite strain type. The fabric of a rock may be planar not due to flattening strain but due to a viscosity contrast below 1. If the fabric is linear the strain type may deviate from constrictional strain as the apparent constrictional shape fabric is only a result of a viscosity contrast above 1. Therefore determination of transpression or transtension using the planar and linear fabrics of a rock may be wrong if the viscosity ratios deviate from 1. The most extreme case is seen at viscosity ratios between 5/100 and 1200, in which case an inclusion will exhibit a pulsating three dimensional shape throughout deformation; its orientation and aspect ratios will mainly be a function of strain but by no means of the general deformation regime.

7.5.3 Effect of shear stress, shear strain and shear strain rate variations on shape development of inclusions - possible use of inclusion shapes to derive viscosity ratios

Considerations given above are simple cases where the viscosity between the matrix and the inclusion do not change with shear stress, shear strain rate or time. If the inclusion or matrix exhibit a viscous non-Newtonian power law behaviour shear stress and shear strain rate are important factors that influence the type of deformation. Power law flow behaviour results in different kinematic viscosity values at different shear stress, therefore if at least one of the components (inclusion or matrix) exhibits power law flow behaviour the viscosity ratios will change with shear stress and shear strain rate. Accordingly, different types of inclusion shape development may be observed in the same rock depending on the applied shear stress or shear strain rate. Shear strain and shear strain rate variations are commonly observed in spatially defined shear zones (Ramsay, 1980; Tullis and Yund, 1985; Passchier and Trouw, 1996; Rutter, 1998; Talbot, 1999). In such discrete shear zones strain rather than stress but is localized (Rutter, 1998, Bons, pers. comm.). This requires that the material in the shear zone is softer than the wall rock. If the stress field imposed on the system is simple shear stress parallel to the shear zone then stresses are equal in both shear zone and wall rock i.e. higher shear strain rates are present in the shear zone (Rutter, 1998); the governing flow laws at different shear strain rates change during progressive deformation. In what way can we apply the experimental results to features that we observe in rocks deformed in shear zones?

Let us envisage the development of an aggregate lineation made of fine grained feldspar embedded in fine grained quartz matrix. Experiments (Tullis and Yund, 1982; Dell'Angelo and Tullis, 1989; Post et al., 1996; Gleason and Tullis, 1993) reveal that flow laws for Qtz and Fsp differ from each other under the same experimental conditions (P, T, fluid, strain rate). From shear zone boundary to shear zone centre two main general features are seen; a) strain and b) strain rate increase. As we know that the flow laws of quartz and feldspar differ from each other with increasing strain, strain rate and onset of dynamic recrystallization of one or both phases (e.g. Tullis and Yund, 1985; Rutter, 1999), the viscosity ratio between an inclusion of fine grained feldspar in a matrix of quartz changes from shear zone boundary to shear zone centre. If this is the case the shape development type of the inclusion should also change (Fig. 7.12). If we now envisage the development of a shear zone in a rock unit of a variety of differ-

ent lithologies, different deformation mechanisms and flow laws will be active in the different lithologies and lination material. This will result in different shape development of inclusions i.e. stretching lineations in different lithologies as shown in experiments. Sometimes during deformation a pre-existing lineation may be lost for parts of the deformation path as illustrated in Fig. 7.5 and observed in experiments. If we know for instance that the deformation type was simple shear plane strain using geometrical methods as proposed by e.g. Ramsay (1980), a detailed study of the change in shape fabric (a) from shear zone boundary to shear zone centre and (b) between different lithologies in shear zones may yield information about the relative viscosity ratio development between an inclusion and matrix within a shear zone.

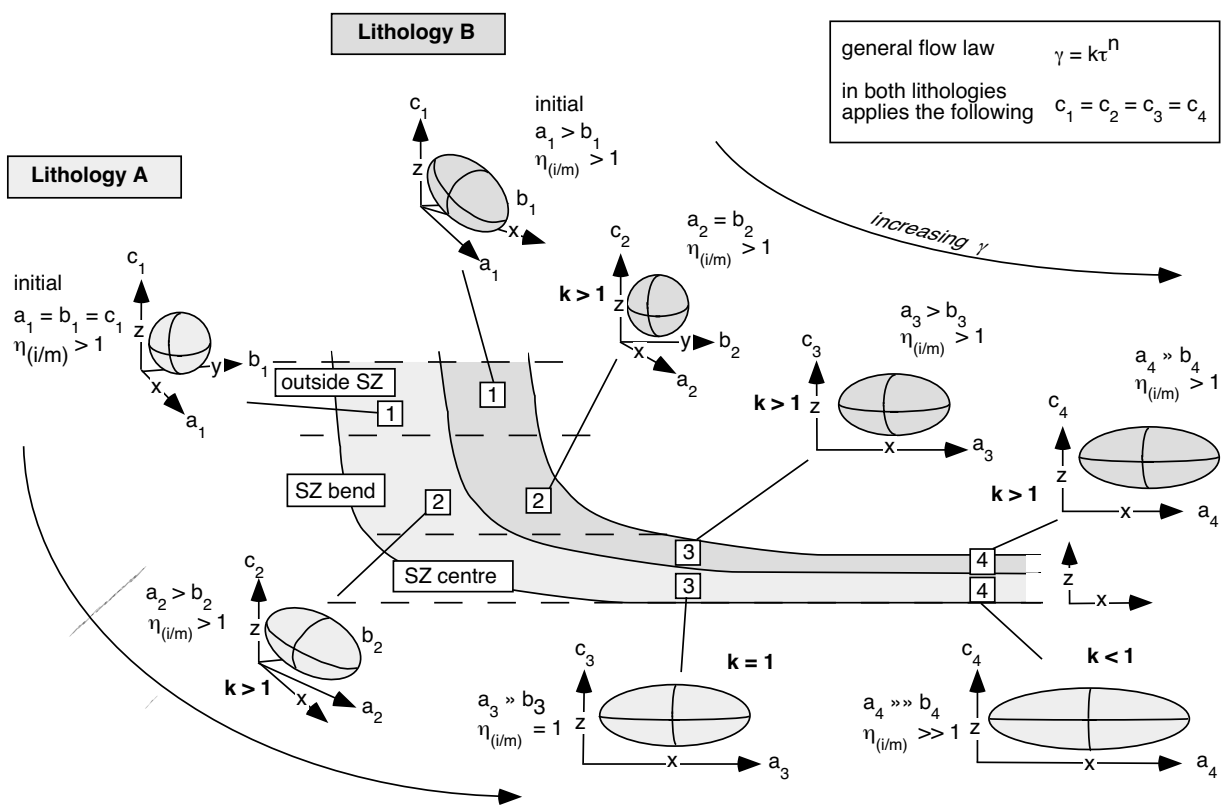


Figure 7.12 Schematic drawing of a discrete shear zone (SZ) from outside the shear zone to bend of shear zone to shear zone centre. The shape development of inclusion within two lithologies are depicted. In lithology A the shape of the initial inclusion is spherical while in lithology B the initial shape is prolate. In both lithologies the initial $\eta_{(i/m)}$ is above 1; symbols a, b and c signify the axis of an inclusion; number 1, 2 etc. correspond to positions within the shear zone, which in turn corresponds to a progression in strain with increasing number; x, y, z the axis of the shear zone (cf. Fig. 7.4); k corresponds to the symbol k introduced by Flinn (1978); $k > 1$, $k = 1$, $k < 1$ signify inclusion shapes that plot in the constrictional, plane and flattening strain field on a Flinn diagram (cf. Fig. 7.8), respectively.

7.6 Conclusions

Experiments in which viscous inclusions in a viscous matrix are deformed within a rotational high strain simple shear zone show that the shape development and finite shape of an inclusion is strongly governed by the effective viscosity ratio between matrix and inclusions, which is partly a material property, but also influenced by stress and strain rate. Five possible types of deformation were observed, depending on the effective viscosity ratio;

- a) rotating rigid sphere or ellipsoid (viscosity ratio ($\eta_{(i/m)}$) larger than 1200)
- b) pulsating ellipsoid ($5/100 (?) < \eta_{(i/m)} < 1200$)
- c) permanently stretching ellipsoid of which the aspect ratio values fall into the constrictional deformation field ($1 < \eta_{(i/m)} < 5/100$)
- d) permanently stretching ellipsoid, where the shape of the inclusion directly reflects the strain ellipsoid if an initial spherical shape can be assumed ($\eta_{(i/m)} = 1$)
- e) permanently stretching ellipsoid of which the aspect ratio values fall into the flattening deformation field ($\eta_{(i/m)} < 1$)

In high strain shear zones complex scenarios for the shape development of inclusions are possible. If either the matrix or the inclusion, or both, deform according to power law flow the viscosity ratio will change from the outer to the inner part of a shear zone and may result in more than one type of inclusion shape development. For instance, in parts of the shear zone lineations may be present while in other parts lineations may be absent. Therefore, to be able to obtain a realistic idea about deformation within a shear zone several lithologies should be monitored, if possible, from the boundary to the centre of the shear zone. Apparent indicators of constrictional, plane or flattening strain, such as shape of mafic enclaves, lineations, different types of tectonites (L-, S-, LS- tectonite) may be misleading and only a result of plane simple shear deformation and specific viscosity contrasts of fabric elements. Not only bulk strain may be under- or overestimated but also the type of strain and the overall deformation regime in terms of transpression and transtension may be misinterpreted.

Acknowledgements

Many thanks to Dr. Pakula and Andreas Hahnewald from the Max-Planck Institut für Polymerforschung, Mainz, for rheological measurements using the torsion rheometer Rheometric RMS 800 and to MERCK GERMANY for making the rotational viscosimeter (Brookfield Digital Viscometer; Model DV II+) available to us for a few days. Comments by Paul Bons (University of Mainz) and Daniel Köhn (University of Mainz) improved an earlier version of the paper, their help is gratefully acknowledged.

Table 7.1 Symbols used

a	longest inclusion axis	[]
a	angle between longest axis of object and normal to shear direction	[i]
b	inclusion axis perpendicular to a and parallel to xy plane	[]
b_r	the distance along the circle with radius r_r	[m]
b	angle between r_{si} and r_{sg}	[β]
c	inclusion axis perpendicular to ab plane	[]
m	mass scale factor	[]
l	length scale factor	[]
$\gamma, \gamma(t)$	shear strain	[s ⁻¹]
$\dot{\gamma}$	shear strain rate	[s ⁻¹]
γ		
h	height of analogue material in apparatus	[m]
h_s	vertical line between incl. & floor, // to vertical axis of inner cylinder	[m]
k	constant in power law flow formula	[]
l_m	length of model	[m]
l_p	length of prototype	[m]
m_m	mass of model	[kg m ⁻¹]
m_p	mass of prototype	[kg m ⁻¹]
n	stress exponent of power law	[]
η	viscosity	[Pas]
η_i	viscosity of inclusion	[Pas]
η_m	viscosity of matrix	[Pas]
$\eta_{(i/m)}$	viscosity ratio of inclusion and matrix	[]
Ω_i	angular velocity of outer cylinder	[m/s]
Ω_e	angular velocity of inner cylinder	[m/s]
P_i	position at time 0 (initial position)	[]
P_γ	position after shear strain of γ	[]
r	distance of object from center of apparatus	[m]
r_s	line between centre of inclusion and centre of rotation	[m]
r_{si}	line between centre of inclusion and centre of rotation	[m]
r_{sg}	line between centre of inclusion and centre of rotation	[m]
r_e	distance of outer boundary of object from center of apparatus	[m]
r_i	distance of inner boundary of object from center of apparatus	[m]
r_r	radius of circle	[m]
$R_{(a/b)}$	axial ratio of axis a and b of an inclusion	[]
$R_{(a/c)}$	axial ratio of axis a and c of an inclusion	[]
$R_{(c/b)}$	axial ratio of axis c and b of an inclusion	[]
R_e	radius of outer cylinder	[m]
R_i	radius of inner cylinder	[m]
ϕ	rotation rate	[rad/s]
$\dot{\Phi}$	rotation rate at strain rate g	[rad/s]
t_m	time of model	[s]
t_p	time of prototype	[s]
T_s	tangent to curvature of shear zone plane in circular flow	[]
T_a	tangent to curvature of inclusion axis a	[]
G	time scale factor	[]
$t, t(t)$	shear stress	[Pa]
x	shear zone axis parallel to shear direction	[]
y	shear zone axis perpendicular to shear direction	[]
z	shear zone axis parallel to shear zone boundary and perpendicular to xy plane	[]

Chapter 8

Conclusions and suggestions for further work

8.1 General remarks

In this research, shape fabric development during progressive deformation was studied by means of field observations, numerical simulations and analogue modelling. Aim of the study was to gain a better understanding of how shape fabrics evolve and on this basis assess the use of shape fabrics in the kinematic and dynamic interpretation of rocks. In the preceding chapters different aspects of shape fabric development were addressed. The purpose of this concluding chapter is to draw general conclusions, based on the findings. Additionally, problems and questions which remain unanswered are addressed and suggestions are made for further research.

8.2 Shape fabric development during progressive deformation

The shape fabric of a rock is the result of a complex system of interacting mechanisms. The way in which a certain mechanism or combination of mechanisms affect the shape fabric of a rock is determined by the values of extrinsic and intrinsic parameters.

Field studies of discrete low to medium grade shear zones in different lithologies show that the intensity of the shape fabric is only in some cases directly proportional to finite strain (Fig. 8.1a₁). Depending on the initial fabric of the rock, the intensity of a shape fabric increases or decreases during progressive deformation. Three different findings that can potentially explain these features were distinguished. (a) The intensity of a shape fabric is strongly influenced by the apparent degree of recrystallization i.e. the area percentage of recognizable recrystallized grains (Fig. 8.1a₂). (b) Intensity of the shape fabric is positively related to the ratio of initial/recrystallized grain size (R_{Φ}).(Fig. 8.1a₃) (c) Alignment of elongate rigid objects is positively related to finite strain (Fig. 8.1a₄).

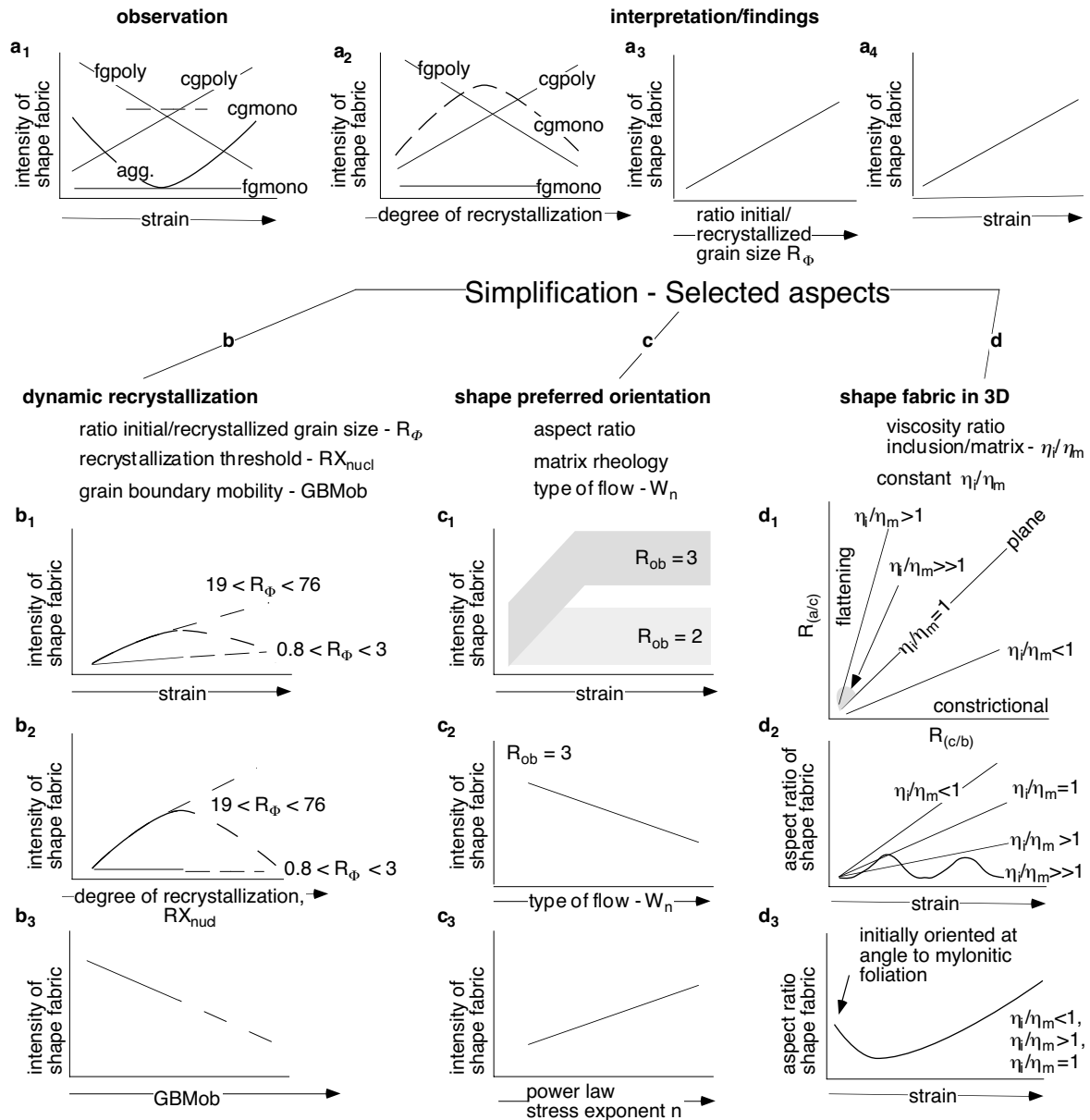
Numerical modelling of dynamic recrystallization (Chapter 3) shows that the intensity of a shape fabric generally increases with increasing strain, although at low R_{Φ} the intensity may decrease (Fig. 8.1b₁). An increase in the degree of recrystallization, which is inversely proportional to the energy threshold value of recrystallization by nucleation (RX_{nucl}), results in an increase of fabric intensity if R_{Φ} is high (Fig. 8.1b₂). With increasing grain boundary mobility (GBMob) the intensity of a linear fabric decreases independently of R_{Φ} (Fig. 8.1b₃).

Analogue modelling of the shape preferred orientation (SPO) (Chapter 6) of a population of rigid objects dispersed in a viscous matrix showed a general dependence of the intensity of a shape fabric on the aspect ratio of the rigid objects (R_{ob}), type of applied flow and flow laws of the matrix. With $R_{\text{ob}} = 3$ the intensity of the shape fabric is higher than with $R_{\text{ob}} = 2$

(Fig. 8.1c₁). A decrease in the kinematic vorticity number (W_n) results in an increase of the shape fabric intensity (Fig. 8.1c₂). Shape fabrics that developed in a non-Newtonian power law matrix material show a higher intensity and a more pronounced strain localization than in a Newtonian matrix material (Fig. 8.1c₃).

Analogue modelling of the shape fabric in a high strain simple shear zone (chapter 7) revealed that the development of the three dimensional shape of a viscous inclusion embedded in a viscous matrix depends on finite strain and the viscosity ratio between inclusion and matrix (η_i/η_m) (Fig. 8.1d₁). Depending on η_i/η_m three types of permanently stretching ellipsoids can be distinguished. These plot either in the flattening strain field, on the line of plane strain or in the constrictional strain field of a Flinn diagram (Flinn, 1978). The intensity of the shape fabric increases with increasing strain. This increase is most profound at low η_i/η_m . An exception is seen at $\eta_i/\eta_m \gg 1$ where the shape of the inclusion pulsates between an ellipse and a sphere (pulsating ellipsoid). Here, the aspect ratios of the three dimensional shape fabric changes continuously from no shape fabric to slight shape fabric with progressive deformation (Fig. 8.1d₂). If a pre-existing shape fabric is oriented with its long axis at a high angle to the shear direction, the intensity may decrease and subsequently increase with progressive deformation (Fig. 8.1 d₃).

Figure 8.1 (opposite page) Schematic summary of results of different Chapters 2, 3, 6 & 7. In Chapters 3, 6 & 7 different sets of experiments/simulations with different parameter values were performed. Varied parameters are given in *italic*. **(a)** Schematic graphs summarizing observations and interpretation described and discussed in Chapter 2 (field studies); *aggr* = aggregate lineation; *cgmono* = coarse grained monomineralic rock (dashed line); *fgmono* = fine grained monomineralic rock; *cgpoly* = coarse grained polymineralic rock; *fgpoly* = fine grained polymineralic rock. **(b)** Graphs summarizing the results of the numerical simulation of dynamic recrystallization (Chapter 3); dashed line = extrapolation of experimental results. RX_{nuc} = energy threshold value for recrystallization by nucleation; $GBMob$ = grain boundary mobility; R_ϕ = ratio of initial grain size to recrystallized grain size. **(c)** Graphs depicting the findings of analogue modelling of shape preferred orientation of rigid objects dispersed in a viscous matrix (Chapter 6); (c₁) grey areas show the general fields of the intensity of shape preferred orientation as for both aspect ratios $R_{ob} = 2$ and $R_{ob} = 3$ the intensity varies during progressive deformation, but general trends can still be seen. (c₂) W_n = kinematic vorticity number. **(d)** Summary of analogue modelling of the three dimensional shape fabric development of deformable objects (Chapter 7). (d₁) Flinn diagram depicting the different types of shape fabric deformation due to different viscosity ratio of inclusion and matrix materials; η_i/η_m = ratio viscosity of inclusion to matrix, $R_{(a/c)}$, $R_{(c/b)}$ = aspect ratio of ellipsoid (cf. Fig. 1.2); (d₂) graph illustrating the function of the intensity of shape fabric with different object/matrix viscosity ratios and finite strain. Here, the intensity of shape fabric corresponds to aspect ratio values of the deformable object in the xy-plane. Low intensities signify aspect ratios close to unity; (d₃) graph showing the shape fabric development of a pre-existing shape fabric when deformed.



Results of the three direction of investigations (Chapter 3, Chapter 6, Chapter 7) explain to a large extent the characteristics of shape fabric development described for natural samples and support the explanation of the findings given in Chapter 2. Due to the effect of dynamic recrystallization the intensity of a shape fabric in a rock with low R_ϕ will decrease if a pre-existing shape fabric was present. If no shape fabric existed before deformation in a rock with low R_ϕ no shape fabric develops during subsequent deformation. In monomineralic rocks with high R_ϕ strong shape fabrics developed as a few strongly elongate grains remain in a small grained, recrystallized matrix. Aggregates of specific mineral species dispersed in a matrix of different mineral species can act as viscous inclusions in a deforming matrix. Therefore, in polymineralic rocks, in which aggregates of specific mineral species are embedded in a matrix, a high fabric intensity is seen at high strain. If there is a population of rigid, elongate

mineral grains dispersed in a matrix, a shape fabric develops during progressive deformation especially if strain is localized. Strain localization may be the result of strain softening in the matrix material due to localized dynamic recrystallization or due to the general non-Newtonian, power law flow behaviour of the matrix material. A pre-existing shape fabric which was initially oriented with its long axis at an angle to the mylonitic foliation may form no shape fabric during parts of the deformation path if it deforms like a viscous inclusion in a viscous matrix (cf. Fig. 8.1d₃).

8.3 Possibilities and limitations of the use of shape fabrics in structural analyses

8.3.1 Strain analysis — analysis of strain magnitude and movement direction

Quantitative analysis of strain magnitude using the three dimensional shape of deformable objects embedded in a viscous matrix material is only possible if η_i/η_m is sufficiently known (Chapter 7). Quantitative and qualitative strain analysis utilizing the intensity of the shape preferred orientation of a population of rigid bodies (Fernandez, 1987, Ildefonse et al. 1992a) can be problematic. In this case, the intensity of the shape fabric strongly depends on the object aspect ratios and amount of strain localization in the matrix material, whereby the amount of strain localization is largely a function of the rheological properties of the matrix (Chapter 6). If dynamic recrystallization is one of the important deformation processes, the intensity of a shape fabric is additionally influenced by the initial fabric and the extrinsic and intrinsic parameters of dynamic recrystallization (Fig. 8.1a, Chapter 2, Chapter 3).

To decide if a volume of rock was subject to non-coaxial deformation and to determine movement direction, the geologist should look for lithologies that are likely to document deformation. Useful for such an analysis are coarse grained (high R_ϕ) mono- and polymineralic rocks (Chapter 2, Chapter 3). In contrast, in fine grained rocks with low R_ϕ it is unlikely to find evidence for deformation and the corresponding movement direction in handspecimen except if metamorphic reactions resulting in syntectonic growth of elongate mineral species took place. If an earlier shape fabric existed, overprinting relationships may result in the destruction of a shape fabric (Chapter 2, Chapter 7). In other cases, the orientation and intensity of a shape fabric will not represent the conditions of the second deformation because the observed fabric is a product of the earlier and later deformation. According to the above, studies of the presence and direction of tectonic transport and finite strain should, if possible, be performed in a variety of different lithologies (Chapter 2).

8.3.2 Strain analysis — analysis of type of deformation

The term type of deformation encompasses the geometry, the kinematic vorticity number and the history of deformation. Theoretically, the geometry of deformation of a volume of rock is reflected by the geometry of the strain ellipsoid. Flinn (1978) suggested to characterize the geometry of deformation in terms of flattening, plane and constrictional strain. If it is assumed that the three dimensional shape of an inclusion deformed in a matrix material represents the three dimensional shape of the strain ellipsoid, the geometry of deformation of a rock volume

can be derived from the shape fabric of individual deformable objects. The method has its limits as the shape of an inclusion is strongly influenced by the viscosity contrast between matrix and inclusion material (e.g. Eshelby, 1957; Chapter 7). For example, the use of the shape of elongated grains in a matrix of recrystallized grains of the same mineral species may yield wrong results. If the included grain is a porphyroclast and harder than the surrounding matrix material the estimation of the geometry of deformation will overestimate the constrictional component of deformation. If the inclusion is deforming as a pulsating ellipsoid i.e. its shape changes periodically from a sphere to an ellipsoid during progressive deformation the shape cannot be used for strain analysis (Chapter 7). As shown in analogue experiments (Ree, 1990) and numerical experiments of monomineralic fabrics (Chapter 3), grains that remain large throughout progressive deformation are less viscous than their surrounding. This means that the flattening component of deformation derived from such grains may be overestimated.

Quantification of the kinematic vorticity number (W_n) using rotated rigid objects (Passchier, 1987), the rotation and stretch of material lines (Passchier and Urai, 1988) or a qualitative determination of the degree of non-coaxiality (e. g. Ghosh and Ramberg, 1976; Ghosh, 1987) may yield relevant results for the scale of the analysed area or volume of rock. Extrapolation of W_n to a larger scale is problematic since partitioning of the type of flow in terms of W_n and strain is probably very common in rocks (Chapter 6).

Investigations of progressive deformation geometries such as different transpressional and transtensional deformation regimes (Tikoff and Greene, 1997; Fossen and Tikoff, 1998; Tikoff and Fossen, 1999) use the geometric relation of different shape fabrics i.e. lineations and foliation. In such analyses different viscosity ratios between an observed deformable inclusion and its matrix material must be considered. Only if the viscosity ratio is close to unity can the orientation of the longest axis of the inclusion with respect to the foliation plane give a good idea of the deformation type (Chapter 7).

8.3.3 Rheological properties of rocks

Assessment of the rheological behaviour of rocks is difficult. The rheology of a rock is characterized by the absolute value of viscosity at a specific strain rate and stress, and the change in viscosity with a change in strain rate and stress if it is assumed that rocks deform as viscous but not elastic materials.

If the geometry and history of deformation are known e. g. by the change of thickness and angle of foliation with progressive deformation (Ramsay, 1980), it is generally possible to derive the relative viscosity contrast between an deformable object and its matrix due to the three dimensional shape development of the object provided the initial shape of the inclusion is known (Chapter 7).

Where the type of flow is known some indicative features for non-Newtonian power law flow can be used. Strong strain localization indicated by shear bands and strong alignment of rigid objects can be indicative for high stress exponent of power law flow (Chapter 6). Also, a change in shape of an inclusion from apparent constrictional to apparent flattening from shear zone boundary to shear zone centre indicates a decreasing viscosity of the inclusion

material with respect to the matrix. This may indicate that for at least one of the components i. e. matrix or object the flow laws at the shear zone boundary are different from those in the shear zone centre. If, for example, the shape changes from apparent flattening to constrictional, the inclusion material became more viscous with respect to its surrounding matrix. A reason for this could be the change in flow law of the matrix with the onset of dynamic recrystallization in the shear zone which "softens" a rock (Tullis and Yund, 1985; Rutter, 1999; Chapter 3; Chapter 7). Still, such findings are qualitative and not quantitative. For a more quantitative analysis, the rheological characteristics of at least one of the materials (inclusion or matrix) must be known.

8.4 Microstructural features associated with shape fabrics: their possible use for kinematic analyses and new tools for their description and analysis

In the course of this research, the study of shape fabrics was expanded to some extent to the study of other microstructural features, which are closely linked to shape fabrics. Examples are grain size distributions, mean grain size and angle of lattice misorientation between neighbouring grains. This led to the recognition of some microstructural features indicative for the dominance of a specific syntectonic processes e.g. recrystallization by nucleation and grain boundary migration and specific parameter values or value ranges. For example, dominance of grain boundary migration generally results in low aspect ratios and increasing mean grain sizes with progressive deformation. Additionally, high angle boundary lengths, total dislocation density and viscosity are low and decrease with progressive deformation (Chapter 3).

Some tools to describe and analyse a microstructure have been developed. The ratio of low ($< 10^\circ$) and high ($>10^\circ$) boundaries lengths proved to be a good tool to distinguish between (a) initially fine and coarse grained fabrics and (b) low and high rates of recrystallization in initially coarse grained fabrics. Grain size distributions of dynamically recrystallized fabrics showed that in particular grain size ranges grain sizes are self-similar. Corresponding fractal dimensions seem to change systematically with different initial fabric, values of grain boundary mobility and rates of recrystallization. A good representation of the microstructure of a rock are grain boundary distance plots (Chapter 3) because in such plots, the aspect ratios of large and small grain distances, grain distance distributions, frequency of grain boundary distances and shape fabric intensity are shown.

More research has to be done to refine the methods described above.

8.5 Remaining problems and suggestions for future research

There are still many remaining problems concerning our understanding of shape fabric development during progressive deformation and the use of shape fabrics in quantitative and qualitative structural analysis. The most important ones that have appeared in the course of this work are listed below. These are grouped according to the methods of investigation.

8.5.1 Analogue modelling

High power law stress exponents (2-5) are predicted for rocks deforming in the ductile regime (e.g. Kirby and Kronenberg, 1987). Most analogue materials except some crystalline materials (e.g. OCP) lack such high power law stress exponents. This inhibits investigations of the influence of high power law matrix materials on the intensity of shape preferred orientation of rigid objects dispersed in viscous matrix material. The viscoelastic behaviour and rheological properties of polymeric materials is controlled by the monomer and polymer chain lengths and addition of specific filler materials (Chapter 4). Therefore, analogue materials with specific power law exponents may be made. The availability of such materials will open up a new range of possible experiments and investigation of the effect of material properties on fabric development. For instance, if suitable materials existed, it would be possible to systematically investigate the effect of power law matrix materials with different power law exponents on shape preferred orientation in the xy - and yz - plane, strain localization, type of flow and particle density.

The type of flow in terms of the kinematic vorticity number W_n has been shown to influence the angle between the developing C' shear bands and the mylonitic foliation (Chapter 6). Experiments involving a systematic analyses of the change in the orientation of C' shear bands with the applied W_n may result in a quantitative tool to determine W_n .

8.5.2 Numerical modelling with Elle

One of the main problems with fabric analysis at the grain scale is the quantitative characterization of active mechanisms during and after deformation. Simulations with the modelling system Elle could yield new insights in the effect of specific processes and associated parameters on microstructural development and may result in the recognition of new microstructural indicators. For example, parameters such as the energy threshold for subgrain formation, the calculation of dislocation density according to the work term of the Taylor-Bishop-Hill routine and the critical resolved stress values for specific slip planes could be varied (Chapter 3). Analyses of these simulations are likely to result in the development of new quantitative tools applicable to natural rock fabrics.

A volume of rock commonly undergoes a large variety of conditions and its microstructure is the result of this history. For example, a deformed rock that acquired a fabric indicative for medium grade deformation may reside at elevated temperatures for a long time interval. Static recrystallization will overprint microstructures and the information about the preceding deformation may be largely lost. In Elle simulations strain rates, temperatures and pressures can be changed during one experiment and therefore it is now possible to forward model the history of a microstructure from its deformation at high pressure and temperature. With such a model the microstructural development of a volume of rock following any PTDt (pressure-temperature-deformation-time) path can be simulated. In this way, it is possible, for example, to determine if a shape fabric is likely to be preserved under such conditions.

The model of dynamic recrystallization is presently using values specific to quartz. Values used include, for example, critical resolved shear stress for different slip planes, the subgrain size range and grain boundary mobility values. Replacing these values with values specific to another mineral phase could be easily done provided these values are known. For example, an extensive set of experimental data exists for olivine. Therefore, modelling the deformation of olivine could be performed and applied to problems concerning mantle deformation.

In addition, numerical simulations could be extended to polyphase fabrics and therefore to modelling a larger variety of rock types. Such simulations may yield new insights in the effect of composite rheologies on flow laws as suggested for example by Handy (1990).

8.5.3 Testing of techniques of microstructural analysis

The new analytical tools to quantitatively describe microstructures presented in Chapter 3 need to be tested and further developed. The analysis of grain size distributions in logarithmic diagrams has a potential to be of use not only to describe a fabric quantitatively but also to determine values of different parameters. Additionally, grain boundary distance plots and the ratio of low/high angle boundaries lengths need to be tested for their use as standard procedures to describe the microstructure of a rock. Such plots could also be useful to determine the dominance of specific active processes, combination of these or values of parameters. A combined study using numerical modelling, analogue experiments with crystalline materials such as octachloropropane (OCP) and norcamphor and subsequent microstructural analyses, and EBSD analysis of naturally and experimentally deformed rock samples may lead to improvement of these techniques as quantitative microstructural tools.

Appendix A

Detailed description of samples of investigated shear zones

This appendix provides a detailed description of the samples and thin sections used and described in Chapter 2. Samples of shear zones 1, 4 and 6 have already been described in detail (Chapter 2) and are not described here. For a summary of the characteristics of the shear zones and samples the reader is referred to Tab 2.1. (Chapter 2)

shear zone 2

This D3 shear zone deforms a granodiorite. SP 151A (margin of shear zone) is characterized by large grains of Fsp and Bt and medium-grained Qtz. The magmatic texture is still well preserved in the undeformed sample. In SP 151B (centre of the shear zone) Qtz forms both stringers of small grained aggregates and medium to large, elongate grains which are characterized by strong undulatory extinction. Fsp is frequently fractured, and along its rims subgrains are present and domains of very small grained equidimensional Fsp (0.01-0.06 mm) and chlorite grains are present. Domains of Fsp and white mica in contrast to recrystallized Qtz aggregates result in a 3.0 i-(Qtz/Fsp) aggregate-lineation.

shear zone 3

Samples SP 160 and SP 163 stem from the same rock unit at the centre of the shear zone. The thickness of this lithology and therefore strain differs between the two sample sites (SP 160: 6.2 cm, SP 163: 2 cm). In both samples Fsp, Qtz, Ep and minor amounts of mica are present. Fsp is strongly sericitized and only present as relicts, Qtz shows small equidimensional grains and medium size grains with irregular grain boundaries. Micas are rare and small grained. Mineral phases of the epidote-zoisite group appear as slightly elongated crystals and aggregates in the matrix of Qtz and Fsp (3.4 i-Ep grain-lineation). In SP 163 relicts of amphiboles are present, which are rimmed by epidote. Ep forms up to 2 mm large clusters (3.0 i-Ep grain-lineation).

shear zone 5

Outside the shear zone the fine-grained metapsammite shows a D2, 2.6 i-Bt grain-lineation formed by oriented Bt grains (0.5-1 mm). In the outer parts of the shear zone the lineation is deflected and Bt are at their rims recrystallized. At the centre of the shear zone Bt is completely recrystallized and Fsp breaks down to Ab-rich Fsp and white mica. Dynamically recrystallized grains are very fine-grained (0.01-0.02 mm) and relict Fsp and Qtz crystals (0.2-0.4 mm) are predominantly rounded (SP 225). Here, the rock does not exhibit any statistically significant preferred dimensional orientation. In the centre of the shear zone a lineation is again developed, this time the lineation is formed by aggregates of recrystallized Bt and chlorite flakes make up 1.4 i-(Bt/Chl) aggregate-lineation. The medium-grained metapelite initially exhibits a D2, strong Bt grain-lineation where Bt grains are aligned in a matrix of medium-grained Fsp

and Qtz. The coarse-grained metapelite has a poor D2 lineation outside the shear zone formed by fibrolite (1.2 i-Fibr aggregate-lineation). In the centre of the shear zone the “strength” of lineation increases ($\kappa = 2.6$) as Fibr is aligned and clusters of fibrolite become more and more elongate and similarly oriented.

shear zone 7

In SP 291 (outside shear zone) some grains of And and a few aggregates of fibrolite are present. In SP 290 and SP 289 which are from the outer part and the centre of the shear zone, respectively, no relict And crystals remain and Fibr aggregates form elongate-shaped bundles. These aggregates show a high degree of preferred dimensional orientation (3.2 s-Fibr aggregate) in contrast to the 0.9 i-And grain lineation and 1.8 i-Fibr aggregate-lineation of sample SP 291.

locality 8

The quartzite has small amounts of Bt and was deformed during D1 and D2 and not during D3. It shows a 2.1 s-Bt grain-lineation due to small Bt grains (0.1 mm) in a matrix of fine-grained Qtz (0.02 mm).

shear zone 9

The shear zone deforms a granodiorite. Outside of the shear zone (SP 416B) at Fsp rims ($\emptyset = 5$ mm) Bt is abundant in up to 1 mm sized grains. Qtz is medium-grained or partly recrystallized. The Bt mineral lineation is a 1.6 s-Bt grain lineation. In SP 416A (centre of shear zone) Fsp is not seen larger than 0.5 mm in diameter and the dimensional orientation of Bt is well developed (2.1 i-Bt aggregate-lineation). The total amount of mica increased from 18 % to 47 %. Individual grains and aggregates of Bt are aligned alongside Fsp grains and dynamically recrystallized Qtz aggregates show a well defined preferred dimensional orientation.

locality 10

The quartzite was deformed during D1 and D2. Elongation of old medium to large Qtz grains and aggregates of small grains and the bimodal distribution of grain sizes result in a well defined lineation (2.1 i-Qtz grain-lineation; SP 463).

Appendix B

The Von Mises Distribution

This appendix gives a detailed account on the characteristics of a von Mises distribution and use of the concentration parameter κ for the evaluation of the "strength" of a shape preferred orientation of a population of objects. This method was used in Chapter 2 and Chapter 6. Additionally, a chart is provided, which can be used to qualitatively derive the κ value from a handspecimen or a thin section.

B1. Statistical evaluation of the degree of shape preferred orientation

Masuda et al. (1999) proposed a statistical approach to determine the degree of preferred dimensional orientation of population of objects such as mineral grains or aggregates quantified by the concentration parameter κ . We further develop this technique by automating measurements of lineations and substituting the χ^2 - test used by Masuda et al. (1999) with a Rayleigh test. The von Mises distribution which underlies the used statistical concept is commonly referred to as the equivalent to a normal distribution which is specifically used to statistically evaluate circular data. The basic assumption for both distributions (normal and von Mises) is that the characteristics of the samples (in our case: measurement of the orientation of one individual mineral grain or mineral aggregate in handspecimen or thinsection) are independent from each other and that their measured values depend on a large number of factors. These assumptions only hold true if grains not directly adjacent to each other are measured, otherwise the dimensional orientation of neighbouring crystals is not necessarily independent from each other (Ildefonse et al. 1992a, 1992b; Masuda et al. 1995b). Work of Masuda et al. (1999) and tests carried out in our laboratory suggest that the distribution of the dimensional orientation of volume-lineations within rocks is well approximated by a von Mises distribution. The reader is referred to Masuda et al. (1999) for the definition of the density function and other properties of a von Mises distribution. The value of the factor R , the value of the mean resultant vector describing circular data, (see Masuda et al. 1999, for further explanation) provides the possibility to estimate the so-called "concentration parameter" κ since κ is a monotonic function of R . R ranges from 0 to 1 whereas κ ranges from 0 to infinity. The value of κ is preferable to R due to its wider range of values. The κ -value needs can be accurately determined using existing tables (Mardia, 1972, p. 298) that tabulate the relationship of R and κ . Nevertheless, we consider the following estimates sufficient for our purpose.

For R values < 0.45

$$\kappa = \frac{R}{6}(12 + 6R^2 + 5R^4)$$

for $0.45 < R < 0.65$

$$\kappa = 2R$$

and for $R > 0.65$ κ is approximated by

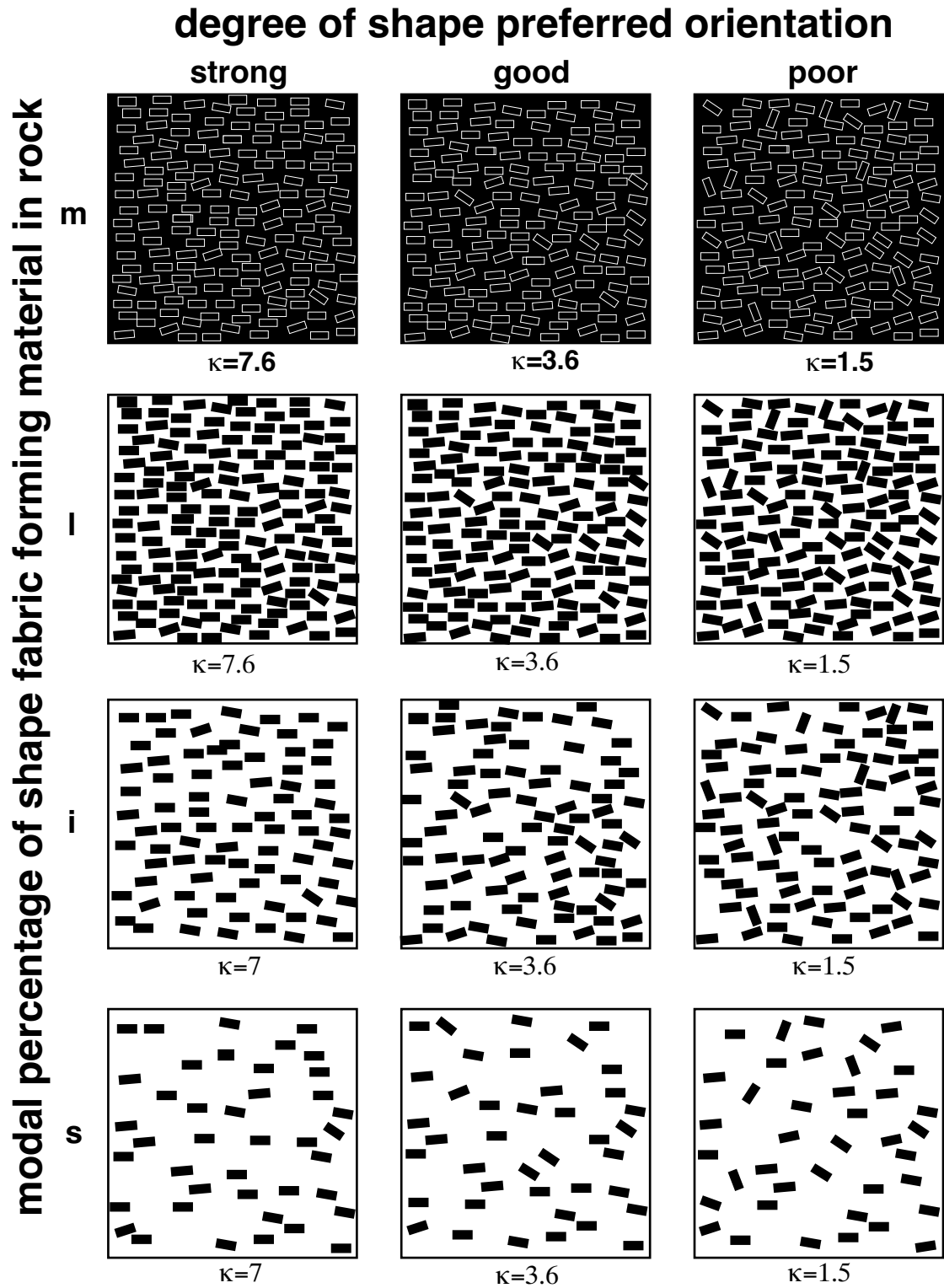
$$\kappa = \frac{1}{2(1 - R) - (1 - R)^2 + (1 - R)^3}$$

The higher the κ -values the 'better'—the preferred shape orientation of a lineation as measurements are concentrated around a certain value. As a rule of thumb, if the κ value is above 1 there is a noticeable but weak preferred dimensional orientation, if it is above 2 it is well defined, if it is above 5 it is exceptionally good. Measurements of κ in a large variety of rocks of different metamorphic grade and strain show that in natural samples κ values commonly range between 0 (no preferred dimensional orientation) and 10 ('very good' lineation). To ensure a statistically significant result the number of single orientation measurements of individual grains or grain aggregates must not be less than 20 although we think one should aim for measurement numbers of at least 30. To test if there is a statistically significant shape preferred orientation, which signifies the presence of a lineation, we suggest the Rayleigh test (for detail see Tab. A1 and explanations in Batschelet, 1981; Mardia, 1972) using a value of $\alpha = 0.05$ signifying the degree of allowable variance. A Rayleigh test chart is provided below for sample numbers $n \geq 30$ (provided on the Excel sheet on the CD-Rom). In the hopefully rare case of a single measurement number n of less than 30 the reader is referred to Mardia (1972; Tab. A1). As a rule of thumb, a κ value of less than 0.2 generally signifies that there is no geologically significant preferred orientation of the measured grains or grain aggregates. The concentration parameter κ of a von Mises distribution can be estimated in the field using a chart provided on the CD-Rom or by a precise analytical method in a laboratory. The latter involves both visual evaluation and statistical testing and analysis as described above. Obviously, it is necessary to ensure a high number of measurements (>30) and to be aware that the outcome of measurements can be bias by preferable measurements of grains with a specific orientation.

n_i	$z(\alpha) = z(0.05)$
30	2.97
50	2.98
100	2.99
200	2.99
500	2.99

Table B1 Rayleigh test chart (valid for $\alpha = 0.05$) to determine if there is a significant dimensional preferred orientation or not. To use this chart, calculate the value for z with z (calculated) = $n_i * r^2$ with n_i = number of samples and r = length of the mean vector and compare the calculated z with the $z(\alpha)$. If $z(\text{calculated}) > z(\alpha)$ then the null hypothesis is rejected which means that the distribution is NOT uniform, therefore the sample has a statistically significant shape preferred orientation. We suggest that $z(\alpha)$ with an α of 0.05 is used as such a allowance of variance is reasonable in geological applications. It should be noted that for the determination of κ -values for lineations both handspecimen and thinsections can be used. For $n_i < 30$ refer to Appendix 3.5 in Mardia (1972; pg. 325).

B2. Chart to qualitatively derive the concentration parameter κ



Appendix C

Additional information on Elle and test experiments

This appendix gives in the first part some additional information on the numerical modelling system Elle which was not provided and discussed in Chapter 3 and in the second part a discussion of the validity of use algorithms and results from test experiments.

C1 Routines entirely concerned with computational problems

C1.1 elle2poly

This routine translates Elle data into a planar straight line graph format which can be used by Triangle, the two-dimensional quality mesh generator of Shewchuck (1996). The output from this routine conforms to the file format of Triangle's *.poly* files and is used by the BASIL program to triangulate the microstructure and create a finite element mesh. Optional data sections are appended to the *.poly* file to allow attributes to be passed to basil and the conversion routine, basil2elle. The Elle microstructure, which wraps in the x and y directions, is "clipped" at the unit cell boundaries. If an Elle boundary wraps around the unit cell, the segment is split by introducing new nodes at the intersection points. Any Elle nodes close to a unit cell boundary are moved to the boundary, to avoid the problem of the triangulation routine producing lots of tiny elements. New nodes are introduced at the corners of the unit cell, if an existing Elle node is not at the location. New boundary segments are created to define the unit cell polygon. These new segments only exist in the polygon format and boundary nodes in the *.poly* file may have more than three neighbours.

An internal point is defined for each polygon which wraps over the unit cell boundaries. It will be represented by more than one polygon and these polygons are found using a polygon clipping routine, gpc (Generic Polygon Clipper; Murta, 2000). Triangle applies a region attribute, the grain identifier, to all the triangles within each polygon. BASIL can then assign attributes to all the polygons which make up a grain.

C1.2 basil2elle

The routine basil2elle combines data from the BASIL solution and the original Elle file to produce an elle data structure output file. The output file includes all the attribute data from the *.elle* file used by elle2poly. The routine calculates and outputs stress and strain values for Elle nodes and polygons. The polygon strain values (4 strain tensor values, incremental strain, bulk strain (= accumulated strain)) are calculated from the area averaged values over the elements in the polygon. A polygon that is not deformed will have a strain of zero.

C2 Definition of Euler angles

Any arbitrary crystal orientation can be defined by three rotations; there are a number of standard schemes for which axes and in which order to perform these rotations. When we say Euler angles we mean

- a) First rotate crystal around positive Z axis by α degrees (anticlockwise)

- b) Then rotate crystal around positive Y axis by β degrees (anticlockwise)
- c) Then rotate crystal around positive Z axis (again) by γ degrees (anticlockwise)

X axis is normal to a and b crystallographic axes. Y axis is the b crystallographic axis. Z axis is normal to X and Y axes, set up system is right handed.

C3 Validity of approach and algorithms and test experiments

C3.1 Validity test of the concurrent simulation of micro-processes

As outlined in Chapter 3 in Elle it is assumed that a fabric is a result of microstructural changes due to process a, b, c, ..., n, and that the fabric development can be simulated by the sum of the microstructural changes of each of the individual processes according to the general relationship

$$\delta f(a, b, \dots, c) = \delta f(a) + \delta f(b) + \dots + \delta f(c)$$

To investigate if this assumption holds true, we performed a number of experiments using the grain boundary migration routine. To do this two sets of experiments were compared:

- 1) one simulation using ELLE_GBM.
- 2) 2 runs in which the two 2 separate routines are called one after the other. These are ELLE_DISLOC (considering energy differences due to dislocation density as the driving force), ELLE_SURF (considering energy differences due to surface energy). The order of these two routines was varied in the two runs.

Results are given in Fig. C1 and Fig. C2. Results of the two different sets of experiments are to a large extent comparable, but small differences in the texture arise (Fig. C1). These differences are in the same order between different runs of the simultaneous combination of different factors regarding grain boundary migration and the combination of the 2 individual grain boundary migration routines. These differences arise from the calls in the routines using random numbers, namely the starting random trial direction vector for movement (Fig. 3.11).

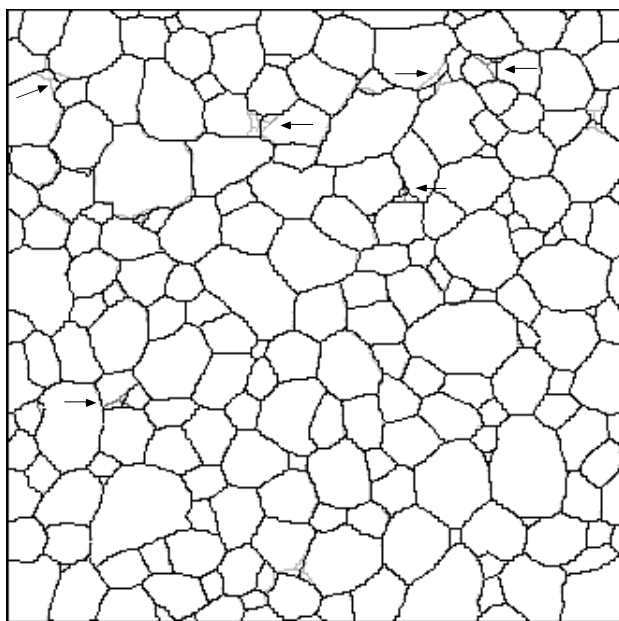


Figure C1 Overlay of grain boundary meshes produced by the 3 different runs (see text for explanation). Arrows point to geometric differences between runs.

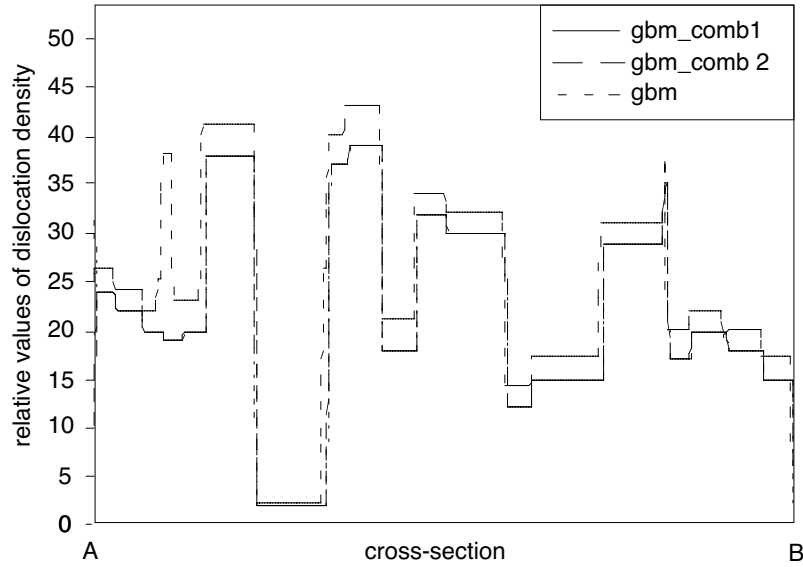


Figure C2 Results of test runs comparing results from combinations of separate grain boundary migration routines (*gbm_comb1*, *gbm_comb2*) see text) and the grain boundary migration routine used in the model. The latter routine combines the 3 separate routines simultaneously (*gbm*). Graph shows the relative values of dislocation density along a chosen line crosscutting the upper part of the meshes (Fig. C1)

C3.2 Discussion of validity of the part of ELLE_GBM only considering surface energy

This part of the Appendix was entirely written by P. D. Bons.

Theory predicts that a cylindrical grain, with radius R , embedded in a homogeneous matrix will shrink as a function of time (t) according to:

$$\frac{\partial R}{\partial t} = \frac{-m\gamma}{R} \quad (\text{Eq. C1})$$

Here, m is the mobility of the grain boundary and γ is the surface energy

From this follows for the area (A), using $A = \pi R^2$, that:

$$A = A_0 - \frac{2m\gamma}{\pi R} \cdot t \quad (\text{Eq. C2})$$

The ELLE routine should produce the same results for a circular grain. How does the routine work and does it produce the theoretical prediction?

The random jump routine

All nodes are linked by straight segments. The lengths of these segments are determined by the user-set parameter L ($MinNodeSeparation$, $MaxNodeSeparation$). If a segment is shorter than L , a node is removed, and if a segment is larger than $2 \times L$, a node is inserted. L thus determines the resolution of the grain aggregate description.

Each time unit a node is displaced. To determine the displacement vector (length & direction), four alternative positions of the node are considered. These positions are calculated by taking a small displacement vector \underline{D} (D_{trial}) in a random direction. The length of \underline{D} is set to be

$$|\underline{D}| = L/100 \quad (\text{Eq. C3})$$

The three other positions are calculated by rotating this vector by 90° . For each of the four new positions the energy state for the two or three adjacent grain boundary segments is calculated. If surface energies and the stored energy of polygons are constant, the energy state is simply the length of the segments multiplied by the surface energy. For the example of a double-node in figure 1, bounding two segments of lengths l_1 and l_2 , the energy is :

$$E = \gamma \cdot (l_1 + l_2) \quad (\text{Eq. C4})$$

The energy after movement over vector \underline{D} would be;

$$E' = \gamma \cdot (l_1' + l_2') \quad (\text{Eq. C5})$$

The change in energy, ΔE , is simply the difference between the two. The energy states for the four possible displacements is calculated and the direction that produces the most energy loss is chosen to determine the actual displacement. If all four displacements produce an increase in energy, no movement takes place.

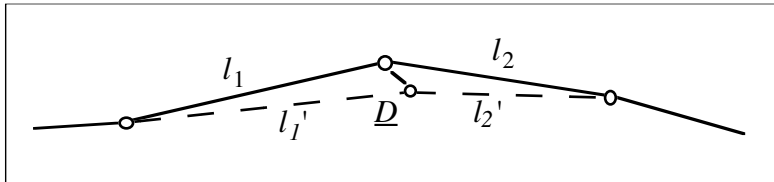


Fig. C3

The actual displacement, \underline{V} , is then taken to be: $\underline{V} = \underline{D} \cdot \Delta E \cdot M$ (Eq. C6)

the parameter M is a user-set mobility factor.

Does the random-jump routine satisfy equations (C1) and (C2)?

Figure C4 shows a node with two of its neighbours on the boundary of a circular grain with radius R . In reality the nodes should be closer to each other, so that the angle α is small. The distance between the nodes is L^* . On average, the node will be displaced towards the centre of curvature, since that will give the most surface energy loss. The displacement, here given as \underline{D}^* , reduces the length of the segments to L^* .

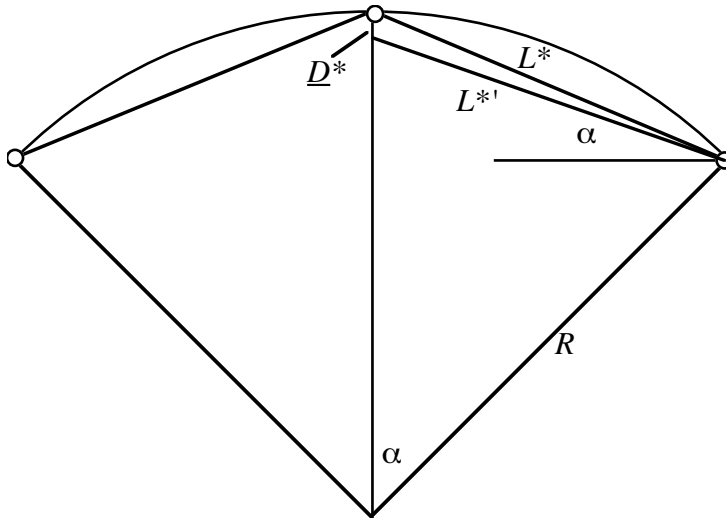


Fig. C4

The energy reduction for this situation is given by: $\Delta E = 2\gamma(L^* - L^*)$ (Eq. C7)

If α is small, we can approximate L^* by: $L^* \approx L^*(1 - D^* \sin \alpha)$, (Eq. C8)

which then gives: $\Delta E = 2\gamma L^* D^* \sin \alpha$ (Eq. C9a)

Using a dimensionless geometric factor C , we can rewrite equation (9) to one with the set parameters L and D , as both D^* and L^* are proportional to D and L respectively. This gives:

$$\Delta E = 2\gamma CLD \sin \alpha \quad (\text{Eq. C9b})$$

If N is the number of nodes on the circle, we get:

$$\alpha = \frac{2\pi}{N} \quad \& \quad L = \frac{2\pi R}{N}, \quad \text{which gives:} \quad \alpha = \frac{L}{R} \quad (\text{Eq. C10})$$

Recalling that $D=L/100$ and that $\sin \alpha \approx \alpha$ for small α , we can rewrite (9b) to:

$$\Delta E = \frac{\gamma CL^3}{50R} \quad (\text{Eq. C11})$$

Combining equations (C6) and (C11) we get:

$$\Delta R / \Delta t = -2M \cdot \Delta E = -\frac{\gamma CML^3}{25R} \quad (\text{Eq. C12})$$

The factor two come into the equation, because for every time-step, a displacement is carried out twice. If we use $\Delta R / \Delta t \approx dR/dt$, we can integrate equation (C12) to get:

$$dR/dt = -\frac{\gamma CML^3}{25R} \Leftrightarrow R^2 = R_0^2 - \frac{2\gamma CML^3}{25} \cdot t \Leftrightarrow A = A_0 - \frac{2\gamma CML^3}{25\pi} \cdot t \quad (\text{Eq. C13})$$

We see that the area of the circle should indeed reduce at a constant rate. This rate, dA/dt is proportional to the set mobility (M , $GBMob$) and proportional to the cube of the set node-distance (L).

At what grain sizes is the above valid?

First, the trial displacement should always be shorter than the distance to straighten a boundary, to avoid overshoot. Assuming that the average distance between nodes is L , this means that we must have $D < L \sin\alpha$ and hence $D < L/R$ (Eq.C 14)

Using equation (C3) we get $L/100 < L/R$ and thus $R < 100$ (Eq.C15)

Considering that the unit cell has dimensions 1×1 , this is easily satisfied.

Secondly, ΔE must be smaller than $2D/M$, because a node is never allowed to move further than the trial distance. This gives:

$$\frac{2D}{M} > \Delta E \Leftrightarrow \frac{2D}{M} > \frac{\gamma CL^3}{50R} \Leftrightarrow R > \gamma CML^3 \quad (\text{Eq. 16})$$

Using $L=0.005$, $C=0.8$ and $\gamma=1$, this gives: $R > 2 \cdot 10^{-7} M$ (Eq.C 16)

At a mobility of 10^4 this gives a minimum radius of $2 \cdot 10^{-3}$. which would be equivalent to about 10^5 grains in the unit cell. One should note that at such a small radius, the assumption that the angle α is small is not valid. We would therefore use a mobility of 10^4 safely for a unit cell with about 2000 grains, as is our starting aggregate.

Symbols used in C3.2

R = radius of grain [m]

t = time [s]

m = mobility [$\text{m}^2 \text{s kg}^{-1}$]

γ = surface energy per unit area [kg s^{-2}]

A = area [m^2]

L = user-defined parameter for distance between nodes. Actual distance varies between L (MinNodeSep) and $2L$ (MaxNodeSep)

l = actual distance between two nodes

\underline{D} , D_{trial} = trial displacement vector. $|\underline{D}| = 0.01 \cdot L$

\underline{V} = actual displacement of a node

M , $GBMob$ = user-defined mobility factor [$\text{s kg}^{-1} \text{m}^{-1}$]

α = angle between nodes on a circular grain

C = dimensionless geometric factor

C3.3 Test experiments

C3.3.1 Reproducibility of results

To investigate the reproducibility of results a set of 5 test experiments using ELLE_GBM were performed (Fig. C3). Results reveal a strong reproducibility of results.

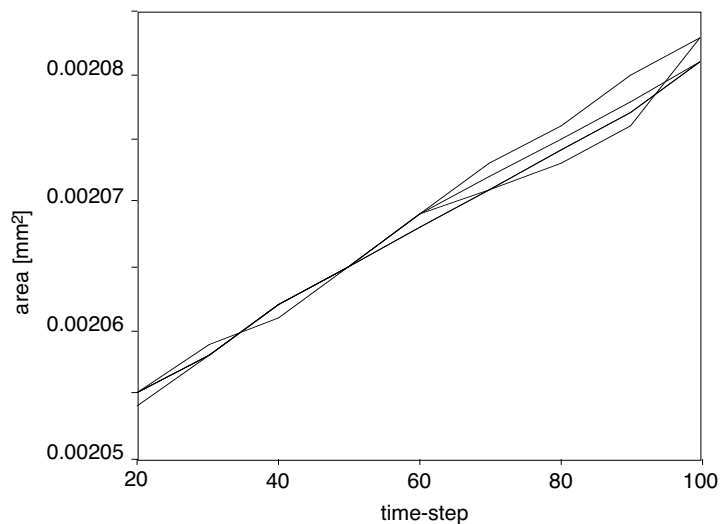


Figure C5 Graph depicting the areal change of a grain during grain boundary migration for the test set (a). 5 different test experiments were performed.

C3.3.2 Scaling tests of ELLE_GBM considering internal energy of polygons

The following tests were performed by M. W. Jessell to investigate the effect of the different scaling parameters on results. These tests apply to GBM driven by an internal energy, with all other driving forces turned off. The results are presented as area versus time step or $\sqrt{\text{area}}$ (= radius if looking at a round object) versus speedup and the slope of the radius versus time step (dR/dt) for each variable (speedup, switch distance, length-scale, time-step).

Results are summarized as follows:

dR/dt proportional to time scale (time steps do not represent equal time intervals) (Fig. C6)

dR/dt proportional to speedup (= mobility) (Fig. C7)

dR/dt proportional to switch distance squared (Fig. C8)

dR/dt proportional to length scale (Fig. C9)

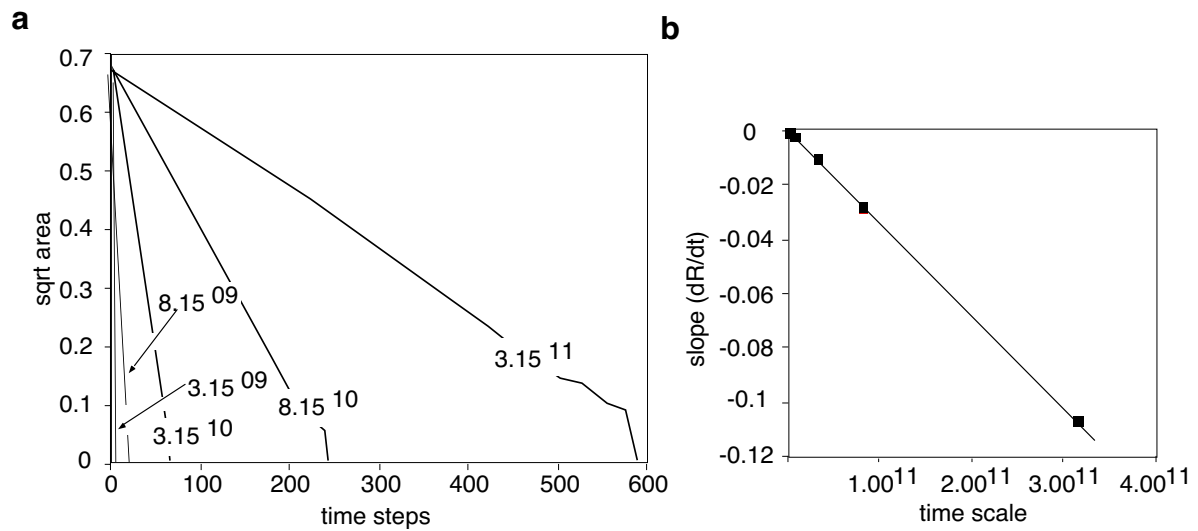


Figure C6 (a) Graph depicting the effect of time scale on the areal change of a grain during grain boundary migration. (b) Graph depicting the effect of time scale on the slope of the area change of a grain during grain boundary migration.

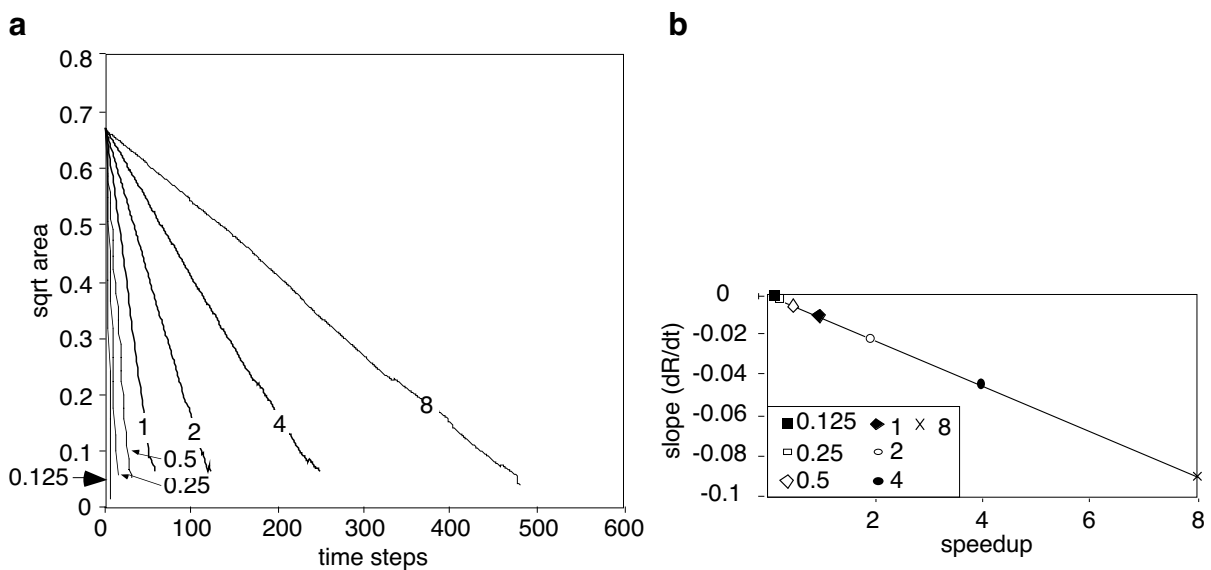


Figure C7 (a) Graph depicting the effect of speedup on the areal change of a grain during grain boundary migration. (b) Graph depicting the effect of speedup on the slope of the area change of a grain during grain boundary migration.

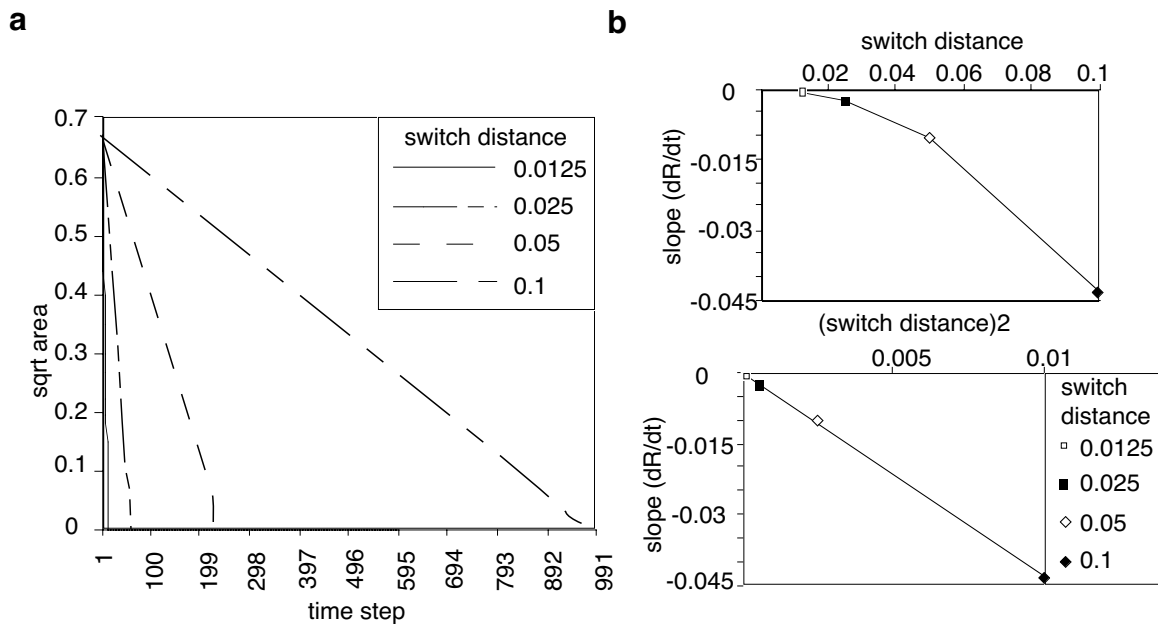


Figure C8 (a) Graph depicting the effect of switchdistance on the areal change of a grain during grain boundary migration. (b) Graph depicting the effect of switchdistance on the slope of the area change of a grain during grain boundary migration

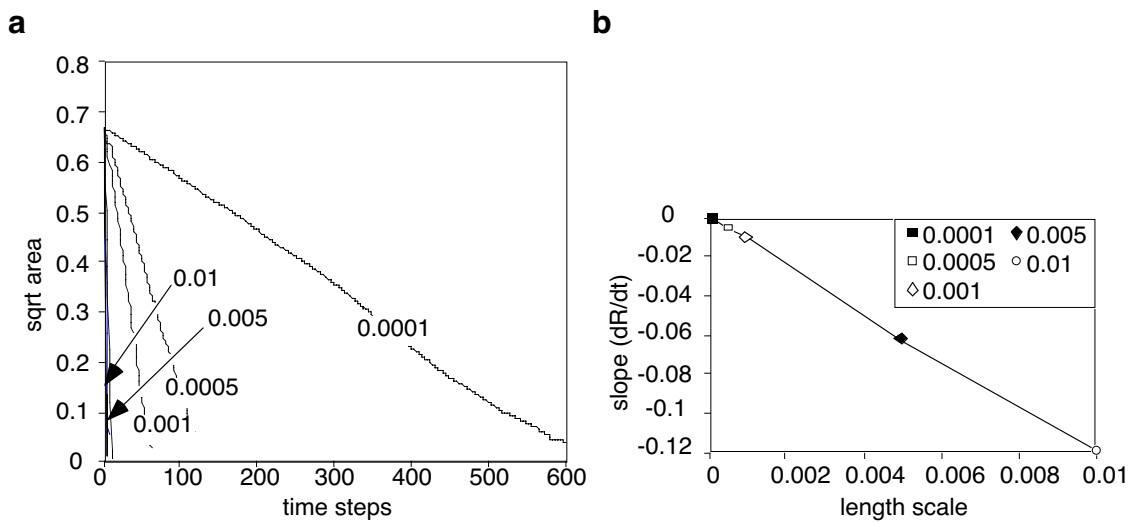


Figure C9 (a) Graph depicting the effect of length scale on the areal change of a grain during grain boundary migration. (b) Graph depicting the effect of length scale on the slope of the area change of a grain during grain boundary migration.

Appendix D

Rheology of a mixture of 60wt% Plastilina/40wt% Rhodorsil Gomme

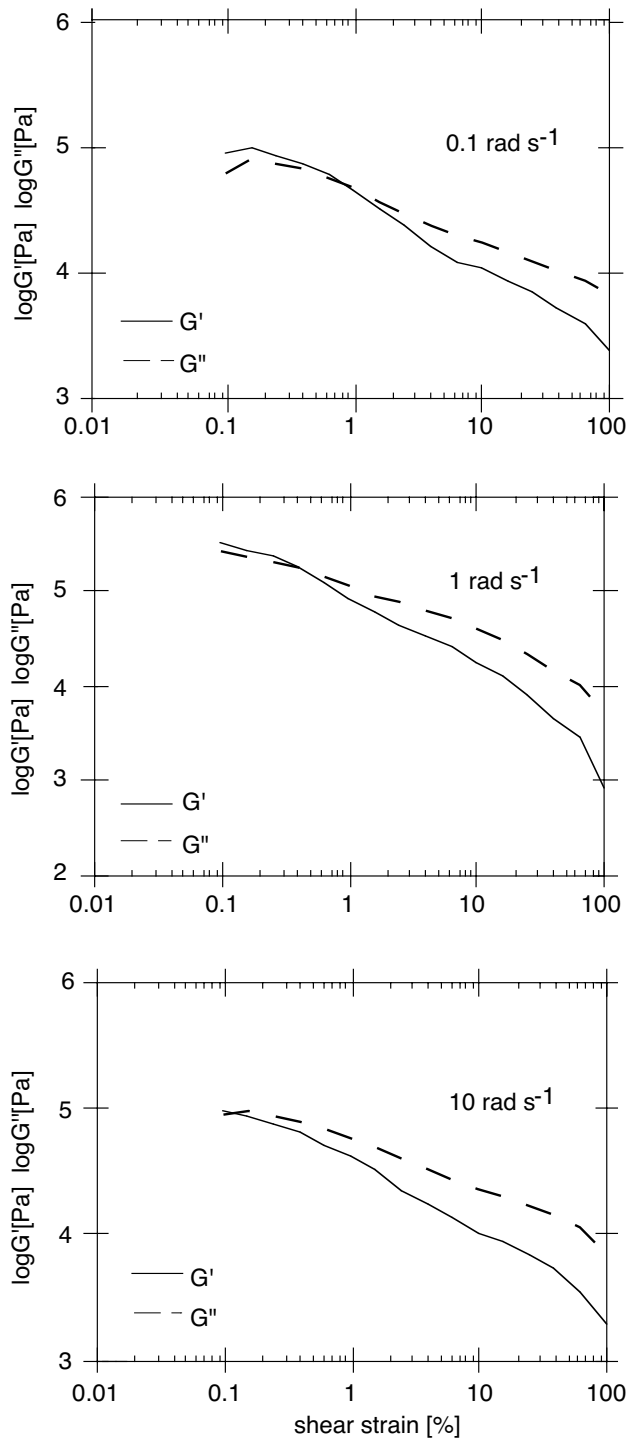


Figure D1 Graphs show the variation of G' and G'' (for further explanation see Chapter 4) with shear strain (in percent) at 3 different shear strain rates (given in radians per second) illustrating the non-linear, strain-dependent viscoelastic behavior of the mixture of 60 wt% plasticine and 40 wt% Rhodorsil Gomme. Measurements are performed as outlined in Chapter

Appendix E

Description and use of programs controlling the new deformation apparatus

In this appendix a detailed account on the programs written for the developed TT (transpression-transension) apparatus described in Chapter 5 is given. The appendix includes a general introduction to the different types of transpressional regimes, available programs, a User Manual, technical specifications and settings used in experiments described in Chapter 5 and Chapter 6.

E1 General Introduction

Transpression is broadly defined as a combination of perpendicular components of pure and simple shear. In three dimensions such a deformation can be described by the following deformation tensor under the assumption that shear occurs exclusively in the x direction:

$$D = \begin{bmatrix} k_1 & \Gamma_{xy} & \Gamma_{xz} \\ 0 & k_2 & \Gamma_{yz} \\ 0 & 0 & k_3 \end{bmatrix}$$

where k_1 , k_2 and k_3 represent extensions along the x, y, and z coordinate axes, respectively, and the off-diagonal terms represent elements of effective shear deformation (Tikoff and Fossen, 1993).

E2 Programs available

The 5 programs available right now model 5 different regimes of transpression assuming shear in the x direction and constant volume ($k_1 \cdot k_2 \cdot k_3 = 1$; $V_n = 1$ (Passchier, 1998)). All programs except Program A model transpressional deformation where the relative components of pure and simple shear i. e. the vorticity number can be varied (e.g. Means et al., 1980; Passchier, 1986; Bobyarchick, 1986).

Program A (*A/ Simple shear.vi*):

Simple shear; $k_1 = k_2 = k_3 = 1$.

Program B (*Transpression B.vi*):

Transpression; extension along the z-axis and $k_1 = 1$.

Program C (*Transpression C.vi*):

Transpression; extension in the x and z direction and $k_1 = k_3$.

Program D (*Transpression D.vi*):

Transpression; plane strain deformation; no extension along the z-axis ($k_3 = 1$).

Program E (*Transpression E.vi*):

Transpression; shortening along the y and z axis with $k_2 = k_3$.

For all five deformation types (Fig. E1) the movement of the 6 stepping motors of the apparatus (see Fig. E2; Fig. 5.2, Fig. 5.3) is calculated for each time step depending on the current dimensions of the deformation box and using dextral shear along the x axis.

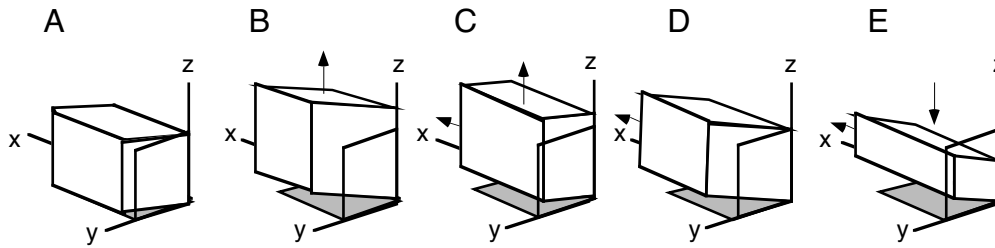


Figure E1 Schematic illustration of the 5 different types of transpressional regimes for which LabView programs exist.

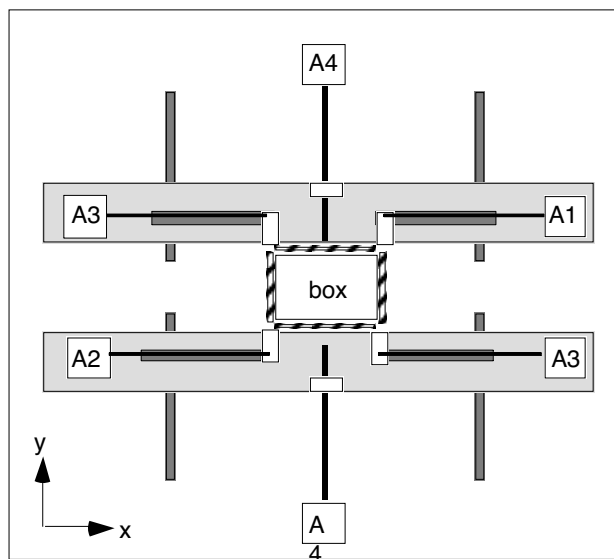


Figure E2 Diagram illustrating setup of the apparatus and the axis numbers (e.g. A1) used by the LabView programs.

Calculations

Based on the deformation matrix given above for each of the programs the movement of the motors i.e. the movement along the x, y and z direction can be calculated. We adopt a similar approach as Tikoff and Fossen (1993) and base our calculation on the division of deformation in a pure and simple shear component as shown below. With this knowledge the extension or shortening along each of the 3 axis can be calculated for each time step. For a specific vorticity number the pure and simple shear components along the different axes must satisfy the following equation.

$$W_n = \frac{\sqrt{(\dot{\gamma}_{yz})^2 + (\dot{\gamma}_{xz})^2 + (\dot{\gamma}_{xy})^2}}{\sqrt{2\left[(\dot{\epsilon}_1)^2 + (\dot{\epsilon}_2)^2 + (\dot{\epsilon}_3)^2\right] + (\dot{\gamma}_{yz})^2 + (\dot{\gamma}_{xz})^2 + (\dot{\gamma}_{xy})^2}}$$

As it is assumed that shear only occurs along the x axis γ_{xz} and γ_{yz} are zero. For each of the programs this equation is modified to meet the definition of the 5 different deformation regimes (see above).

Program A:

Simple shear; $W_n = 1$.

Program B:

$$W_n = \frac{\sqrt{(\dot{\gamma}_{yz})^2}}{\sqrt{2\left[(\dot{\varepsilon}_2)^2 + (\dot{\varepsilon}_3)^2\right] + (\dot{\gamma}_{yz})^2}}$$

Program C

$$W_n = \frac{\sqrt{(\dot{\gamma}_{yz})^2}}{\sqrt{2\left[2 \cdot (\dot{\varepsilon}_1)^2 + (\dot{\varepsilon}_2)^2\right] + (\dot{\gamma}_{yz})^2}} :$$

Program D:

$$W_n = \frac{\sqrt{(\dot{\gamma}_{yz})^2}}{\sqrt{2\left[(\dot{\varepsilon}_1)^2 + (\dot{\varepsilon}_2)^2\right] + (\dot{\gamma}_{yz})^2}}$$

Program E:

$$W_n = \frac{\sqrt{(\dot{\gamma}_{yz})^2}}{\sqrt{2\left[(\dot{\varepsilon}_1)^2 + 2 \cdot (\dot{\varepsilon}_2)^2\right] + (\dot{\gamma}_{yz})^2}}$$

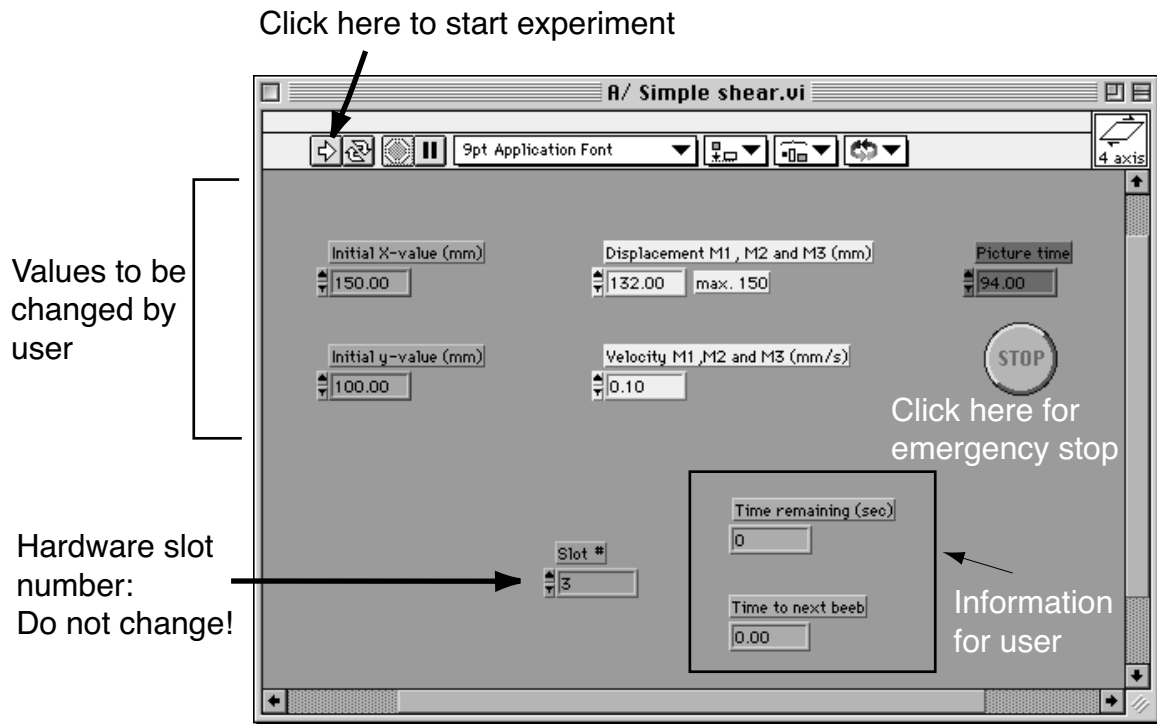
E3 User Manual

Open one of the 5 programs, located at folder LabView -> programmes for shearapparatus (e.g. *Transpression B.vi*). For each program the control panel shows five types of boxes (Fig. E3)

- 1) Green boxes are inputs concerning the initial dimensions of the deformation box,
- 2) yellow boxes specify the deformation rate, vorticity number and amount of final deformation,
- 3) red box characterizes the timing of a signal (e.g. to alert the user to take pictures),
- 4) orange boxes and diagram provide information about the deformation during the experiment, remaining time of the experiment and to next beep,
- 5) grey box specifies the slot for the hardware card (PCI-STEP-4OX).

The user should ONLY change values in the green, yellow and red boxes. If by accident the slot number is changed the motors will not respond. Resetting the slot number to 3 fixes the problem. Additionally, there is an emergency STOP button, which can be pressed (mouse click) if desired.

a



b

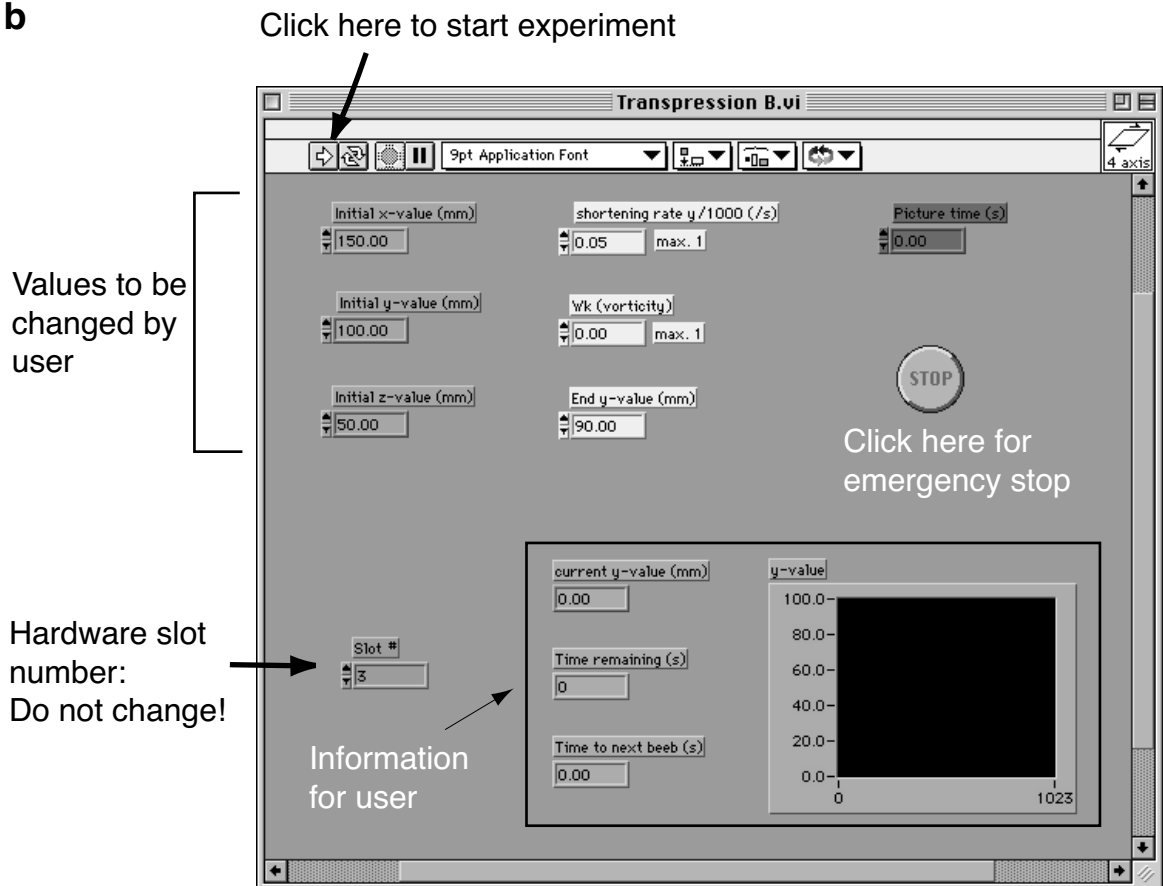


Figure E3 (a) Control panel of program A (A/Simple Shear.vi), (b) Control panel of program B (Transpression B.vi)

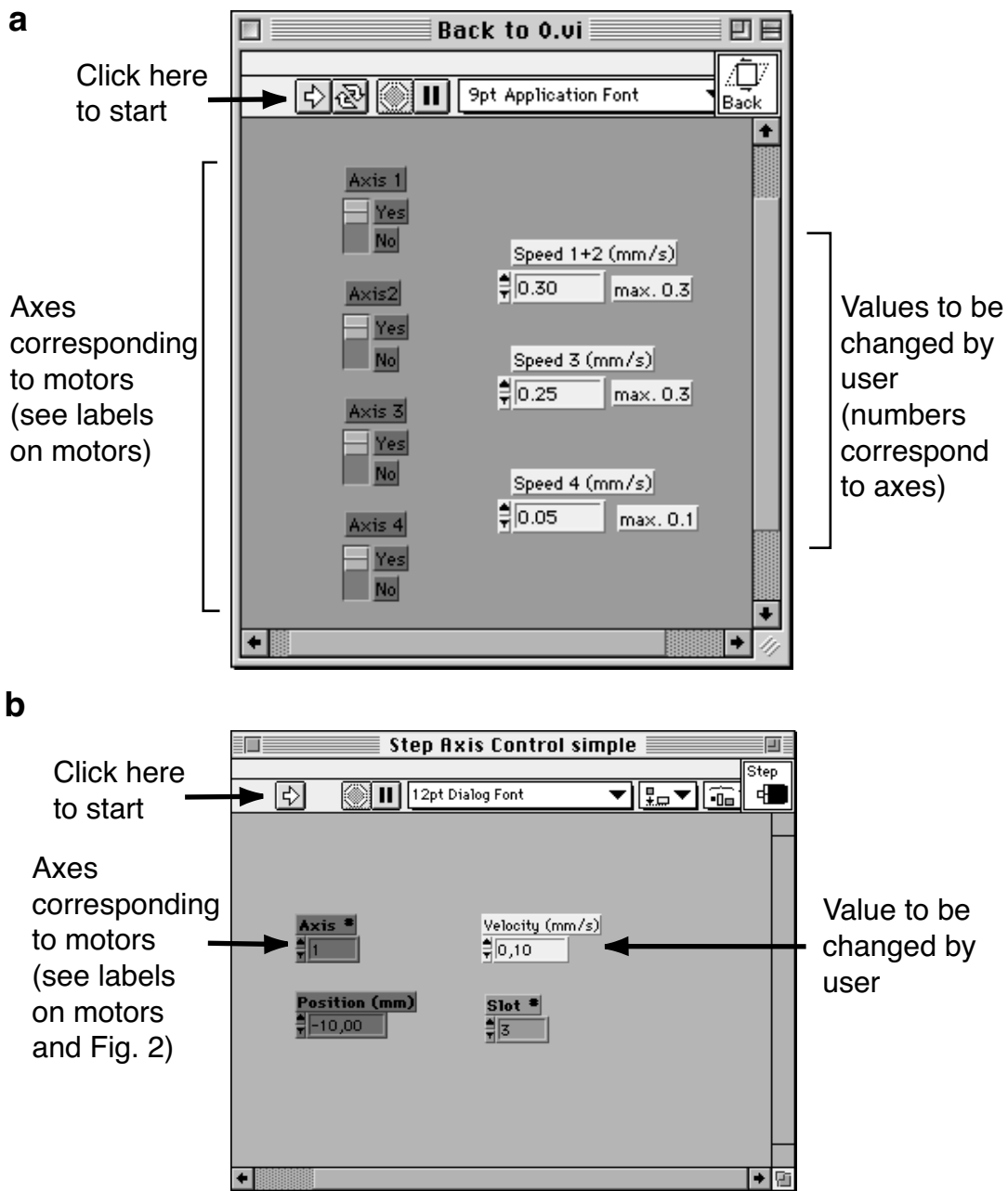


Figure E4 (a) Control panel of Back to 0.vi, (b) Control panel of Step Axis Control Simple

Once an experiment has finished or is stopped manually by the user (emergency STOP), open program Back to 0.vi (Fig. E4a). This program will move the deformation box to its initial position. Here, the velocity of movement is given by the user. NEVER quit LabView or turn off the computer before the deformation box is returned to its initial position, otherwise the true initial position of the box will not be "remembered" by the program. If for unforeseen reason this does happen, the program Step Axis Control Simple (Fig. E3) can be used to repo-

sition the deformation box. The same program can be used to reposition the deformation box e.g. if a different initial position is required. After repositioning, restart the computer so that the position is recognized by LabView as the new default zero position. Figure E2 shows axis numbers as used by the programs.

E4 Technical specifications

Product	Description	Manufacturer
LabView 5.0	Graphical Programming for Instrumentation	National Instruments Germany GmbH Konrad-Celtis-Str. 79 81369 München Tel.: 089-7413130
ValueMotion	Additional LabView library for stepping motors	National Instruments
PCI-STEP-4OX 4-Axis Open Loop Step controller for Macintosh	Hardware card to communicate with power device and personal computer	National Instruments
Power Device Connection block CB-50 + MTL-400/6 4 axis multiplier	Electronic link between personal computer and stepping motors	MovTec Stuetz & Wacht GmbH Goldschmiedeschulstr.6 75173 Pforzheim Tel.: 07231/299669 Email: movtex@t-online.de
Stepping Motors MTS-230-E80		MovTec
Latex sheet	Thickness 0.35 mm, Width ± 21 cm Length ± 28 cm	Skintight Netherlands Email: linda@skintight.nl
Shaft 270-164	M6, messing	RS Components GmbH Hessenring 13b 64546 Mörfelden-Walldorf Tel.: 06105-401234 Email: rs-gmbh@rs-components.com
Shaft joint 689-007	Shaft diameter 6 mm	RS Components GmbH
Springs: Zugfeder 12/3/5	Length l_0 128 mm, R 0.11 N/mm	Federntechnik Knörzer GmbH Postfach 7282 72785 Pfullingen Tel.: 07121-97840
Zugfeder 11/5/2	Length l_0 60.8 mm, R 0.09 N/mm	
Carriages	Length 300 mm	Baumarkt Mainz
PVC platelets and board	different thickness and length	Cadillac Plastic GmbH Mainz-Kastel Tel.: 06134-22036

E5 Used set-up for experiments:**Chapter 5: Experimental set 1 - Flow experiments**

Program type	D
Initial dimensions [mm]	100 x 150 x 100
W_n	0.8, 0.6
Shortening rate [s^{-1}]	$3.3 \times 10^{-4} s^{-1}$
Matrix material	PDMS
Object dimensions [mm]	no object
Object material	no object

Chapter 5: Experimental set 2 - Boundary conditions experiment

Program type	D
Initial dimensions [mm]	100 x 150 x 100
W_n	0.8, 0.6
Shortening rate [s^{-1}]	$2.0 \times 10^{-4} s^{-1}$, $3.3 \times 10^{-4} s^{-1}$, $4.7 \times 10^{-4} s^{-1}$
Matrix material	PDMS, Rhodorsil Gomme
Object dimensions [mm]	no object
Object material	no object

Chapter 5: Experimental set 3 - Pilot experiment

Program type	D
Initial dimensions [mm]	100 x 150 x 100
W_n	1, 0.8, 0.6
Shortening rate [s^{-1}]	$1 \times 10^{-3} s^{-1}$ ($W_n=1$), $3.3 \times 10^{-4} s^{-1}$ ($W_n=0.8, 0.6$)
Matrix material	PDMS
Object dimensions [mm]	10 mm x 7 mm x 16 mm
Object material	rigid India rubber

Chapter 6: Experimental set 1 - Object aspect ratio 3

Program type	D
Initial dimensions [mm]	100 x 150 x 100
W_n	1, 0.8, 0.6
Shortening rate [s^{-1}]	$1 \times 10^{-3} s^{-1}$ ($W_n=1$), $3.3 \times 10^{-4} s^{-1}$ ($W_n=0.8, 0.6$)
Matrix material	PDMS, PDMS + 25% BaSO ₄
Object dimensions [mm]	6 mm x 2 mm
Object material	rigid India rubber

Chapter 6: Experimental set 2 - Object aspect ratio 2

Program type	D
Initial dimensions [mm]	100 x 150 x 100
W_n	1, 0.8, 0.6
Shortening rate [s^{-1}]	$1 \times 10^{-3} s^{-1}$ ($W_n=1$), $3.3 \times 10^{-4} s^{-1}$ ($W_n=0.8, 0.6$)
Matrix material	PDMS
Object dimensions [mm]	5 mm x 2.5 mm
Object material	rigid India rubber

Appendix F

CD-Rom: Calculations and Movies

A CD-Rom is normally attached to this thesis. It contains an excell calculation sheet to quickly calculated the concentration parameter κ from a set of directional data (folder A), the Elle source code used for the numerical simulations (folder B1), the elle manual to the Elle source code (folder B2), and Quicktime movies of selected simulation runs discussed in Chapter 3 (folder B3), Quicktime movies of analogue experiments described and discussed in Chapter 5 (folder C), and 6 (folder D). Please refer to the Read me files on the CD-Rom for further details. The files can be obtained from the author.

References

- Abbassi, M. R. & Mancktelow, N. S. 1990. The effect of initial perturbation shape and symmetry on fold development. *Journal of Structural Geology* 15, 293-307.
- Albaret, L., Diot, H., Bouchéz, J. L., Lespinasse, P. & Saint-Blanquat, M. 1997. Analogue 3D simple-shear experiments of magmatic biotite subfabrics. In: Bouchéz, J. L., Hutton, D. H. W., Stephens, W. E., (Eds) *Granite: From Segregation of melt to emplacement fabrics*, 129-143.
- Anma, R. 1997. Oblique diapirism of the Yakushima granite in the Ryukyu arc, Japan. In: Bouchéz, J. L., Hutton, D. H. W., W. E. Stephens (Eds.) *Granite: From Segregation of melt to emplacement fabrics*, 295-318.
- Anma, R. & Sokoutis, D. 1997. Experimental pluton shapes and tracks above subduction zones. In: Bouchéz, J. L., Hutton, D. H. W., Stephens, W. E., (Eds) *Granite: From Segregation of melt to emplacement fabrics*, 319-334.
- Argon, A. S. 1970. Internal stresses arising from the interaction of mobile dislocations. *Scripta Metallurgica* 4, 1001-1004.
- Anderson, M. P., Grest, G. S. & Srolovitz, D. J. 1984. Grain growth in three dimensions: a lattice model. *Scripta Metallurgica* 19, 225-230.
- Askeland, D. R. 1990. *The Science and Engineering of Materials*, Chapman and Hall, London.
- Azor, A., Simancas, J. F., Exposito, I., Lodeiro, F. G. & Poyatos, D. J. M. 1997. Deformation of garnets in a low-grade shear zone. *Journal of Structural Geology* 19, 1137-1148.
- Barber, D. J. 1985. Dislocations and Microstructures. In Wenk, H.-R. (Eds.) *Preferred Orientation in Deformed Metals and Rocks: An Introduction to Modern Texture Analysis*, Academic Press, London, 149-182.
- Barr, T. D. & Houseman, G. A. 1992. Distribution of deformation around a fault in a non-linear ductile medium. *Geophysical Research Letters* 19, 1145-1148.
- Barr, T. D. & Houseman, G. A. 1996. Deformation fields around a fault embedded in a non-linear ductile medium. *Geophysical Journal International* 125, 473-490.
- Batschelet, E. 1981. *Circular Statistics in Biology*. Academic Press, London.
- Beach, A. 1980. Retrogressive metamorphic processes in shear zones with special reference to the Lewisian complex. *Journal of Structural Geology* 2, 257-263.
- Beam, E., C. & Fisher, D. M. 1999. An estimate of kinematic vorticity from rotated elongate porphyroblasts. *Journal of Structural Geology* 21, 1553-1559.
- Beeman, M. I. & Kohlstedt, D. I. 1988. Dislocation density: stress relationships in natural and synthetic sodium chloride. *Tectonophysics* 149, 147-161.
- Bell, T. H. & Cuff, C. 1989. Dissolution, solution transfer, diffusion versus fluid flow and volume loss during deformation and metamorphism. *Journal of Metamorphic Geology* 7, 425-447.
- Bentley, B. J. & Leal, L. G. 1986. An experimental investigation of drop deformation and breakup in steady, two-dimensional linear flows. *Journal of Fluid Mechanics* 167, 241-283.
- Berthé, D., Choukroune, P. & Jegouzo, P. 1979. Orthogneiss, mylonite and non-coaxial deformation of granites: the example of the South Armorican shear zone. *Journal of Structural Geology* 1, 31-2.
- Bhattacharyya, D. S. 1966. Orientation of mineral lineation along the flow direction in rocks. *Tectonophysics* 3, 29-33.

- Bilby, B. A., Eshelby, J. D. & Kundu, A. K. 1975. The change of shape of a viscous ellipsoidal region embedded in a slowly deforming matrix having a different viscosity. *Tectonophysics* 28, 265-274.
- Bilby, B. A., Eshelby, J. D., Kolbuszewski, M. L. & Kundu, A. K. 1976. The change of shape of a viscous ellipsoidal region embedded in a slowly deforming matrix having a different viscosity. Some comments on a discussion by N. C. Gay. *Tectonophysics* 35, 408-409.
- Bishop, J. F. W. & Hill, R. 1951a. A theory of plastic distortion of a polycrystalline aggregated under combined stresses. *Philos. Magazine* 42, 414-427.
- Bishop, J. F. W. & Hill, R. 1951b. A theoretical derivation of the plastic properties of a polycrystalline face-centered metal. *Philos. Magazine* 42, 1298-1307.
- Board, M. 1989. *FLAC: Fast Lagrangian Analysis of Continua, User Manual, Version 2.20, Software Summary*, Itasca Consulting Group, Inc., Minneapolis.
- Bobyarchick, A. R. 1986. The eigenvalues of steady flow in Mohr space. *Tectonophysics* 122, 35-51.
- Bons, P. D. 1993. Experimental deformation of polyphase rock analogues. *Geologica Ultraiectina* 110, 207 pp.
- Bons, P. D., Barr, T. D. & ten Brink, C. E. 1997. The development of d-clasts in non-linear viscous materials: a numerical approach. *Tectonophysics* 270, 29-41.
- Bons, P. D. & Jessell, M. W. 1995. Strain analysis in deformation experiments with pattern matching or a stereoscope. *Journal of Structural Geology* 17, 917-921.
- Bons, P.D. & Jessell, M.W. 1996. Image analysis of microstructures in natural and experimental samples. In D.G. DePaor (Ed.), *Structural Geology and personal computers*. Pergamon, 135-166.
- Bons, P. D. & Jessell, M.W. 1999. Micro-shear zones in experimentally deformed octachloropropane. *Journal of Structural Geology* 21, 323-334.
- Bons, P. D. & Urai, J. L. 1992. Syndeformational grain growth: microstructures and kinetics. *Journal of Structural Geology* 14, 1101-1109.
- Bons, P. D. & Urai, J. L. 1994. Experimental deformation of two-phase rock analogues. *Materials Science and Engineering A175*, 221-229.
- Bons, P. D. & Urai, J. L. 1995. An apparatus to experimentally model the dynamics of ductile shear zones. *Tectonophysics* 256, 145-164
- Bons, P. D., Jessell, M. W., Evans, L., Barr, T. D. & Stüwe, K. in press. Modelling of anisotropic grain growth in minerals. In: Koyi, A. H. & Mancktelow, N. S. (Eds.). Chapter 4: *Tectonic Modeling: A Volume in Honor of Hans Ramberg*, Geological Society of America Memoir 193.
- Bouchéz, J. L. 1997. Granite is not isotropic: An introduction to AMS Studies of granitic rocks, In: Bouchéz, J. L., Hutton, D. H. W., Stephens, W. E., (Eds) *Granite: From Segregation of melt to emplacement fabrics*, 95-112.
- Brace, W. F. & Kohlstedt, D. L. 1980. Limit on lithospheric stress imposed by laboratory experiments. *Journal of Geophysical Research* 85, 6248-6252.
- ten Brink, C. E., 1996. Development of porphyroclast geometries during non-coaxial flow. *Geologica Ultraiectina* 142, 163 pp.
- ten Brink, C. E. & Passchier, C. W., 1995. Modelling of mantled porphyroclasts using non-Newtonian rock analogue materials. *Journal of Structural Geology* 17, 131-146.
- Brun, J.-P., D. Sokoutis & Van Den Driessche, J. 1994. Analogue modeling of detachment fault systems and core complexes, *Geology* 22, 319-322.

- Carreras, J. 1975. Determinación de las relaciones angulares y de la deformación por cizalla, para cizallamientos en materiales con una heterogeneidad planar. *Acta geol. Hisp.* 10, 141-145.
- Carreras, J. & Casas, J. M. 1987. On folding and shear zone development: a mesoscale structural study on the transition between two different tectonic styles. *Tectonophysics* 135, 87-98.
- Carreras, J. & Druguet, E. 1994a. Structural zonation as a result of inhomogeneous non-coaxial deformation and its control on syntectonic intrusions: an example from the Cap de Creus area (eastern-Pyrenees). *Journal of Structural Geology* 16, 1525-1534.
- Carreras, J. & Druguet, E. 1994b. El papel de las zonas de cizalla en la configuración estructural del complejo migmatítico del sector septentrional de la península del Cap de Creus (Girona). *Rev. Soc. geol. España* 7, 21-29.
- Carreras, J., Estrada, A. & White, S. 1977. The effects of folding on the c-axis fabrics of a quartz mylonite. *Tectonophysics* 39, 3-24.
- Carreras, J. & García, A. 1982. Quartz c-axis fabric variation at the margins of a shear zone developed in schists from Cap de Creus (Spain). *Acta geol. Hisp.* 17, 137-149.
- Carter, N. L. 1976. Steady state flow of rocks. *Rev. Geophys. Space Phys.* 14, 301-360.
- Carter, N. L. & Tsenn, M. C. 1987. Flow properties of continental lithosphere. *Tectonophysics* 136, 27-63.
- Carter K. E. & Winter C. L. 1995. Fractal nature and scaling of normal faults in the Española Basin, Rio Grande rift, New Mexico: implications for fault growth and brittle strain. *Journal of Structural Geology* 17, 863-873.
- Castelnaud, O., Duval, P., Lebensohn, R. A. & Canova, G. R. 1996. Viscoplastic modeling of texture development in polycrystalline ice with a self-consistent approach: Comparison with bound estimates. *Journal of Geophysical Research* 101, 13851-13868.
- Christie, J. M. & Ord, A. 1980. Flow stress from microstructures of mylonites: Example and current assessment. *Journal of Geophysical Research* 85, 62537-6262.
- Clark, M. K. & Royden, L. H. 2000. Topographic ooze: Building the eastern margin of Tibet by lower crustal flow. *Geology* 28, 703-706.
- Cobbold, P. R. 1983. Kinematic and mechanical continuity at a coherent interface. *Journal of Structural Geology* 5, 341-349.
- Cruden, A. & Robin, P.-Y. 1999. Analogue models of ductile transpression zones. *Journal of Conference Abstracts* 4, 604.
- Dealy, J. M. & Broadhead, T. O. 1993. Rheometry for Process Control. In: Collyer, A. A. (Eds.) *Techniques in rheological measurement*, Chapman and Hall, 285-331.
- De Bresser, J. H. P., Peach, C. J., Reijs, J. P. J. & Spiers, C. J. 1998. On dynamic recrystallization during solid state flow: Effects of stress and temperature. *Geophysical Research Letters* 25, 3457-3460.
- De Bresser, J. H. P. 1996. Steady state dislocation densities in experimentally deformed calcite materials: Single crystals versus polycrystals. *Journal of Geophysical Research* 101, 22189-22201.
- Dell'Angelo, L. N. & Tullis, J. 1989. Fabric development in experimentally sheared quartzites. *Tectonophysics* 169, 1-21.
- Derby, B. & Ashby, M. F. 1987. On dynamic recrystallization. *Scripta Metallurgica* 21, 879-885.
- Dewers, T. & Ortoleva, P. 1990. Geochemical self-organization.III: A mechano-chemical model for metamorphic differentiation. *American Journal Science* 290, 473-521.
- Dewey, J., Holdsworth, R. E., & Strachan, R. A., 1998, Transpression and transtension zones, In: Holdsworth, R. E., Strachan, R. A. and Dewey, J. F. (Eds) *Continental Transpressional and Transtensional Tectonics*. Geological Society, London, Special Publications 135, 1-14.

- Dipple, G. M. & Ferry, J. M. 1992. Metasomatism and fluid flow in ductile fault zones. *Contributions to Mineralogy and Petrology* 112, 149-164.
- Dixon, J. M. & Summers, J. M. 1985. Recent developments in centrifuge modelling of tectonic processes: equipment, model construction techniques and rheology of model materials. *Journal of Structural Geology* 7, 83-102.
- Dixon, J. M. & Summers, J. M. 1986. Another word on the rheology of silicone putty: Bingham. *Journal of Structural Geology* 8, 593-595.
- Donnadieu, F. & Merle, O. 1998. Experiments on the indentation process during cryptodome intrusions: New insights into Mount St. Helens deformation. *Geology* 26, 79-82.
- Druguet, E. 1997. The structure of the NE Cap de Creus peninsula. Relationships with metamorphism and magmatism. Unpubl. Thesis, Univ. Autònoma de Barcelona.
- Druguet, E., & Hutton, D. H. W. 1998. Syntectonic anatexis and magmatism in a mid-crustal transpressional shear zone: an example from the Hercynian rocks of the eastern Pyrenees. *Journal of Structural Geology* 20, 905-916.
- Druguet, E., Passchier, C. W., Carreras, J., Victor, P. & den Brok, S. 1997. Analysis of a complex high-strain zone at Cap de Creus, Spain. *Tectonophysics* 280, 31-45.
- Drury, M. R. 1984. Geological implications of deformation studied on magnesium. PhD Thesis, University of London (Unpublished).
- Drury, M. R., Humphreys, F. J. & White, S. H. 1985. Large strain deformation studies using polycrystalline magnesium as rock analogue. Part II. Dynamic recrystallization mechanisms at high temperatures. *Phys. Earth Planet. Inter.* 40, 208-222.
- Drury, M. R. & Urai, J. L. 1990 Deformation-related recrystallization processes. *Tectonophysics* 172, 235-253.
- Durham, W. B., Goetze, C. & Blanke B. 1977. Plastic flow of oriented single crystals of olivine, 2, Observations and interpretations of the dislocation structures. *Journal of Geophysical Research* 82, 5755-5770.
- Ellis, M. & Watkinson, A. J. 1987. Orogen-parallel extension and oblique tectonics: The relation between stretching lineations and relative plate motions. *Geology* 15, 1022-1026.
- Eshelby, J. D. 1957. The determination of the elastic field of an ellipsoidal inclusion and related problems. *Proceedings of the Royal Society London* 241, 376-396.
- Etheridge, M. A. 1971. Experimental investigations of the mechanisms of mica preferred orientation in foliated rocks. Ph. D. Thesis, Australian National University, 165 pp.
- Evans, B. & Kohlstedt, D. L. 1995. Rheology of Rocks. In: Ahrens, T. J. (Eds.) *Rock Physics & Phase relations: A handbook of physical constants*, AGU Reference Shelf 3, Washington, 148-165.
- Faul, U. H. & Fitz Gerald, J. D. 1999. Grain misorientations in partially molten olivine aggregates: an electron backscatter diffraction study. *Physics and Chemistry of Minerals* 26, 187-197.
- Ferguson, C. C. 1979. Rotations of elongate rigid particles in slow non-newtonian flows. *Tectonophysics* 60, 247-262.
- Fernandez, A. 1978. Fonction de distribution de l'orientation de marqueurs linéaires lors de la déformation par aplatissement à deux dimensions. *C. R. Acad. Sci. Paris* 286, 1857-1860.
- Fernandez, A. 1987. Preferred orientation developed by rigid markers in two-dimensional simple shear strain: a theoretical and experimental study. *Tectonophysics* 136, 151-158.

- Fernandez, A. & Fernandez-Catuxo, J. 1997. 3D biotite shape fabric experiments under simple shear strain. In: Bouch ez, J. L., Hutton, D. H. W., Stephens, W. E., (Eds) *Granite: From Segregation of melt to emplacement fabrics*, 145-157.
- Fernandez, A., Feybesse, J.-L. & Mezure, J.-F. 1983. Theoretical and experimental study of fabrics developed by different shaped markers in two-dimensional simple shear. *Bull. Soc. Geol. France* 25, 319-326.
- Fitz Gerald, J. D., Etheridge, M. A. & Vernon, R. H. 1993. Dynamic recrystallization in a naturally recrystallized albite. *Textures and Microstructures* 5, 219-237.
- Fliervoet, T. F., Drury, M. R. & Chopra, P. N. 1999. Crystallographic preferred orientations and misorientations in some olivine rocks deformed by diffusion or dislocation creep. *Tectonophysics* 303, 1-27.
- Fliervoet, T. F. & White, S. H. 1995. Quartz deformation in very fine grained quartzo-felspathic mylonite: a lack of evidence for dominant grain boundary sliding deformation. *Journal of Structural Geology* 17, 1095-1109.
- Flinn, D. 1978. Construction and computation of three-dimensional progressive deformations. *Journal of the Geological Society, London* 135, 291-305.
- Fossen, H. & Tikoff, B. 1998. Extended models of transpression and transtension, and application to tectonic settings. In: Holdsworth, R. E., Strachan, R. A., Dewey, J. F. (Eds.) *Continental Transpressional and Transtensional Tectonics*. Geological Society, London, Special Publications 135, 15-33.
- Freeman, B. 1985. The motion of rigid ellipsoidal particles in slow flows. *Tectonophysics* 113, 163-183.
- Freeman, B. 1987. The behaviour of deformable ellipsoidal particles in three dimensional slow flows: Implications for geological strain analysis. *Tectonophysics* 132, 297-309.
- Freeman, B., & Lisle, R. J. 1987. The relationship between tectonic strain and the three-dimensional shape fabrics of pebbles in deformed conglomerates. *Journal of the Geological Society of London* 144, 635-639.
- Frost, H. J. & Ashby, M. F. 1983. *Deformation – Mechanism Maps: The Plasticity and Creep of Metals and Ceramics*. Pergamon Press, Oxford.
- Fry, N. 1979. Random points distributions and strain measurement in rocks. *Tectonophysics* 60, 89-105.
- Gay, N. C. 1966. Orientation of mineral lineation along the flow direction in rocks: a discussion. *Tectonophysics* 3, 559-564.
- Gay, N. C. 1968a. Pure shear and simple shear deformation of inhomogeneous viscous fluids 1. Theory. *Tectonophysics* 5, 211-234.
- Gay, N. C. 1968b. Pure shear and simple shear deformation of inhomogeneous viscous fluids 2. The determination of the total finite strain in a rock from objects such as deformed pebbles. *Tectonophysics* 5, 295-302.
- Gay, N. C. 1976. The change in shape of a viscous ellipsoidal region embedded in a slowly deforming matrix having a different viscosity - Discussion. *Tectonophysics* 35, 403-407.
- Gay, N. C. & Fripp, R. E. P. 1976. The control of ductility on the deformation of pebbles and conglomerates. *Philosophical Transactions of the Royal Society* 283, 109-128.
- Ghosh, S. K. 1987. Measure of non-coaxiality. *Journal of Structural Geology* 7, 111-113.
- Ghosh, S. K. 1993. *Structural Geology: Fundamentals and modern developments*. Pergamon Press, U.S.A..
- Ghosh S. K. & Ramberg H. 1976. Reorientation of inclusions by combination of pure shear and simple shear. *Tectonophysics* 34, 1-70.
- Ghosh, S. K. & Sengupta, S. 1973. Compression and simple shear of test models with rigid and deformable inclusions, *Tectonophysics* 17, 133-175.

- Giesekeus, H. 1962. Strömungen mit konstantem Geschwindigkeitsgradienten und die Bewegung von darin suspendierten Teilchen, Teil II: Ebene Strömungen und eine experimentelle Anordnung zu ihrer Realisierung. *Rheologica Acta* 2, 112-122.
- Giuseppe, C. 1997. Fractal analysis of a Quaternary fault array in the central Apennines, Italy. *Journal of Structural Geology* 19, 945-953.
- Gleason, G. C. & Tullis, J. 1993. The role of dynamic recrystallization in the development of lattice preferred orientations in experimentally deformed quartz aggregates, *Journal of Structural Geology* 15, 1145-1168.
- Gohr, K., Pakula, T., Tsutsumi, K. & Schärfl, W. 1999. Dynamics of copolymer micelles in an entangled homopolymer matrix. *Macromolecules* 32, 7156-7165.
- Gottstein, G. & Mecking, H. 1985. Recrystallization. In: Wenk, H.-R. (Eds.) *Preferred Orientation in Deformed Metals and Rocks: An Introduction to Modern Texture Analysis*, Academic Press, London, 183-214.
- Gottstein, G. & Shvindlerman, L. S. 1999. *Grain Boundary Migration in Metals: thermodynamics, Kinetics, Applications*, CRC Press, LLC, Boca Roca.
- Grest, G. S., Srolovitz, D. J. & Anderson, M. P. 1985. Computer simulation of grain growth IV. Anisotropic grain boundary energies. *Acta Metallurgica* 33, 509-520.
- Griera, A. & Carreras, J. 1999. Mechanical instabilities associated to rod development: Preliminary results from analogue modelling. *Journal of Conference Abstracts* 4, 603.
- ten Grotenhuis, S. M., & Passchier, C. W., 1999, Mica fish and other fish-shaped shear sense indicators: *Journal of Conference Abstracts* 4, 828
- Grujic, D. 1993. The influence of initial fold geometry on Type 1 and Type 2 interference patterns: an experimental approach. *Journal of Structural Geology* 15, 293-307.
- Guillopé, M. & Poirier, J. P. 1979. Dynamic recrystallization during creep of single crystalline halite: an experimental study. *Journal of Geophysical Research* 4, 5557-5567.
- Hacker, B. R. & Kirby, S. H. 1993. High-pressure deformation of calcite marble and its transformation to aragonite under non-hydrostatic conditions. *Journal of Structural Geology* 15, 1207-1222.
- Handy, M. R. 1990. The solid-state flow of polymineralic rocks. *Journal of Geophysical Research* 95, 8647-8661.
- Hardwick, D., Sellars, C. M. & Tegart, W. J. McG. 1961. *Journal of the Institute of Metals* 90, 21.
- Heidelbach, F., Kunze K. & Wenk, H.-R. 2000. Texture analysis of a recrystallized quartzite using electron diffraction in the scanning electron microscope. *Journal of Structural Geology* 22, 91-104.
- Heilbronner Panozzo, R. 1992. The autocorrelation function: an image processing tool for fabric analysis. *Tectonophysics* 212, 351-370.
- Heilbronner, R. P. & Pauli, C. 1993. Integrated spatial and orientation analysis of quartz c-axes by computer-aided microscopy. *Journal of Structural Geology* 15, 369-382.
- Herwegh, M. & Handy, M. R. 1998. The origin of shape preferred orientations in mylonite, inferences from in-situ experiments on polycrystalline norcamphor. *Journal of Structural Geology* 20, 681-694.
- Hippert, J. F. 1998. Breakdown of feldspar, volume gain and lateral mass transfer during mylonitization of granitoid in a low metamorphic grade shear zone. *Journal of Structural Geology* 20, 175-193.

- Hirth, G. & Tullis J. 1992. Dislocation creep regimes in quartz aggregates. *Journal of Structural Geology* 14, 145-159.
- Hobbs, B. E. 1985. The geological significance of microfabric analyses. In: Wenk, H. -R. (Eds.) Preferred orientation in deformed metals and rocks. Academic Press, Orlando, 463-484.
- Hobbs, B. E., Means, W. D. & Williams, P. F. 1976. An outline of structural geology. Wiley, New York
- Hu, H. 1963. Annealing of silicon-iron single crystals. In: L. Himmel (Eds.) Recovery and Recrystallization of Metals, Wiley, New York, 311-378.
- Ildefonse, B., Lardeaux, J.-M. & Caron, J.-M. 1990. The behaviour of shape preferred orientation in metamorphic rocks: amphiboles and jadeites from the Monte Mucrone area (Sesia-Lanzo zone, Italian Western Alps). *Journal of Structural Geology* 12, 1005-1011.
- Ildefonse, B., Launeau, P., Bouchéz, J.-L. & Fernandez, A. 1992a. Effect of mechanical interactions on the development of shape preferred orientations: a two-dimensional experimental approach. *Journal of Structural Geology* 14, 73-83.
- Ildefonse, B., Sokoutis, D. & Mancktelow, N. 1992b. Mechanical interactions between rigid particles in a deforming ductile matrix. Analogue experiments in simple shear flow. *Journal of Structural Geology* 14, 1253-1266.
- Ildefonse, B. & Mancktelow, N. 1993. Deformation around rigid particles: the influence of slip at the particle/matrix interface. *Tectonophysics* 221, 345-359.
- Ion, S. E., Humphreys, F. J. & White, S. H. 1982. Dynamic recrystallization and the development of microstructure during the high temperature deformation of magnesium. *Acta Metallurgica* 30, 1909-1919.
- Jeffery, G. B. 1922. The motion of ellipsoidal particles in a viscous fluid. *Proceedings of the Royal Society, London* 102, 161-179.
- Jeffrey Giacomini, A. & Dealy J. M. 1993. Large-amplitude oscillatory shear. In: Collyer, A. A. (Eds.) Techniques in rheological measurement. Chapman and Hall, Cambridge, 285-331.
- Jessell, M. W. 1986. Grain boundary migration and fabric development in experimentally deformed octachloropropane. *Journal Structural Geology* 8, 527-542.
- Jessell, M. W. 1987. Grain-boundary migration microstructures in a natureally deformed quartzite. *Journal of Structural Geology* 9, 1007-1014.
- Jessell, M. W. & Lister, G. S. 1990. A simulation of the temperature dependence of quartz fabrics. In: R. J. Knipe & E. H. Rutter (Eds) Deformation Mechanisms, Rheology and Tectonics. Geological Society Special Publications 54, 353-362.
- Jessell, M. W., Bons P. D., Evans L., Barr T. D. & Stüwe K. 2001. Elle: the numerical simulation of metamorphic and deformation microstructures. *Computers and Geosciences* 27, 17-30.
- Jezek J., Melka R., Schulmann K. & Venera, Z. 1994. The behaviour of rigid triaxial ellipsoidal particles in viscous flows - modeling of fabric evolution in a multiparticle system. *Tectonophysics* 229, 165-180.
- Jezek, J., Schulmann, K. & Segeth, K. 1996. Fabric evolution of rigid inclusions during mixed coaxial and simple shear flows. *Tectonophysics* 257, 203-221.
- Jiang, D. 1999. Vorticity decomposition and its application to sectional flow characterization. *Tectonophysics* 301, 243-259.
- Johnston J. D. & McCaffrey K. J. W. 1996. Fractal geometries of vein systems and the variation of scaling relationships with mechanism. *Journal of Structural Geology* 18, 349-358.
- Karato, S. I. & Masuda, T. 1989. Anisotropic grain growth in quartz aggregates under stress and its implication for foliation development. *Geology* 14, 1253-1266.

- Kerrich, R. 1986. Fluid transport in lineaments. Royal Society of London Philosophical Transactions 317, 219-251.
- Kerrick, D. M. 1987. Fibrolite in contact aureoles of Donegal, Ireland. American Mineralogist 72, 240-254.
- Kirby, S. H. 1983. Rheology of the lithosphere. Rev. Geophys. Space Physics 21, 1458-1487.
- Kirby, S. H. & Kronenberg, A. K. 1987. Rheology of the lithosphere: selected topics. Reviews in Geophysics 25, 1219-1244.
- Koyi, H., 1988. Experimental modeling of role of gravity and lateral shortening in Zagros Mountain belt. Bull. Am. Ass. Petrol. Geol. 72, 1381-1394.
- Kobberger, G. & Zulauf, G. 1995. Experimental folding and boudinage under pure constrictional conditions. Journal of Structural Geology 17, 1055-1063.
- Kocks, U. F., 1976. Laws for work-hardening and low-temperature creep. J. Engl. Mat. Tech. 98, 76-85.
- Kocks, U. F. 1985. Dislocation interactions: flow stress and strain hardening. In: Proceedings of the conference to celebrate the fiftieth anniversary of the concept of dislocation in crystals: Dislocations and Properties of real Materials, the Institute of Metals, London, 125-143.
- Kocks, U. F., Argon, A. S. & Ashby, M. F. 1975. Program Material Science 19.
- Kohlstedt, D. L. & Weathers, M. S. 1980. Deformation induced microstructures, paleo-piezometers and differential stresses in deeply eroded fault zones, Journal of Geophysical Research 85, 6269-6285.
- Krabbendam, M. & Dewey, J. F. 1998. Exhumation of UHP rocks by transtension in the Western Gneiss Region, Scandinavian Caledonides. In: Holdsworth, R. E., Strachan, R. A., Dewey, J. F. (Eds.) Continental Transpressional and Transtensional Tectonics. Geological Society, London, Special Publications 135, 159-181.
- Kretz, R. 1983. Symbols for rock-forming minerals. American Mineralogist 68, 277-279.
- Kruhl, J. H. (Eds.) 1994. Fractals and Dynamic Systems in Geosciences. Springer-Verlag Berlin Heidelberg.
- Knipe, R. J. 1989. Deformation mechanisms - recognition from natural tectonites. Journal of Structural Geology 11, 127-146.
- Knipe, R. J. & White, S. H. 1979. Deformation in low grade shear zones in the old red sandstone, S. W. Wales. Journal of Structural Geology 1, 53-66.
- Knipe, R. J. & Law, R. D. 1987. The influence of crystallographic orientation and grain boundary migration on microstructural and textural evolution in a S-C mylonite. Tectonophysics 135, 155-169.
- Knopf, E. B. 1933. Petrotectonics. American Journal of Science 225, 433-470.
- Kronenberg, A. K. & Tullis, J. 1984. Flow strengths of quartz aggregates: Grain size and pressure effects due to hydrolic weakening. Journal of Geophysical Research 89, 4281-4297.
- Law, R. D. 1990. Crystallographic fabrics: a selective review of their applications to research in structural geology. In: Knipe, R. J. & Rutter, E. H. (Eds) Deformation Mechanisms, Rheology and Tectonics, Geological Society Special Publications 54, 335-352.
- Launeau, P., Bouchéz, J-L & Benn, K. 1990. Shape preferred orientation of object populations: automatic analysis of digitized images. Tectonophysics 180, 201-211.
- Lewis G. N. & Randall, M. 1961. Thermodynamics. McGraw Hill, New York.
- Lisle, R. J. 1985. Geological Strain Analysis. In: A Manual for the Rf/F Technique. Pergamon Press, Oxford.
- Lisle, R. J., Rondeel, H. E., Doorn, D., Brugge, J. & van de Gaag, P. 1983. Estimation of viscosity contrast and finite strain from deformed elliptical inclusions. Journal of Structural Geology 5, 603-609.

- Lister, G. S., Paterson, M. S. & Hobbs, B. E. 1978. The simulation of fabric development in plastic deformation and its application to quartzite, the model. *Tectonophysics* 45, 107-158.
- Lister, G. S. & Hobbs, B. E. 1980. The simulation of fabric development during plastic deformation and its application to quartzite-the influence of deformation history. *Journal of Structural Geology* 2, 355-371.
- Lister, G. S. & Paterson, M. S. 1979. The simulation of fabric development during plastic deformation and its application to quartzite: fabric transitions. *Journal of Structural Geology* 1, 99-115.
- Lister, G. S. & Williams, P. F. 1979. Fabric development in shear zones theoretical controls and observed phenomena. *Journal of Structural Geology* 1, 283-297.
- Lister, G. S. & Hobbs, B. E. 1980. The simulation of fabric development during plastic deformation and its applications to quartzite: the influence of deformation history. *Journal of Structural Geology* 2, 99-115.
- Lister, G. S. & Snoke & A. W. 1984. S-C Mylonites. *Journal of Structural Geology* 6, 617-638.
- Lloyd, G. E., Law, R. D., Mainprice, D. & Wheeler, J. 1992. Microstructural and crystal fabric evolution during shear zone formation. *Journal of Structural Geology* 14, 1079-1100.
- Lloyd, G. E. & Freeman, B. 1994. Dynamic recrystallization of quartz under greenschist conditions. *Journal of Structural Geology* 16, 867-881.
- Mackinnon, P., Fueten, F. & Robin, P. F. 1997. A fracture model for quartz ribbons in straight gneisses. *Journal of Structural Geology* 19, 1-14.
- Mardia, K. V. 1972. *Statistics of directional data*. Academic Press, London.
- Marsh, B. D. 1988. Crystal size distribution (CSD) in rocks and the kinetics and dynamics of crystallization. I. Theory. *Contributions to Mineralogy and Petrology* 99, 277-291.
- Mandelbrot, B. B. 1967. How long is the coast of Britain? Statistical self-similarity and fractional dimension. *Science* 156, 636-638.
- March, A. 1932. Mathematische Theorie bei Regelung nach Korngestalt bei affiner Deformation. *Zeitschrift für Kristallographie* 81, 285-298.
- Masuda, T. & Fujimura, A. 1981. Microstructural development of fine-grained quartz aggregates by syntectonic recrystallization. *Tectonophysics* 72, 105-128.
- Masuda, T., Kugimiya, Y., Aoshima, I., Hara, Y. & Ikei, H. 1999. A statistical approach to determination of mineral lineation. *Journal of Structural Geology* 21, 467-472.
- Masuda, T., Mizuno N., Kobayashi, M. & Nam, T. N. 1995a. Stress and strain estimates for Newtonian and non-Newtonian materials in a rotational shear zone, *Journal of Structural Geology* 17, 451-454.
- Masuda, T., Michibayashi, K. & Ohta, H. 1995b. Shape preferred orientation of rigid particles in a viscous matrix: re-evaluation to determine kinematic parameters of ductile deformation. *Journal of Structural Geology* 17, 115-130.
- Masuda, T. & Mizuno, N. 1996. Deflection of non-Newtonian simple shear flow around a rigid cylindrical body by the Finite Element Method. *Journal of Structural Geology* 17, 115-130.
- McClay, K. R. 1976. The rheology of plasticine. *Tectonophysics* 33, T7-T15.
- McLelland, J. M. 1984. The origin of ribbon lineation within the southern Adirondacks, U.S.A.. *Journal of Structural Geology* 6, 147-157.
- Means, W. D. 1981. The concept of steady-state foliation. *Tectonophysics* 78, 179-199.
- Means, W. D. 1983. Microstructure and micromotion in recrystallization flow of octachloropropane, a first look. *Geologische Rundschau* 72, 511-528.

- Means, W. D. 1989. Synkinematic microscopy of transparent polycrystals. *Journal of Structural Geology* 11, 163-174.
- Means, W. D., Hobbs, B. E., Lister, G. S. & Williams, P.F. 1980. Vorticity and non-coaxiality in progressive deformation. *Journal of Structural Geology* 2, 371-378.
- Means, W. D. & Paterson M. S. 1966. Experiments on preferred orientation of platy minerals. *Contributions to Mineralogy and Petrology* 13, 108-133.
- Means, W. D. & Ree, J. H. 1988. Seven types of sub-grain boundaries in octachloropropane. *Journal of Structural Geology* 10, 765-770.
- Mecking, H. & Kocks, U. F. 1981. Kinetics of flow and strain-hardening. *Acta Metallurgica* 29, 1865-1875.
- Nataf, H.-C., Hager, B. H. & Scott, R. F. 1984. Convection experiments in a centrifuge and the generation of plumes in a very viscous fluid. *Ann. Geophys.* 2, 303-310.
- Nelson, B. I. & Dealy, J. M. 1993. Dynamic mechanical analysis using complex waveforms. In: Collyer, A. A. (Eds.) *Techniques in rheological measurement*, Chapman and Hall, 197-224.
- Nicolls, J. H. & McCormick, P. G. 1970. *Metallurgical Transactions* 1, 3469.
- Odonne, F. 1994. Kinematic behaviour of an interface and competence contrast: analogue models with different degrees of bonding between deformable inclusions and their matrix. *Journal of Structural Geology* 16, 997-1006.
- O'Hara, K. 1990. State of strain in mylonites from the western Blue Ridge province, southern Appalachians: the role of volume loss. *Journal of Structural Geology* 12, 419-430.
- Olding, N. E. 1984. Strain analysis and strain path modelling in the Loch Tollie gneisses, Gairloch, NW Scotland. *Journal of Structural Geology* 6, 543-562.
- Olgaard, D. L. & Evans, B. 1986. Effect of second phase particles on grain growth in calcite. *Journal of the American Ceramical Society* 69C, 272-277.
- Olgaard, D. L. & Evans, B. 1988. Grain growth in synthetic marbles with added mica and water. *Contributions to Mineralogy and Petrology* 100, 246-260.
- Olsen T. S. & Kohlstedt, D. L. 1985. Natural deformation and recrystallization of some intermediate plagioclase feldspars. *Tectonophysics* 111, 107-131.
- Pakula, T., Geyler, S. , Edling, T. & Boese, D. 1996. Relaxation and viscoelastic properties of complex polymer systems. *Rheologica Acta* 35, 631-644.
- Pan, J., Cocks, A. C. F. & Kucherenko, S. 1997. Finite element formulation of coupled grain-boundary and surface diffusion with grain-boundary migration. *Proc. R. Soc. London* 453, 2161-2184.
- Panozzo, R. 1983. Two dimensional analysis of shape-fabric using projections of digitized lines in a plane. *Tectonophysics* 95, 279-294.
- Panozzo, R. 1984. Two-dimensional strain from the orientation of lines in a plane. *Journal of Structural Geology* 6, 215-221.
- Passchier, C. W. 1982. Mylonitic deformation in the Saint-Barthélemy Massif, French Pyrenees, with emphasis on the genetic relationship between ultramylonite and pseudotachylite. *GUA Pap. Geo. Ser.1-16*, 1-173.
- Passchier, C. W. 1986. Flow in natural shear zones – the consequences of spinning flow regimes. *Earth and Planetary Science Letters* 77, 70-80.
- Passchier, C. W. 1987. Stable positions of rigid objects in non-coaxial flow- a study in vorticity analysis. *Journal of Structural Geology* 9, 679-690.

- Passchier, C. W. 1991a. The classification of dilatant flow types. *Journal of Structural Geology* 13, 101-104.
- Passchier, C. W. 1991b. Geometric constraints on the development of shear bands in rocks. *Geologie en Mijnbouw* 30, 203-211.
- Passchier, C. W. 1994. Mixing in flow perturbations: a model for development of porphyroclasts in mylonites. *Journal of Structural Geology* 16, 733 - 736.
- Passchier, C. W. 1993. Stair stepping around rigid objects: a tool in kinematic analysis. *Terra Abs.* 5, 308-309.
- Passchier, C. W. 1997. The fabric attractor. *Journal of Structural Geology* 19, 113-127.
- Passchier, C. W. 1998. Monoclinic model shear zones. *Journal of Structural Geology* 20, 1121-1137.
- Passchier, C. W., & Simpson, C. 1986. Porphyroclast systems as kinematic indicators. *Journal of Structural Geology* 8, 831-844.
- Passchier, C. W. & Sokoutis, D. 1993. Experimental modelling of mantled porphyroclasts. *Journal of Structural Geology* 15, 895-909.
- Passchier, C. W., ten Brink, C. E., Bons, P. D. & Sokoutis, D. 1994. Stair stepping as a natural gauge for the strain-rate sensitivity of stress in deformed rocks. *Earth and Planetary Science Letters* 120, 239-245.
- Passchier, C. W. & Trouw, R. A. J. 1996. *Microtectonics*: Springer, Berlin.
- Paterson, S. R. 1983. A comparison of methods used in measuring finite strains from ellipsoidal objects. *Journal of Structural Geology* 5, 611-618.
- Pennacchioni, G., Fasolo, L., Cecchi, M. M. & Salasnich, L. 2000. Finite-element modelling of simple shear flow in Newtonian and non-Newtonian fluid around a circular rigid particle. *Journal of Structural Geology* 22, 683-692.
- Peterson, V. L. & Robinson, P. 1993. Progressive evolution from uplift to orogen-parallel transport in a late-acadian, upper amphibolite- to granulite-facies shear zone, south-central Massachusetts. *Tectonics* 12, 550-567.
- Pfiffner, O. A. & Ramsay, J. G. 1982. Constraints on geological strain rates: Arguments from finite strain states of naturally deformed rocks. *Journal of Geophysical Research* 87, 311-321.
- Platt, J. P. 1979. Extensional crenulation cleavage. *Journal of Structural Geology* 1, 95-96.
- Platt, J. P. & Vissers, R. I. M. 1980. Extensional structures in anisotropic rocks. *Journal of Structural Geology* 2, 397-410.
- Poirier, J.-P. 1985. *Creep of Crystals*. Cambridge University Press, Cambridge.
- Poirier, J.-P. & Nicolas A. 1975. Deformation-induced recrystallization due to progressive misorientation of subgrains with special reference to mantle peridotites. *Journal of Geology* 83, 707-720.
- Post, A. D., Tullis, J. & Yund, R. A. 1996. Effect of chemical environment on dislocation creep of quartzite. *Journal of Geophysical Research* 101, 22143-22155.
- Price, N. J. & Cosgrove, J. W. 1990. *Analysis of geological structures*. Cambridge University Press, Cambridge.
- Price, G. P., & Torok, P. A. 1989. A new simple shear deformation apparatus for rocks and soils. *Tectonophysics* 158, 291-309
- Prior, D. J., Knipe, R. J. & Handy, M. R. 1990. Estimates of the rates of microstructural changes in mylonites. In: Knipe, R. J. and Rutter, E. H. (Eds) *Deformation Mechanisms, Rheology and Tectonics*, Geological Society Special Publication 54, 309-319.
- Rallison, J. M. 1984. The deformation of small viscous drops and bubbles in shear flows. *Ann. Rev. Fluid Mech.* 16, 45-66.
- Ramberg, H. 1975. Particle paths, displacement and progressive strain applicable to rocks. *Tectonophysics* 28, 1-37

- Ramberg, H. 1955. Natural and experimental boudinage and pinch-and-swell structures. *Journal of Geology* 63, 512-526.
- Ramsay, J. G. 1958. Superposed folding in Loch Mona, Inverness-shire and Ross-shire. *Quarterly Journal of the Geological Society of London* 113, 271-308.
- Ramsay, J. G. 1967. *Folding and Fracturing of Rocks*. Mac-Graw-Hill, New York, N. Y.
- Ramsay, J. G. 1980. Shear zone geometry: a review. *Journal of Structural Geology* 2, 83-99.
- Ramsay, J. F. & Huber, M. I. 1983. *The techniques of modern structural geology*, Volume 1, Strain analysis. Academic Press.
- Randle, V., Ralph, B. & Hansen, N. 1986. Grain growth in crystalline materials, In: Shewchuk, J.R. (Eds.) *First Workshop on Applied Computational Geometry*, ACM, 124-133.
- Randle, V. 1992. Microtexture determination and its applications. *The Institute of Materials*, London.
- Read, W. T. & Shockley, E. 1950. Dislocation models of crystal grain boundaries. *Physical Review* 78, 275-289.
- Rees, A. I. 1968. The production of preferred orientation in a concentrated dispersion of elongated and flattened grains. *Journal of Geology* 76, 457-465.
- Rees, A. I. 1979. The orientation of grains in a sheared dispersion. *Tectonophysics* 58, 275-287.
- Ree, J.-H. 1990. High temperature deformation of octachloropropane: dynamic grain growth and lattice reorientation. In: R. J. Knipe & E. H. Rutter (Eds) *Deformation Mechanisms, Rheology and Tectonics*. Geological Society Special Publications 54, 363-368.
- Reed, L. J. & Tryggvason, E. 1974. Preferred orientation of rigid particles in a viscous matrix deformed by pure shear and simple shear. *Tectonophysics* 24, 85-98.
- Rees A. I. 1979. The orientation of grains in a sheared dispersion. *Tectonophysics* 58, 275-287.
- Robertson, C. R. & Acrivos, A. 1970. Low Reynolds number shear flow past a rotating circular cylinder. Part 1. Momentum transfer. *Journal of Fluid Mechanics* 40, 68-704.
- Robin, P.-Y. F. 1979. Theory of metamorphic segregation and related processes. *Geochimica Cosmochimica Acta* 43, 1587-1600.
- Robin, P.-Y. F. & Cruden, A. R. 1994. Strain and vorticity patterns in ideally ductile transpression zones. *Journal of Structural Geology* 16, 447-466.
- Roman-Berdiel, T., Gapai, D. & Brun, J. P. 1995. Analogue models of laccolith formation. *Journal of Structural Geology* 17, 1337-1346.
- Rutter, E. H. 1998. On the relationship between the formation of shear zones and the form of the flow law for rocks undergoing dynamic recrystallization. *Tectonophysics* 303, 147-158.
- Rutter, E. H. & Brodie, K. H. 1995. Mechanistic interaction between deformation and metamorphism. *Geological Journal* 30, 227-240.
- Sander, B. 1948. *Einführung in die Gefügekunde der geologischen Körper*. Bd. I, Springer Verlag, Wien.
- Sander, B. 1950. *Einführung in die Gefügekunde der geologischen Körper*. Bd. II, Springer Verlag, Wien.
- Sanderson, D. J., & Marchini, W. R. D. 1984. Transpression. *Journal of Structural Geology* 6, 449-458.
- Sandström, R. 1977. Subgrain growth occurring by boundary migration. *Acta Metallurgica* 25, 905-911.
- Schmid, S. M. 1976. Rheological evidence for changes in the deformation mechanism of Solnhofen limestone towards low stresses. *Tectonophysics* 31, T21-T28.

- Schmid, S. M. & Casey, M. 1986. Complete fabric analysis of some commonly observed quartz c-axis patterns. In: Hobbs, B. E. Heard, H. C. (Eds) *Mineral and Rock Deformation: Laboratory Studies – The Paterson volume*. American Geophysical Union, Geophysical Monograph 36, 263 – 286.
- Schulmann, K., Jezek, J. & Venera, Z. 1997. Perpendicular linear fabrics in granite: marked combined simple shear and pure shear flows? In: Bouchéz, J. L., Hutton, D. H. W., Stephens, W. E. (Eds.) *Granite: From Segregation of Melt to Emplacement Fabrics*, 159-176.
- Sellars, C. M. 1978. Recrystallization of metals during hot deformation. *Philosophical Transactions of the Society of London* 288, 147-158.
- Shackleton, R. 1993. Tectonics of the lower crust: a view from the Usambara Mountains, NE Tanzania. *Journal of Structural Geology* 15, 663-671.
- Shackleton, R. M. & Ries, A. C. 1984. The relation between regionally consistent stretching lineations and plate motions. *Journal of Structural Geology* 6, 111-117.
- Shewchuk, J. R. 1996. First Workshop on Applied Computational Geometry, ACM, 124-133.
- Shigematsu, N. 1999. Dynamic recrystallization in deformed plagioclase during progressive shear deformation. *Tectonophysics* 305, 437-452.
- Shimamoto, T., Ikeda, Y. 1976. A simple algebraic method for strain estimation from deformed ellipsoidal objects. 1. Basic theory. *Tectonophysics* 36, 315-337.
- Sinha, A. K., Hewitt, D. A. & Rimstidt, F. D. 1986. Fluid interaction and element mobility in the development of ultramylonites. *Geology* 14, 883-886.
- Simpson, C. 1983. Strain and shape fabric variations associated with ductile shear zones. *Journal of Structural Geology* 5, 61-73.
- Stephens, M. B., Glasson, M. J. & Keays, R. R. 1979. Structural and chemical aspects of metamorphic layering development in metasediments from Clunes, Australia. *American Journal of Science* 29, 129-160.
- Stöckhert, B. & Duyster, J. 2000. Discontinuous grain growth in recrystallised vein quartz - implications for grain boundary structure, grain boundary mobility, crystallographic preferred orientation, and stress history. *Journal of Structural Geology* 21, 1477-1490.
- Stöckhert, B., Brix, M. R., Kleinschrodt, R., Hurford, A. J. & Wirth, R. 1999. Thermochronometry and microstructures of quartz – a comparison with experimental flow laws and prediction on the temperature of the brittle-plastic transition. *Journal of Structural Geology* 21, 351-369.
- Stüwe, H. P. 1965. *Acta Metallurgica* 13, 1337.
- Soares, A. Ferro, A. C. & Fortes, M. A. 1985. Computer simulation of grain growth in a bimodal polycrystal. *Scripta Metallurgica* 19, 1491-1496.
- Sokoutis, D. 1987. Finite strain effects in experimental mullions. *Journal of Structural Geology* 9, 233-242.
- Srolovitz, D. J., Anderson, M. P., Grest, G. S. & Sahini, P. S. 1984. Computer simulation of grain growth – III. Influence of particle dispersion. *Acta Metallurgica* 32, 1429-1438.
- Sutton, J. & Watson, J. 1955. The structure and stratigraphic succession of the Moines of Fannich Forest and Strath Bran, Ross-shire. *Quarterly Journal of the Geological Society of London* 110, 21-53.
- Talbot, C. J. 1999. Ductile shear zones as counter-flow boundaries in pseudoplastic fluids. *Journal of Structural Geology*, 21, 1535-1551.
- Takahashi, M., Nagahama, H., Masuda, T. I. & Fujimura, A. 1998. Fractal analysis of experimentally, dynamically recrystallized quartz grains and its possible application as a strain rate meter. *Journal of Structural Geology* 20, 269-275.

- Takeshita, T., Wenk, H.-R. & Lebensohn, R. 1999. Development of preferred orientation and microstructure in sheared quartzite: comparison of natural data and simulated results. *Tectonophysics* 312, 133-155.
- Taylor, G. I. 1938. Plastic strain in metals. *J. Inst. Metals* 62, 307-324.
- Tikoff, B. & Greene, D. 1997. Stretching lineations in tranpressional shear zones: an example from the Sierra Nevada Batholith, California. *Journal of Structural Geology* 19, 29-39.
- Tikoff, B. & Fossen, H. 1993. Simultaneous pure and simple shear: the unifying deformation matrix. *Tectonophysics* 217, 267-283.
- Tikoff, B. & Fossen, H. 1999. Three-dimensional reference deformations and strain facies. *Journal of Structural Geology* 21, 1497-1512.
- Treagus, S. H. & Sokoutis, D. 1992. Laboratory modelling of strain variation across rheological boundaries. *Journal of Structural Geology* 14, 405-424.
- Treagus, S. H., Hudleston, P. J., Lan, L. 1996. Non-ellipsoidal inclusions as geological strain markers and competence indicators. *Journal of Structural Geology* 18, 1167-1172.
- Treagus, S. H. & Lan, L. 2000. Pure shear deformation of square objects, and applications to geological strain analysis. *Journal of Structural Geology* 22, 105-122.
- Trimby, P. W., Prior, D. J. & Wheeler, J. 1998. Grain boundary hierarchy development in a quartz mylonite. *Journal of Structural Geology* 20, 913-935.
- Trimby, P. W. & Prior, D. J. 1999. Microstructural imaging techniques - a comparison between light and scanning electron microscopy. *Tectonophysics* 303, 71-81.
- Trimby, P. W., Drury, M. R. & Spiers, C. J. 2000. Misorientations across etched boundaries in deformed rocksalt: a study using electron backscatter diffraction. *Journal of Structural Geology* 22, 81-89.
- Tsenn, M. C. & Carter, N. I. 1987. Upper limits of power law creep of rocks. *Tectonophysics* 136, 1-26.
- Tobisch, O. T. & Williams, Q. 1998. Use of microgranitoid enclaves as solid state strain markers in deformed granitic rock: an evaluation. *Journal of Structural Geology* 20, 727-743.
- Tullis, J. & Yund, R. A. 1982. Grain growth kinetics of quartz and calcite aggregates. *Journal of Geology* 90, 301-318.
- Tullis, J. & Yund, R. A. 1985. Dynamic recrystallization of feldspar: a mechanism for ductile shear zone formation. *Geology* 13, 238-241.
- Tullis, J. & Yund, R. A. 1988. The effects of hydrogen, oxygen and water fugacities and confining pressure on the strength of quartz aggregates. *Trans. AGU* 69, 478.
- Tullis, J. & Yund, R. A. 1989. Hydrolytic weakening of quartz aggregates: the effects of water and pressure on recovery. *Geophysical Research Letters* 16, 1343-1346.
- Turcotte, D. L. 1993. *Fractals and chaos in geology and geophysics*. Cambridge University Press, Cambridge.
- Turner, F. J. & Weiss, L. E. 1968. *Structural Analysis of Metamorphic Tectonites*. McGraw-Hill Book Company, New York.
- Twiss, R. J. 1977. Theory and applicability of recrystallized grain size paleopiezometer. *Pure and Applied Geophysics* 115, 199-226.
- Twiss, R. J. & Moores, M. E. 1992. *Structural Geology*. W. H. Freeman and Company, New York.
- Urai, J. L. 1983. Deformation of wet salt rocks. Ph D thesis, Utrecht Univ, pp 1-223.
- Urai, J. L., Humphreys, F. J. & Burrows, E. 1980. In situ studies of the deformation and dynamic recrystallization of rhombohedral camphor. *Journal of Material Sciences* 15, 1231-1240.
- Urai, J. L., Means, W. D. & Lister, G. S. 1986. Dynamic recrystallization of minerals. *American Geophysical Union Geophysical Monograph* 36, 161-199.

- Vernon, R. H., Etheridge, M. A. & Wall, V. J. 1988. Shape and microstructure of microgranitoid enclaves: Indicators of magma mingling and flow. *Lithos* 22, 1-11.
- Vernon, R. H. 1987. Growth and concentration of fibrous sillimanite related to heterogeneous deformation in K-feldspar-sillimanite metapelites. *Journal of Metamorphic Geology* 5, 51-68.
- Vernon, R. H. 1981. Optical microstructure of partly recrystallised calcite in some naturally deformed marbles. *Tectonophysics* 78, 601-612.
- Vissers, R. L. M. 1989. Asymmetric quartz c-axis fabric and flow vorticity: a study using rotated garnet. *Journal of Structural Geology* 11, 231-244.
- von Mises, R. 1928. *Mechanik der plastischen Formänderung von Kristallen*. *Z. Angew. Math. Mech.* 8, 161-185.
- Wallis, S. 1995. Vorticity analysis and recognition of ductile extension in the Sanbagawa belt, SW Japan. *Journal of Structural Geology* 17, 1077-1093.
- Weaire, D. & Riviere, N. 1984. Soap, Cells and Statistics – Random Patterns in Two Dimensions. *Contemporary Physics* 25, 59-99.
- Weijermars, R. 1986. Flow behaviour and physical chemistry of bouncing putties and related polymers in view of tectonic laboratory applications. *Tectonophysics* 124, 325-358.
- Weijermars, R. 1992. Progressive deformation in anisotropic rocks. *Journal of Structural Geology* 14, 723-742.
- Weijermars, R. 1993. Pulsating strains. *Tectonophysics* 220, 51-67.
- Weijermars, R. 1997. Pulsating oblate and prolate three-dimensional strains. *Mathematical Geology* 29, 17-41.
- Weijermars, R. 1998. Taylor-mill analogs for patterns of flow and deformation in rocks: *Journal of Structural Geology* 20, 77-92.
- Weiss, L.E. & Wenk H.- R. 1985. An introduction. In: Wenk, H.-R. (Eds.) *Preferred Orientation in Deformed Metals and Rocks: An Introduction to Modern Texture Analysis*, Academic Press, London, pg. 1-9.
- Wenk, H. R. 1998. Deformation of mylonites in Palm Canyon, California, based on xenolith geometry. *Journal of Structural Geology* 20, 559-571.
- Wenk, H. R., Bennett, K., Canove, G. R. , Molinari, A. 1991. Modelling plastic deformation of peridotite with the self-consistent theory. *Journal of Geophysical Research* 96, 8337-8349.
- Wenk, H.-R., Takeshita, T., Bechler, E. Erskine, B. G. & Matthies, S. 1987. Pure and simple shear calcite textures. Comparison of experimental, theoretical and natural data. *Journal of Structural Geology* 9, 731-745.
- Wenk, H. R. & Tomé, C. N. 1999. Modeling dynamic recrystallization of olivine aggregates deformed in simple shear. *Journal of Geophysical Research* 104, 25523-25527.
- White, S. H. 1977. Geological significance of recovery and recrystallization processes in quartz. *Tectonophysics* 39, 143-170.
- White, S. H. 1979a. Grain and sub-grain size variations across a mylonite zone. *Contributions to Mineralogy and Petrology* 70, 193-202.
- White, S. H. 1979b. Large strain deformation: report on a Tectonic Studies Group discussion meeting held at Imperial College London. *Journal of Structural Geology* 1, 333-339.
- Whitehead, J. A. & Luther, D. S. 1975. Dynamics of laboratory diapir and plume models. *Journal of Geophysical Research* 80, 705-717.
- Williams, Q. & Tobisch, O. T. 1994. Microgranitic enclave shapes and magmatic strain histories: Constraints from drop deformation theory. *Journal of Geophysical Research* 99, 24359-24368.

- Wilson, C. J. L. 1986. Deformation induced recrystallization of ice: the application of in situ experiments. *Geophysical Monograph* 36, 213-232.
- Winter, H. H., Baumgärtel, M. & Soskey, P. R. 1993. A parsimonious model for viscoelastic liquids and solids. In: Collyer, A. A (Eds.) *Techniques in rheological measurement*. Chapman and Hall, 123-160.
- Zhang, Y. & Wilson C J. L. 1997. Lattice rotation in polycrystalline aggregates and single crystals with one slip system, a numerical and experimental approach. *Journal of Structural Geology* 19, 875-885.

Internet References

- Barr & Houseman, 1999. Basil – Finite element program, <http://www.earth.monash.edu.au/Research/Basil>
- Evans et al. 1999. Elle – Micro-process based simulation of metamorphic and deformation texture development, <http://www.earth.monash.edu.au/Research/Elle>
- Evans et al. 2000. Elle Manual, <http://orion.earth.monash.edu.au/Research/Elle/Monash/index.html>
- Murta. Generic Polygon Clipper library, <http://www.cs.man.ac.uk/aig/staff/alan/software>
- Radhikrishnan et al. <http://www.ornl.gov/ORNLReview/v30n3-4>
- Shewchuk, Triangle: A Two-Dimensional quality Mesh Generator and Delaunay Triangulator, <http://www.cs.cmu.edu/~quake/triangle.html>

Zusammenfassung für Laien

Diese Zusammenfassung ist für den interessierten Leser ohne geologischen Hintergrund gedacht, der wissen möchte was in dieser Doktorarbeit untersucht wird. Der Leser mit geologischem Hintergrund hingegen wird gebeten die wissenschaftliche Zusammenfassung am Anfang der Doktorarbeit zu lesen.

Ein wichtiges Ziel der Forschung in den Geowissenschaften ist die Entwicklung und Verfeinerung der Kunst, ein Gestein lesen und verstehen zu können. Das bedeutet, daß ein Geologe einen Stein, den er an der Erdoberfläche findet, aufheben, analysieren und charakterisieren will. Mit Hilfe der so gewonnenen Informationen will er die Geschichte des Gesteins und damit seiner Umgebung nachvollziehen und verstehen. Besondere Beachtung findet dabei die Art und Weise der Verformung (Kinematik) und die der Beanspruchung (Dynamik) des Gesteins.

In Gesteinen sind Strukturen zu beobachten, die durch ihre längliche, dreidimensionale Form und durch die Einregelung, das heißt ähnliche oder gleiche Orientierung der längsten Achse von solchen länglichen Elementen charakterisiert sind. Diese Strukturen nennt der Geologe Formregelungs-Gefüge (engl. shape fabric).

In der vorliegenden Arbeit wird die Entwicklung von Formregelungs-Gefügen während der fortschreitenden Verformung untersucht. Ziel ist es, ein besseres Verständnis für die Gefügeentwicklung zu erarbeiten und, basierend auf diesem Verständnis, neue Methoden zur Charakterisierung und zur Interpretation von beobachteten Gefügen dem Geologen bereitzustellen.

Folgende Fragen müssen hierbei beantwortet werden:

1. Erlaubt die dreidimensionale Form und Art der Einregelung Rückschlüsse auf die Art des Fließens und des Beanspruchungsplans?
2. Welche Faktoren müssen beobachtet und beachtet werden, um qualitative und quantitative Aussagen über die Entwicklung eines Gesteins treffen zu können?

Nun geht die natürliche Verformung des Gesteins so langsam von statten, daß ein Menschenleben zu kurz ist, um bedeutsame Verformungen beobachten zu können. Dennoch gibt es Möglichkeiten, die Entwicklung eines Gesteins nachzuvollziehen.

Eine Möglichkeit ist die Untersuchung von ausgewählten Gesteinproben, bei denen wenigstens ein Teil der Parameter, wie zum Beispiel die vorherrschende Temperatur, der Druck und die Art der Verformung, bereits bekannt sind. Um zum Beispiel die Entwicklung des Gefüges während der fortschreitenden Verformung zu untersuchen, können Gesteinsproben genommen werden, die sukzessive keine, eine schwache, starke und sehr starke Vorformung aufweisen.

Eine weitere Möglichkeit ist es, die Verformung "nachzuspielen", also im Labor zu simulieren. In der Erdtiefe bei hohen Temperaturen (400-1000 °C) und hohen Drucken (5-30 kbar) verhalten sich Gesteine wie sehr zähfließende Flüssigkeiten. Soll nun die Entwicklung eines Gesteines während der Verformung in relative kurzen Zeiträumen (z.B. 5-120 min.) simuliert werden, kann man eine teigartige Masse kontrolliert verformen. Der Vergleich der in den Teigmassen (z. B. Polymeren) beobachteten Strukturen, die sich unter bekannten Bedingungen gebildet haben, mit Strukturen, die in Gesteinen beobachtet werden, bietet neue Interpretationsansätze. Diese Art der Untersuchung nennt man Analogmodellierung.

Bei der Suche nach der "Lesekunst" helfen als dritte Möglichkeit computergestützte, numerische Modellierungen, mit denen die Verformung eines Gesteins und dessen Gefügeentwicklung simuliert werden können. Diese Modellierungen stützen sich auf physikalische Gesetze. Auch können in den Modellen verschiedene Parameter systematisch variiert werden. So läßt sich der Einfluß der gewählten Parameter auf die Gefügeentwicklung untersuchen, und es lassen sich die Resultate auf Gesteine übertragen.

Diese drei Methoden kommen in der vorliegenden Arbeit zur Anwendung und führen zu den folgenden beiden Ergebnissen:

A. Neue Erkenntnisse über den Nutzen von Formregelungs-Gefügen zur Erfassung der Deformationsgeschichte eines Gesteins.

B. Die Entwicklung und/oder Ausweitung von neuen Methoden, die in Zukunft zur Lösung geologischer Fragestellungen beitragen können.

Folgende neue Erkenntnisse (zu A.) haben sich aus der Arbeit ergeben:

1. Der Grad der Einregelung ist nicht zwingend mit dem Ausmaß der Verformung gleichzusetzen. Wichtige beeinflussende Faktoren sind das Gefüge des Gesteines vor der Verformung, das Fließverhalten der einzelnen Komponenten des Gesteines, die Art und Weise der Rekristallisation (Neuwachstum von Körnern, Verschiebung von Korngrenzen) und der Typ der Verformung.

2. Die verschiedenen Formen eines Elements in einer Matrix lassen auf den Viskositätskontrast bzw. -unterschied zwischen dem Element und dessen umgebenden Materials rückschließen. Aus diesen Formen kann in günstigen Fällen die Art der Verformung bestimmt und der Viskositätskontrast ermittelt werden.

3. Die Einregelung von länglichen Objekten und entstehender Strukturen ist abhängig vom relativen Einfluß von einfacher und reiner Scherung. Bei der einfachen Scherung wird ein Quadrat zum geneigten Parallelogramm und bei der reinen Scherung zum Rechteck. Je höher der Einfluß der reinen Scherung, desto höher ist der Grad der Einregelung. Diese Eigenschaft kann zur Quantifizierung der Art der Verformung zur Hilfe genommen werden.

4. In einem Material, welches mit steigender Beanspruchung exponentiell weniger viskös wird, ist die Einregelung von länglichen Objekten stärker als in einem nicht exponentiell reagierenden Material. Deswegen kann der Grad der Einregelung als Hinweis für das Fließverhalten der Matrix genommen werden.

5. Die Rekristallisation des Gesteins während der Verformung kann maßgeblich das Gefüge des Gesteines beeinflussen. Welche Verformungsmechanismen dominieren, bestimmt die Charakteristik des Gefüges. Die Quantifizierung der Effekte von verschiedenen Verformungsmechanismen kann Aufschluß über die physikalischen Bedingungen während Verformung geben.

Folgende Erkenntnisse bei der Anwendung und Neuentwicklung von Methoden (zu B.) haben sich ergeben:

1. Polymere, die häufig als Materialien zur Analogmodellierung von geologischen Problemen benutzt werden, haben ein komplizierteres Fließverhalten als bisher angenommen. Um Ergebnisse von Experimenten mit diesen Materialien zur Interpretation von Gesteinen zur Hilfe zu nehmen, ist es notwendig das Fließverhalten der Materialien genau zu studieren.

2. Ein neues Deformationsgerät wurde entwickelt, mit dem eine große Anzahl von verschiedenen Beanspruchungsregimen modelliert werden kann.

3. Das numerische Modellierungsprogramm "Elle" wurde weiterentwickelt.

4. Eine neue Methode der Charakterisierung des Gefüges eines Gesteins wurde entwickelt. Diese Methode beschreibt die Geometrie von Korngrenzen in zwei Dimensionen.

Schließlich zeigt diese Arbeit, daß die Kombination von verschiedenen Untersuchungsmethoden nützlich ist, um die "Lese-Kunst" von Gesteinen zu verfeinern.

Curriculum Vitae

Sandra Caroline Piazolo
born 26. 05.1971 in Ulm, Germany

- 1988 exchange student in Hobart, Australia; Australian Higher School Certificate
- June 1991 German "Abitur" (Higher School Certificate), Majors in English, Geography and Mathematics
- October 1991- study of geology at the University of Freiburg, Germany
- July 1993 "Vordiplom" (BSc) in geology
- Sept- Nov. 1993 Internship at the Hawaiian Undersea Research Laboratory (HURL), Honolulu, USA
- Sept. 94 - July 95 study at the University College of Wales, Aberystwyth, UK. Modules taken: 2nd and 3rd year of geology and earth studies
- Nov. 95 - April 96 expedition to Antarctica as a member of the international German geoscientific expedition (GeoMaud 95/96); joined mapping of the mountain belt of Central Dronning Maud Land, sampling with special emphasis on calcsilicates and marbles.
- April - June 1997 research at Johns Hopkins University, Baltimore, USA
- Sept. 1997 "Diplom" (MSc); Masters thesis on Geological and petrological investigations in Central Dronning Maud Land, Antarctica.
- 1.Nov. 1997 - PhD within the Graduiertenkolleg at the University of Mainz, Supervisor: Prof. C. W. Passchier
Title: Shape fabric development during progressive deformation.
- June 1998 field work in Cap de Creus, Spain and Pyrennees, Andorra
- August 1998 field assistant in South Greenland studying the layered intrusion Illemausaq, co-supervision of 3 Master students
- Sept. 1998 field work in the southern Menderes Massif, Turkey
- Jan.- March 1999 research, further development of the numerical simulation environment Elle at the Monash University, Melbourne, Australia; DAAD (German Academic Exchange Service) scholarship
- August 1999 field assistant in SW Greenland studying intrusions of the Gardar Province
- Febr. - March 2000 visit at Monash University, Clayton, Melbourne (Australia). Further development and experimental runs using the numerical modelling system Elle.